PNNL-26399

Pacific Northwest
NATIONAL LABORATORY
Proudly Operated by Battelle Since 1965

Analysis of PARENT Technique Data

February 2018

RM Meyer
PG Heasler
AE Holmes

Prepared for the U.S. Nuclear Regulatory Commission
under a Related Services Agreement with the U.S. Department of Energy
CONTRACT DE-AC05-76RL01830

U.S. DEPARTMENT OF ENERGY

PACIFIC NORTHWEST NATIONAL LABORATORY
operated by
BATTELLE
for the
UNITED STATES DEPARTMENT OF ENERGY
under Contract DE-AC05-76RL01830

PNNL-26399

Analysis of PARENT Technique Data

RM Meyer
PG Heasler
AE Holmes

February 2018

Prepared for
the U.S. Nuclear Regulatory Commission
under a Related Services Agreement
with the U.S. Department of Energy
Contract DE-AC05-76RL01830

Pacific Northwest National Laboratory
Richland, Washington 99352

Summary

In this report, analysis of the Program for Assessing the Reliability of Emerging Nondestructive Technologies (PARENT) blind test data at the technique level of inspection data is documented along with a combined analysis of the Program for Inspection of Nickel-Alloy Components (PINC) and PARENT data collected from inspection of bottom-mounted instrumentation (BMI) test blocks. In PARENT, an inspection was defined as the application of a procedure by a team to examine a test block. The procedure could include the implementation of one or more techniques for flaw detection and sizing purposes. The outcome of an inspection by a procedure is then determined from combined information obtained from each technique employed by the procedure. In this effort, the analysis of data at the technique level is motivated by the desire to increase the sample size of eddy current testing (ECT) data collected from dissimilar metal weld test blocks in PARENT and to provide opportunity for more extensive comparison of data collected during "Blind" and "Quickblind" testing. The motivation for performing a combined analysis on data collected on BMIs in PINC and PARENT is also to increase sample size in an effort to derive more insight on the performance of techniques applied to inspect BMI test blocks.

The result of increasing the PARENT ECT data sample size by including technique-level ECT data was an improvement in the estimated detection performance. The sample size was increased by more than a factor of two and the probability of detection at 5 mm and 10 mm flaw depths increased substantially (from 23% to 34% at 5 mm and from 76% to 93% at 10 mm, respectively), making the results more consistent with PINC (80% at 5 mm and 99% at 10 mm).

A more extensive comparison between Blind and Quickblind testing was facilitated by analyzing phased-array ultrasonic testing (PAUT) and conventional ultrasonic testing (UT) data at the technique level. The result of this analysis indicates that detection performance in Quickblind testing was better than detection performance in Blind testing for both PAUT and conventional UT techniques. The comparison of depth sizing analysis results shows that depth sizing performance is similar between Blind and Quickblind testing for both PAUT and conventional UT techniques. Length sizing performance comparisons show that length sizing exhibits a negative bias in Quickblind testing relative to Blind testing when length sizing is performed by comparing the longest dimensions of flaws and associated indications. However, when length sizing is limited to axial flaws in the Blind testing and performed by only comparing the axial dimensions of flaws and associated indications in Blind testing and Quickblind testing, this negative bias is eliminated. The latter analysis was performed because the flaws in Quickblind testing were intended to be axially oriented even though destructive analysis indicated the flaws had a significant circumferential extent. These results indicate that the flaws in Quickblind test blocks produce nondestructive examination (NDE) responses consistent with axial flaws even though destructive analysis indicated significant branching of the flaws extending in the circumferential direction.

Finally, the sample size for BMI data was increased by combining PARENT data with PINC data. In this case, the number of teams from which results were available increased from two teams to six teams and the sample size more than doubled. The results indicated that higher frequency (> 250 kHz) ECT techniques performed better than lower frequency (< 250 kHz) ECT techniques and that techniques implemented with an array probe configuration performed worse than techniques not implemented in an array probe configuration. Array probe configurations also appeared to be associated with high false call rates. Low frequency (< 250 kHz) techniques were also associated with high false call rates; however, due to some confounding between frequency and array variables, it is likely that the array variable contributed strongly to these false call rates. Finally, significant difference in performance is observed, overall, between PINC and PARENT with PARENT performing better. This is likely caused by the nature of simulated flaws in the test blocks. PARENT test blocks utilized thermal fatigue cracks, which exhibited significant branching at the surface that could make them easier to detect with ECT.

Acknowledgments

The authors express appreciation to Bruce Lin and Iouri Prokofiev of the U.S. Nuclear Regulatory Commission (NRC) for their leadership of the PARENT extension efforts. Several people and organizations in Japan, South Korea, Finland, Switzerland, Sweden, and the United States contributed to the PARENT program. Specific contributing individuals and organizations are acknowledged in NUREG/CR-7235 and NUREG/CR-7236. For the sake of brevity, the list of participating organizations is not repeated here.

The authors would also like to thank Ms. Kay Hass for typing and editing versions and revisions of this document.

Acronyms and Abbreviations

BMI	bottom-mounted instrumentation
Circ.	circumferential
DMW	dissimilar metal weld
ECT	eddy current testing
FCP	false call probability
FCR	false call rate
ID	identification number
I.D.	inner diameter
LBDMW	large-bore dissimilar metal weld
LOB	lack of bond
NDE	nondestructive examination
NOBS	number of observations
O.D.	outer diameter
PARENT	Program for Assessing the Reliability of Emerging Nondestructive Technologies
PAUT	phased-array ultrasonic testing
PINC	Program for Inspection of Nickel Alloy Components
POD	probability of detection
RMSE	root-mean-square error
SBDMW	small-bore dissimilar metal weld
SC	solidification crack
SCC	stress corrosion crack
SI	slag inclusion
StDev	standard deviation
TFC	thermal fatigue crack
TOFD	time-of-flight diffraction
UT	ultrasonic testing

Contents

Figures

Tables

1.0 Introduction

In this report, analysis of The Program for Assessing the Reliability of Emerging Nondestructive Technologies (PARENT) blind test data at the technique level of inspection data is documented along with a combined analysis of the Program for Inspection of Nickel-Alloy Components (PINC) (Cumblidge et al. 2010) and PARENT data collected from inspection of bottom-mounted instrumentation (BMI) test blocks. In PARENT, an inspection was defined as the application of a procedure by a team to examine a test block. The procedure could include the implementation of one or more techniques. The outcome of an inspection by a procedure is then determined from combined information obtained from each technique employed by the procedure. The procedures are provided with specific identifications referred to as procedure IDs. The procedure ID is expressed as "Tech1.Tech2…TechN.TeamID" where Tech1 through TechN represent all the techniques used for a given procedure ID. The possible techniques include conventional ultrasonic testing (UT), phased-array UT (PAUT), eddy current testing (ECT), and time-of-flight diffraction UT (TOFD). For example, team 126 employs a procedure that includes a TOFD technique and an ECT technique; thus, its procedure name is TOFD.ECT.126. More information about how technique level data was recorded and combined to generate procedure level data is provided in Sections 4.1 and 4.2 of NUREG/CR-7235 (Meyer and Heasler 2017). In this effort, the analysis of data at the technique level is motivated by the desire to increase the sample size of ECT data collected from dissimilar metal weld (DMW) test blocks in PARENT and to provide opportunity for more extensive comparison of data collected during "Blind" and "Quickblind" testing. The motivation for performing a combined analysis on data collected on BMIs in PINC and PARENT is also to increase sample size in an effort to derive more insight on the performance of techniques applied to inspect BMI test blocks. Additional details about the PARENT blind testing, and the distinction between "Blind" testing and "Quickblind" testing can be accessed by reviewing NUREG/CR-7235 (Meyer and Heasler 2017).

The ECT performance reported in PARENT was worse than the performance reported in PINC. In PINC, ECT techniques were applied to small bore DMWs (SBDMWs); in PARENT, they were applied to large bore DMWs (LBDMWs). However, it is not clear why the test block size would have an influence on ECT performance. Another possible factor contributing to the difference in observed ECT performance in PINC and PARENT was the limited sample size in PARENT. In PARENT, only one ECT procedure was applied. Thus, the objective was to increase sample size by analyzing ECT data collected at the technique level and observe the influence on performance.

In PARENT, comparison between Blind and Quickblind testing was made by comparing the performance of procedures that were common to both tests. This limited the comparison to procedure UT.PAUT.113, which was applied in both Blind and Quickblind testing, and to procedures UT.ECT.144 and UT.ECT.106. These procedures are mostly identical with UT.ECT.144 applied to the Blind test and UT.ECT.106 applied to the Quickblind test. A comparison of Quickblind and Blind test results from procedures UT.PAUT.113, UT.ECT.144, and UT.ECT.106 is summarized in Section 6.3 of NUREG/CR-7235 (Meyer and Heasler 2017). A meaningful comparison of detection performance could not be performed because detection performance in Quickblind testing was perfect at the procedure level. With respect to sizing performance, the only distinct trend observed between Blind and Quickblind testing was an apparent strong negative bias in Quickblind length-sizing performance relative to Blind length-sizing performance.

Section 2.0 of this report includes a description of LBDMW test blocks P13 and P33 and Quickblind test blocks (P15, P16, P17, and P45) on which technique-level analysis of ECT, PAUT, and conventional UT data is performed. Section 3.0 describes the data analysis methodology. Section 4.0 documents the ECT technique analysis while the PAUT and conventional UT technique analysis is documented in Section 5.0. The results of BMI analysis are documented in Section 6.0. Finally, summary and conclusions are provided in Section 7.0.

2.0 Large-Bore Dissimilar Metal Weld Test Blocks

This section briefly describes the test blocks that are relevant to the technique-level analysis of PARENT blind test data. As noted, in Section 1.0, technique-level analysis was performed for several objectives, which included supplementing the ECT results obtained from procedure-level data in PARENT and to expand comparisons between Quickblind and Blind test results. For both of these objectives, LBDMW test blocks are the only applicable test blocks because SBDMW test blocks were not examined by any ECT procedures or techniques and the Quickblind test blocks are LBDMW test blocks. Thus, the description of test blocks is limited to LBDMW test blocks P33 and P13, and Quickblind test blocks P15, P16, P17, and P45 below.

2.1 Test Block P33

Test block P33 is a LBDMW test block with full circumference and it was inspected by procedures ECT.135, UT.TOFD. ECT.101, and UT.ECT.144 in PARENT. The coordinate system defined for acquiring and reporting data on test block P33 is provided in Figure 2.1. The zero point is defined as that location on the test block where X=0, Y=0, and Z=0. Figure 2.1 also provides the definitions for the directional vectors X+, Y+, and Z+ in relation to the zero point and with respect to the material construction of the test block. The location for Z=0, Y=0 is at the outer diameter (O.D.) surface of the test block, at the center of the weld, and is located a distance “D” from the face edge of the carbon steel pipe. The X=0 location is indicated by a punch marking on the test block outer surface. A summary of dimensions for test block P33 is provided in Table 2.1.

Artificial flaws were fabricated into test block P33 using a process known as weld solidification cracking. Weld solidification cracks (SCs) may be used to simulate service-type defects such as interdendritic stress corrosion cracking (IDSCC) or primary water stress corrosion cracking (PWSCC). The region where the cracks are fabricated are excised and filled with a “poisoned” weld metal that is designed to crack upon cooling. In this case, the SCs are tightened either through a welding process or through application of a mechanical pressure during fabrication to result in cracks with narrower width. Care must be taken when SCs are to be used to determine the capability of nondestructive examination (NDE) methods because the region of flaw fabrication may be too obvious for the examination, similar to flaws that are implanted, especially in base metal. For this reason, SCs are recommended for simulating flaws in weld regions.

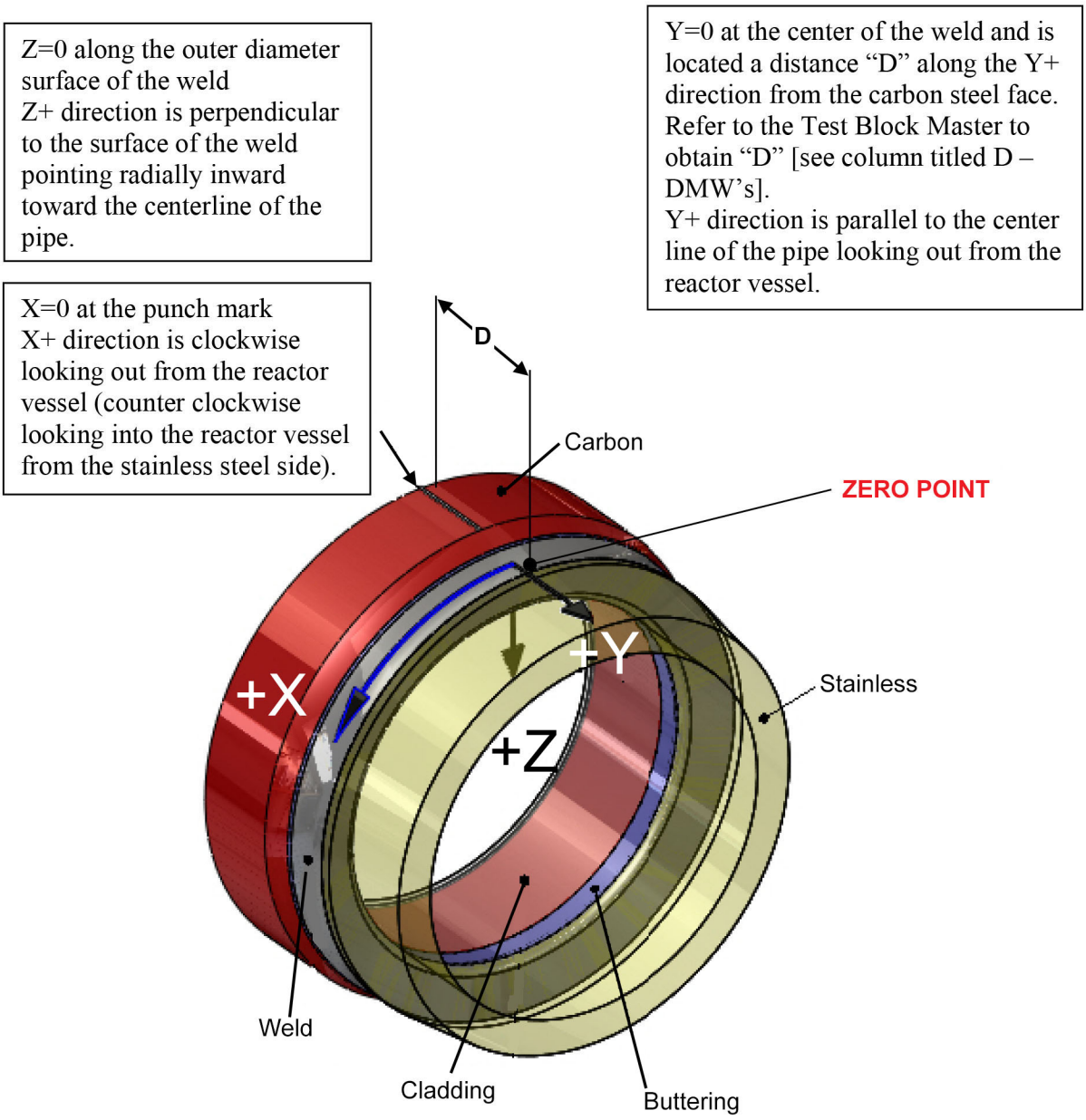

Figure 2.1. Coordinate System Definition for LBDMW Test Block P33

Table 2.1. Summary of Dimensions for P33

Test Block ID	Inner Diameter, mm	Outer Diameter, mm	Thickness, mm	D, mm	Circumferential Extent, degrees
P33	741.0	895.0	77.0	300.0	360.0

2.2 Test Block P13

Test block P13 and Quickblind test blocks P15, P16, P17, and P45 are distinct from test block P33 in that these test blocks are only sector portions of the DMW cut-out; whereas, the P33 test block is full circumference. Thus, the X=0 point is defined at a sector edge for these test blocks. The coordinate system defined for test block P13 is shown in Figure 2.2. A summary of dimensions for test block P13 is provided in Table 2.2.

Flaws were fabricated in test block P13 and Quickblind test blocks P15, P16, P17, and P45 using laboratory methods for introducing stress corrosion cracking (SCC) flaws. This allowed for the deliberate introduction of realistic flaws into test pieces at desired locations. However, even under laboratory conditions, the dimensions of SCC flaws can be difficult to control. In addition, it can be difficult to grow SCC flaws into complex geometries as it can be difficult to generate the necessary stresses to promote SCC growth. The morphology of the SCC flaws generated by this technique were clustered in nature.

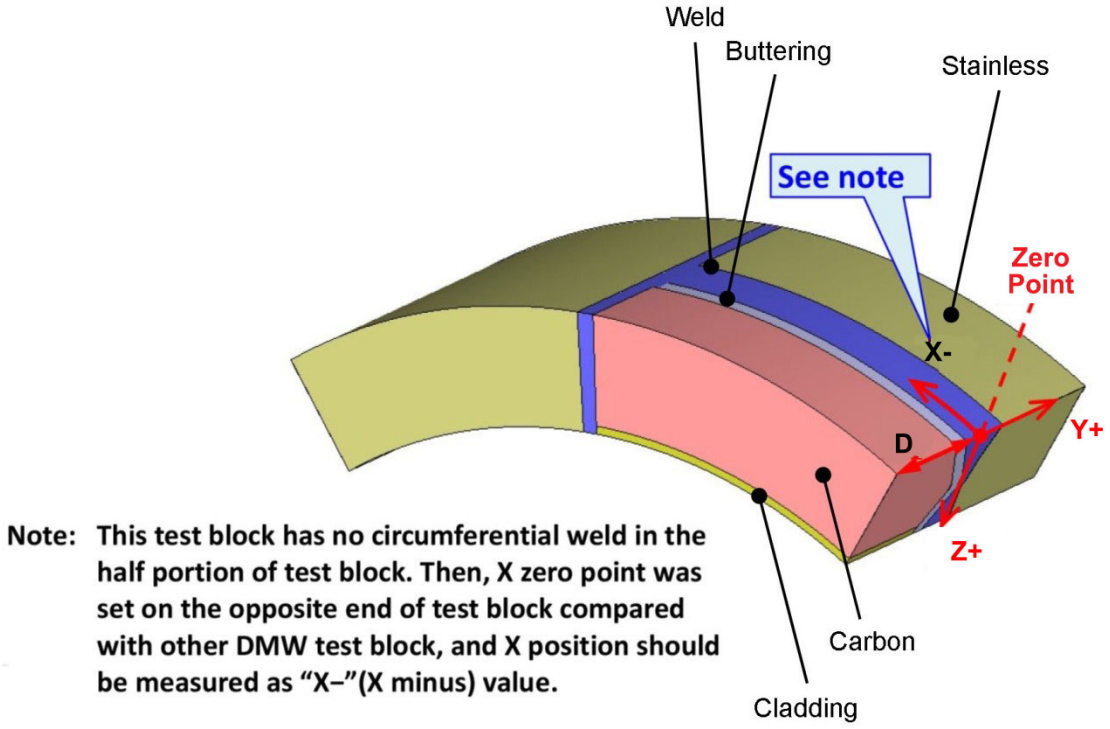

Figure 2.2. Coordinate System for LBDMW Test Block P13

Table 2.2. Summary of Dimensions for LBDMW Test Block P13

Test Block ID	Inner Diameter, mm	Outer Diameter, mm	Thickness, mm	D, mm	Axial Extent, mm	Circumferential Extent, degrees
P13	698.5	852.5	77.0	100.0	200.0	64.5

2.3 Quickblind Test Blocks (P15, P16, P17, and P45)

Four LBDMW test blocks (P15, P16, P17, and P45) were utilized in the Quickblind testing of PARENT. Similar to test block P13, the Quickblind test blocks are only sector portions of the DMW cut-out and are not full circumference like test block P33. Thus, the X=0 point is defined at a sector edge for those test blocks. Figure 2.3 depicts the coordinate system defined for these test blocks. Test blocks P15, P16, and P17 each contain one flaw, which is a SCC grown in situ to the test block through a laboratory process. Test block P45 is blank. A summary of dimensions for Quickblind test blocks is provided in Table 2.3. As noted in Section 2.2, the flaws introduced to Quickblind test blocks were fabricated by a laboratory process for growing SCC flaws.

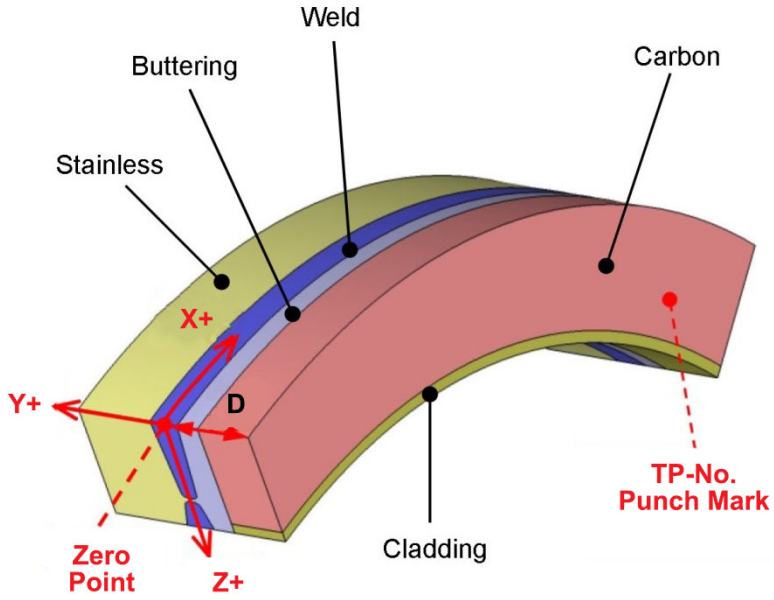

Figure 2.3. Coordinate System for Quickblind Test Blocks P15, P16, P17, and P45

Table 2.3. Summary of Dimensions for Quickblind Test Blocks P15, P16, P17, and P45

Test Block ID	Inner Diameter, mm	Outer Diameter, mm	Thickness, mm	D, mm	Axial Extent, mm	Circumferential Extent, degrees
P15	736.6	873.0	68.2	50.0	100.0	60.0
P16	736.6	873.0	68.2	50.0	100.0	60.0
P17	736.6	873.0	68.2	50.0	100.0	60.0
P45	736.6	873.0	68.2	51.5	105.0	60.0

3.0 Data Analysis Methodology

3.1 Scoring Procedure Used for PARENT Blind Round Robin

PARENT utilized the scoring criteria as described for the Program for Inspection of Nickel Alloy Components (PINC) which is described in Section 4.1 of NUREG/CR-7019 (Cumblidge et al. 2010). Similar to PINC, a tolerance was added to flaw true-state dimensions in PARENT to limit systematic positioning error resulting in legitimate detections being classified as misses. More precisely, however, tolerance was added to both flaws and indications in the actual scoring procedure in PARENT. Equal tolerances (i.e., δX/2 and δY/2) are added to the flaw and indication boundaries in the X (circumferential) and Y(axial) directions, respectively. The flaw cuboid, denoted by uppercase X_1, X_2; Y_1, Y_2; Z_1, Z_2, becomes,

$$(X_1 - \delta X/2,\ X_2 + \delta X/2,\ Y_1 - \delta Y/2,\ Y_2 + \delta Y/2,\ Z_1,\ Z_2) \tag{3.1}$$

and the indication cuboid, denoted by lowercase x_1, x_2; y_1, y_2; z_1, z_2, becomes,

$$(x_1 - \delta X/2,\ x_2 + \delta X/2,\ y_1 - \delta Y/2,\ y_2 + \delta Y/2,\ z_1,\ z_2)\,. \tag{3.2}$$

An illustration of tolerance applied to flaw (solid red) dimensions and indication (solid black) dimensions is provided in Figure 3.1, resulting in enlarged regions represented by white space with red and black borders, respectively. Any overlap of the areas defined by the tolerance boundaries for a flaw and indication results in classification of the indication as a hit (detection). In this effort scoring tolerances of δX = 10 mm and 15 mm were applied. The larger tolerance (δX = 15 mm) was found to be more appropriate for adequately correcting for positioning error and the smaller tolerance (δX = 10 mm) analysis was also performed so that results could be directly compared to results from the PARENT blind procedure in NUREG/CR-7235 (Meyer and Heasler 2017) and PINC results in NUREG/CR-7019 (Cumblidge et al. 2010), which were both performed with δX = 10 mm. The δY tolerance was maintained at 10 mm in all of the analysis.

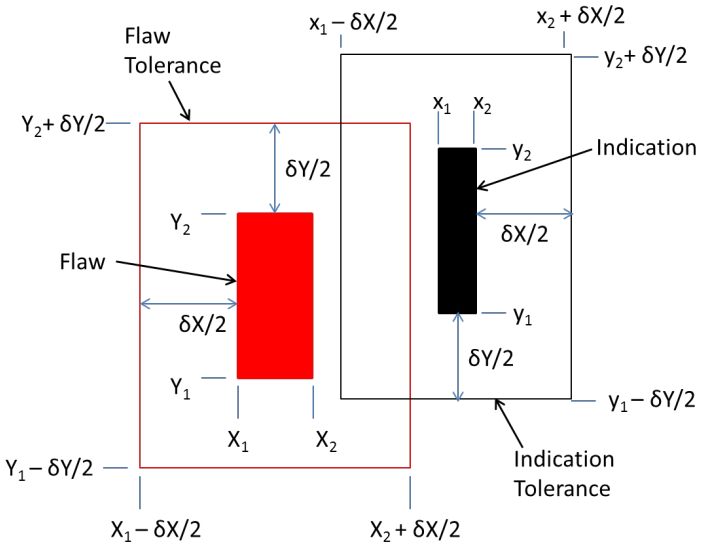

Figure 3.1 Illustration of Tolerance Divided Between Flaw and Indication in Detection Scoring Algorithm

3.2 Probability of Detection Representation

A logistic regression model was used to relate POD to flaw size, S. Flaw size represents either depth or length. The logistic regression model is given by,

$$\mathrm{POD(S)} = \mathrm{logistic}\left(\beta_1 + \beta_2 S\right), \tag{3.3}$$

where $\beta = (\beta_1, \beta_2)$ are unknown parameters to be determined by the regression algorithm and the function, logistic(x) is defined as

$$\mathrm{logistic\ (x)} = \frac{1}{1+e^{-x}} \tag{3.4}$$

Estimates produced by the algorithm are maximum-likelihood estimates.

Detection performance is presented in a tabular format with POD values provided at discrete flaw sizes (i.e., at 0 mm, 5 mm, 10 mm, 15 mm, etc.). The values of POD at these discrete flaw sizes are the values estimated by the logistic regression model expressed by Eqs. (3.3) and (3.4). This is represented by an example of PAUT procedures applied to the O.D. of LBDMW test blocks in Table 3.1 and by a plot of the corresponding logistic regression model in Figure 3.2. Table 3.1 includes a column with heading "NOBS," which refers to the number of flaw observations in the sample that POD data in the row is calculated from. In addition, the first column includes POD data for flaws that are 0 mm deep. In this case, the value at 0 mm [POD(0)] can also be interpreted as the false call probability (FCP) determined by the regression fit. The value of the regression fit at 0 mm is influenced by the measured FCP, which is calculated from the false call rate (FCR), which is described in the next section. FCR has units of number of false calls per meter. Figure 3.2 also illustrates 95% confidence intervals for the logistic regression curve.

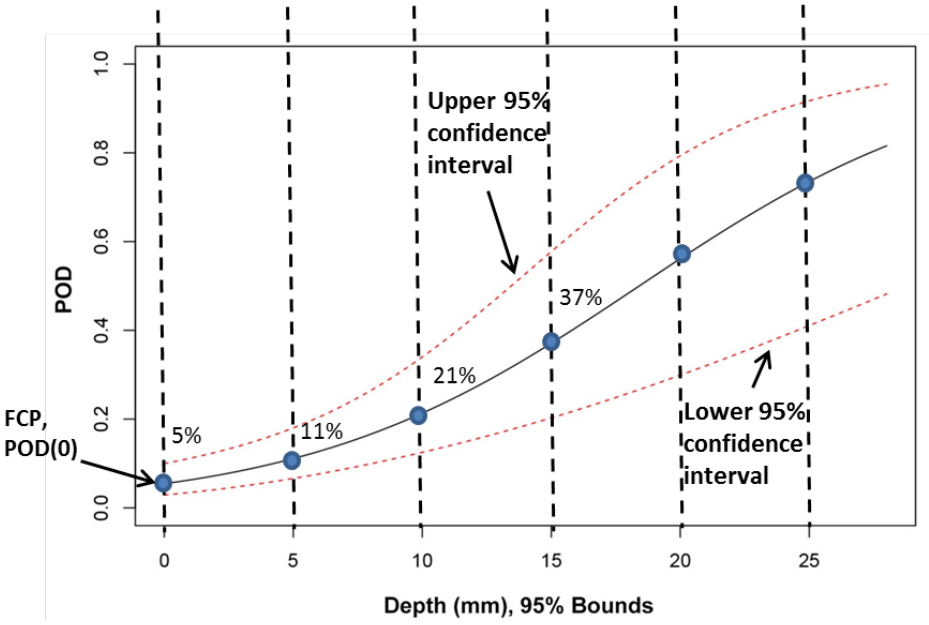

Figure 3.2 POD versus Depth (mm) for PAUT Procedures Applied to LBDMW Test Blocks with O.D. Access (w/o Quick-blind)

Table 3.1 Summary of POD (%) versus Depth for Procedure Types for LBDMWs (O.D. Access)

	NOBS	0 mm	5 mm	10 mm	15 mm
PAUT	38	5	11	21	37
⋮	⋮	⋮	⋮	⋮	⋮

3.3 Calculation of FCP

A false call is defined as a called hit (detection) that does not intersect with a flawed grading unit. These false calls were used to estimate a false call rate, λ_{fc} (false calls per meter),

$$\lambda_{fc} = \frac{\#\text{False Calls}}{\text{Length of Blank Material Inspected}} \tag{3.5}$$

The length of blank material inspected is calculated by summing the lengths (circumferential dimension) of all flaws, including the tolerance added to each flaw, within the inspected region and subtracting this quantity from the total length of material inspected. As a consequence, the FCR does exhibit some dependence on the selected tolerance in the circumferential (X) direction. For ECT, non-surface–breaking flaws are excluded from the analysis and the length of blank material inspected is adjusted for this.

Using this rate and the assumption that false calls are randomly (i.e., Poisson) distributed, one can then calculate the probability that a call would intersect a blank grading unit of length L_{gu}. Assuming that the average length of a false call is L_{fc}, the probability of a false call intersecting the grading unit is

$$\text{FCP} = \Pr(\text{Grading Unit Intersection}) = 1 - \exp\left(-\lambda_{fc}\left(L_{gu} + L_{fc}\right)\right) \tag{3.6}$$

3.4 Sizing Analysis for PARENT Blind Round-Robin Test

Linear regression was used to analyze sizing data (depth and length) in PARENT Blind testing. An error relation between the measured and true sizes of the flaws is defined by the following regression formula:

$$M_i = B1 + B2 \times T_i + E_i \tag{3.7}$$

where M_i represents the measured size associated with flaw i
T_i represents the true size of flaw i
E_i represents the measurement error in sizing flaw i.

$B1$ and $B2$ are the regression parameters usually associated with the Y intercept and slope of the linear regression. Ideal performance for sizing would occur when $B1 = 0$, $B2 = 1$, and $E_i = 0$. To compare two different regressions, and to order a set of regression fits (from most accurate to least accurate as an example), the metric of root mean square error (RMSE) is used. RMSE is a statistic that summarizes the three deviations of regression analyses from their respective ideals. RMSE is defined by

$$RMSE^2 = \frac{\sum_I \left(M_I - T_I\right)^2}{n} \tag{3.8}$$

where all the variables are the same as in the preceding descriptions and n is the total number of measurements. RMSE can also be represented in terms of bias and standard deviation as,

$$\mathrm{RMSE}^2 = \mathrm{bias}^2 + \mathrm{StDev}^2 . \tag{3.9}$$

In this formula, standard deviation is represented with the variable StDev. The bias and StDev represent systematic and random components to the error and are calculated with the following formulas,

$$\mathrm{bias} = \frac{\sum_i \left(M_i - T_i\right)}{n}, \tag{3.10}$$

$$\mathrm{StDev} = \sqrt{\frac{\sum_i \left[\left(M_i - T_i\right) - \mathrm{bias}\right]^2}{n}} . \tag{3.11}$$

Sizing analysis results are presented in this report in tabulated format providing Bias and RMSE data and as plots of the sizing regressions calculated from Eq. (3.7). An example of sizing analysis data provided in tabular format is provided in Table 3.2. This table includes sizing analysis data for two techniques (101-ECT1 and 135-ECT1) and aggregated sizing analysis results for both techniques (101-ECT1 + 135-ECT1). In this case, by referring to Eq. (3.10), it is evident that the aggregated Bias can be computed by taking the average Bias for each technique being aggregated weighted with the NOBS for each technique. The aggregated RMSE value is not as straightforward to calculate, but can be determined from the following generalized formula,

$$RMSE_{sum} = \sqrt{\frac{\sum_i n_i RMSE_i^{\,2}}{n_1 + n_2 + n_3 \ldots}} . \tag{3.12}$$

An example of a plot of a sizing regression curve calculated by Eq. (3.7) is provided in Figure 3.3.

Table 3.2. Example of Tabulated Sizing Analysis Data

	NOBS	Bias	RMSE
101-ECT1	4	−2.0	5.2
135-ECT1	7	0.1	2.0
135-ECT1 + 101-ECT1	11	−0.6	3.6

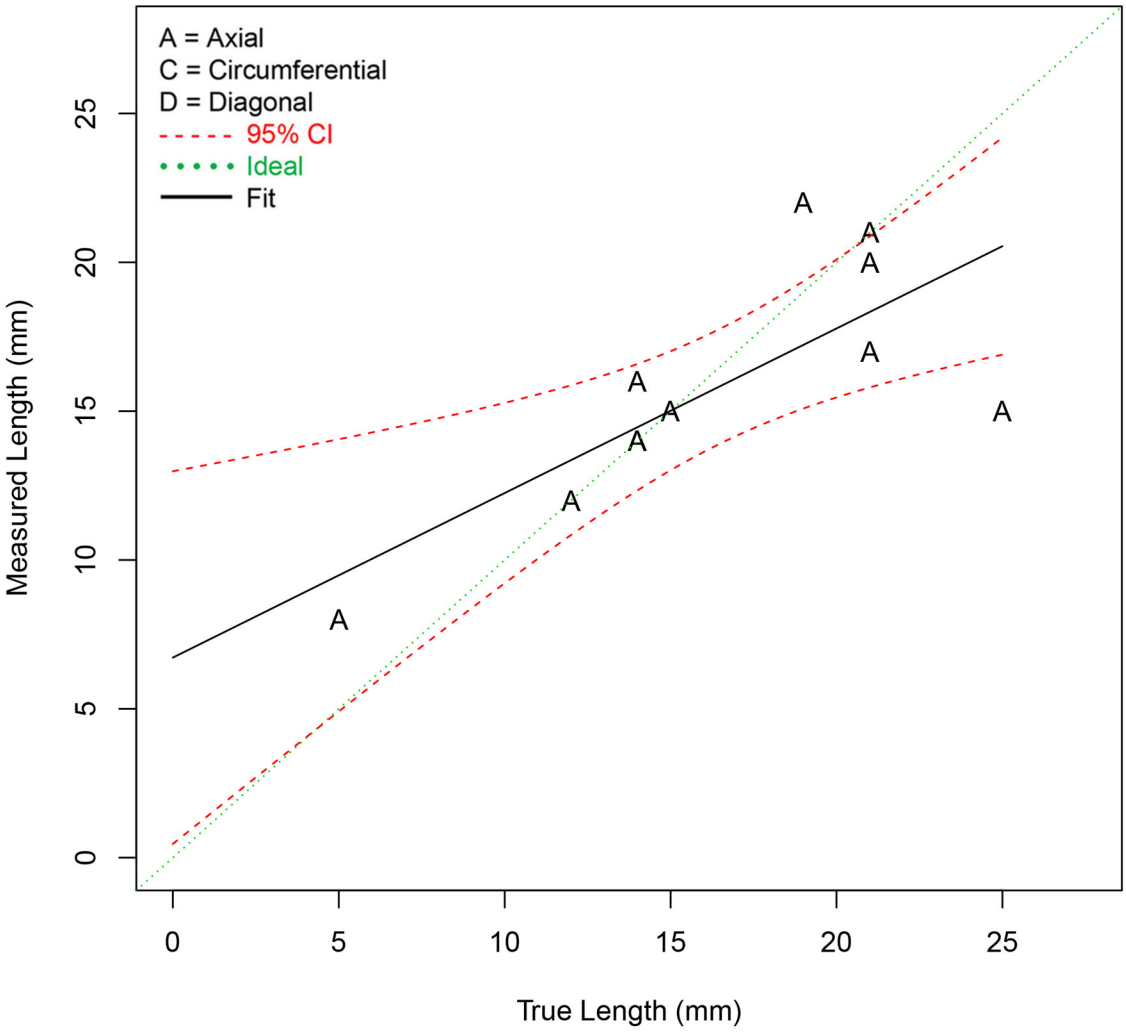

Figure 3.3. Example of a Plot of a Sizing Regression Calculated from Eq. (3.7)

4.0 ECT Technique Analysis

ECT technique analysis was performed to supplement the limited amount of data collected for ECT at the procedure level in PARENT blind testing. This section includes a summary of the procedures in PARENT blind testing that incorporated ECT techniques and provides a review of the performance of procedures incorporating ECT techniques. This is followed by a summary of the inspections that are included in the ECT technique analysis, the results of detection performance analysis of ECT techniques, and the results of length-sizing performance analysis of ECT techniques.

4.1 Summary of ECT Techniques to be Analyzed

Four procedures in PARENT blind testing incorporated ECT techniques and these are summarized in Table 4.1. The four procedure identifications (IDs) are UT.TOFD.ECT.101, UT.ECT.144, ECT.135, and UT.ECT.106. The procedure IDs indicate that these procedures include some combination of ECT techniques with conventional UT techniques and time-of-flight diffraction (TOFD) techniques. General descriptions of these techniques are provided in Sections 3.2 and 3.3 of the PARENT Blind test report NUREG/CR-7235 (Meyer and Heasler 2017). Summaries of individual procedures are provided in Appendix B of NUREG/CR-7235 (Meyer and Heasler 2017) with information obtained from procedure datasheets that were filled out by participating teams and which are included in Appendix C of NUREG/CR-7235 (Meyer and Heasler 2017).

4.1.1 Summary of UT.TOFD.ECT.101

Procedure UT.TOFD.ECT.101 is a combination of conventional UT, TOFD, and ECT techniques. As Table 4.1 indicates, the conventional UT and TOFD techniques are combined and reported as a single technique with ID 101-UT0 for this procedure. Conventional UT in pulse-echo mode at 2 MHz is employed for detection, length sizing, and depth sizing while TOFD is utilized for depth sizing. Technique 101-ECT1 is utilized for detection and length sizing and incorporated a cross coil probe in transmit-receive configuration and operated at a frequency of 300 kHz.

4.1.2 Summary of UT.ECT.106 and UT.ECT.144

Procedures UT.ECT.106 and UT.ECT.144 are very similar but they are distinguished because UT.ECT.106 was applied to the Quickblind inspections and UT.ECT.144 was applied in the Blind inspections. The procedures incorporate a conventional UT technique (144-UT0 and 106-UT0) in pulse-echo mode at angles of 45° and 55° and a frequency of 2 MHz. Technique 144-UT0/106-UT0 is utilized for detection, length sizing, and depth sizing while ECT (144-ECT0 and 106-ECT0) is employed for detection and length sizing. The probe used for 144-ECT0/106-ECT0 is described as a driver pick-up probe with ferrite core that is operated at 200 kHz.

4.1.3 Summary ECT.135

Procedure ECT.135 consisted of only one technique—135-ECT1. Technique 135-ECT1 is utilized for detection and length sizing and is described as an array probe with 16 channels (8 × 2) incorporating cross coil sensors. The pitch of the probe is 0.5 mm in the circumferential direction and 2.75 mm in the axial direction and the probe is operated predominantly at 400 kHz.

Table 4.1. Summary of Procedures Incorporating ECT Techniques in PARENT Blind Testing

Procedure ID	Technique ID	Manual or Automated	Encoded (Y/N)	Exam Surface	Probe Frequency	Technique Comment
UT.TOFD.ECT.101	101-ECT1	Automated	Y	I.D.	300 kHz	Cross-coil probe with transmit-receive configuration Detection and length sizing
	101-UT0	Automated	Y	I.D.	2 MHz	Conventional UT pulse-echo at multiple angles for detection, length sizing, depth sizing TOFD for depth sizing
UT.ECT.144	144-ECT0	Automated	Y	I.D.	200 kHz	Driver pick-up probe with ferrite core Detection and length sizing
	144-UT0	Automated	Y	I.D.	2 MHz	Conventional UT pulse-echo at 45° and 55° Detection, length sizing, and depth sizing
ECT.135	135-ECT1	Manual	Y	I.D.	50 kHz–1 MHz/ 400 kHz dominant	8×2 channels; 16 cross coils total 0.5 mm pitch in circumferential direction 2.75 mm pitch in axial direction Detection and length sizing
UT.ECT.106	106-ECT0	Automated	Y	I.D.	200 kHz	Driver pick-up probe with ferrite core Detection and length sizing
	106-UT0	Automated	Y	I.D.	2 MHz	TRL probes at 45° and 55° Detection, length sizing, and depth sizing

I.D. = inner diameter

4.2 Review of ECT Performance in PARENT Blind Testing

This section summarizes the results of the performance analysis of procedures UT.TOFD.ECT.101, UT.ECT.144, ECT.135, and UT.ECT.106 in PARENT blind testing. The only performance data that can be attributed to ECT techniques in PARENT blind testing is the performance data for procedure ECT.135 because the specific contributions of individual techniques to the overall performance of procedures UT.ECT.106, UT.ECT.144, and UT.TOFD.ECT.101 was not analyzed. A summary of overall detection and false call performance for these procedures is included in Table 4.2 and a summary of probability of detection (POD) as a function of depth is provided in Table 4.3. Finally, a summary of length sizing error in terms of length sizing bias and root-mean-square error (RMSE) is provided in Table 4.4.

Tables 4.2 and 4.3 indicate that UT.ECT.144 performed comparatively worse than ECT.135 and UT.TOFD.ECT.101 in the Blind test (distinguished from the Quickblind test); however, as noted in Section 6.4 of Meyer and Heasler (2017), systematic positioning error appeared to have a significant impact on the results of UT.ECT.144. The indication plots for the UT.ECT.144 inspection of P33 are provided in NUREG/CR-7235 Meyer and Heasler (2017). These figures indicate that the procedure consistently erred in positioning axially oriented flaws. Five indications are highlighted in Meyer and Heasler (2017) that were originally classified as misses, but which are considered likely detections. The summaries in Tables 4.2 and 4.3 are based on classifying these five indications as false calls instead of hits. Additional analysis was performed by adjusting the tolerance from 10 mm to 15 mm, as summarized in Section 6.4 of Meyer and Heasler (2017). Comparisons of overall detection and false call rate performance and length sizing error performance for tolerances of 10 mm and 15 mm are provided later in Tables 4.6 and 4.7. The increased tolerance has an obvious impact on overall detection and sizing performance since four of the five indications highlighted as probable detections were reclassified from false calls to hits. The length sizing performance appears to be modestly impacted by the change in tolerance.

Table 4.2. Summary of Overall Detection and False Call Performance for Procedures Incorporating ECT Techniques in PARENT Blind Testing

	NOBS	POD, %	FCP, %	FCR, #/m	LBDMW
ECT.135	16	75	1	0.4	P33
UT.ECT.106 (Quickblind)	3	100	0	0.0	P15, P16, P17, P45
UT.ECT.144	19	58	6	2.3	P13, P33
UT.TOFD.ECT.101	19	79	3	1.1	P13, P33

FCP = false call probability
FCR = false call rate
NOBS = number of observations

Table 4.3. Probability of Detection versus Depth for Procedures Incorporating ECT Techniques in PARENT Blind Testing

	NOBS	0 mm	5 mm	10 mm	15 mm	30 mm
ECT.135	16	3	23	76	97	100
UT.ECT.106 (Quickblind)	3	3	10	27	56	97
UT.ECT.144	19	9	17	30	46	84
UT.TOFD.ECT.101	19	7	22	48	76	99

UT = conventional UT

Table 4.4. Length Sizing Results Summary for Procedures Incorporating ECT Techniques in PARENT Blind Testing

	NOBS	Bias, mm	RMSE, mm
ECT.135	12	−2.2	6.2
UT.ECT.106 (Quickblind)	3	−9.3	10.0
UT.ECT.144	11	2.9	4.2
UT.TOFD.ECT.101	15	1.1	5.3

(a) Procedure PAUT.132 was not qualified for length sizing and this data is not included in the summary.
UT = conventional UT

4.3 ECT Inspections of Test Block P33

The indication plot for procedure ECT.135 and technique 135-ECT1 for inspection of test block P33 is provided in Figure 4.1. The only technique applied in procedure ECT.135 is 135-ECT1; thus, the indication plot is identical for procedure ECT.135 and technique 135-ECT1 in this case. The indication plot in Figure 4.1 shows that two sub-surface flaws in P33 were not detected by ECT.135 and 135-ECT1, as would be expected. The subsurface flaws were excluded from analysis of ECT data and ECT procedures and techniques were not penalized for missing these flaws. Otherwise, ECT.135 and 135-ECT1 did miss three circumferentially oriented flaws and one axially oriented flaw. In reviewing the indication plot in Figure 4.1, it is apparent that multiple indications can be associated with a single flaw (indications 10 and 11). The ASME Section XI IWA-3400 rules for combining linear surface flaws to account for multiple flaws that are in close proximity are followed for these scenarios.

Section XI, IWA-3400 of the ASME Code states the following:

> *(a)* Linear flaws detected by surface (PT/MT) or volumetric (RT) examination methods shall be considered single linear surface flaws provided the separation distance between flaws is equal to or less than the dimension S, where S is determined as shown in Figure IWA-3400-1.
>
> *(b)* The overall length of a single and discontinuous linear flaw shall be determined as shown in Figure IWA-3400-1.

Figure 4.2 is a reproduction of part of IWA-3400-1 to show the methodology used to determine whether multiple flaws should be combined as one flaw with length or whether the flaws should be considered as single individual flaws. Thus, this rule provides criteria to follow for combining indications. If the criteria for combining indications are not met, then the indications are considered individually. If multiple (but individual) indications intersect the tolerance boundary for a flaw, then the indication with the largest area of intersection with the region defined by the flaw tolerance boundary will be selected for sizing evaluations.

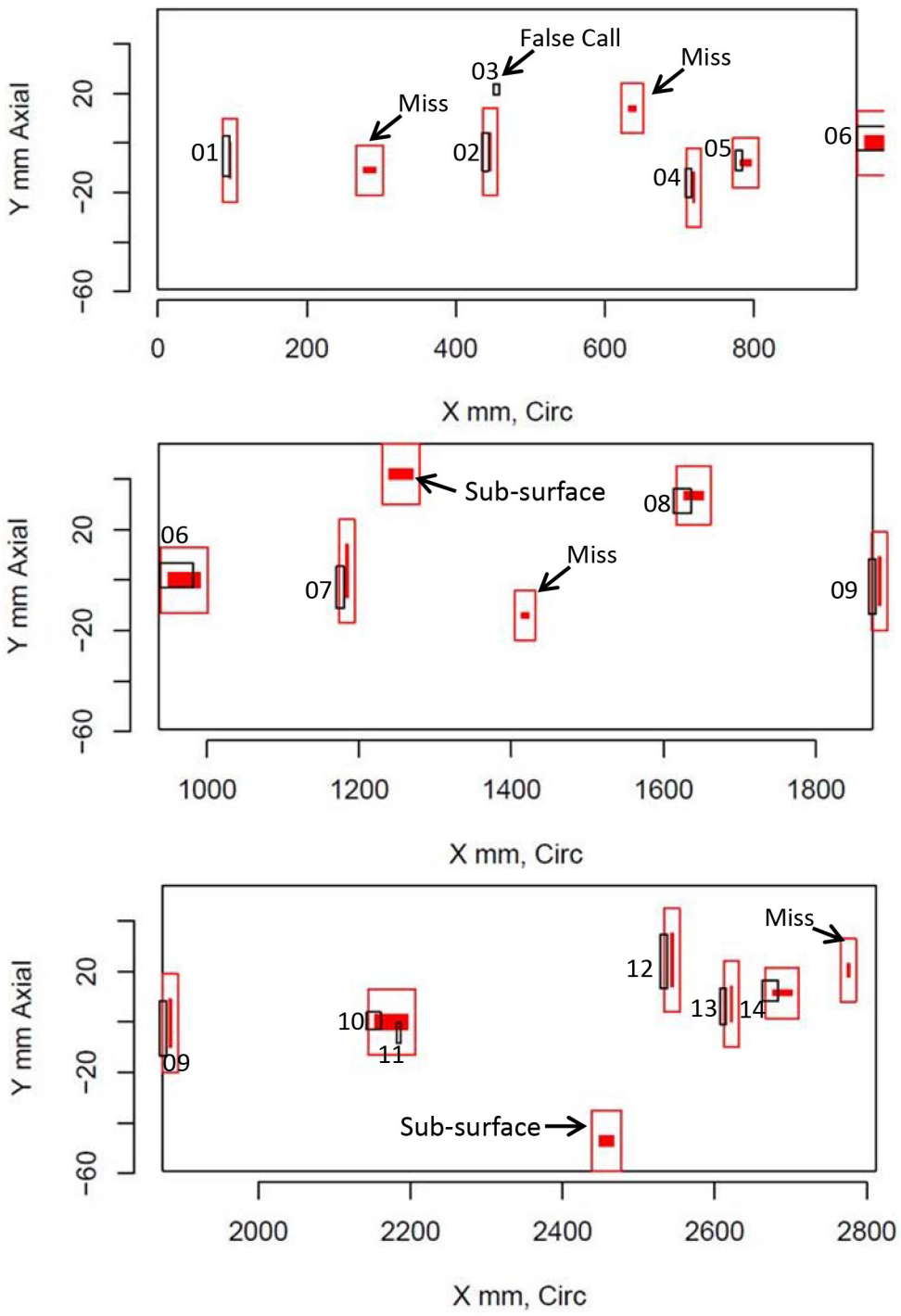

Figure 4.1. Indication Plot for Procedure ECT.135 and Technique 135-ECT1 Applied to Test Block P33 in PARENT Blind Testing (X–Y view)

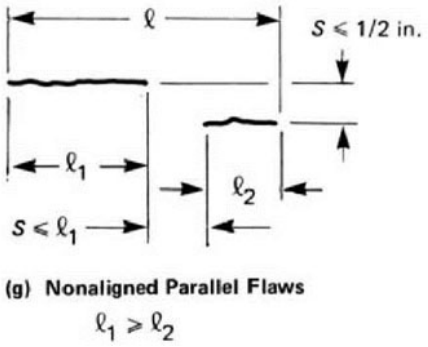

Figure 4.2. Methodology for Determining Singularity or Multiplicity of Linear Surface Flaws. Reprinted from ASME 2015 BPVC Section XI, Figure IWA-3400-1, by permission of The American Society of Mechanical Engineers. All rights reserved.

An example of the effect of the application of the ASME procedures for combining flaws is considered for indications numbers 10 and 11 which have the X1, X2, Y1, and Y2 coordinates as indicated in Table 4.5. If these two indications were combined, they will have length of 2187.1–2142.4 = 44.7 mm, which is very close to the true length of a nearby flaw. However, according to the procedure for combining flaws indicated in Figure 4.2, these indications should not be combined because the distance, S, separating the flaws is greater than the longest flaw. In this case, S = 20.6 mm, and the longer of the two indications has a length of 18.6 mm. As a result, the two indications must be treated individually and the calculated length sizing error will be greater than if the two indications are combined.

Table 4.5. X1, X2, Y1, and Y2 Coordinates for Indication Numbers 10 and 11 in Test Block P33 by Procedure ECT.135

Indication No.	X1, mm	X2, mm	Y1, mm	Y2, mm
10	2142.4	2161.0	−3.0	3.9
11	2181.6	2187.1	−8.5	−0.2

Tolerance bounds are described that are used to determine if an indication should be classified as a hit or miss based on how close an indication is to a flaw. Initially, a 10 mm tolerance is applied to flaw true states as forgiveness for positioning error. However, this also resulted in several genuine detections being classified as misses by procedure UT.ECT.144 on test block P33, as shown by the indication plot in Figure 4.3. In this case, there were five axial indications located 10 mm to 20 mm from the flaw true states and four of these indications were located within 15 mm of the true state. These misses are highlighted in Figure 4.3 as “Probable Detections.”

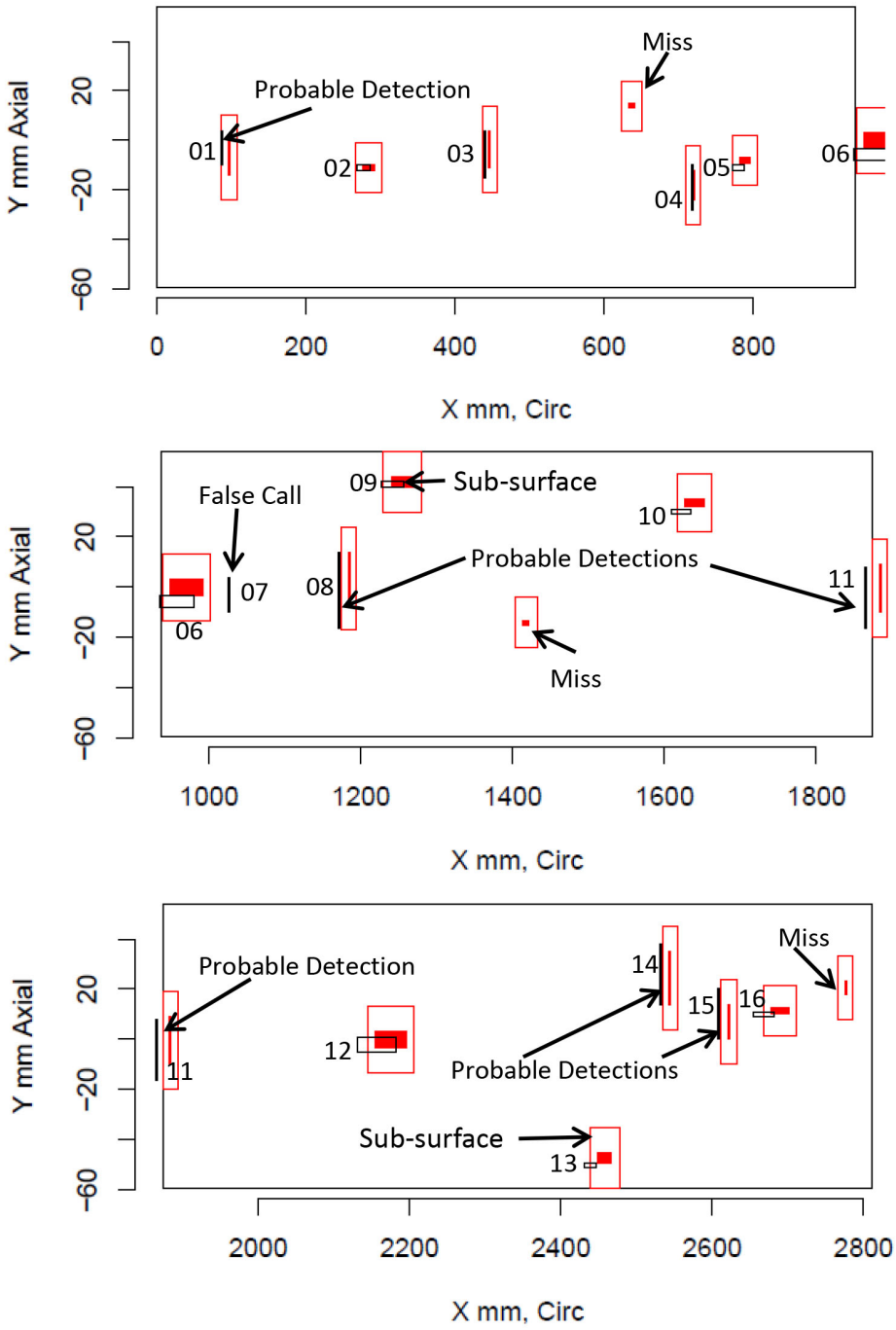

Figure 4.3. Indication Plot for Procedure UT.ECT.144 Applied to Test Block P33 in PARENT Blind Testing (X–Y view)

A comparison of performance results obtained from using a 10 mm tolerance versus a 15 mm tolerance for UT.ECT.144 is presented in Tables 4.6 and 4.7. Table 4.6 is a comparison of detection and false call performance for a 10 mm tolerance versus a 15 mm tolerance and shows that the overall POD increases from 58% for a 10 mm tolerance to 79% for a 15 mm tolerance. Table 4.7 provides a comparison of length sizing errors and indicates a slight increase in length sizing bias and RMSE as a consequence of increasing the tolerance from 10 mm to 15 mm.

Table 4.6. Detection and False Call Comparison for 10 mm and 15 mm Tolerances Applied for Procedure UT.ECT.144

	NOBS	POD, %	FCP, %	FCR, #/m	Access	Test Blocks (LBDMWs)
10 mm tolerance	19	58	6	2.3	I.D.	P13, P33
15 mm tolerance	19	79	2	0.8	I.D.	P13, P33

Table 4.7. Length Sizing Error Comparison for 10 mm and 15 mm Tolerances Applied for Procedure UT.ECT.144

	NOBS	Bias, mm	RMSE, mm
10 mm tolerance	11	2.9	4.2
15 mm tolerance	15	3.3	4.6

Additional review of Figure 4.3 indicates that procedure UT.ECT.144 detected both subsurface flaws and that it missed two circumferentially oriented flaws and one axially oriented flaw. Technique data was not provided for UT.ECT.144. Therefore, an analysis of data contributed by technique 144-ECT0 could not be performed in this effort.

The indication plot for procedure UT.TOFD.ECT.101 is provided in Figure 4.4. The indication plot shows that procedure UT.TOFD.ECT.101 was able to detect both subsurface flaws and that positioning error appears to have resulted in two missed detections (and two false calls) of axial flaws. These are labeled as "probable detections." In addition, it appears that two circumferentially oriented flaws were missed. The indication plot for technique 101-ECT1 is provided in Figure 4.5. This indication plot shows that the subsurface flaws were not detected, as would be expected for the ECT technique. Further, the indication plot revealed significant positioning error for axial flaws, similar to the positioning error exhibited by procedure UT.ECT.144 and, to a lesser extent, by procedure UT.TOFD.ECT.101. The positioning error resulted in five misses (and five false calls) for 101-ECT1 and these are labeled as "probable detections." Otherwise, it appears that two circumferentially oriented flaws were missed by 101-ECT1. Considering indication plots in Figures 4.4 and 4.5 together, it appears that the UT and TOFD techniques applied in procedure UT.TOFD.ECT.101 were able to sufficiently correct the position of three of the indications that are labeled as "probable detections" in Figure 4.5.

Figure 4.5 shows that technique 101-ECT1 produced two indications that can be associated with a single flaw (indications 10 and 11), which is similar to the result observed for procedure ECT.135 and technique 135-ECT1. As was performed for procedure ECT.135 and technique 135-ECT1, the ASME Section XI IWA-3400 rules for combining linear surface flaws to account for multiple flaws that are in close proximity are followed for this scenario. Thus, the methodology depicted in Figure 4.2 is followed here and provides another example of the effect of the application of the ASME procedures for combining flaws. The X1, X2, Y1, and Y2 coordinates for indications 10 and 11 are summarized in Table 4.8. If these two indications were combined, they will have length of 2181.2–2137.6 = 43.6 mm, which is very close to the true length of a nearby flaw. According to the procedure for combining flaws indicated in Figure 4.2, these indications should be combined because the distance, S, separating the flaws is less than the longest flaw. In this case, S = 16.9 mm, and the longer of the two indications has a length of 18.2 mm. A depiction of a portion of the indication plot with indications 10 and 11 combined (and relabeled as indication 10) is provided in Figure 4.6. This outcome is different than resulted from application of the ASME procedures for combining flaws to indication 10 and 11 in Figure 4.1 for procedure ECT.135 and technique 135-ECT1.

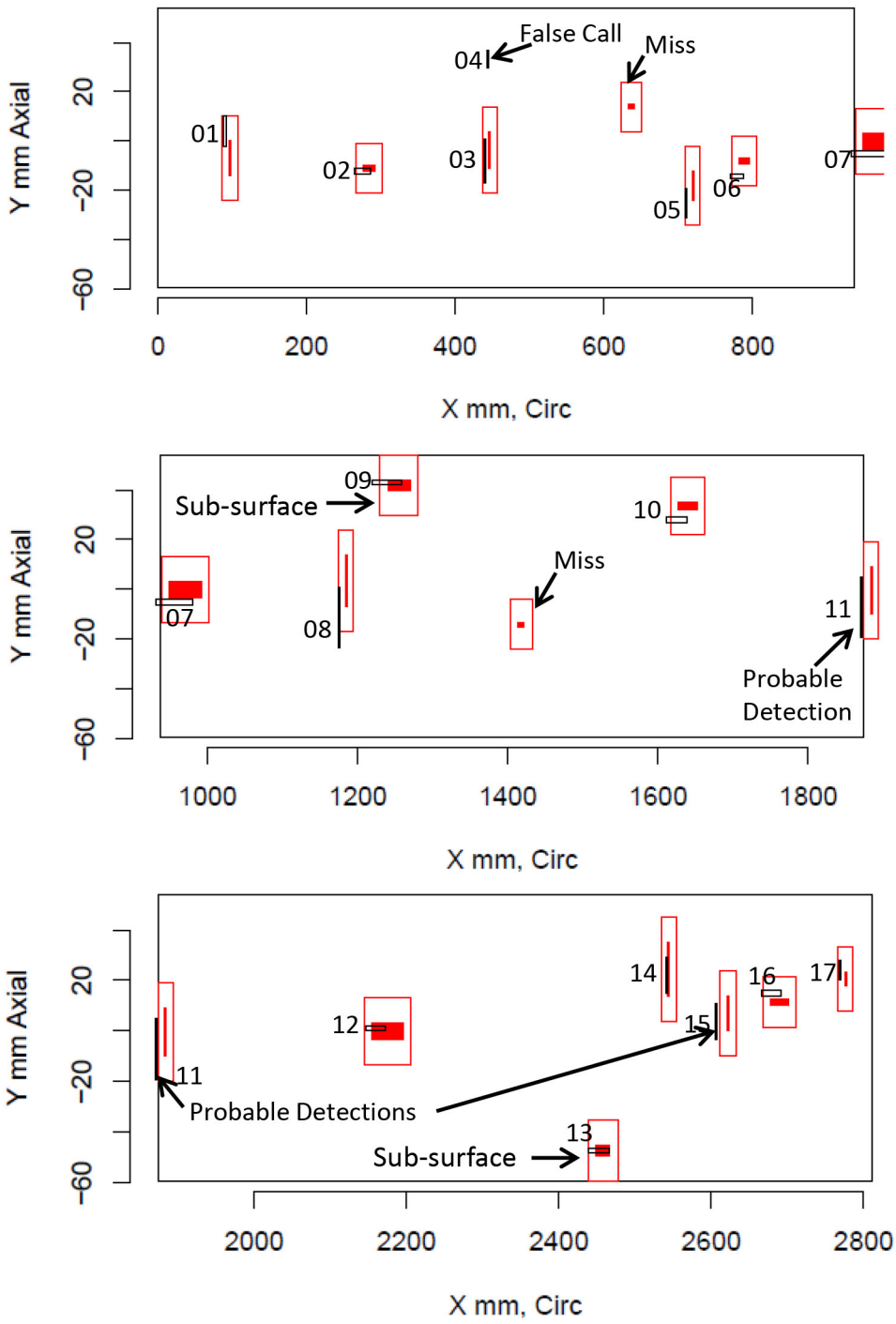

Figure 4.4. Indication Plot for Procedure UT.TOFD.ECT.101 Applied to Test Block P33 in PARENT Blind Testing (X–Y view)

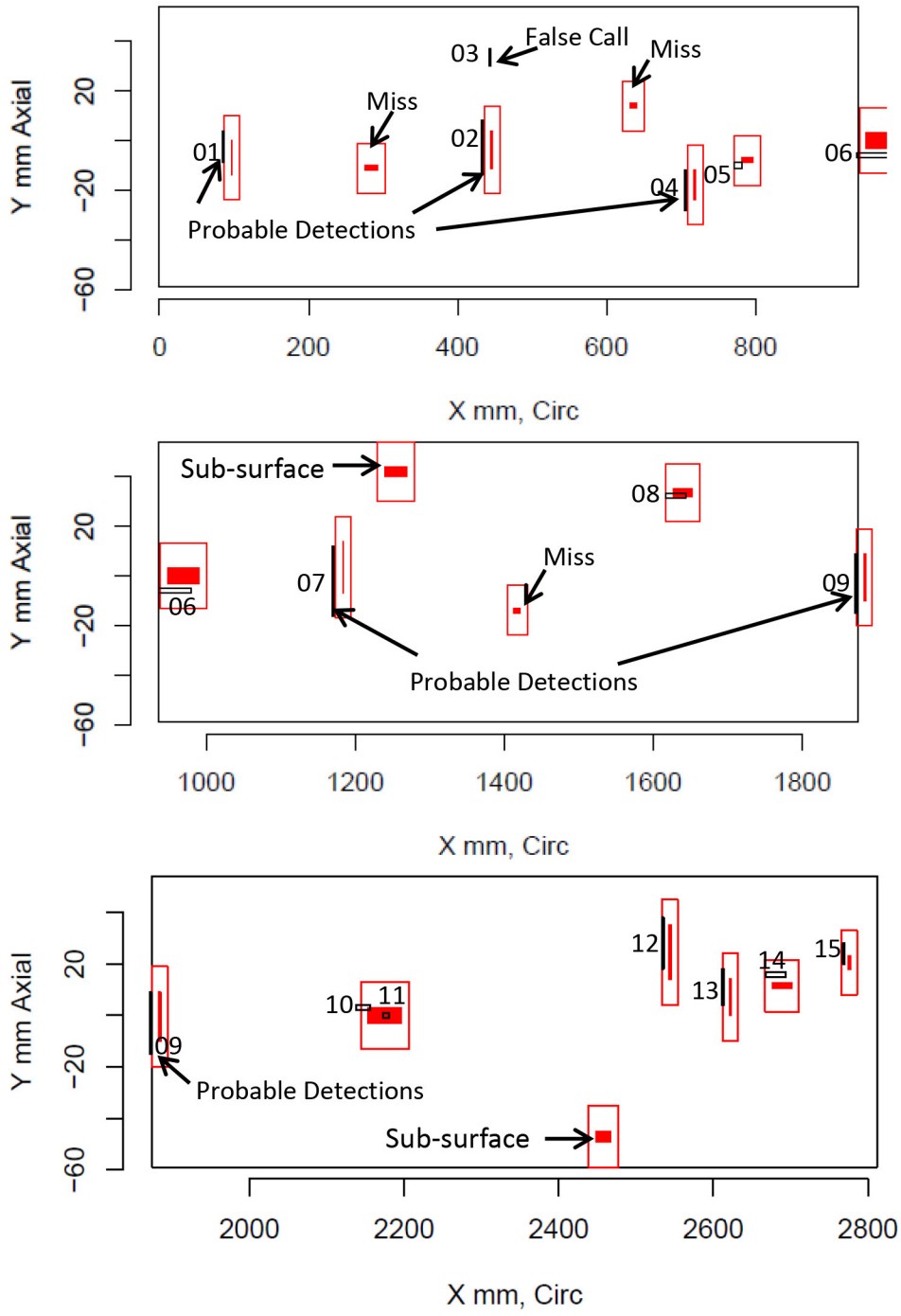

Figure 4.5. Indication Plot for Technique 101-ECT1 Applied to Test Block P33 in PARENT Blind Testing (X–Y view)

Table 4.8. X1, X2, Y1, and Y2 Coordinates for Indications No. 10 and 11 in Test Block P33 by Technique 101-ECT1

Indication No.	X1, mm	X2, mm	Y1, mm	Y2, mm
10	2137.6	2155.8	3.0	3.0
11	2172.7	2181.2	0.0	0.0

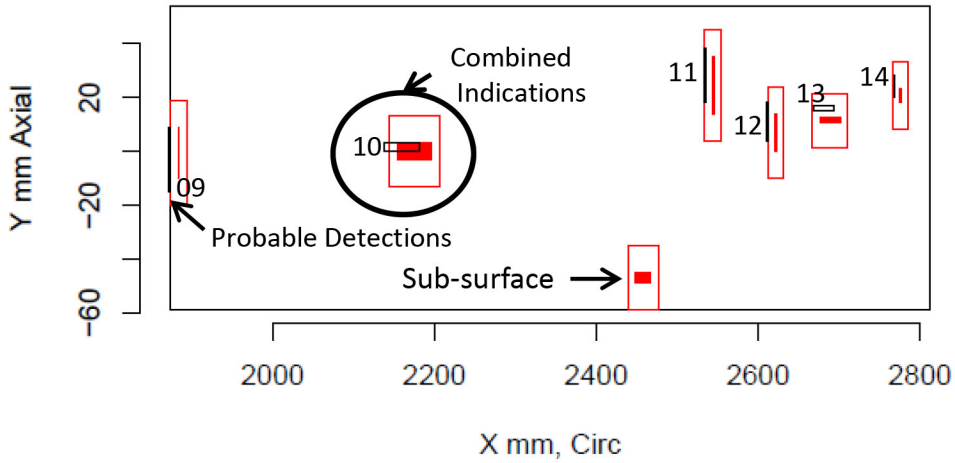

Figure 4.6. Indication Plot for Technique 101-ECT1 Applied to Test Block P33 in PARENT Blind Testing with Indications 10 and 11 from Figure 4.5 Combined into a Single Indication (X–Y view)

4.4 ECT Inspections of Test Block P13

The indication plots for inspections of P13 by procedure UT.TOFD.ECT.101 and by technique 101-ECT1 are provided in Figures 4.7 and 4.8, respectively. The indication plot by procedure UT.TOFD.ECT.101 in Figure 4.7 is obtained by combining the results of examinations by techniques 101-UT0 and 101-ECT1.

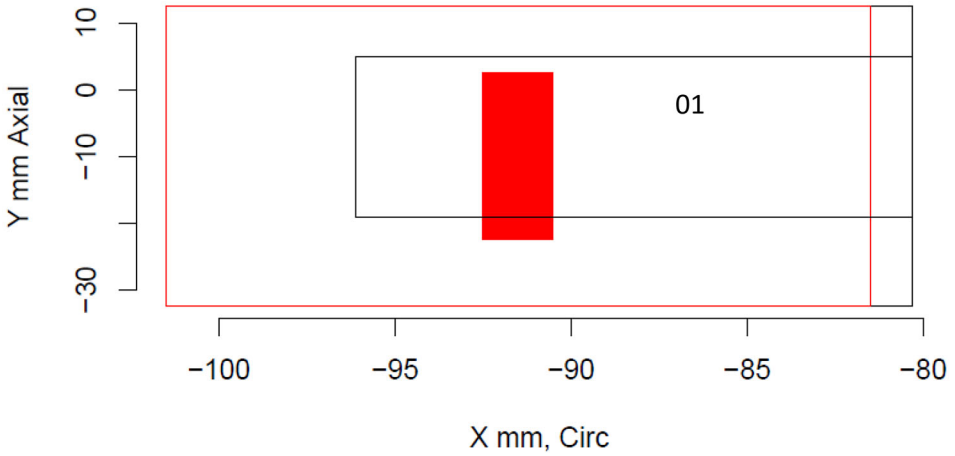

Figure 4.7. Indication Plot for Procedure UT.TOFD.ECT.101 Applied to Test Block P13 in PARENT Blind Testing (X–Y view)

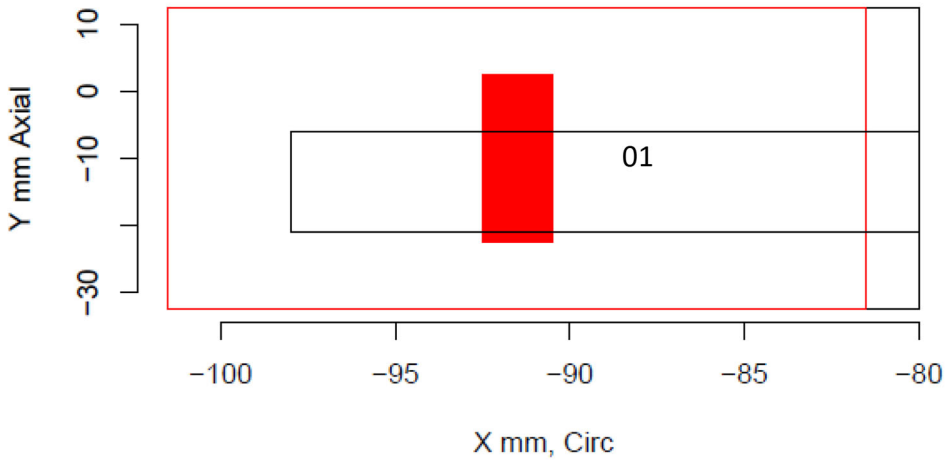

Figure 4.8. Indication Plot for Technique 101-ECT1 Applied to Test Block P13 in PARENT Blind Testing (X–Y view)

4.5 ECT Inspections of Test Block P15 by Team 106 (Quickblind)

Indication plots for inspections performed on Quickblind test block P15 by procedure UT.ECT.106 and technique 106-ECT0 are provided in Figures 4.9 and 4.10, respectively. The indication plot by procedure UT.ECT.106 in Figure 4.9 is obtained by combining the results of examinations by techniques 106-UT0 and 106-ECT0.

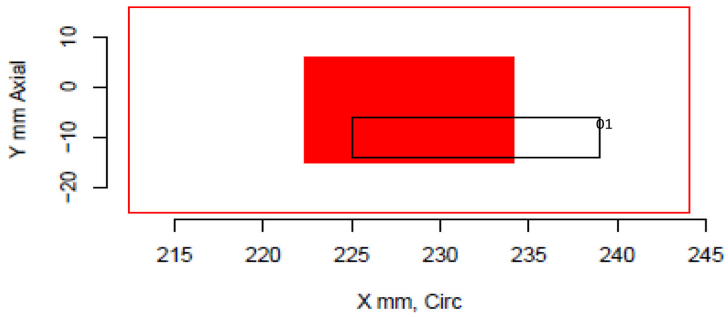

Figure 4.9. Indication Plot for Procedure UT.ECT.106 Applied to Quickblind Test Block P15 in PARENT Blind Testing (X–Y view)

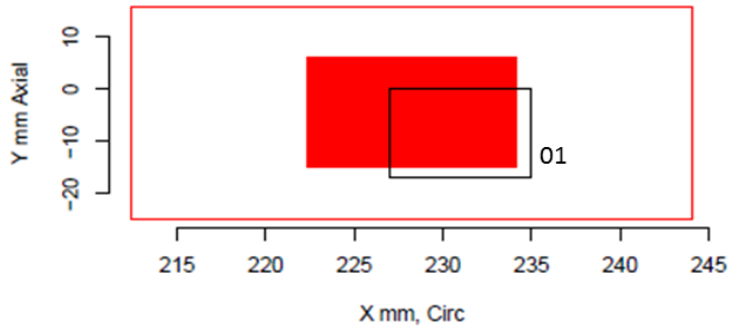

Figure 4.10. Indication Plot for Technique 106-ECT0 Applied to Quickblind Test Block P15 in PARENT Blind Testing (X–Y view)

4.6 ECT Inspections of Test Block P16 by Team 106 (Quickblind)

Indication plots for inspections performed on Quickblind test block P16 by procedure UT.ECT.106 and technique 106-ECT0 are provided in Figures 4.11 and 4.12, respectively. The indication plot by procedure UT.ECT.106 in Figure 4.11 is obtained by combining the results of examinations by techniques 106-UT0 and 106-ECT0.

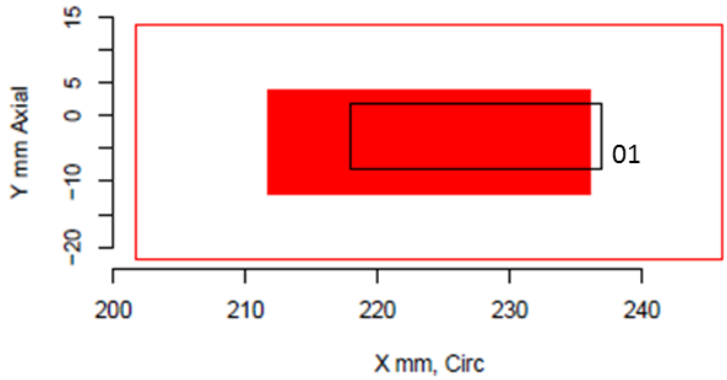

Figure 4.11. Indication Plot for Procedure UT.ECT.106 Applied to Quickblind Test Block P16 in PARENT Blind Testing (X–Y view)

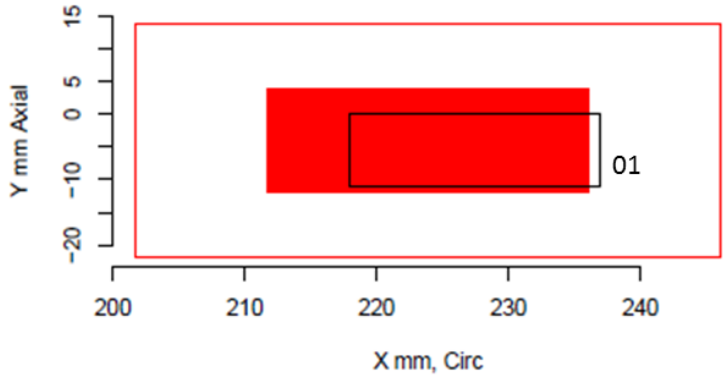

Figure 4.12. Indication Plot for Technique 106-ECT0 Applied to Quickblind Test Block P16 in PARENT Blind Testing (X–Y view)

4.7 ECT Inspections of Test Block P17 by Team 106 (Quickblind)

Indication plots for inspections performed on Quickblind test block P17 by procedure UT.ECT.106 and technique 106-ECT0 are provided in Figures 4.13 and 4.14, respectively. The indication plot by procedure UT.ECT.106 in Figure 4.13 is obtained by combining the results of examinations by techniques 106-UT0 and 106-ECT0.

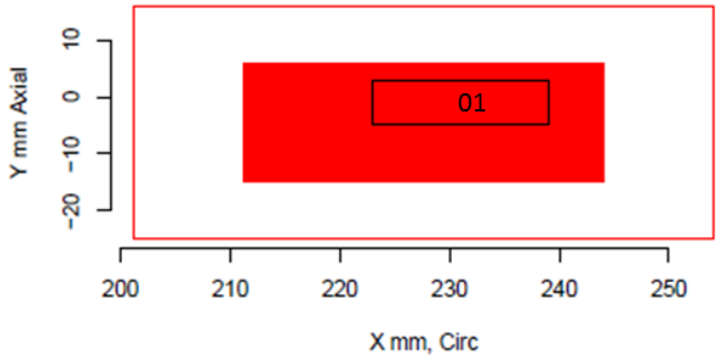

Figure 4.13. Indication Plot for Procedure UT.ECT.106 Applied to Quickblind Test Block P17 in PARENT Blind Testing (X–Y view)

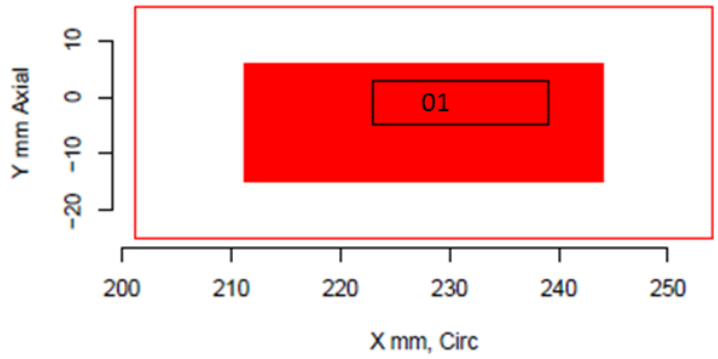

Figure 4.14. Indication Plot for Technique 106-ECT0 Applied to Quickblind Test Block P17 in PARENT Blind Testing (X–Y view)

4.8 ECT Inspections of Test Block P45 by Team 106 (Quickblind)

Indication plots for inspections performed on Quickblind test block P45 by procedure UT.ECT.106 and technique 106-ECT0 are provided in Figures 4.15 and 4.16, respectively. The indication plot by procedure UT.ECT.106 in Figure 4.15 is obtained by combining the results of examinations by techniques 106-UT0 and 106-ECT0.

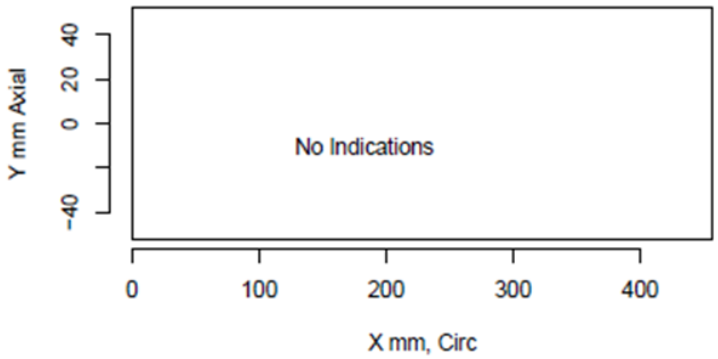

Figure 4.15. Indication Plot for Procedure UT.ECT.106 Applied to Quickblind Test Block P45 in PARENT Blind Testing (X–Y view)

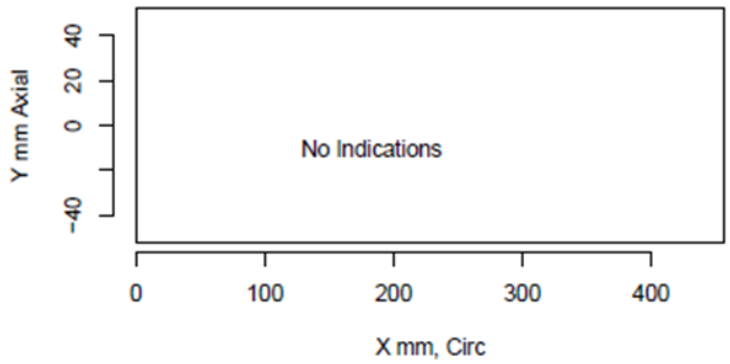

Figure 4.16. Indication Plot for Technique 106-ECT0 Applied to Quickblind Test Block P45 in PARENT Blind Testing (X–Y view)

4.9 Detection Performance Analysis

This section presents the results of the detection performance analysis of ECT techniques applied to LBDMW test blocks in PARENT. Results are presented as tables of POD at several discrete flaw sizes (depth and length) and as plots of POD curves as a function of flaw size. The tables also include tabulation of the FCR. The following section includes a tabulated summary of overall detection performance for ECT techniques for scoring tolerances of 10 mm and 15 mm to account for the positioning error observed for axial flaws in test block P33. This summary is followed by sections presenting the detection performance results obtained from the total flaw population, the axial flaw population, and the circumferential flaw population as a function of depth and length. In these sections, results are also presented for scoring tolerances of 10 mm and 15 mm.

4.9.1 Overall Detection Analysis Results

This section provides tabulated summaries of the overall detection performance of ECT techniques in PARENT for scoring tolerances of 10 mm (Table 4.9) and 15 mm (Table 4.10). In these tables, NOBS refers to "number-of-observations," which, for overall detection performance, refers to the total number of flaws in the inspected test blocks. However, because ECT techniques are evaluated, subsurface flaws are not included. For example, NOBS for 101-ECT1 is 17 because there are a total of 17 surface-breaking flaws in test blocks P33 and P13. POD in these tables is not expressed as a function of any parameter, but is simply the overall POD obtained by dividing the detected flaws by NOBS.

The impact of increasing the tolerance from 10 mm and 15 mm on the detection performance of 101-ECT1 is evident in Tables 4.9 and 4.10. These tables reveal that the overall POD increases from 53% to 82%, and the FCR and FCP experience significant reductions as the tolerance is increased from 10 mm to 15 mm.

Table 4.9. Overall Detection Performance by ECT Techniques on LBDMW Blocks with a tolerance = 10 mm

	NOBS	POD, %	FCP, %	FCR, #/m
101-ECT1	17	53	5	2.1
106-ECT0	3	100	0	0.0
135-ECT1	16	75	1	0.4
All	36	67	3	1.0

Table 4.10. Overall Detection Performance by ECT Techniques on LBDMW Blocks with a tolerance = 15 mm

	NOBS	POD, %	FCP, %	FCR, #/m
101-ECT1	17	82	1	0.4
106-ECT0	3	100	0	0.0
135-ECT1	16	75	1	0.4
All	36	81	1	0.3

4.9.2 Summary of Detection Analysis Results for All Flaws

This section presents the detection performance results obtained from the total flaw population as POD versus depth and length. Detection performance is presented in a tabular format with POD values provided at discrete flaw sizes (i.e., at 0 mm, 5 mm, 10 mm, 15 mm, etc.). The values of POD at these discrete flaw sizes are the values estimated by the logistic regression model expressed by Eqs. (3.3) and (3.4). In tabulated summaries, NOBS refers to the total number of flaws in the test blocks inspected by a given technique. The value of POD at 0 mm [POD(0)] is the value of the regression fit at S = 0 mm. The value of the regression fit at 0 mm is influenced by the measured FCP, which is calculated from the FCR by Eq. (3.6).

4.9.2.1 Summary of Detection Performance as a Function of Flaw Depth

This section summarizes detection performance results obtained from the total flaw population as POD versus depth. Tables 4.11 and 4.12 provide the POD values at discrete flaw sizes (i.e., at 0 mm, 5 mm, 10 mm, 15 mm, and 30 mm) for scoring tolerances of 10 mm and 15 mm, respectively. A column for NOBS and FCR is also included in the tables. Comparison of Tables 4.11 and 4.12 can illustrate how aggregate detection performance (i.e., for 135-ECT1 + 101-ECT1 + 106-ECT0, and for 135-ECT1 + 101-ECT1) and detection performance for 101-ECT1 is impacted by the increase in tolerance from 10 mm to 15 mm. As the tables show, the increase in scoring tolerance results in a decrease in the FCR and POD at 0 mm, which is anticipated considering the positioning error that results in several misses of axial flaws for a scoring tolerance of 10 mm. Further, an increase in the POD at 5 mm, 10 mm, 15 mm, and 30 mm is observed for the aggregate summaries and for 101-ECT1.

Plots of aggregate POD curves versus flaw depth (i.e., for 135-ECT1 + 101-ECT1 + 106-ECT0) for scoring tolerances of 10 mm and 15 mm are provided in Figures 4.17 and 4.18, respectively. The solid black line represents the regression fit to the data and the red dashed lines represent 95% confidence bounds for the regression fit. The change in shape from Figure 4.17 to Figure 4.18 indicates improvement in detection performance, which is anticipated for an increase in tolerance from 10 mm to 15 mm, which

resulted in reclassification of several misses and false calls resulting from positioning error of axial flaws as hits.

Table 4.11. Summary of POD (%) versus Flaw Depth for All Flaw Orientations (tolerance = 10 mm)

	NOBS	FCR	0 mm	5 mm	10 mm	15 mm	30 mm
101-ECT1	17	2.09	8	14	23	35	72
106-ECT0	3	0.00	3	10	27	56	97
135-ECT1	16	0.40	3	23	76	97	100
135-ECT1 + 101-ECT1	33	1.31	6	15	32	57	95
135-ECT1 + 101-ECT1 + 106-ECT0	36	1.04	5	14	34	62	97

Table 4.12. Summary of POD (%) versus Flaw Depth for All Flaw Orientations (tolerance = 15 mm)

	NOBS	FCR	0 mm	5 mm	10 mm	15 mm	30 mm
101-ECT1	17	0.36	3	25	78	97	100
106-ECT0	3	0.00	3	10	27	56	97
135-ECT1	16	0.42	3	23	76	97	100
135-ECT1 + 101-ECT1	33	0.39	2	32	91	100	100
135-ECT1 + 101-ECT1 + 106-ECT0	36	0.31	2	34	93	100	100

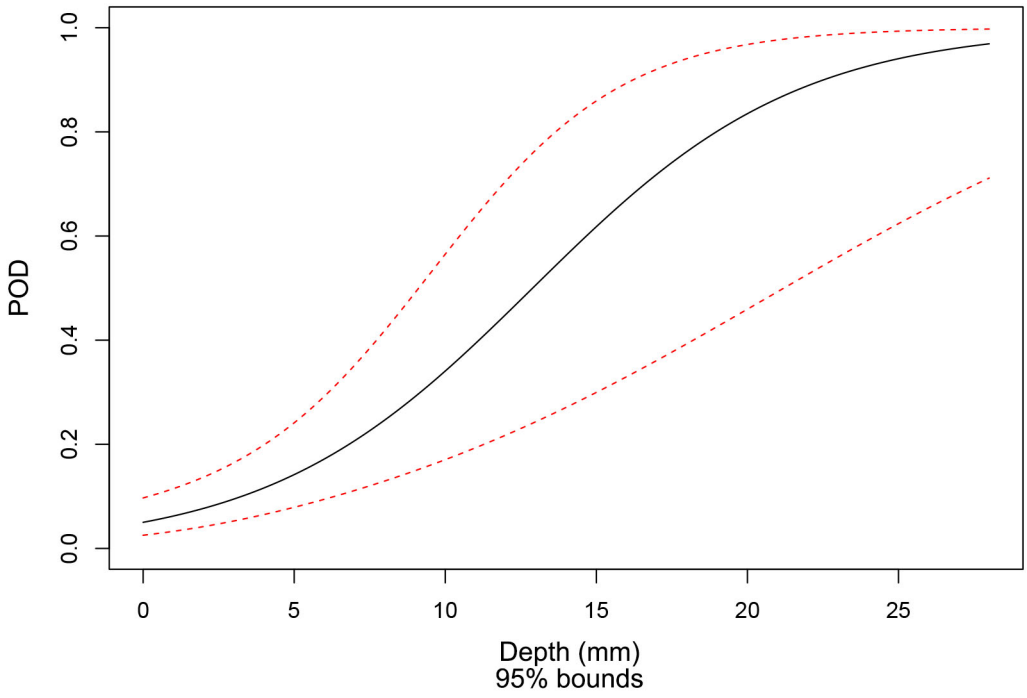

Figure 4.17. Aggregate Probability of Detection Curve versus Depth for ECT Techniques 135-ECT1, 101-ECT1, 106-ECT0 and for All Flaw Orientations (tolerance = 10 mm)

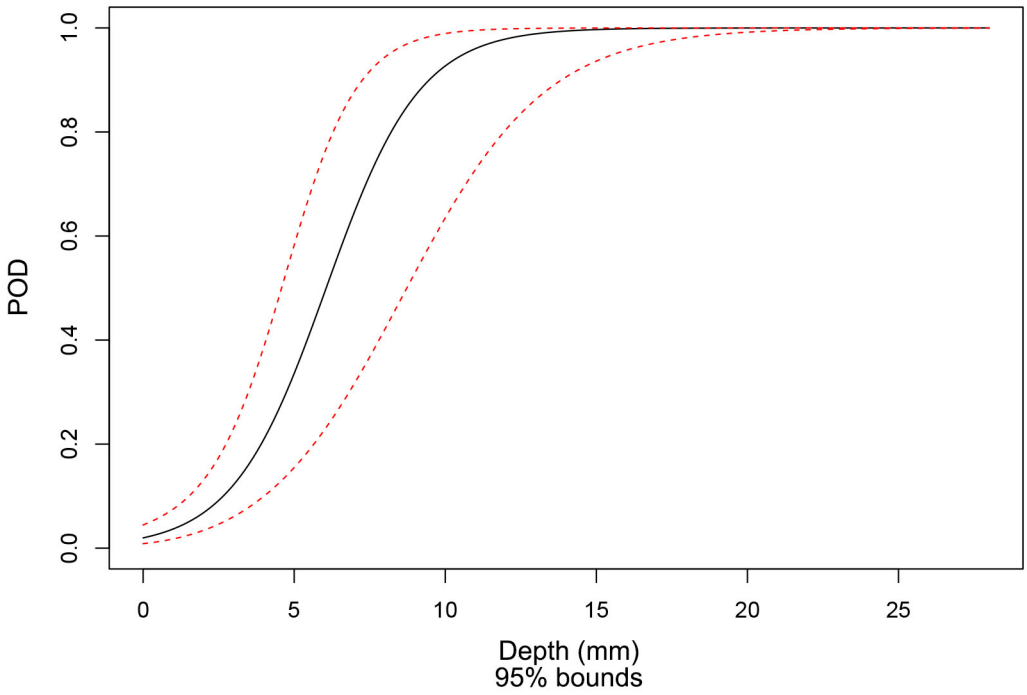

Figure 4.18. Aggregate Probability of Detection Curve versus Depth for ECT Techniques 135-ECT1, 101-ECT1, 106-ECT0 and for All Flaw Orientations (tolerance = 15 mm)

4.9.2.2 Summary of Detection Performance as a Function of Flaw Length

This section summarizes detection performance results obtained from the total flaw population as POD versus length. Tables 4.13 and 4.14 provide the POD values at discrete flaw sizes (i.e., at 0 mm, 5 mm, 10 mm, 15 mm, and 30 mm) for scoring tolerances of 10 mm and 15 mm, respectively. Comparison of Table 4.13 and Table 4.14 can illustrate how aggregate detection performance (i.e., for 135-ECT1 + 101-ECT1 + 106-ECT0, and for 135-ECT1 + 101-ECT1) and detection performance for 101-ECT1 is impacted by the increase in tolerance from 10 mm to 15 mm. As the tables show, the increase in scoring tolerance results in a decrease in the FCR and POD at 0 mm, which is anticipated considering the positioning error that results in several misses of axial flaws for 101-ECT1 for a scoring tolerance of 10 mm. Further, an increase in the POD at 5 mm, 10 mm, 15 mm, and 30 mm is observed for the aggregate summaries and for 101-ECT1.

Plots of aggregate POD curves versus flaw length (i.e., for 135-ECT1 + 101-ECT1 + 106-ECT0) for scoring tolerances of 10 mm and 15 mm are provided in Figures 4.19 and 4.20, respectively. The solid black line represents the regression fit to the data and the red dashed lines represent 95% confidence bounds for the regression fit. As with Figures 4.17 and 4.18, the change in shape from Figure 4.19 to Figure 4.20 indicates improvement in detection performance, which is anticipated for an increase in tolerance from 10 mm to 15 mm.

Table 4.13. Summary of POD versus Flaw Length for All Flaw Orientations (tolerance = 10 mm)

	NOBS	FCR	0 mm	5 mm	10 mm	15 mm	30 mm
101-ECT1	17	2.09	6	12	23	39	86
106-ECT0	3	0.00	1	4	13	32	94
135-ECT1	16	0.40	2	10	37	76	100
135-ECT1 + 101-ECT1	33	1.31	4	11	29	56	98
135-ECT1 + 101-ECT1 + 106-ECT0	36	1.04	3	10	28	58	98

Table 4.14. Summary of POD versus Flaw Length for All Flaw Orientations (tolerance = 15 mm)

	NOBS	FCR	0 mm	5 mm	10 mm	15 mm	30 mm
101-ECT1	17	0.36	2	11	42	80	100
106-ECT0	3	0.00	1	4	13	32	94
135-ECT1	16	0.42	2	10	37	76	100
135-ECT1 + 101-ECT1	33	0.39	2	10	45	85	100
135-ECT1 + 101-ECT1 + 106-ECT0	36	0.31	1	9	44	86	100

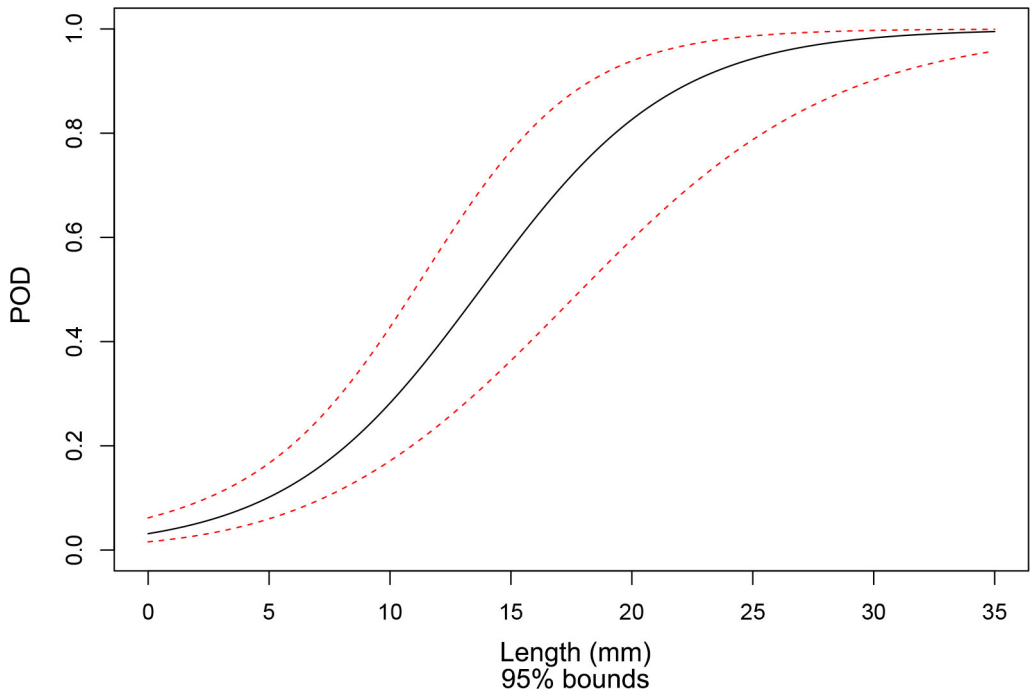

Figure 4.19. Aggregate Probability of Detection Curve versus Length for ECT Techniques 135-ECT1, 101-ECT1, 106-ECT0 and for All Flaw Orientations (tolerance = 10 mm)

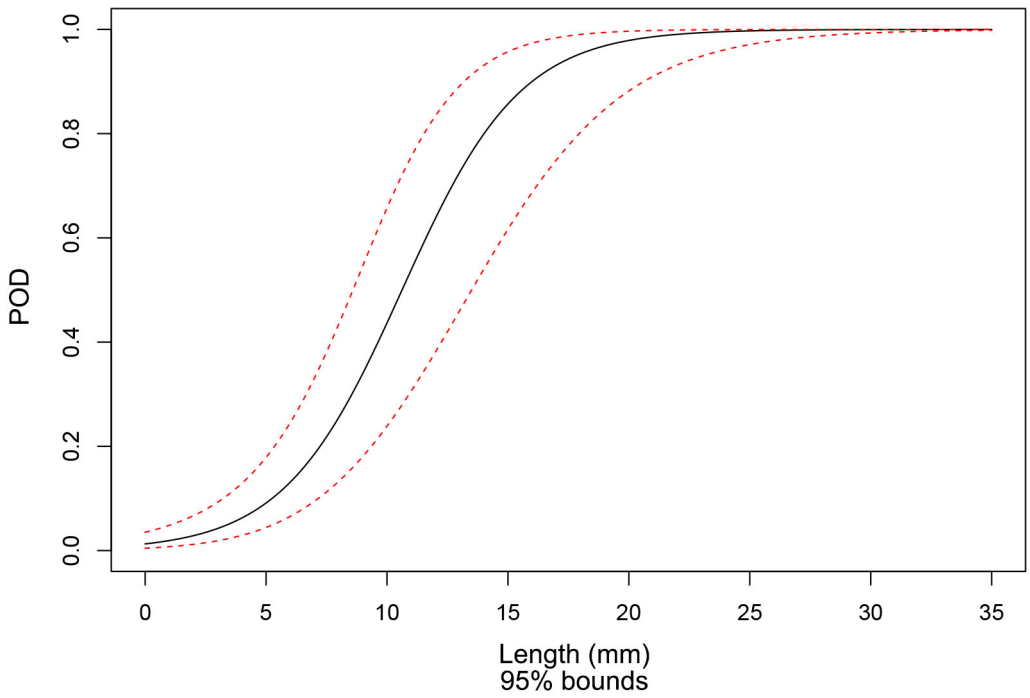

Figure 4.20. Aggregate Probability of Detection Curve versus Length for ECT Techniques 135-ECT1, 101-ECT1, 106-ECT0 and for All Flaw Orientations (tolerance = 15 mm)

4.9.3 Summary of Detection Analysis Results for Axial Flaws

This section presents the detection performance results obtained from the axial flaw population as POD versus depth and length. The data is presented in tabular form and as plots of POD curves, as is done for detection performance data collected from the population of all flaws in Section 4.9.2.

4.9.3.1 Summary of Detection Performance as a Function of Flaw Depth

This section summarizes detection performance results obtained from the axial flaw population as POD versus depth. Tables 4.15 and 4.16 provide the POD values at discrete flaw sizes (i.e., at 0 mm, 5 mm, 10 mm, 15 mm, and 30 mm) for scoring tolerances of 10 mm and 15 mm, respectively. A column for NOBS and FCR is also included in the tables. In this case, NOBS represents the total number of axial flaws in the test blocks inspected by a given technique. Comparison of Tables 4.15 and 4.16 illustrates how aggregate detection performance (i.e., for 135-ECT1 + 101-ECT1) and detection performance for 101-ECT1 is impacted by the increase in tolerance from 10 mm to 15 mm. As the tables show, the increase in scoring tolerance results in a decrease in the FCR and POD at 0 mm, which is anticipated considering the positioning error that results in several misses of axial flaws for 101-ECT1 for a scoring tolerance of 10 mm. Further, an increase in the POD at 5 mm, 10 mm, 15 mm, and 30 mm is observed for the aggregate summary and for 101-ECT1.

Plots of aggregate POD curves versus flaw depth (i.e., for 135-ECT1 + 101-ECT1) for axial flaws and for scoring tolerances of 10 mm and 15 mm are provided in Figures 4.21 and 4.22, respectively. The solid black line represents the regression fit to the data and the red dashed lines represent 95% confidence bounds for the regression fit. The change in shape from Figure 4.21 to Figure 4.22 indicates improvement in detection performance, which is anticipated for an increase in tolerance from 10 mm to 15 mm. In this

case, the POD exhibits saturation (100% POD) at 15 mm flaw depth for a tolerance of 15 mm, whereas the POD for a 30 mm deep flaw is just 79% when the tolerance is 10 mm.

Table 4.15. Summary of POD versus Flaw Depth for Axially Oriented Flaws (tolerance = 10 mm)

	NOBS	FCR	0 mm	5 mm	10 mm	15 mm	30 mm
101-ECT1	9	2.09	7	10	14	20	39
135-ECT1	8	0.40	3	18	62	92	100
135-ECT1 + 101-ECT1	17	1.31	5	11	20	35	79

Table 4.16. Summary of POD versus Flaw Depth for Axially Oriented Flaws (tolerance = 15 mm)

	NOBS	FCR	0 mm	5 mm	10 mm	15 mm	30 mm
101-ECT1	9	0.36	3	21	68	94	100
135-ECT1	8	0.42	3	18	62	92	100
135-ECT1 + 101-ECT1	17	0.39	2	36	93	100	100

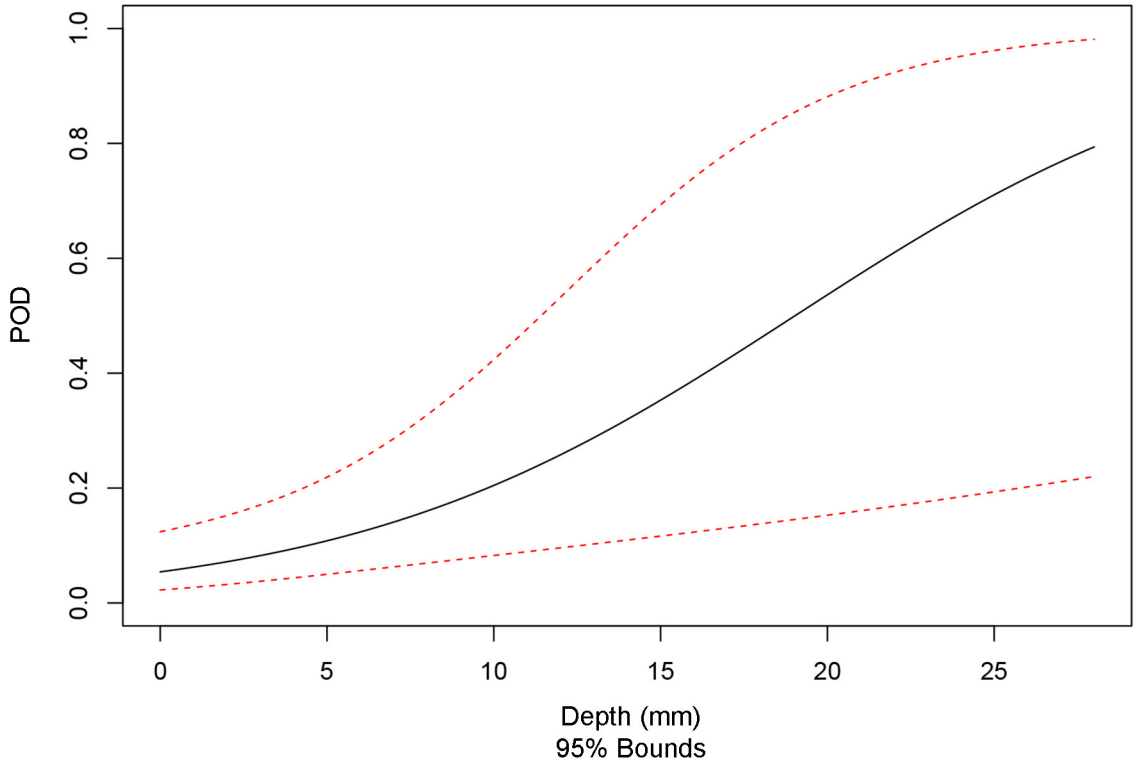

Figure 4.21. Aggregate Probability of Detection Curve versus Depth for ECT Techniques 135-ECT1 and 101-ECT1 for Axial Flaws (tolerance = 10 mm)

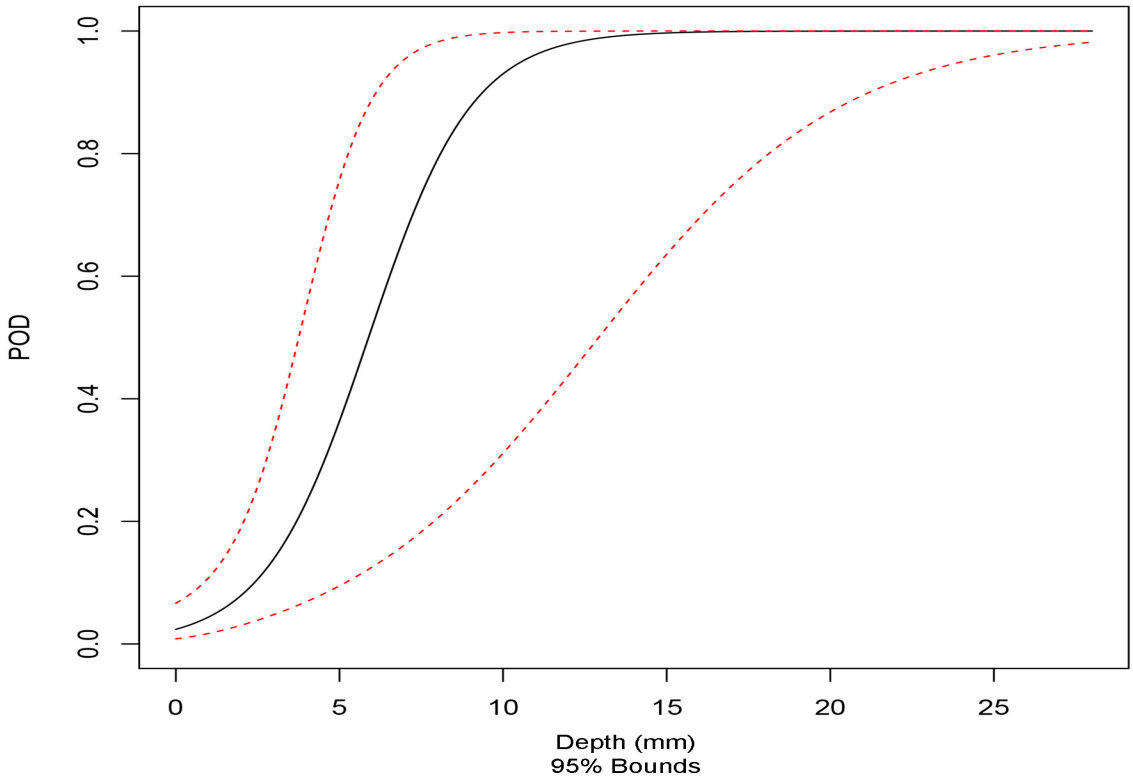

Figure 4.22. Aggregate Probability of Detection Curve versus Depth for ECT Techniques 135-ECT1 and 101-ECT1 for Axial Flaws (tolerance = 15 mm)

4.9.3.2 Summary of Detection Performance as a Function of Flaw Length

This section summarizes detection performance results obtained from the axial flaw population as POD versus length. Tables 4.17 and 4.18 provide the POD values at discrete flaw sizes (i.e., at 0 mm, 5 mm, 10 mm, 15 mm, and 30 mm) for scoring tolerances of 10 mm and 15 mm, respectively. Comparison of Table 4.17 and Table 4.18 illustrates how aggregate detection performance (i.e., for 135-ECT1 + 101-ECT1) and detection performance for 101-ECT1 is impacted by the increase in tolerance from 10 mm to 15 mm. As the tables show, the increase in scoring tolerance results in a decrease in the FCR and POD at 0 mm, which is anticipated considering the positioning error that results in several misses of axial flaws for a scoring tolerance of 10 mm for 101-ECT1. Further, an increase in the POD at 5 mm, 10 mm, 15 mm, and 30 mm is observed for the aggregate summary and for 101-ECT1.

Plots of aggregate POD curves versus flaw length (i.e., for 135-ECT1 + 101-ECT1) for axial flaws and for scoring tolerances of 10 mm and 15 mm are provided in Figures 4.23 and 4.24, respectively. The change in shape from Figure 4.23 to Figure 4.24 indicates improvement in detection performance, which is anticipated for an increase in tolerance from 10 mm to 15 mm. There is apparent saturation of the POD curve at a flaw length of less than 30 mm for a tolerance of 15 mm. In the case of a 10 mm tolerance, no saturation of the curve is evident for flaw lengths of 30 mm or less.

Table 4.17. Summary of POD versus Flaw Length for Axially Oriented Flaws (tolerance = 10 mm)

	NOBS	FCR	0 mm	5 mm	10 mm	15 mm	30 mm
101-ECT1	9	2.09	6	11	19	32	63
135-ECT1	8	0.40	2	11	47	86	100
135-ECT1 + 101-ECT1	17	1.31	4	11	27	53	91

Table 4.18. Summary of POD versus Flaw Length for Axially Oriented Flaws (tolerance = 15 mm)

	NOBS	FCR	0 mm	5 mm	10 mm	15 mm	30 mm
101-ECT1	9	0.36	2	15	58	92	100
135-ECT1	8	0.42	2	12	47	86	100
135-ECT1 + 101-ECT1	17	0.39	2	16	67	96	100

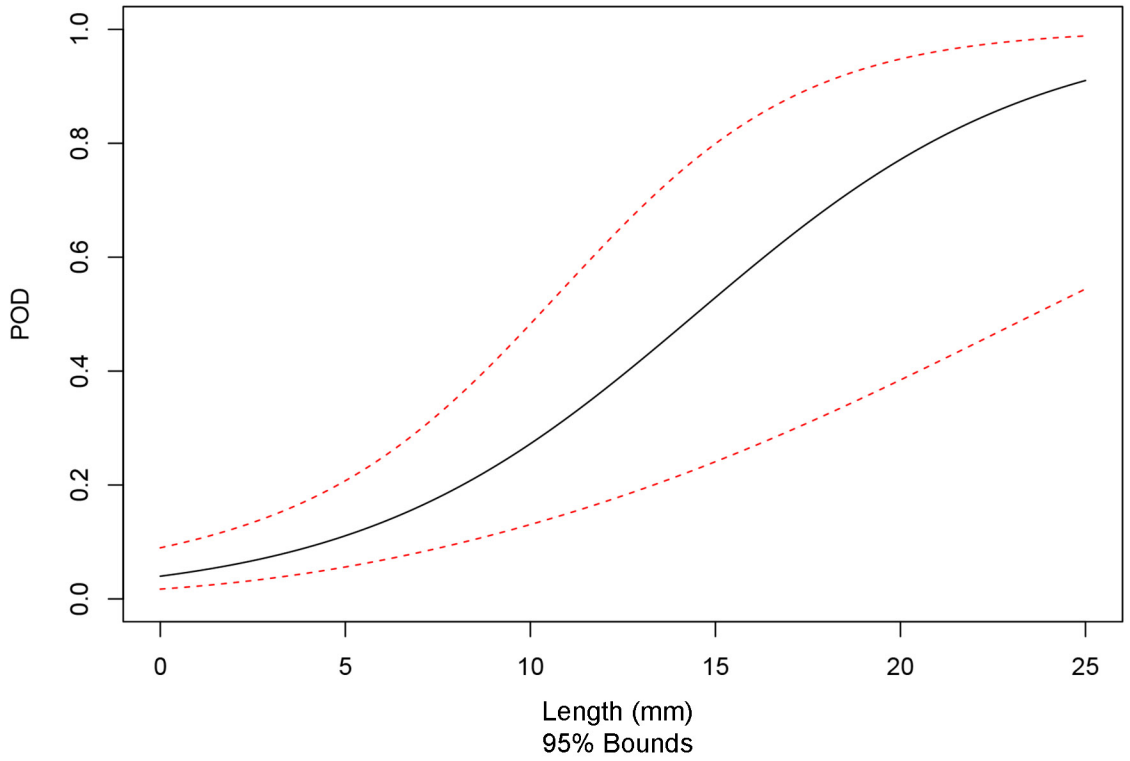

Figure 4.23. Aggregate Probability of Detection Curve versus Length for ECT Techniques 135-ECT1 and 101-ECT1 for Axial Flaws (tolerance = 10 mm)

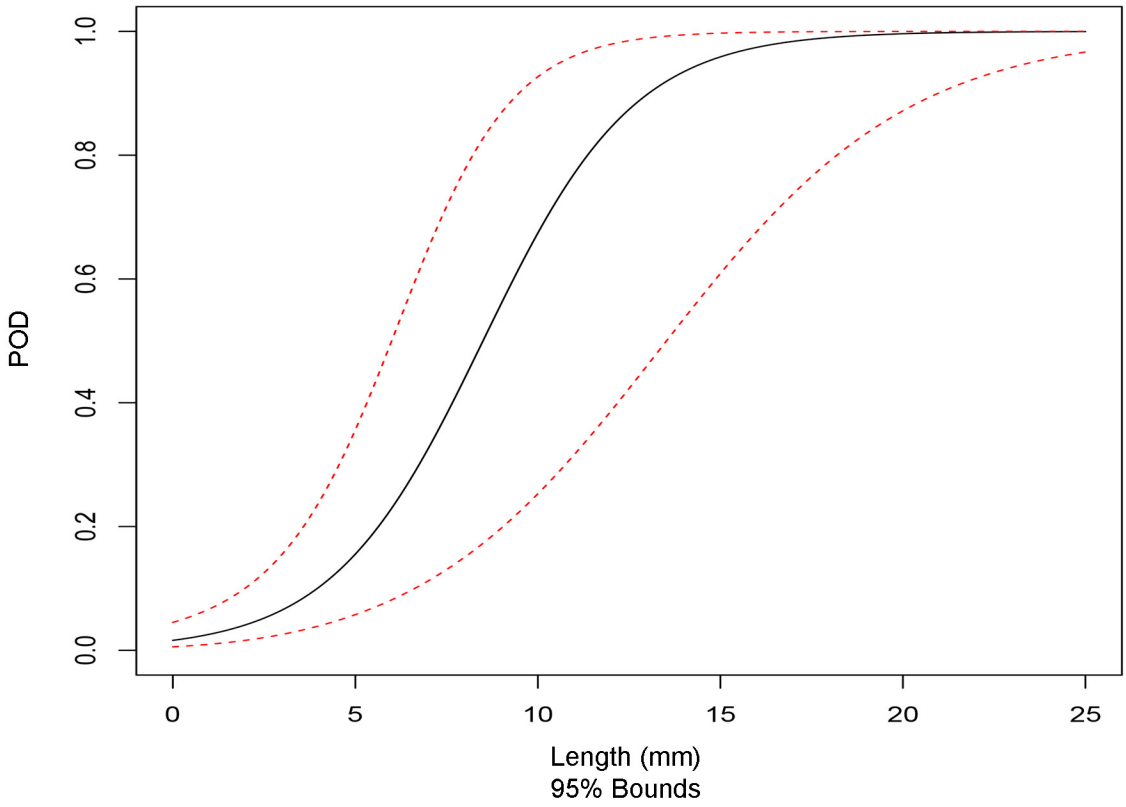

Figure 4.24. Aggregate Probability of Detection Curve versus Length for ECT Techniques 135-ECT1 and 101-ECT1 for Axial Flaws (tolerance = 15 mm)

4.9.4 Summary of Detection Analysis Results for Circumferential Flaws

This section presents the detection performance results obtained from the circumferential flaw population as POD versus depth and length. The data is presented in tabular form and as plots of POD curves, as is done for detection performance data collected from the population of all flaws in Section 4.9.2 and the population of axial flaws in Section 4.9.3.

4.9.4.1 Summary of Detection Performance as a Function of Flaw Depth

This section summarizes detection performance results obtained from the circumferential flaw population as POD versus depth. Tables 4.19 and 4.20 provide the POD values at discrete flaw sizes (i.e., at 0 mm, 5 mm, 10 mm, 15 mm, and 30 mm) for scoring tolerances of 10 mm and 15 mm, respectively. A column for NOBS and FCR is also included in the tables. In this case, NOBS represents the total number of circumferential flaws in the test blocks inspected by a given technique. Comparison of Table 4.19 and Table 4.20 illustrates that detection performance for circumferential flaws is modestly affected for any techniques by the increase in tolerance from 10 mm to 15 mm. This is anticipated considering the positioning error is only associated with axial flaws. Differences in Tables 4.19 and 4.20 are observed in FCR; however, this is because false calls are irrespective of the orientation of flaws in the test block. It is the change in FCR that results in the modest impact on POD between tolerances of 10 mm to 15 mm.

Plots of aggregate POD curves versus flaw depth (i.e., for 135-ECT1 + 101-ECT1) for circumferential flaws and for scoring tolerances of 10 mm and 15 mm are provided in Figures 4.25 and 4.26, respectively.

The solid black line represents the regression fit to the data and the red dashed lines represent 95% confidence bounds for the regression fit. As can be seen from Figures 4.25 and 4.26, the difference in appearance of the POD plots as a consequence of the increase in tolerance from 10 mm to 15 mm is barely perceptible. This is anticipated considering the positioning error is only associated with axial flaws.

Table 4.19. Summary of POD versus Flaw Depth for Circumferentially Oriented Flaws (tolerance = 10 mm)

	NOBS	FCR	0 mm	5 mm	10 mm	15 mm	30 mm
101-ECT1	8	2.09	6	19	47	77	99
135-ECT1	8	0.40	2	11	42	81	100
135-ECT1 + 101-ECT1	16	1.31	4	20	63	92	100

Table 4.20. Summary of POD versus Flaw Depth for Circumferentially Oriented Flaws (tolerance = 15 mm)

	NOBS	FCR	0 mm	5 mm	10 mm	15 mm	30 mm
101-ECT1	8	0.36	2	11	42	81	100
135-ECT1	8	0.42	2	11	42	81	100
135-ECT1 + 101-ECT1	16	0.39	1	14	63	95	100

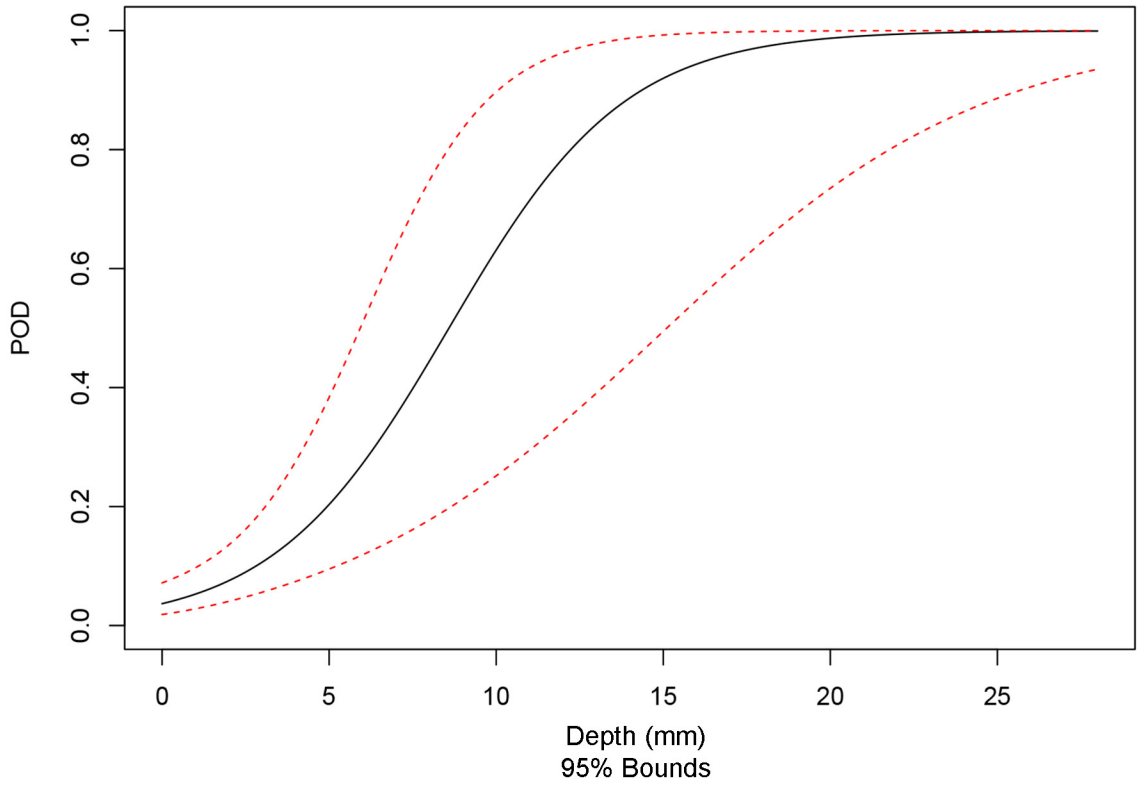

Figure 4.25. Aggregate Probability of Detection Curve versus Depth for ECT Techniques 135-ECT1 and 101-ECT1 for Circumferential Flaws (tolerance = 10 mm)

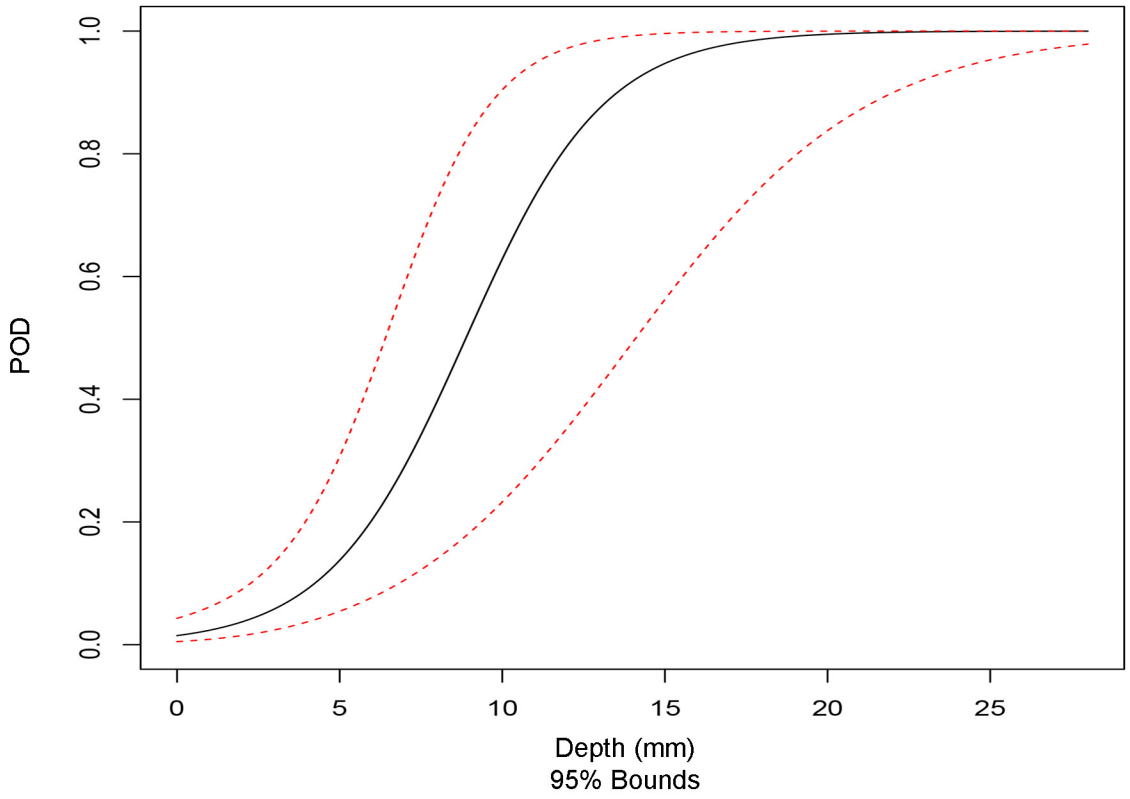

Figure 4.26. Aggregate Probability of Detection Curve versus Depth for ECT Techniques 135-ECT1 and 101-ECT1 for Circumferential Flaws (tolerance = 15 mm)

4.9.4.2 Summary of Detection Performance as a Function of Flaw Length

This section summarizes detection performance results obtained from the circumferential flaw population as POD versus length. Tables 4.21 and 4.22 provide the POD values at discrete flaw sizes (i.e., at 0 mm, 5 mm, 10 mm, 15 mm, and 30 mm) for scoring tolerances of 10 mm and 15 mm, respectively. Comparison of Tables 4.21 and 4.22 illustrates that detection performance for circumferential flaws is modestly affected for any techniques by the increase in tolerance from 10 mm to 15 mm. This is anticipated considering the positioning error is only associated with axial flaws. Differences in Tables 4.21 and 4.22 are observed in FCR; however, this is because false calls are irrespective of the orientation of flaws in the test block.

Plots of aggregate POD curves versus flaw depth (i.e., for 135-ECT1 + 101-ECT1) for circumferential flaws and for scoring tolerances of 10 mm and 15 mm are provided in Figures 4.27 and 4.28, respectively. As can be seen from Figures 4.27 and 4.28, the change in the POD curve as a consequence of the increase in tolerance from 10 mm to 15 mm is small. This is anticipated considering the positioning error is only associated with axial flaws.

Table 4.21. Summary of POD versus Flaw Length for Circumferentially Oriented Flaws (tolerance = 10 mm)

	NOBS	FCR	0 mm	5 mm	10 mm	15 mm	30 mm
101-ECT1	8	2.09	6	13	26	45	92
135-ECT1	8	0.40	2	6	17	40	96
135-ECT1 + 101-ECT1	16	1.31	4	10	27	54	97

Table 4.22. Summary of POD versus Flaw Length for Circumferentially Oriented Flaws (tolerance = 15 mm)

	NOBS	FCR	0 mm	5 mm	10 mm	15 mm	30 mm
101-ECT1	8	0.36	2	5	16	39	96
135-ECT1	8	0.42	2	6	17	40	96
135-ECT1 + 101-ECT1	16	0.39	1	6	20	52	99

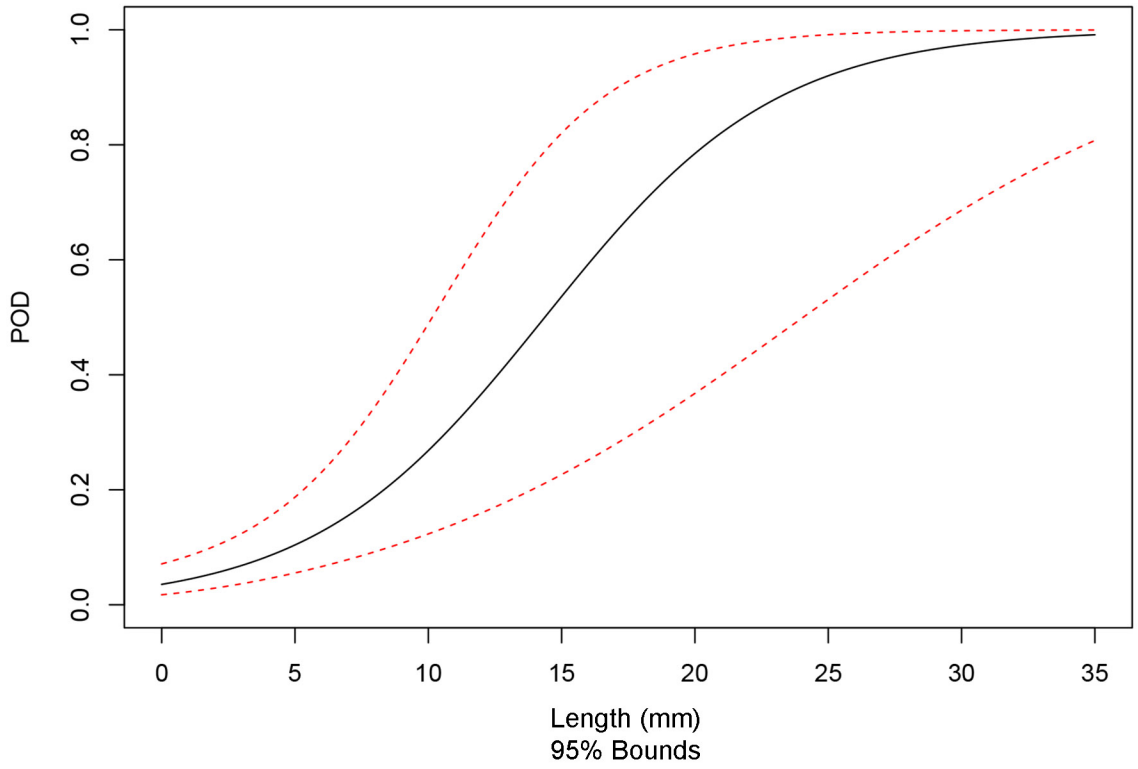

Figure 4.27. Aggregate Probability of Detection Curve versus Length for ECT Techniques 135-ECT1 and 101-ECT1 for Circumferential Flaws (tolerance = 10 mm)

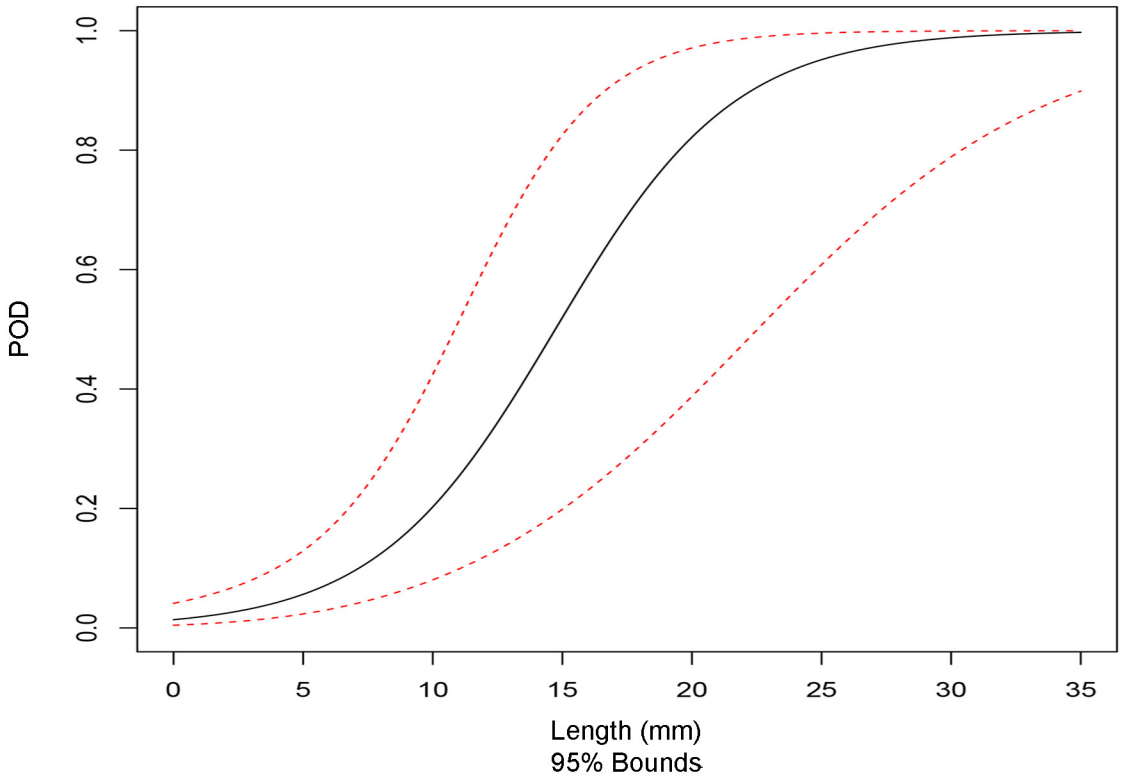

Figure 4.28. Aggregate Probability of Detection Curve versus Length for ECT Techniques 135-ECT1 and 101-ECT1 for Circumferential Flaws (tolerance = 15 mm)

4.10 Length Sizing Analysis

This section presents the results of the length sizing performance analysis of ECT techniques applied to LBDMW test blocks in PARENT. Results are presented as tabulations of bias and RMSE and as plots of length sizing regression curves. The following sections include tabulated summaries of length sizing performance for ECT techniques for scoring tolerances of 10 mm and 15 mm to account for the positioning error observed for axial flaws in test block P33. Summaries of length sizing results are provided for the total flaw population, the axial flaw population, and the circumferential flaw population.

4.10.1 Summary of Length Sizing Analysis Results for All Flaws

This section presents the results of the length sizing performance analysis of ECT techniques applied to the total detected flaw population. Tabulation of length sizing bias and RMSE for ECT techniques are provided in Tables 4.23 and 4.24 for scoring tolerances of 10 mm and 15 mm, respectively. The NOBS column refers to the sample size used for length sizing analysis. It is equal to the number of detections.

Aggregate length sizing regression plots are provided in Figure 4.29 through Figure 4.32 for the total detected flaw population. Symbols “A” and “C” are used to represent axially oriented flaws and circumferentially oriented flaws, respectively. The symbol “D” in Figure 4.29 and Figure 4.31 refers to flaws with a diagonal orientation. The designation of diagonal orientation is used to denote flaws that do not have a dominant orientation based on dimensions. In this case, flaws in the Quickblind test blocks P15, P16, and P17 were denoted as diagonal. Figure 4.29 and Figure 4.31 provide aggregate regression plots for ECT techniques 135-ECT1, 101-ECT1, and 106-ECT0 for scoring tolerances of 10 mm and

15 mm, respectively. Figure 4.30 and Figure 4.32 provide aggregate regression plots for ECT techniques 135-ECT1 and 101-ECT1, for scoring tolerances of 10 mm and 15 mm, respectively.

Table 4.23. Summary of Length Sizing Error for ECT Techniques for All Flaw Orientations (tolerance = 10 mm)

	NOBS	Bias	RMSE
101-ECT1	9	−0.6	3.7
106-ECT0	3	−7.7	8.9
135-ECT1	12	−2.2	6.2
135-ECT1 + 101-ECT1	21	−1.5	5.3
135-ECT1 + 101-ECT1 + 106-ECT0	24	−2.3	5.8

Table 4.24. Summary of Length Sizing Error for ECT Techniques for All Flaw Orientations (tolerance = 15 mm)

	NOBS	Bias	RMSE
101-ECT1	14	1.2	4.3
106-ECT0	3	−7.7	8.9
135-ECT1	12	−2.2	6.2
135-ECT1 + 101-ECT1	26	−0.4	5.3
135-ECT1 + 101-ECT1 + 106-ECT0	29	−1.1	5.7

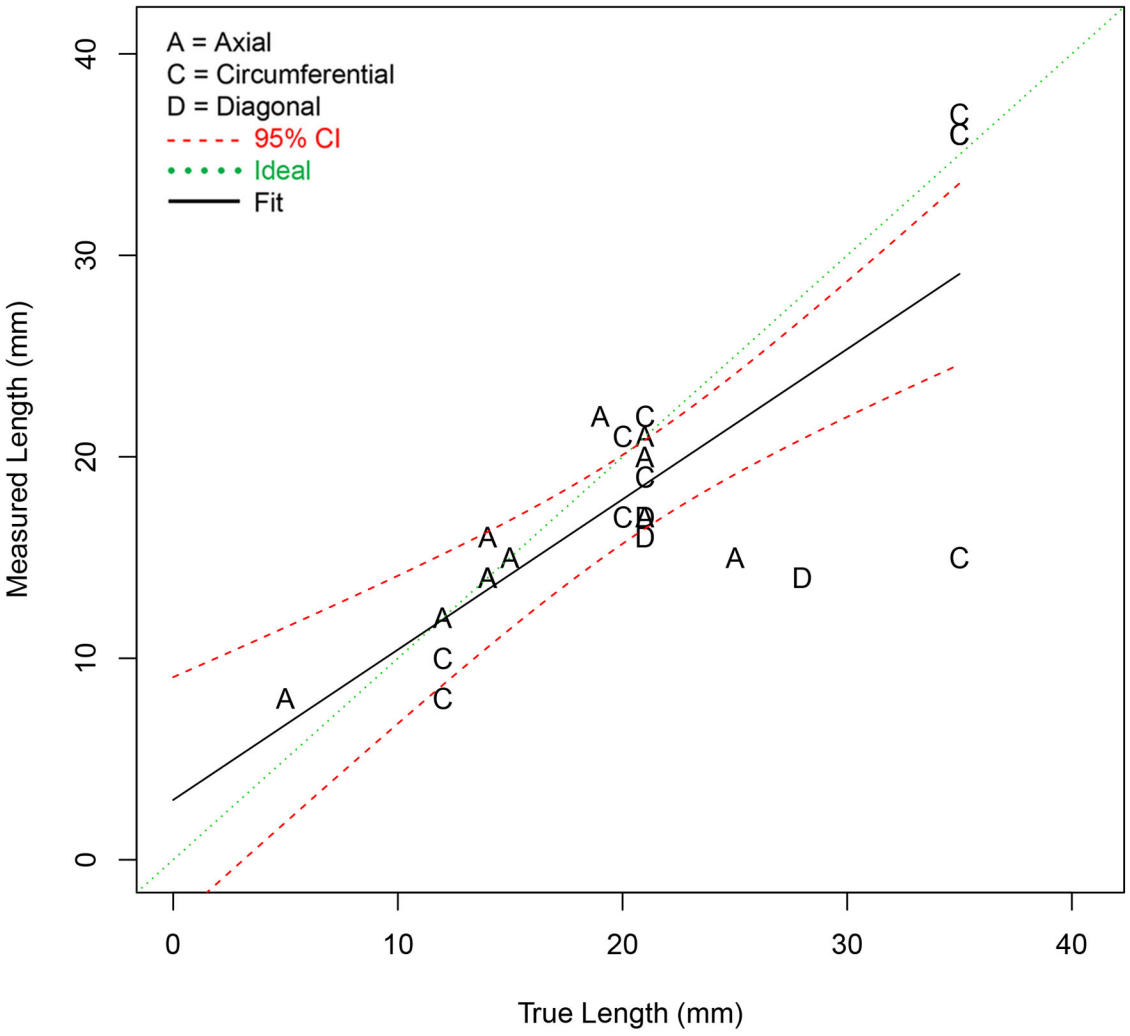

Figure 4.29. Aggregate Length Sizing Regression Fit for ECT Techniques 135-ECT1, 101-ECT1, and 106-ECT0 for All Flaw Orientations (tolerance = 10 mm)

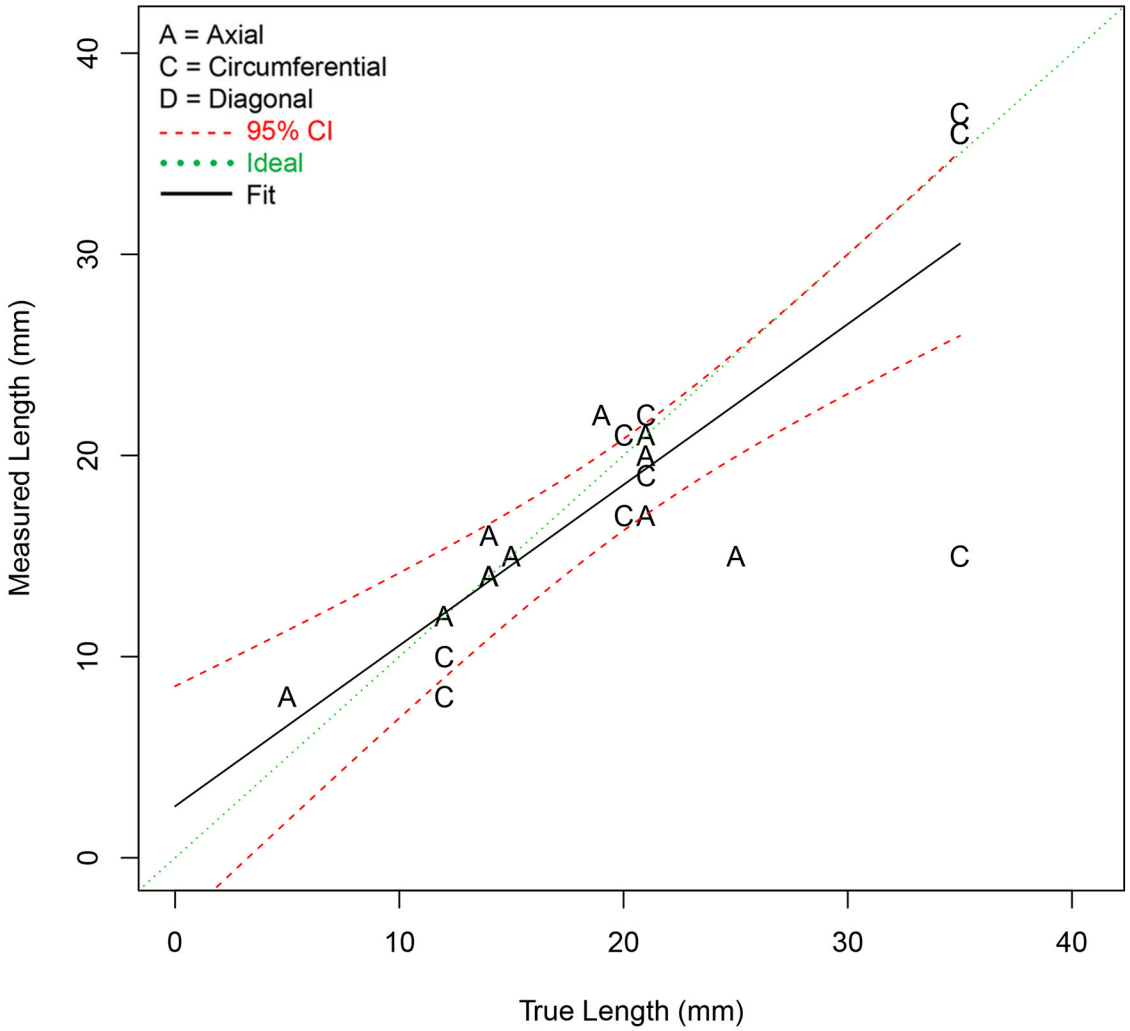

Figure 4.30. Aggregate Length Sizing Regression Fit for ECT Techniques 135-ECT1 and 101-ECT1 for All Flaw Orientations (tolerance = 10 mm)

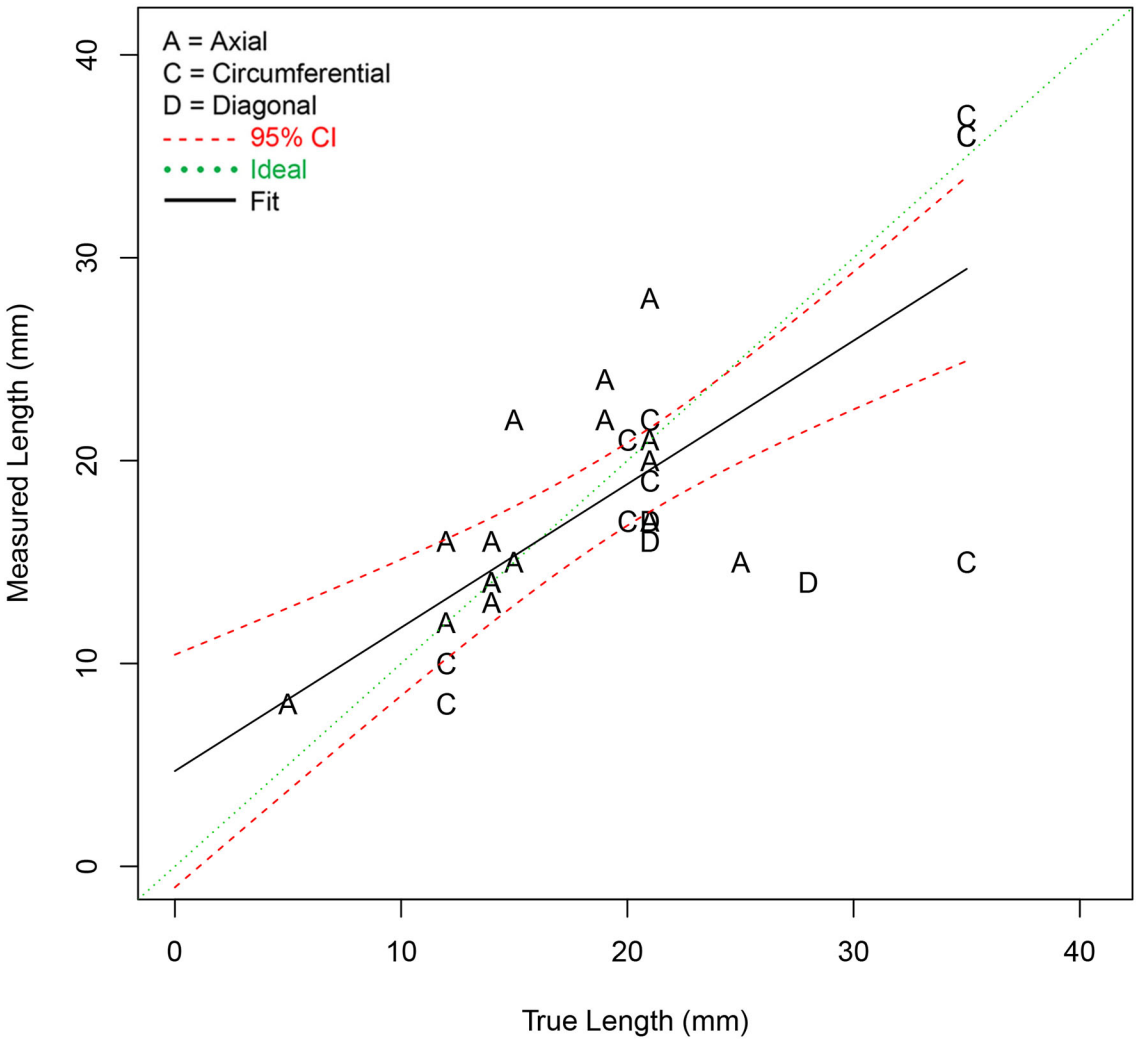

Figure 4.31. Aggregate Length Sizing Regression Fit for ECT Techniques 135-ECT1, 101-ECT1, and 106-ECT0 for All Flaw Orientations (tolerance = 15 mm)

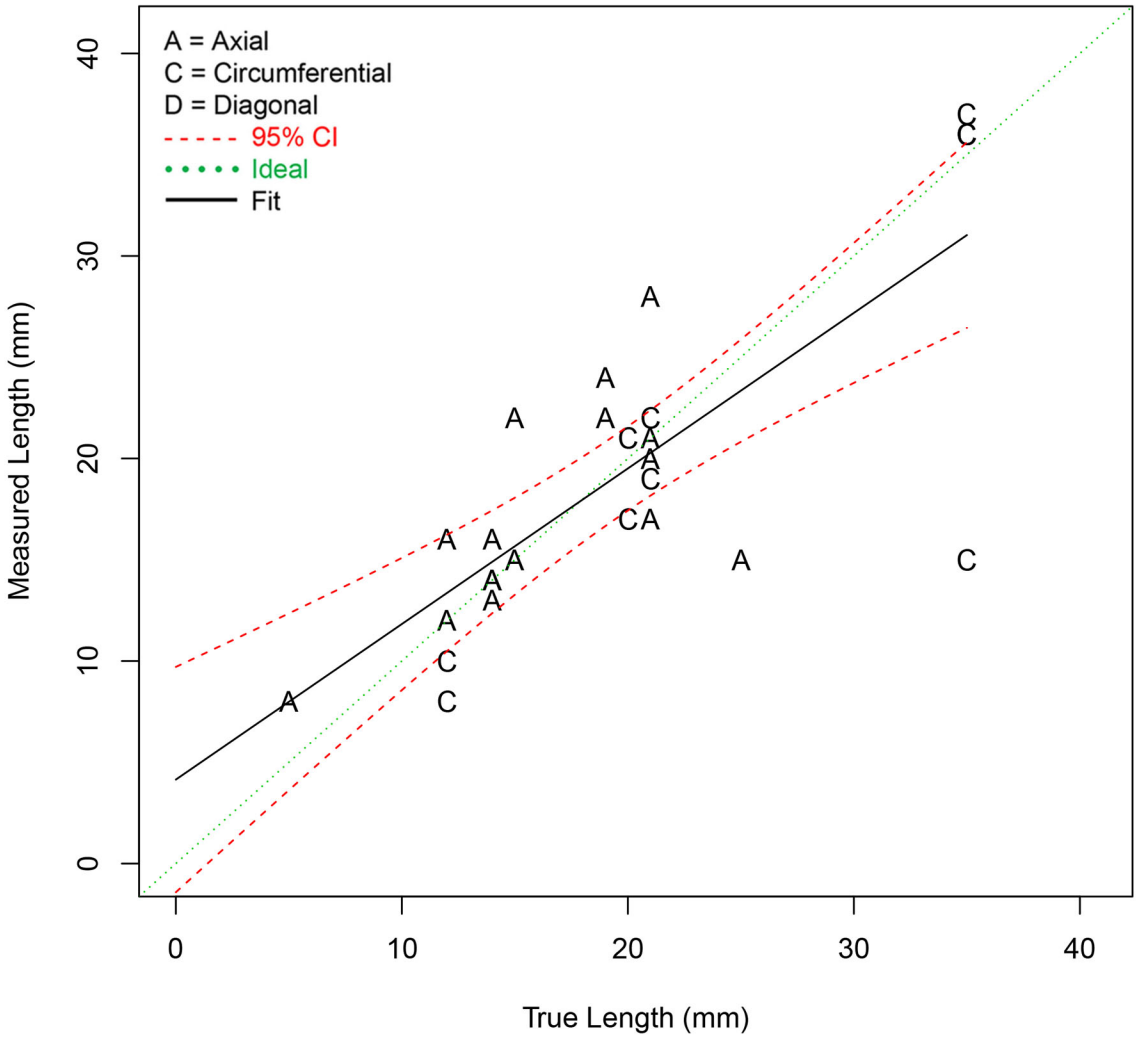

Figure 4.32. Aggregate Length Sizing Regression Fit for ECT Techniques 135-ECT1 and 101-ECT1 for All Flaw Orientations (tolerance = 15 mm)

4.10.2 Summary of Length Sizing Analysis Results for Axial Flaws

This section presents the results of the length sizing performance analysis of ECT techniques applied to the population of detected axial flaws. Tabulation of length sizing bias and RMSE for ECT techniques are provided in Table 4.25 and Table 4.26 for scoring tolerances of 10 mm and 15 mm, respectively. In this case, NOBS is equal to the number of detected axial flaws.

Aggregate length sizing regression plots are provided in Figure 4.33 and Figure 4.34 for the population of detected axial flaws for scoring tolerances of 10 mm and 15 mm, respectively.

Table 4.25. Summary of Length Sizing Error for ECT Techniques for Axial Flaws (tolerance = 10 mm)

	NOBS	Bias	RMSE
101-ECT1	4	−2.0	5.2
135-ECT1	7	0.1	2.0
135-ECT1 + 101-ECT1	11	−0.6	3.6

Table 4.26. Summary of Length Sizing Error for ECT Techniques for Axial Flaws (tolerance = 15 mm)

	NOBS	Bias	RMSE
101-ECT1	9	1.6	5.3
135-ECT1	7	0.1	2.0
135-ECT1 + 101-ECT1	16	0.9	4.2

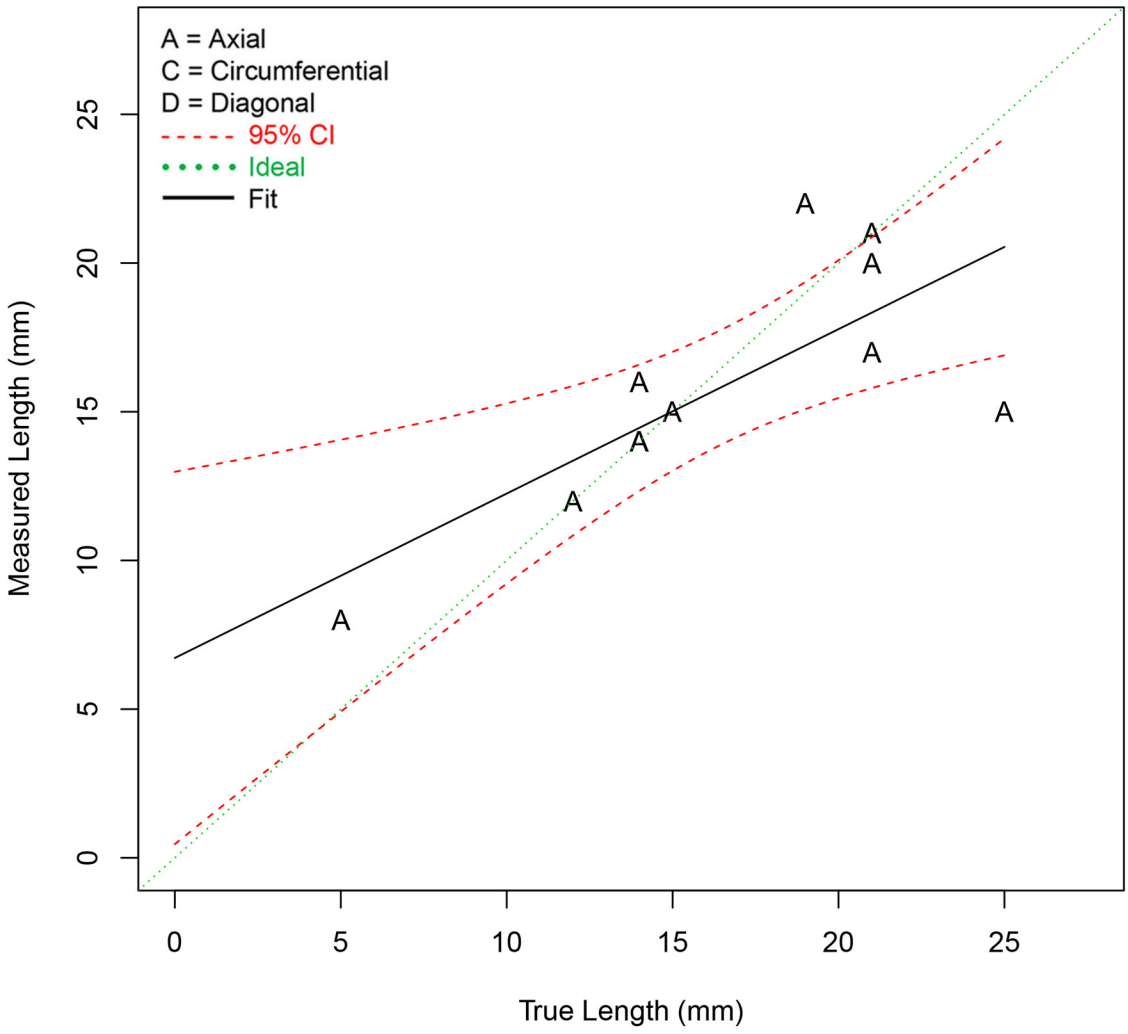

Figure 4.33. Aggregate Length Sizing Regression Fit for ECT Techniques 135-ECT1 and 101-ECT1 for Axial Flaws (tolerance = 10 mm)

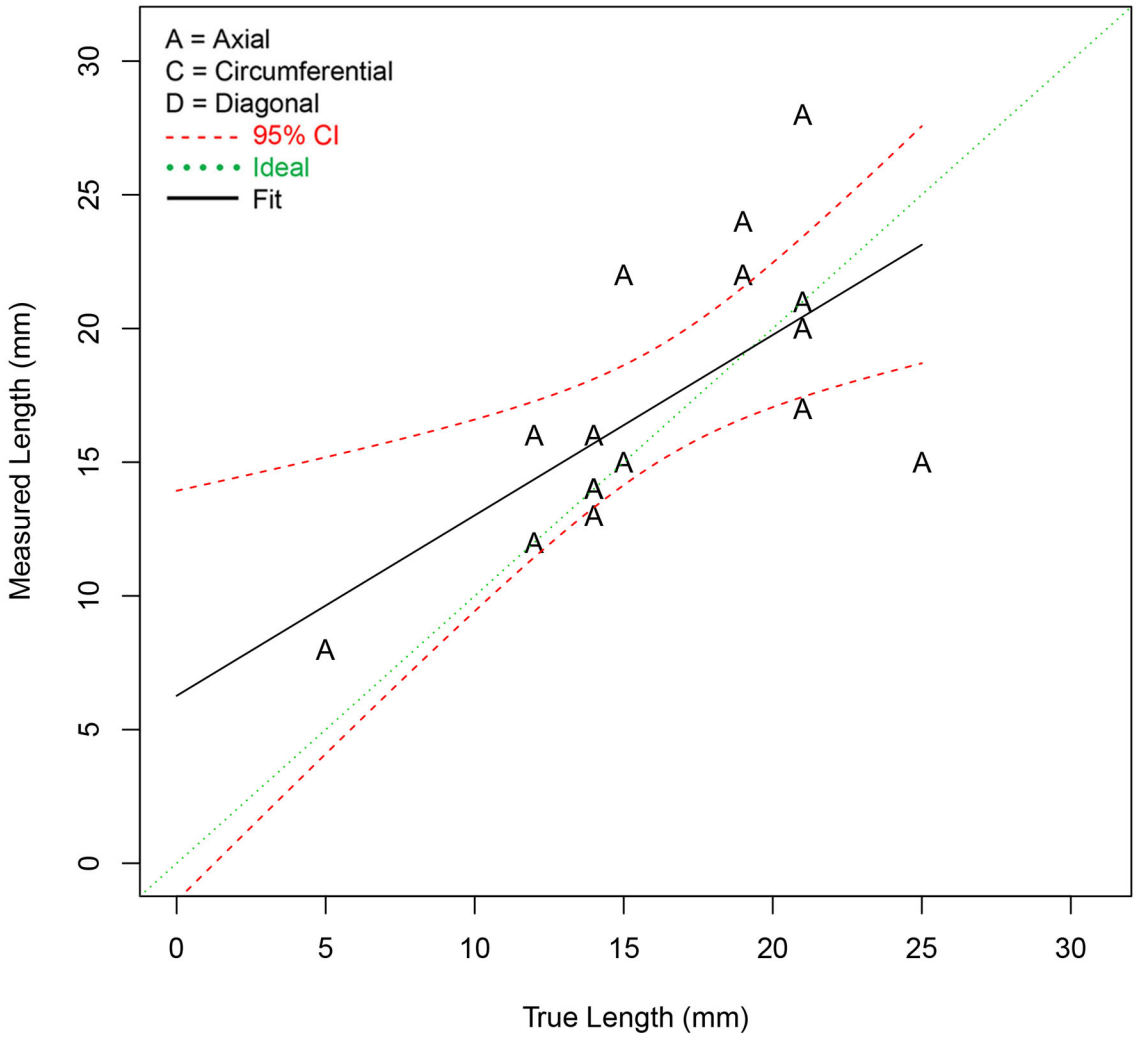

Figure 4.34. Aggregate Length Sizing Regression Fit for ECT Techniques 135-ECT1 and 101-ECT1 for Axial Flaws (tolerance = 15 mm)

4.10.3 Summary of Length Sizing Analysis Results for Circumferential Flaws

This section presents the results of the length sizing performance analysis of ECT techniques applied to the population of detected circumferential flaws. Tabulation of length sizing bias and RMSE for ECT techniques are provided in Table 4.27 and Table 4.28 for scoring tolerances of 10 mm and 15 mm, respectively. In this case, NOBS is equal to the number of detected circumferential flaws. Table 4.27 and Table 4.28 indicate no changes as a result of the increase in scoring tolerance from 10 mm to 15 mm, which is expected because the number of circumferential flaw detections is not impacted by the scoring tolerance change.

The aggregate length sizing regression plot is provided in Figure 4.35 and represents the length sizing regression curve for scoring tolerances of 10 mm and 15 mm.

Table 4.27. Summary of Length Sizing Error for ECT Techniques for Circumferential Flaws (tolerance = 10 mm)

	NOBS	Bias	RMSE
101-ECT1	5	0.6	1.5
135-ECT1	5	−5.6	9.3
135-ECT1 + 101-ECT1	10	−2.5	6.6

Table 4.28. Summary of Length Sizing Error for ECT Techniques for Circumferential Flaws (tolerance = 15 mm)

	NOBS	Bias	RMSE
101-ECT1	5	0.6	1.5
135-ECT1	5	−5.6	9.3
135-ECT1 + 101-ECT1	10	−2.5	6.6

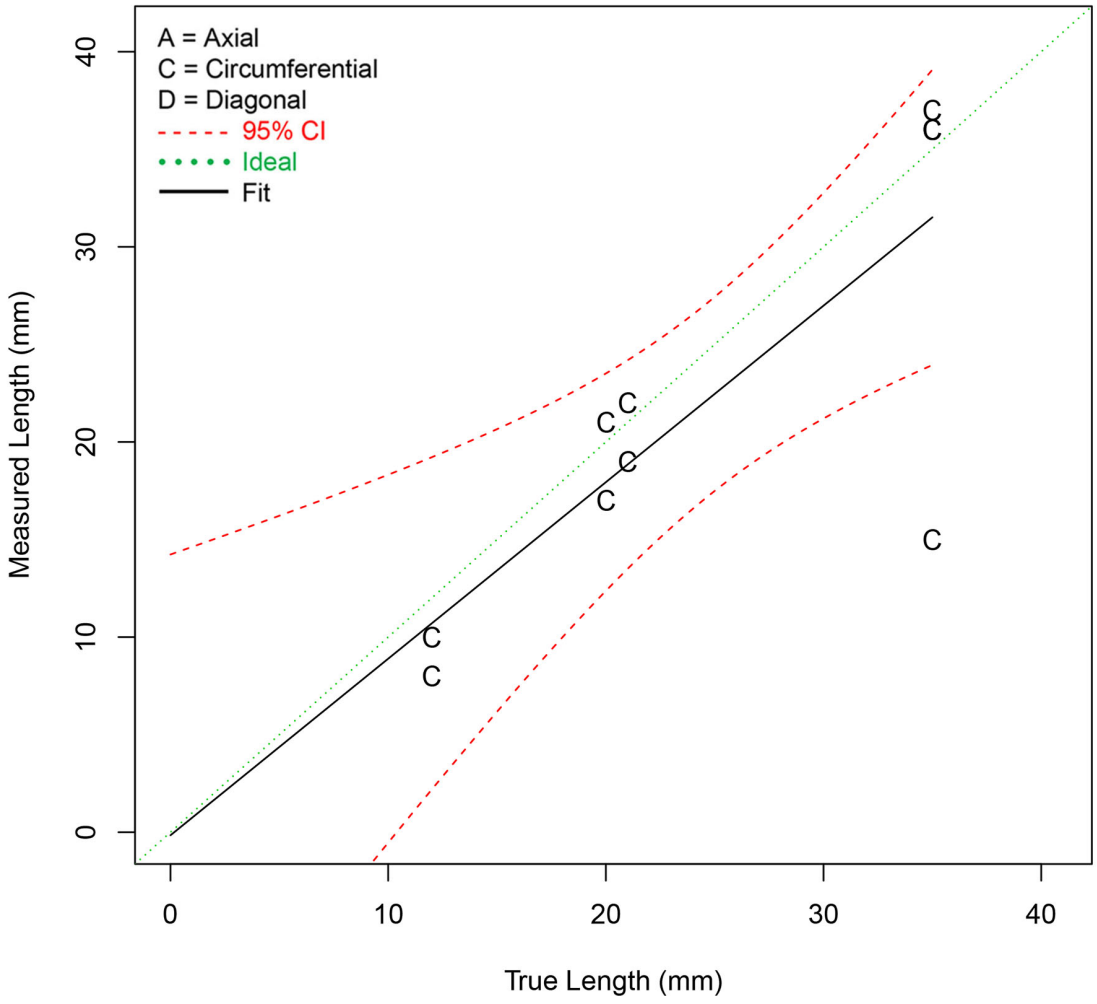

Figure 4.35. Aggregate Length Sizing Regression Fit for ECT Techniques 135-ECT1 and 101-ECT1 for Circumferential Flaws (tolerance = 10 mm and 15 mm)

5.0 Comparison of Quickblind and Blind Test Techniques

This section documents analysis of PARENT technique data that was performed with the objective of enhancing the amount of data available for comparisons of results between inspections performed on Quickblind test blocks and inspections performed on test blocks in the regular portion of blind testing. Both PAUT and conventional UT data were analyzed at the technique level to perform these comparisons. Documentation of the analysis of PAUT technique data is provided in Section 5.1 and documentation of conventional UT technique data is provided in Section 5.2.

5.1 PAUT Technique Analysis

PAUT technique analysis was performed in an attempt to enhance the amount of inspection data available for comparisons of results between inspections performed on Quickblind test blocks and inspections performed on test blocks in Blind testing. This section includes a summary of the procedures in PARENT blind testing that incorporated PAUT techniques for inspections of LBDMW test blocks by O.D. access and provides a review of the performance of these procedures. This is followed by a summary of the inspections that are included in the PAUT technique analysis, the results of detection performance analysis of PAUT techniques, and the results of depth sizing and length sizing performance analysis of PAUT techniques.

5.1.1 Summary of PAUT Techniques to be Analyzed

Table 5.1 summarizes four procedures in PARENT blind testing incorporated PAUT techniques. The four procedure IDs are PAUT.126.1, PAUT.108.1, UT.PAUT.108, and UT.PAUT.126. Procedures UT.PAUT.108 and UT.PAUT.126 where incorporated in the Quickblind test and procedures PAUT.126.1 and PAUT.108.1 where incorporated in the Blind test. The procedure IDs indicate that these procedures include some combination of PAUT techniques with conventional UT techniques. General descriptions of these techniques are provided in Sections 3.2 and 3.3 of the PARENT Blind test report (Meyer and Heasler 2017). Summaries of individual procedures are provided in Appendix B of Meyer and Heasler (2017) with information obtained from procedure datasheets that were filled out by participating teams and which are included in Appendix C of Meyer and Heasler (2017).

5.1.1.1 Summary of PAUT.126.1

Procedure PAUT.126.1 consisted only of technique 126-PA1. Technique 126-PA1 was utilized for detection, characterization, length sizing, depth sizing, and positioning. The technique was manually scanned and encoded and accessed the component O.D. For detection of circumferential and axial flaws, the technique was applied at 1.5 MHz in linear scans at angles specified in Table 5.1.

5.1.1.2 Summary of PAUT.108.1

Procedure PAUT.108.1 consisted only of technique 108-PA1. Technique 108-PA1 was utilized for detection, characterization, length sizing, depth sizing, and positioning. The technique was manually scanned and not encoded and accessed the component O.D. The technique was applied at 2.0 MHz in a sectorial scan from 0° to 85°.

Table 5.1. Summary of Procedures Incorporating PAUT Techniques

Procedure ID	Technique ID	Manual or Automated	Encoded (Y/N)	Exam Surface	Probe Frequency/Inspection Angle (Deg.)	Comments
PAUT.126.1	126-PA1	Manual	Y	O.D.	Circ. Scan 1.5 MHz/L22.5° 1.5 MHz/L25° 1.5 MHz/L35° 1.5 MHz/L37.5° 1.5 MHz/L45° 1.5 MHz/L55° Axial Scan 1.5 MHz/L45° 1.5 MHz/L60° 1.5 MHz/L70°	Detection, characterization, length, depth, positioning
PAUT.108.1	108-PA1	Manual	N	O.D.	2.0 MHz/L0°~L85°	Detection, characterization, length, depth, positioning
UT.PAUT.108	108-PA0	Manual	N	O.D.	2.0 MHz/L0°~L85°	Detection, characterization, length, depth, positioning
	108-UT0	Manual	N	O.D.	1.0 MHz/L45° 1.0 MHz/L60° 1.5 MHz/L35° 1.5 MHz/L45° 2.0 MHz/L33° 2.0 MHz/L45	Detection, characterization, length, depth, positioning
UT.PAUT.126	126-PA0	Manual	Y	O.D.	Circ. Scan 1.5 MHz/L25° 1.5 MHz/L35° 1.5 MHz/L45° 1.5 MHz/L55°	Detection, characterization, length, depth, positioning
	126-UT0	Manual	N	O.D.	2.0 MHz/L45° 2.0 MHz/L60°	Detection, characterization, length, depth, positioning

5.1.1.3 Summary of UT.PAUT.126

Procedure UT.PAUT.126 consisted of techniques 126-UT0 and 126-PA0. Both techniques were utilized for detection, characterization, length sizing, depth sizing, and positioning. In addition, both techniques were manually scanned and accessed the component O.D. Technique 126-PA0 was encoded and technique 126-UT0 was not encoded. Both techniques were applied as linear scans at angles specified in Table 5.1. Technique 126-PA0 was applied at a frequency of 1.5 MHz and technique 126-UT0 was applied at a frequency of 2.0 MHz.

5.1.1.4 Summary of UT.PAUT.108

Procedure UT.PAUT.108 consisted of techniques 108-UT0 and 108-PA0. Both techniques were utilized for detection, characterization, length sizing, depth sizing, and positioning. In addition, both techniques were manually scanned, accessed the component O.D, and were not encoded. Technique 108-PA0 was applied at 2.0 MHz in a sectorial scan from 0° to 85°. Technique 108-UT0 was applied as linear scans at frequencies from 1.0 MHz to 2.0 MHz at the angles specified in Table 5.1. Review of PAUT Performance in PARENT Blind Testing

5.1.2 Review of PAUT Performance in PARENT Blind Testing

This section provides a review of performance data for procedures that incorporated PAUT techniques in PARENT blind testing. This review is provided so that results of analysis of performance of PAUT techniques can be conveniently compared to the results obtained from these procedures. A summary of the overall detection and false call performance for procedures incorporating PAUT techniques on LBDMW test blocks with O.D. access in PARENT blind testing is provided in Table 5.2. The two procedures implemented in the Quickblind study (UT.PAUT.108 and UT.PAUT.126) detected all flaws, while the procedures implemented in Blind testing (PAUT.108.1 and PAUT.126.1) exhibited lower PODs.

POD as a function of flaw depth is summarized in Table 5.3. This table includes data for each of the procedures in Table 5.1, as well as aggregate POD data for procedures implemented in the Blind and Quickblind studies, respectively. Table 5.4 provides a summary of POD versus flaw length for each procedure in Table 5.1 and aggregate POD results for procedures implemented in the Blind and Quickblind studies, respectively. Finally, summaries of sizing analyses results are provided in Table 5.5 and Table 5.6 for depth sizing error and length sizing error, respectively.

Table 5.2. Summary of Overall Detection and False Call Performance for Procedures Incorporating PAUT Techniques on LBDMW Test Blocks with O.D. Access in PARENT Blind Testing

	NOBS	POD, %	FCP, %	FCR, #/m	Access	LBDMW
PAUT.108.1	47	64	1	0.6	O.D.	P13, P33
PAUT.126.1	47	51	3	1.2	O.D.	P13, P33
UT.PAUT.108 (Quickblind)	3	100	0	0.0	O.D.	P15, P16, P17, P45
UT.PAUT.126 (Quickblind)	3	100	7	2.9	O.D.	P15, P16, P17, P45

Table 5.3. Probability of Detection versus Depth for Procedures Incorporating PAUT Techniques on LBDMW Test Blocks with O.D. Access in PARENT Blind Testing

	NOBS	0 mm	5 mm	10 mm	15 mm	30 mm
PAUT.108.1	19	3	8	16	30	79
PAUT.126.1	19	7	14	24	40	81
UT.PAUT.108 (Quickblind)	3	2	8	25	55	97
UT.PAUT.126 (Quickblind)	3	9	20	39	61	94
PAUT.108.1 + PAUT.126.1	38	5	10	21	37	82
UT.PAUT.108 + UT.PAUT.126 (Quickblind)	6	5	19	49	80	99

Table 5.4. Probability of Detection versus Length for Procedures Incorporating PAUT Techniques on LBDMW Test Blocks with O.D. Access in PARENT Blind Testing

	NOBS	0 mm	5 mm	10 mm	15 mm	30 mm
PAUT.108.1	19	2	5	11	23	80
PAUT.126.1	19	6	11	19	30	72
UT.PAUT.108 (Quickblind)	3	1	4	12	31	94
UT.PAUT.126 (Quickblind)	3	8	16	30	48	91
PAUT.108.1 + PAUT.126.1	38	4	8	16	28	78
UT.PAUT.108 + UT.PAUT.126 (Quickblind)	6	4	12	29	55	97

Table 5.5. Depth Sizing Results Summary for Procedures Incorporating PAUT Techniques on LBDMW Test Blocks with O.D. Access in PARENT Blind Testing

	NOBS	Bias, mm	RMSE, mm
PAUT.108.1	7	−2.8	5.0
PAUT.126.1	8	2.6	12.5
UT.PAUT.108 (Quickblind)	3	−9.1	11.4
UT.PAUT.126 (Quickblind)	3	−3.5	6.2
PAUT.108.1 + PAUT.126.1	15	0.1	9.7
UT.PAUT.108 + UT.PAUT.126 (Quickblind)	6	−6.3	9.2

Table 5.6. Length Sizing Results Summary for Procedures Incorporating PAUT Techniques on LBDMW Test Blocks with O.D. Access in PARENT Blind Testing

	NOBS	Bias, mm	RMSE, mm
PAUT.108.1	7	-0.4	7.2
PAUT.126.1	7	6.6	10.3
UT.PAUT.108 (Quickblind)	3	−9.0	11.1
UT.PAUT.126 (Quickblind)	3	−0.7	6.4
PAUT.108.1 + PAUT.126.1	14	3.1	8.9
UT.PAUT.108 + UT.PAUT.126 (Quickblind)	6	−4.2	9.0

5.1.3 PAUT Inspections of Test Block P33

Figure 5.1 shows indication plots for procedure PAUT.108 and technique 108-PA1 examinations of test block P33. The only technique applied in procedure PAUT.108 was technique 108-PA1 so their results are represented by the same indication plots. Figure 5.1 shows that 8 of 18 flaws were missed by procedure PAUT.108 and technique 108-PA1 and that only 1 of 2 subsurface flaws were detected. Also, Figure 5.1 indicates some positioning error for axial flaws that resulted in indications 02 and 07 being recorded outside of the tolerance boundary for nearby flaws. These are marked with the label “Probable

Detection." As a consequence, detection and sizing analysis is performed with a tolerance of 10 mm and a tolerance of 15 mm, respectively.

Figure 5.2 shows indication plots for procedure PAUT.126 and technique 126-PA1 examinations of test block P33. The only technique applied in procedure PAUT.126 was technique 126-PA1 so their results are represented by the same indication plots. Figure 5.2 shows that 10 of 18 flaws were missed by procedure PAUT.126 and technique 126-PA1 and that both of the subsurface flaws were detected. Also, Figure 5.2 indicates that there were three false calls and large length sizing error associated with indication 10.

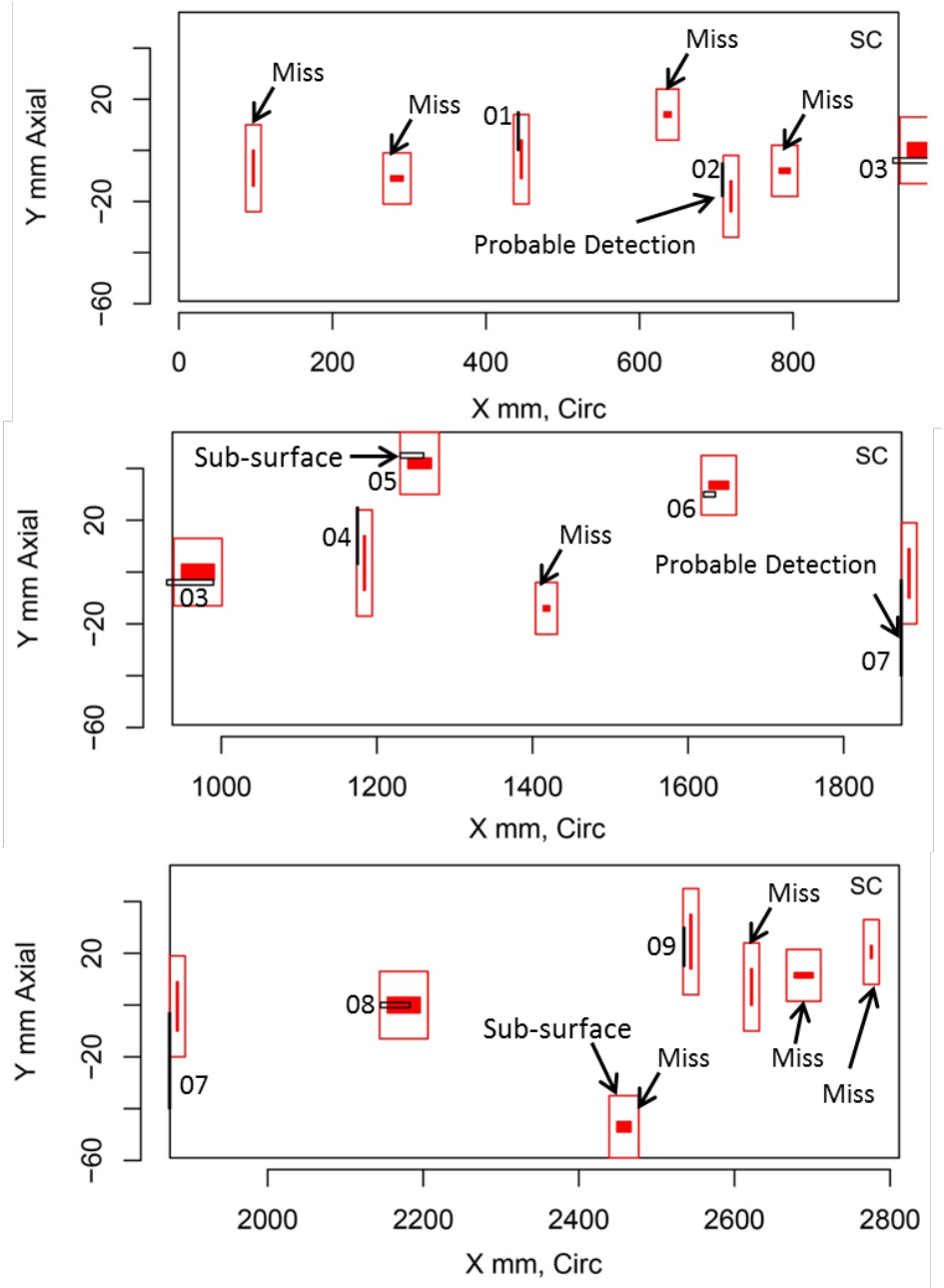

Figure 5.1. Indication Plot for Procedure PAUT.108 and Technique 108-PA1 Applied to Test Block P33 in PARENT Blind Testing (X–Y view)

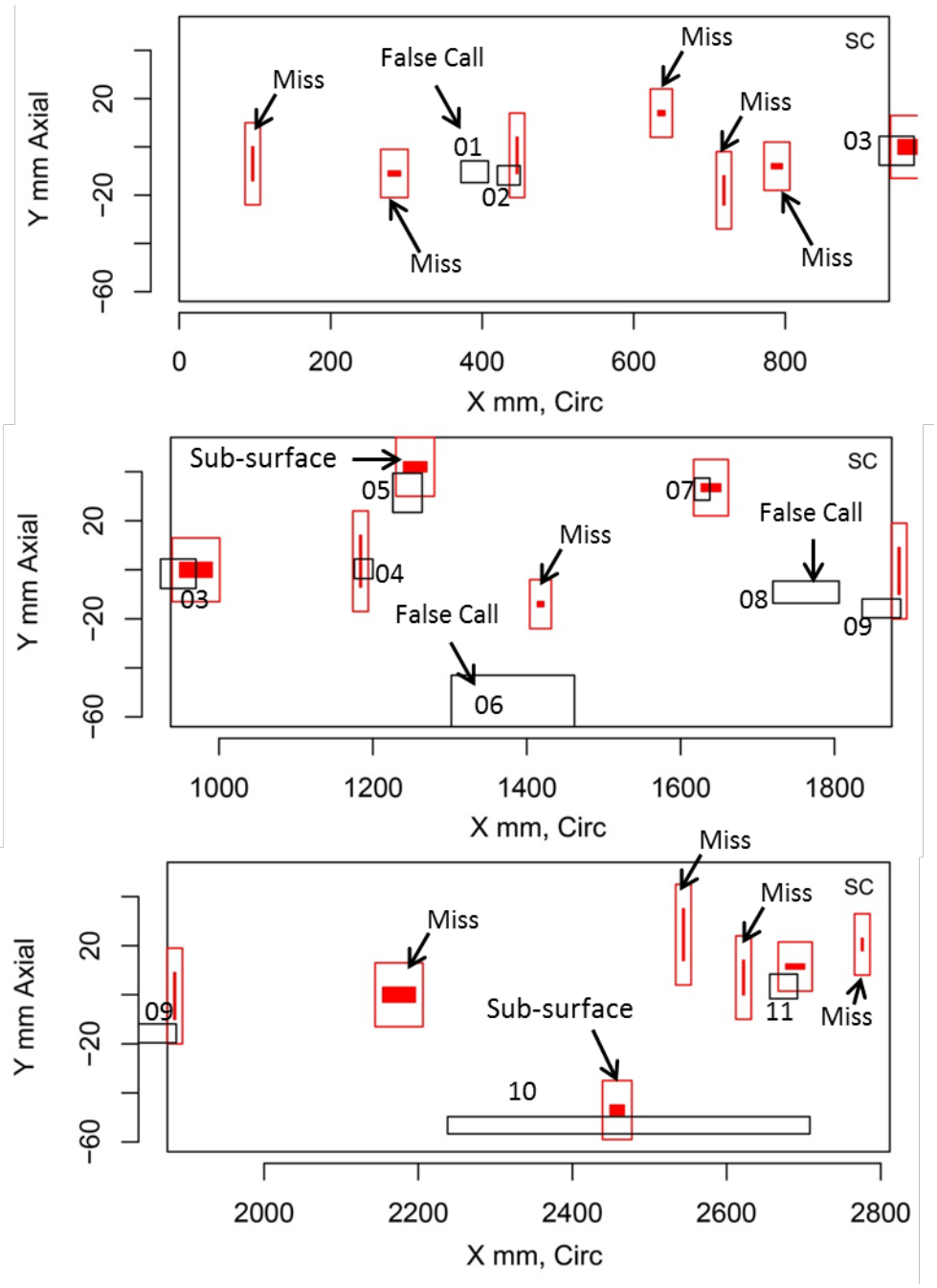

Figure 5.2. Indication Plot for Procedure PAUT.126 and Technique 126-PA1 Applied to Test Block P33 in PARENT Blind Testing (X–Y view)

5.1.4 PAUT Inspections of Test Block P13

Figure 5.3 and Figure 5.4 show indication plots for procedure PAUT.108 and technique 108-PA1 and for procedure PAUT.126 and technique 126-PA1, respectively, for examinations of test block P13, which contained one flaw. Figure 5.3 and Figure 5.4 show that the flaw was not detected by any of these procedures and techniques. Further, Figure 5.4 shows that procedure PAUT.126 and technique 126-PA1 reported three false calls in P13.

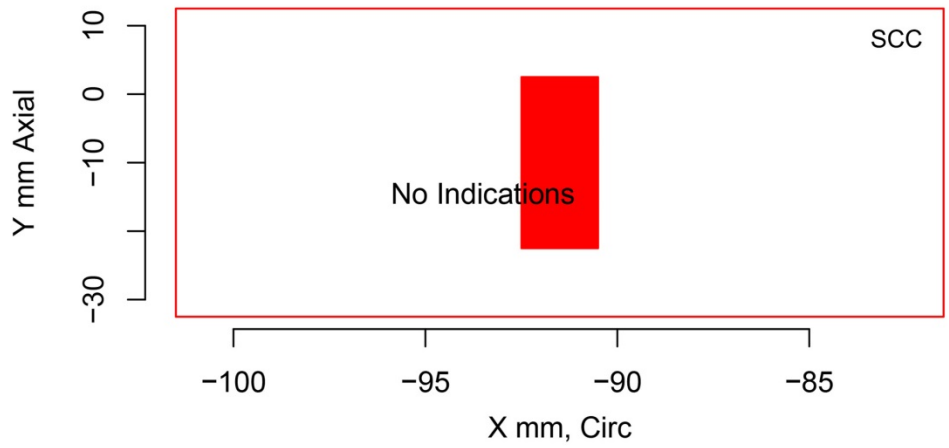

Figure 5.3. Indication Plot for Procedure PAUT.108 and Technique 108-PA1 Applied to Test Block P13 in PARENT Blind Testing (X–Y view)

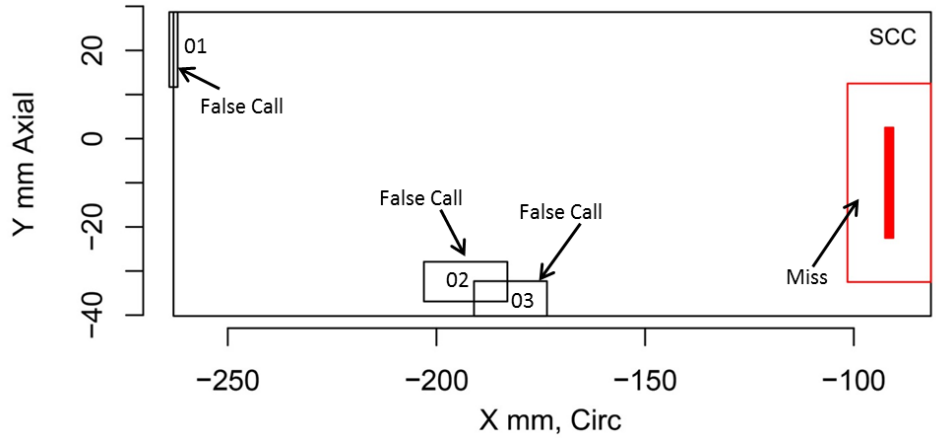

Figure 5.4. Indication Plot for Procedure PAUT.126 and Technique 126-PA1 Applied to Test Block P13 in PARENT Blind Testing (X–Y view)

5.1.5 PAUT Inspections of Test Block P15 (Quickblind)

Figure 5.5 and Figure 5.6 show indication plots for procedure UT.PAUT.108 and technique 108-PA0 and for procedure UT.PAUT.126 and technique 126-PA0, respectively, for examinations of Quickblind test block P15, which contained one flaw. Procedure UT.PAUT.108 and technique 108-PA0 produced identical indication plots, as did procedure UT.PAUT.126 and technique 126-PA0. Figure 5.5 and Figure 5.6 show that the flaw was detected by all of these procedures and techniques. Figure 5.6 shows that procedure UT.PAUT.126 and technique 126-PA0 also reported a false call in P15 (indication 02).

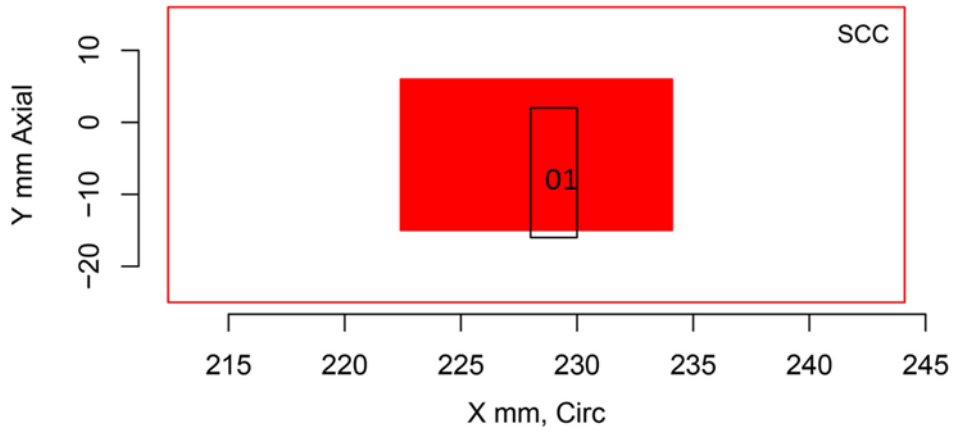

Figure 5.5. Indication Plot for Procedure UT.PAUT.108 and Technique 108-PA0 Applied to Quickblind Test Block P15 in PARENT Blind Testing (X–Y view)

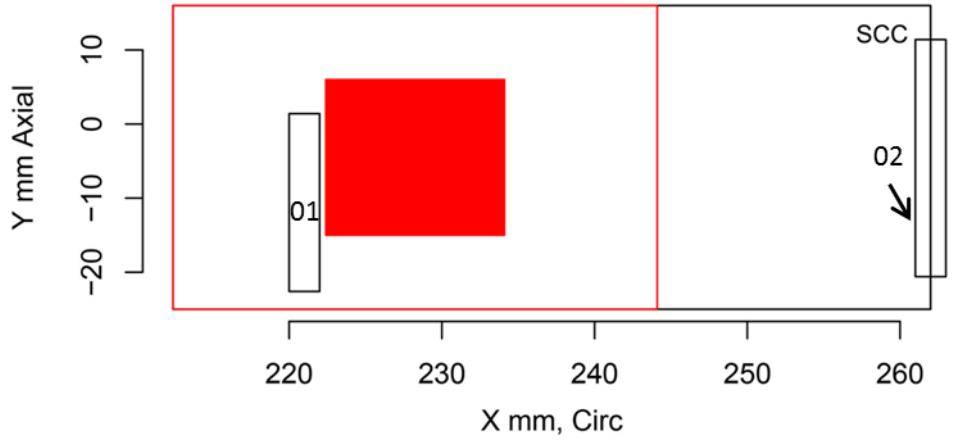

Figure 5.6. Indication Plot for Procedure UT.PAUT.126 and Technique 126-PA0 Applied to Quickblind Test Block P15 in PARENT Blind Testing (X–Y view)

5.1.6 PAUT Inspections of Test Block P16 (Quickblind)

Figure 5.7 and Figure 5.8 show indication plots for procedure UT.PAUT.108 and for technique 108-PA0, respectively, for examinations of Quickblind test block P16, which contained one flaw. Figure 5.7 and Figure 5.8 show that the flaw was detected by both procedure UT.PAUT.108 and technique 108-PA0. The indication reported by technique 108-PA0 in Figure 5.8 is shorter in the axial direction and shifted slightly in the negative axial direction in comparison to the indication reported by procedure UT.PAUT.108 in Figure 5.7.

Figure 5.9 shows the indication plot for both procedure UT.PAUT.126 and technique 126-PA0 for examinations of Quickblind test block P16. Procedure UT.PAUT.126 and technique 126-PA0 resulted in identical indication plots, which are both represented by Figure 5.9. Figure 5.9 shows that both procedure UT.PAUT.126 and technique 126-PA0 detected the flaw (indication 02) and that both reported a false call (indication 01).

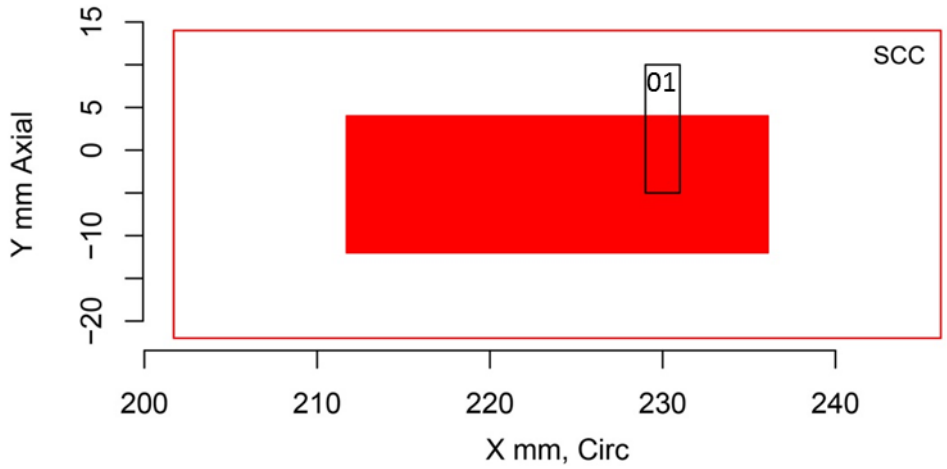

Figure 5.7. Indication Plot for Procedure UT.PAUT.108 Applied to Quickblind Test Block P16 in PARENT Blind Testing (X–Y view)

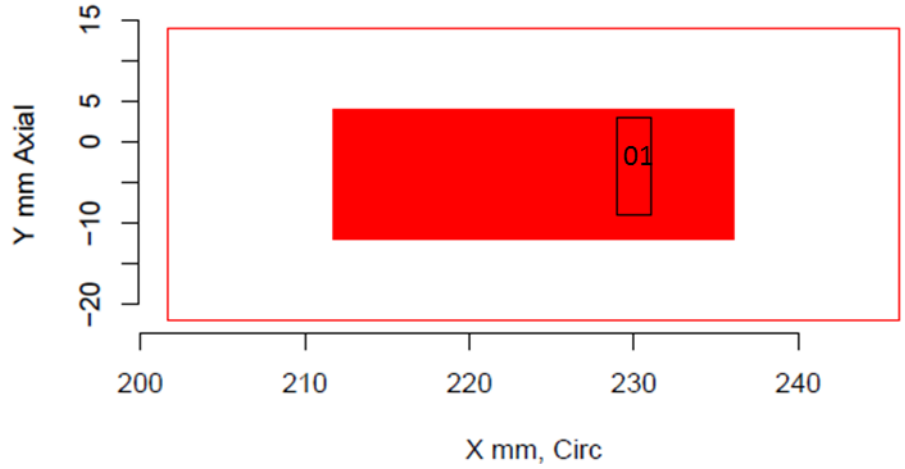

Figure 5.8. Indication Plot for Technique 108-PA0 Applied to Quickblind Test Block P16 in PARENT Blind Testing (X–Y view)

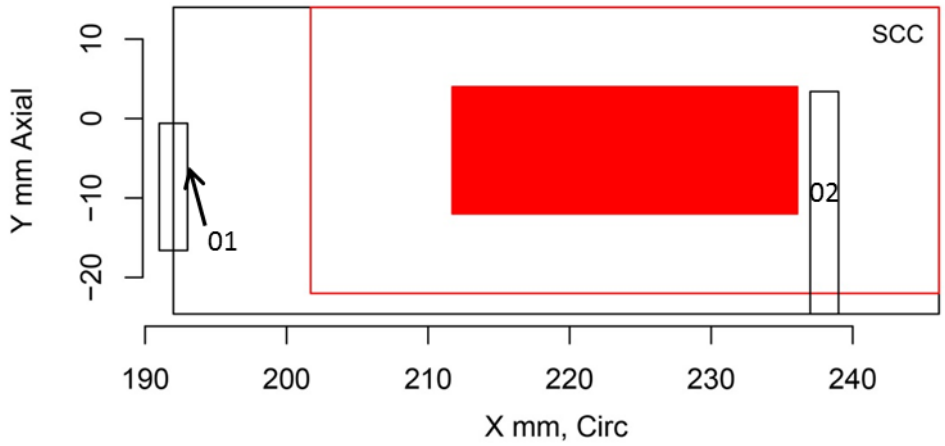

Figure 5.9. Indication Plot for Procedure UT.PAUT.126 and Technique 126-PA0 Applied to Quickblind Test Block P16 in PARENT Blind Testing (X–Y view)

5.1.7 PAUT Inspections of Test Block P17 (Quickblind)

Figure 5.10 and Figure 5.11 show indication plots for procedure UT.PAUT.108 and for technique 108-PA0, respectively, for examinations of Quickblind test block P17, which contained one flaw. Figure 5.10 and Figure 5.11 show that the flaw was detected by procedure UT.PAUT.108 but was not detected by technique 108-PA0.

Figure 5.12 shows the indication plot for both procedure UT.PAUT.126 and technique 126-PA0 for examinations of Quickblind test block P17. Procedure UT.PAUT.126 and technique 126-PA0 resulted in identical indication plots, which are both represented by Figure 5.12. Figure 5.12 shows that both procedure UT.PAUT.126 and technique 126-PA0 detected the flaw (indication 02) and that both reported a false call (indication 01).

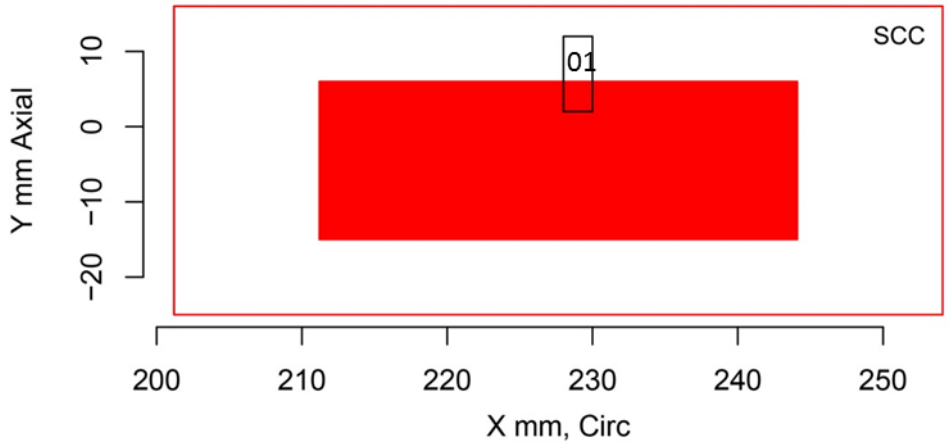

Figure 5.10. Indication Plot for Procedure UT.PAUT.108 Applied to Quickblind Test Block P17 in PARENT Blind Testing (X–Y view)

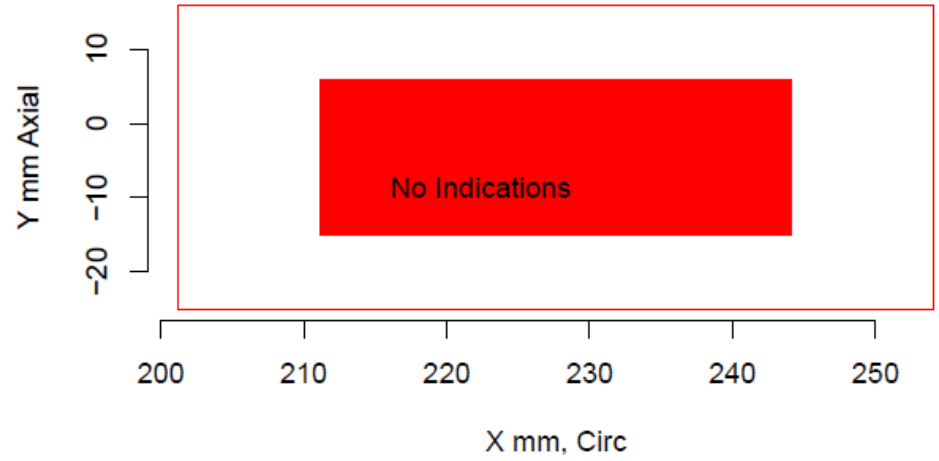

Figure 5.11. Indication Plot for Technique 108-PA0 Applied to Quickblind Test Block P17 in PARENT Blind Testing (X–Y view)

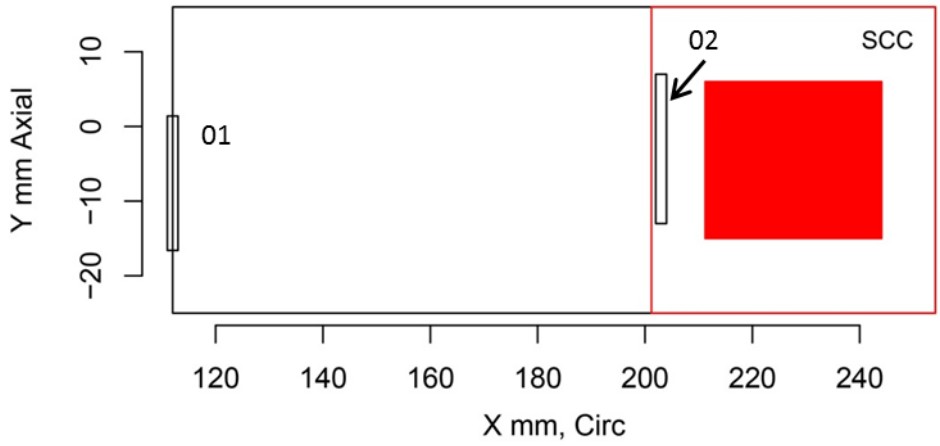

Figure 5.12. Indication Plot for Procedure UT.PAUT.126 Applied to Quickblind Test Block P17 in PARENT Blind Testing (X–Y view)

5.1.8 PAUT Inspections of Test Block P45 (Quickblind)

Figure 5.13 and Figure 5.14 show indication plots for procedure UT.PAUT.108 and technique 108-PA0 and for procedure UT.PAUT.126 and technique 126-PA0, respectively, for examinations of test block P45, which contained no flaws. Procedure UT.PAUT.108 and technique 108-PA0 resulted in identical indication plots, which are both represented by Figure 5.13. Procedure UT.PAUT.126 and technique 126-PA0 also resulted in identical indication plots, which are both represented by Figure 5.14. Figure 5.13 shows that procedure UT.PAUT.108 and technique 108-PA0 properly reported no indications in P45, while Figure 5.14 shows that two false calls were reported in P45 by procedure UT.PAUT.126 and technique 126-PA0.

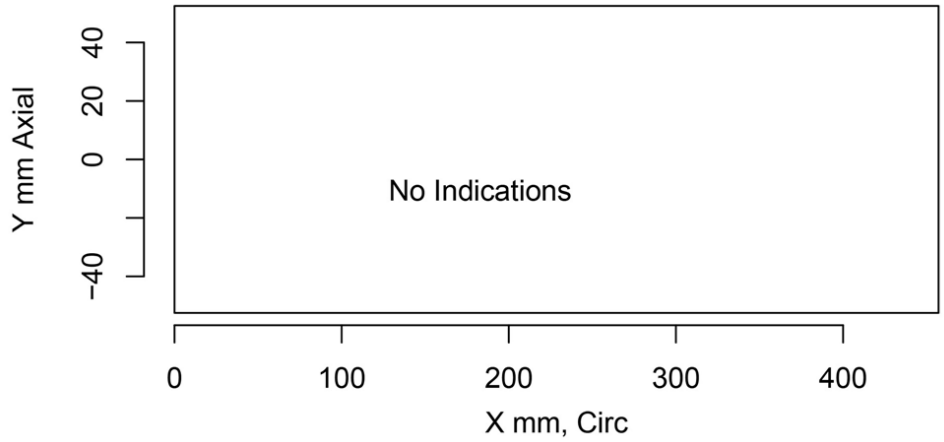

Figure 5.13. Indication Plot for Procedure UT.PAUT.108 and Technique 108-PA0 Applied to Quickblind Test Block P45 in PARENT Blind Testing (X–Y view)

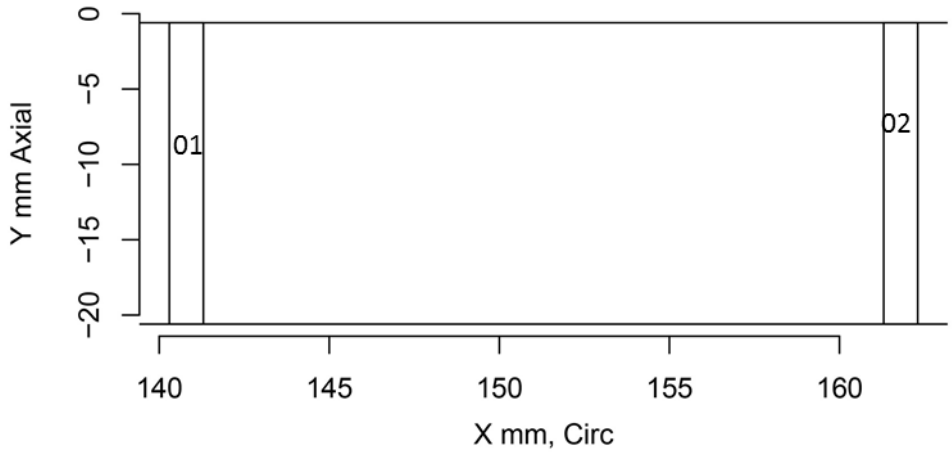

Figure 5.14. Indication Plot for Procedure UT.PAUT.126 and Technique 126-PA0 Applied to Quickblind Test Block P45 in PARENT Blind Testing (X–Y view)

5.1.9 Detection Performance Analysis

This section presents the results of the detection performance analysis of PAUT techniques applied to the O.D. surface of LBDMW test blocks in PARENT. Results are presented as tables of POD at several discrete flaw sizes (depth and length) and as plots of POD curves as a function of flaw size. The tables also include tabulation of the FCR. The following section includes a tabulated summary of overall detection performance for PAUT techniques for scoring tolerances of 10 mm and 15 mm to account for the positioning error observed for axial flaws in test block P33. This summary is followed by sections presenting the detection performance results obtained from the total flaw population, the axial flaw population, and the circumferential flaw population as a function of depth and length. In these sections, results are also presented for scoring tolerances of 10 mm and 15 mm.

5.1.9.1 Overall Detection Analysis Results

This section provides tabulated summaries of the overall detection performance of PAUT techniques in PARENT for scoring tolerances of 10 mm (Table 5.7) and 15 mm (Table 5.8). In these tables, NOBS refers to the total number of flaws in the inspected test blocks. POD is these tables is not expressed as a function of any parameter, but is simply the overall POD obtained by dividing the detected flaws by NOBS. The FCR is the number of observed false calls per unit length. The FCP is calculated from Eq. (3.6) (Section 3.3).

The impact of increasing the tolerance from 10 mm and 15 mm on the detection performance of technique 108-PA1 is evident in Table 5.7 and Table 5.8. These tables reveal that the overall POD increases from 37% to 47%, and the FCR and FCP experience reductions as the tolerance is increased from 10 mm to 15 mm.

Table 5.7. Overall Detection Performance by PAUT Techniques Applied to the O.D. Surface of LBDMW Blocks with a Tolerance = 10 mm

	NOBS	POD, %	FCP, %	FCR, #/m
108-PA0	3	67	0	0.0
108-PA1	19	37	2	0.8
126-PA0	3	67	7	2.9
126-PA1	19	42	5	1.9
All	44	43	3	1.4

Table 5.8. Overall Detection Performance by PAUT Techniques Applied to the O.D. Surface of LBDMW Blocks with a Tolerance = 15 mm

	NOBS	POD, %	FCP, %	FCR, #/m
108-PA0	3	67	0	0.0
108-PA1	19	47	0	0.0
126-PA0	3	67	7	2.9
126-PA1	19	42	5	2.0
All	44	48	3	1.2

5.1.9.2 Summary of Detection Analysis Results for All Flaws

This section presents the detection performance results obtained from the total flaw population as POD versus depth and length. A logistic regression model was used to relate POD to flaw size, S. Flaw size represents either depth or length. The logistic regression model is defined by Eqs. (3.3) and (3.4) (Section 3.2). Estimates produced by the algorithm are maximum-likelihood estimates. Detection performance is presented in a tabular format with POD values provided at discrete flaw sizes (i.e., at 0 mm, 5 mm, 10 mm, 15 mm, etc.). The values of POD at these discrete flaw sizes are the values estimated by the logistic regression model expressed by Eqs. (3.3) and (3.4). In tabulated summaries, NOBS refers to the total number of flaws in the test blocks inspected by a given technique. The value of POD at 0 mm [POD(0)] is the value of the regression fit at S = 0 mm. The value of the regression fit at 0 mm is influenced by the measured FCP, which is calculated from the measured FCR by Eq. (3.6).

Summary of Detection Performance as a Function of Flaw Depth

This section summarizes detection performance results obtained from the total flaw population as POD versus depth. Table 5.9 and Table 5.10 provide the POD values at discrete flaw sizes (i.e., at 0 mm, 5 mm, 10 mm, 15 mm, 30 mm, and 60 mm) for scoring tolerances of 10 mm and 15 mm, respectively. A column for NOBS and FCR is also included in the tables. Comparison of Table 5.9 and Table 5.10 illustrates how aggregate detection performance (i.e., for 108-PA1 + 126-PA1 [Blind], and for 108-PA0 + 126-PA0 + 108-PA1 + 126-PA1 [Blind + Quickblind]) and detection performance for technique 108-PA1 is impacted by the increase in tolerance from 10 mm to 15 mm. As the tables show, the increase in scoring tolerance results in a decrease in the FCR, which is anticipated considering the positioning error that results in misses of axial flaws for a scoring tolerance of 10 mm. Further, an increase in the POD is observed, especially at 15 mm and 30 mm.

Table 5.9. Summary of POD (%) versus Flaw Depth for All Flaw Orientations (tolerance = 10 mm)

	NOBS	FCR	0 mm	5 mm	10 mm	15 mm	30 mm	60 mm
108-PA0	3	0.00	1	5	17	45	98	100
108-PA1	19	0.76	3	8	16	30	84	100
126-PA0	3	2.90	8	18	34	55	94	100
126-PA1	19	1.88	6	12	23	39	86	100
108-PA0 + 126-PA0 (Quickblind)	6	1.45	4	14	39	71	99	100
108-PA1 + 126-PA1 (Blind)	38	1.32	5	10	20	36	87	100
108-PA0 + 126-PA0 + 108-PA1 + 126-PA1 (Blind + Quickblind)	44	1.37	4	10	23	43	93	100

Table 5.10. Summary of POD (%) versus Flaw Depth for All Flaw Orientations (tolerance = 15 mm)

	NOBS	FCR	0 mm	5 mm	10 mm	15 mm	30 mm	60 mm
108-PA0	3	0.00	1	5	17	46	98	100
108-PA1	19	0.00	2	7	19	43	96	100
126-PA0	3	2.92	8	18	34	55	94	100
126-PA1	19	1.95	6	13	23	39	86	100
108-PA0 + 126-PA0 (Quickblind)	6	1.46	4	14	39	71	99	100
108-PA1 + 126-PA1 (Blind)	38	0.98	4	10	22	43	93	100
108-PA0 + 126-PA0 + 108-PA1 + 126-PA1 (Blind + Quickblind)	44	1.17	4	11	26	51	96	100

Plots of aggregate POD curves versus flaw depth for scoring tolerances of 10 mm and 15 mm are provided in Figure 5.15 and Figure 5.16 (i.e., for 108-PA0 + 126-PA0 + 108-PA1 + 126-PA1 [Blind + Quickblind]), respectively, and in Figure 5.17 and Figure 5.18 (i.e., for 108-PA1 + 126-PA1 [Blind]), respectively. Finally, the plot in Figure 5.19 is of the aggregate POD for 108-PA 0 + 126-PA0 (Quickblind) data. The POD for Quickblind data is the same for 10 mm and 15 mm tolerance values. The solid black line represents the regression fit to the data and the red dashed lines represent 95% confidence bounds for the regression fit.

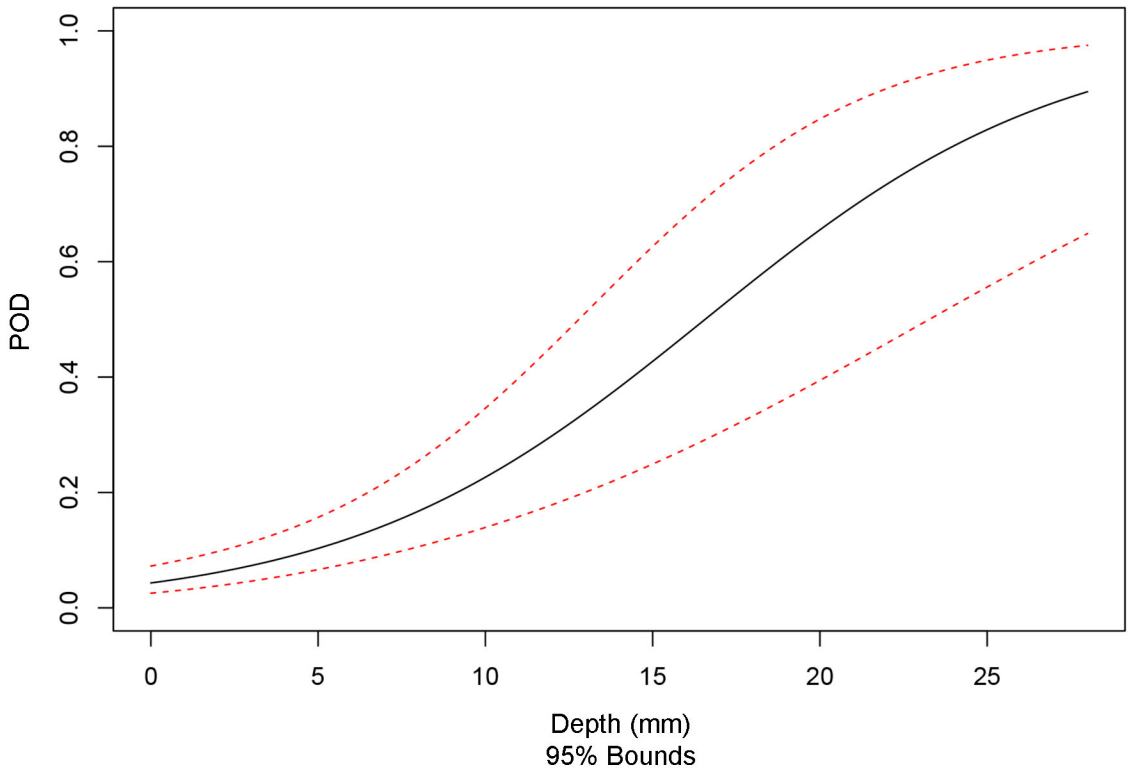

Figure 5.15. Aggregate Probability of Detection Curve versus Depth for PAUT Techniques 108-PA0, 126-PA0, 108-PA1, 126-PA1 (Blind + Quickblind) and for All Flaw Orientations (tolerance = 10 mm)

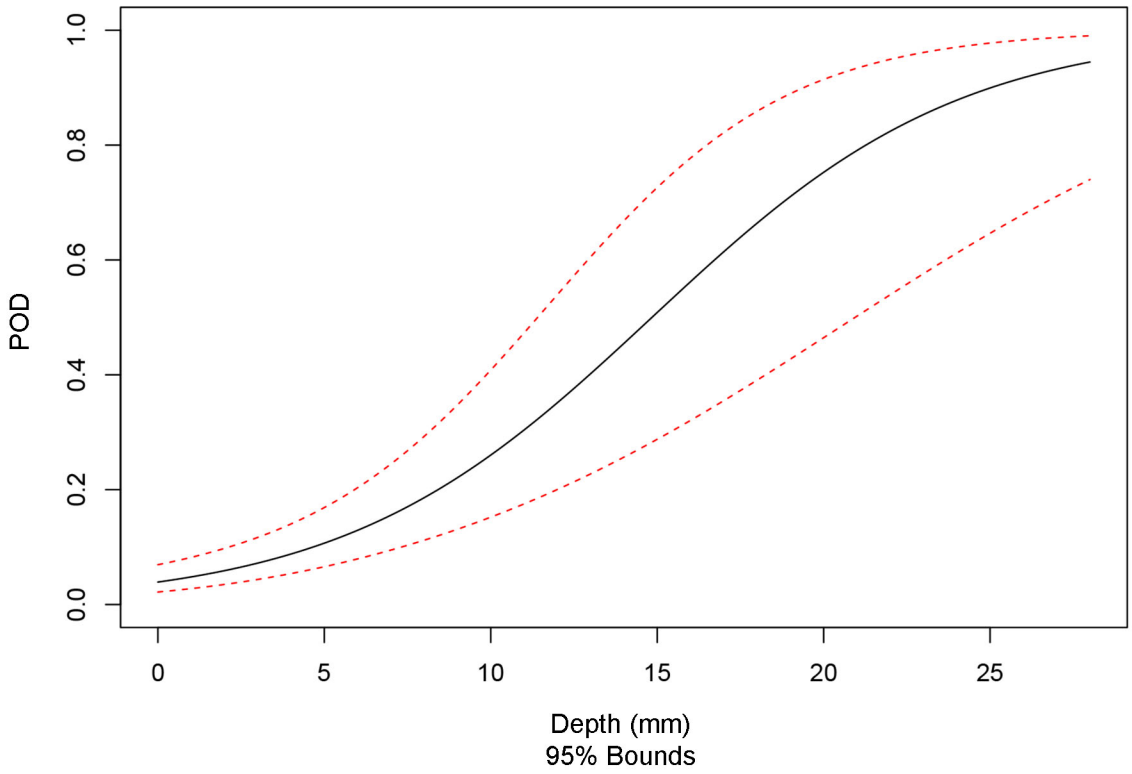

Figure 5.16. Aggregate Probability of Detection Curve versus Depth for PAUT Techniques 108-PA0, 126-PA0, 108-PA1, and 126-PA1 (Blind + Quickblind), and for All Flaw Orientations (tolerance = 15 mm)

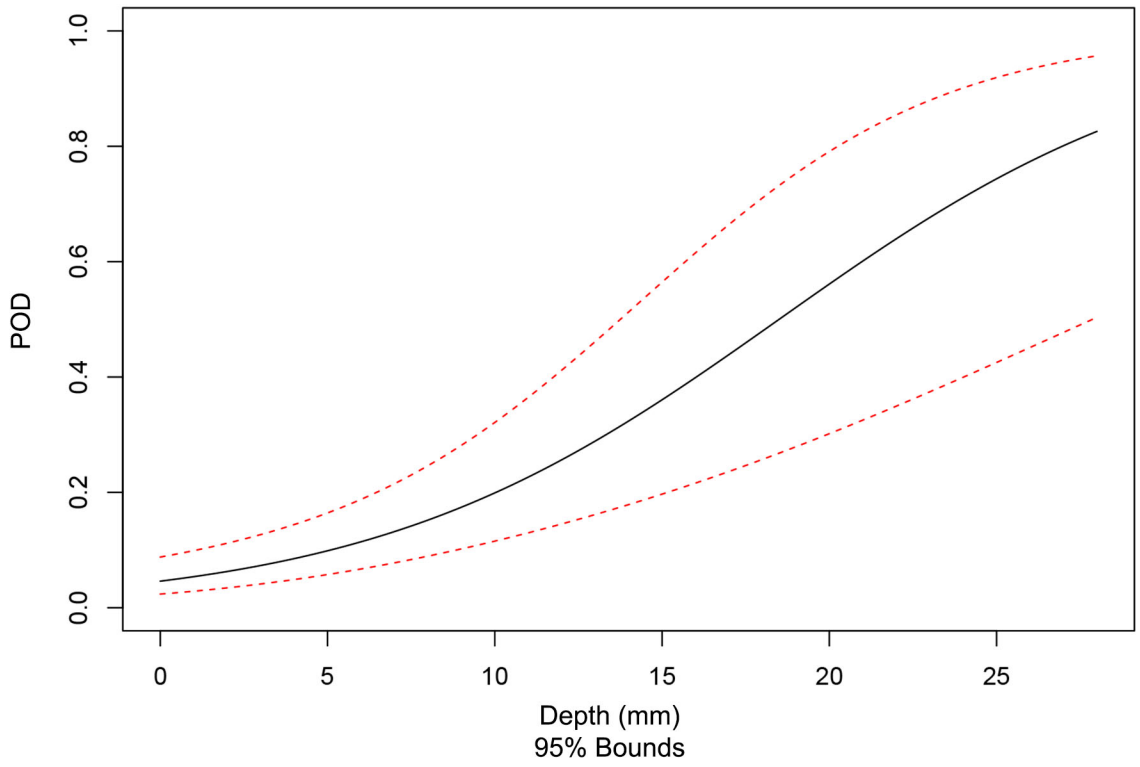

Figure 5.17. Aggregate Probability of Detection Curve versus Depth for PAUT Techniques 108-PA1 and 126-PA1 (Blind), and for All Flaw Orientations (tolerance = 10 mm)

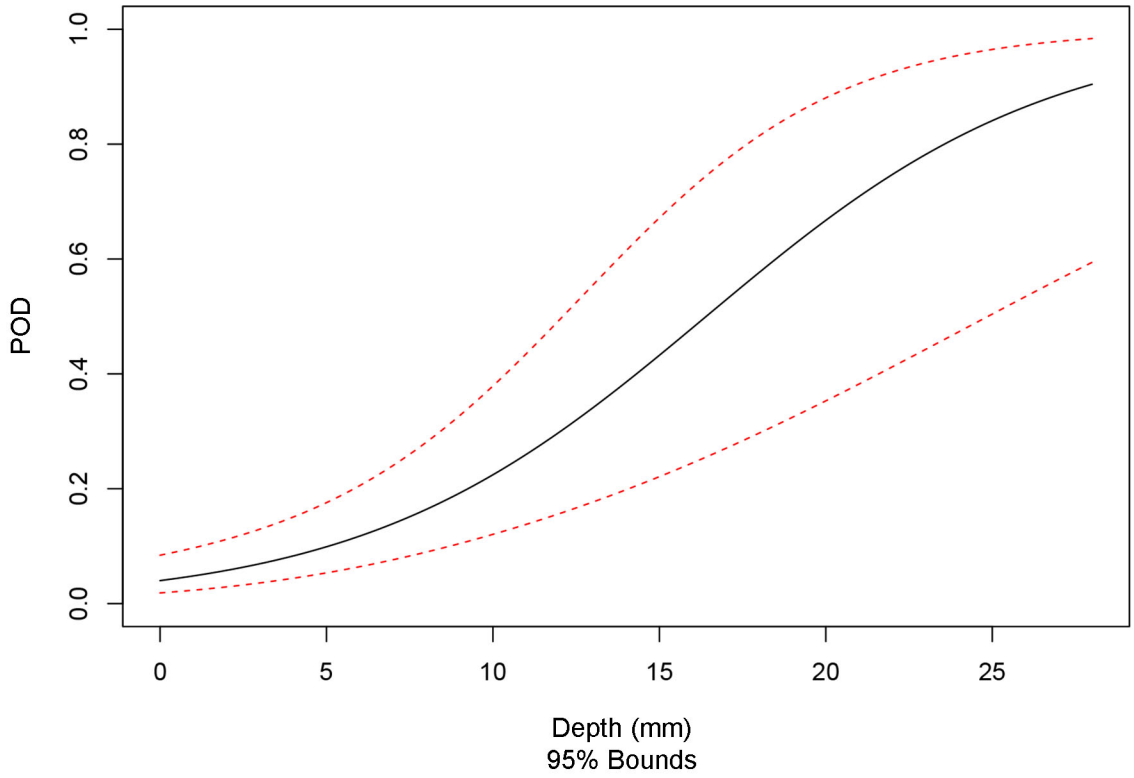

Figure 5.18. Aggregate Probability of Detection Curve versus Depth for PAUT Techniques 108-PA1 and 126-PA1 (Blind), and for All Flaw Orientations (tolerance = 15 mm)

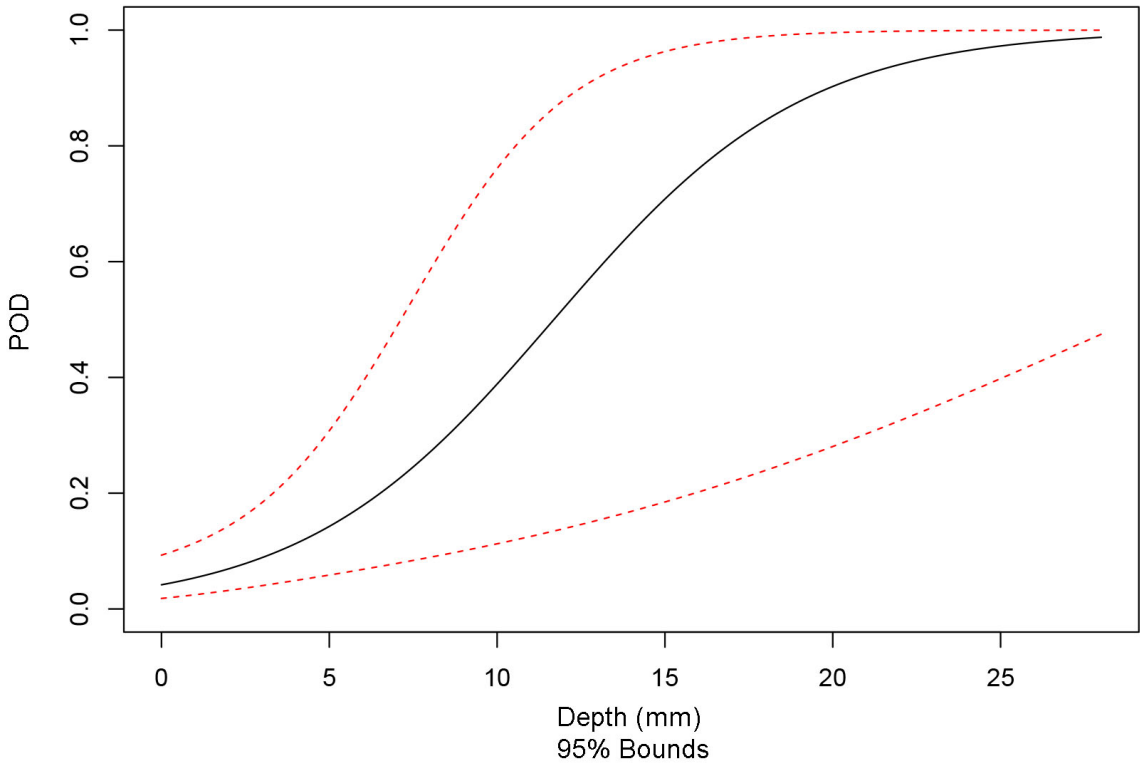

Figure 5.19. Aggregate Probability of Detection Curve versus Depth for PAUT Techniques 108-PA0 and 126-PA0 (Quickblind), and for All Flaw Orientations (tolerance = 10 mm and 15 mm)

Summary of Detection Performance as a Function of Flaw Length

This section summarizes detection performance results obtained from the total flaw population as POD versus length. Table 5.11 and Table 5.12 provide the POD values at discrete flaw sizes (i.e., at 0 mm, 5 mm, 10 mm, 15 mm, 30 mm, and 60 mm) for scoring tolerances of 10 mm and 15 mm, respectively. A column for NOBS and FCR is also included in the tables. Comparison of Table 5.11 and Table 5.12 illustrates how aggregate detection performance (i.e., for 108-PA1 + 126-PA1 [Blind] and for 108-PA0 + 126-PA0 + 108-PA1 + 126-PA1 [Blind + Quickblind]) and detection performance for technique 108-PA1 is impacted by the increase in tolerance from 10 mm to 15 mm. As the tables show, the increase in scoring tolerance results in a decrease in the FCR. Further, an increase in the POD is observed, especially at 15 mm and 30 mm.

Plots of aggregate POD curves versus flaw length for scoring tolerances of 10 mm and 15 mm are provided in Figure 5.20 and Figure 5.21 (i.e., for 108-PA0 + 126-PA0 + 108-PA1 + 126-PA1 [Blind + Quickblind]), respectively, and in Figure 5.22 and Figure 5.23 (i.e., for 108-PA1 + 126-PA1 [Blind]), respectively. Finally, the plot in Figure 5.24 is of the aggregate POD for 108-PA 0 and 126-PA0 (Quickblind) data. The POD for Quickblind data is the same for 10 mm and 15 mm tolerance values. The solid black line represents the regression fit to the data and the red dashed lines represent 95% confidence bounds for the regression fit in these plots.

Table 5.11. Summary of POD (%) versus Flaw Length for All Flaw Orientations (tolerance = 10 mm)

	NOBS	FCR	0 mm	5 mm	10 mm	15 mm	30 mm	60 mm
108-PA0	3	0.00	1	3	7	14	68	100
108-PA1	19	0.76	2	5	11	23	80	100
126-PA0	3	2.90	8	13	19	28	63	97
126-PA1	19	1.88	6	10	17	29	73	99
108-PA0 + 126-PA0 (Quickblind)	6	1.45	4	8	15	25	71	99
108-PA1 + 126-PA1 (Blind)	38	1.32	4	7	15	27	79	100
108-PA0 + 126-PA0 + 108-PA1 + 126-PA1 (Blind + Quickblind)	44	1.37	4	8	15	28	79	100

Table 5.12. Summary of POD versus Flaw Length for All Flaw Orientations (tolerance = 15 mm)

	NOBS	FCR	0 mm	5 mm	10 mm	15 mm	30 mm	60 mm
108-PA0	3	0.00	1	3	7	15	68	100
108-PA1	19	0.00	1	3	10	27	93	100
126-PA0	3	2.92	8	13	20	28	63	97
126-PA1	19	1.95	6	10	18	29	73	99
108-PA0 + 126-PA0 (Quickblind)	6	1.46	4	8	15	25	71	99
108-PA1 + 126-PA1 (Blind)	38	0.98	3	7	15	30	85	100
108-PA0 + 126-PA0 + 108-PA1 + 126-PA1 (Blind + Quickblind)	44	1.17	3	8	16	30	84	100

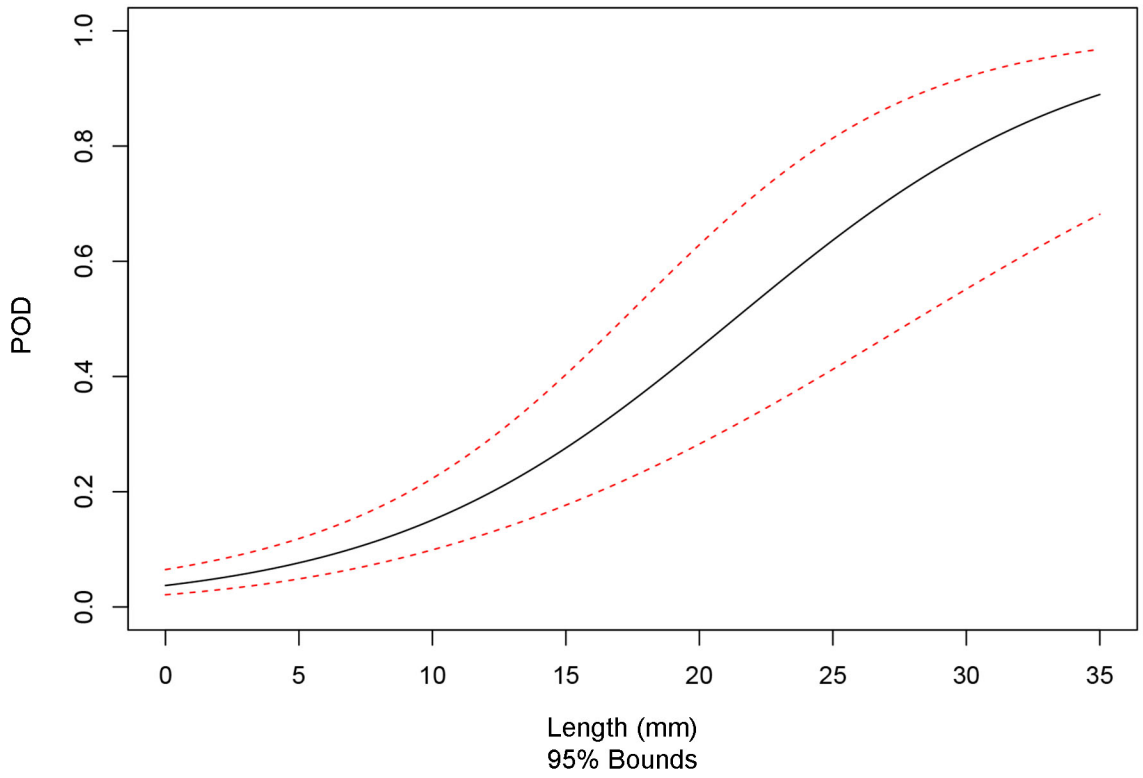

Figure 5.20. Aggregate Probability of Detection Curve versus Length for PAUT Techniques 108-PA0, 126-PA0, 108-PA1, and 126-PA1 (Blind + Quickblind), and for All Flaw Orientations (tolerance = 10 mm)

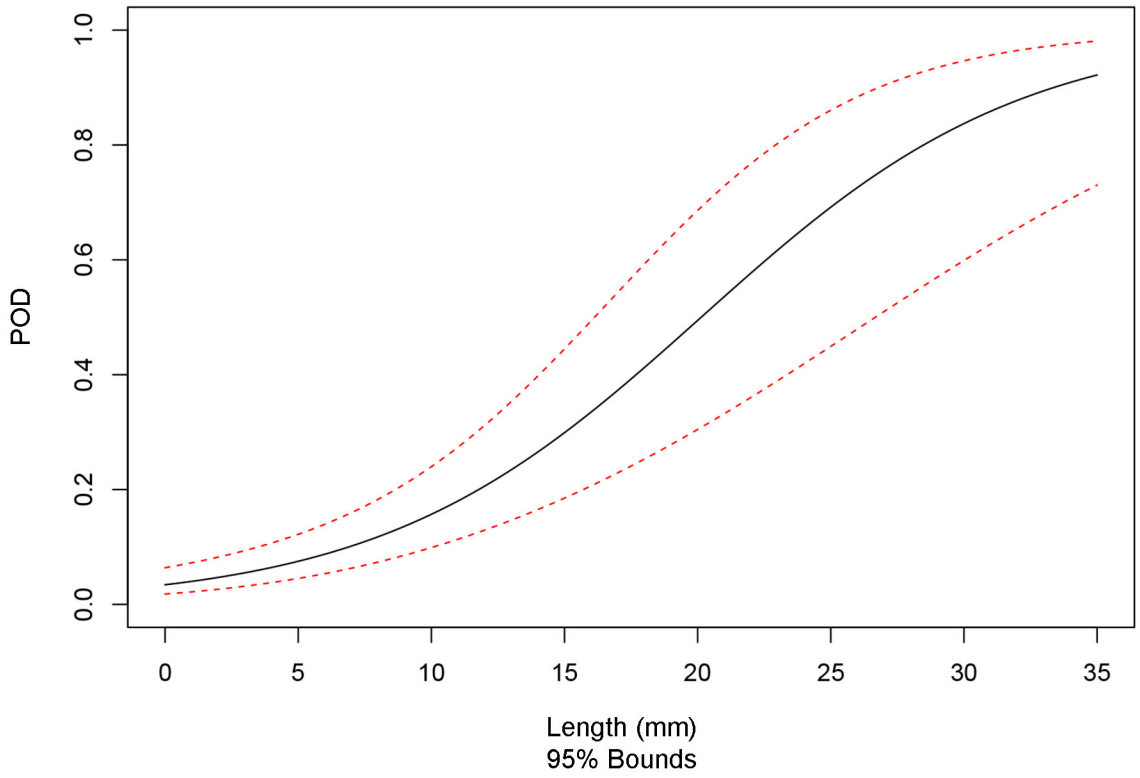

Figure 5.21. Aggregate Probability of Detection Curve versus Length for PAUT Techniques 108-PA0, 126-PA0, 108-PA1, and 126-PA1 (Blind + Quickblind), and for All Flaw Orientations (tolerance = 15 mm)

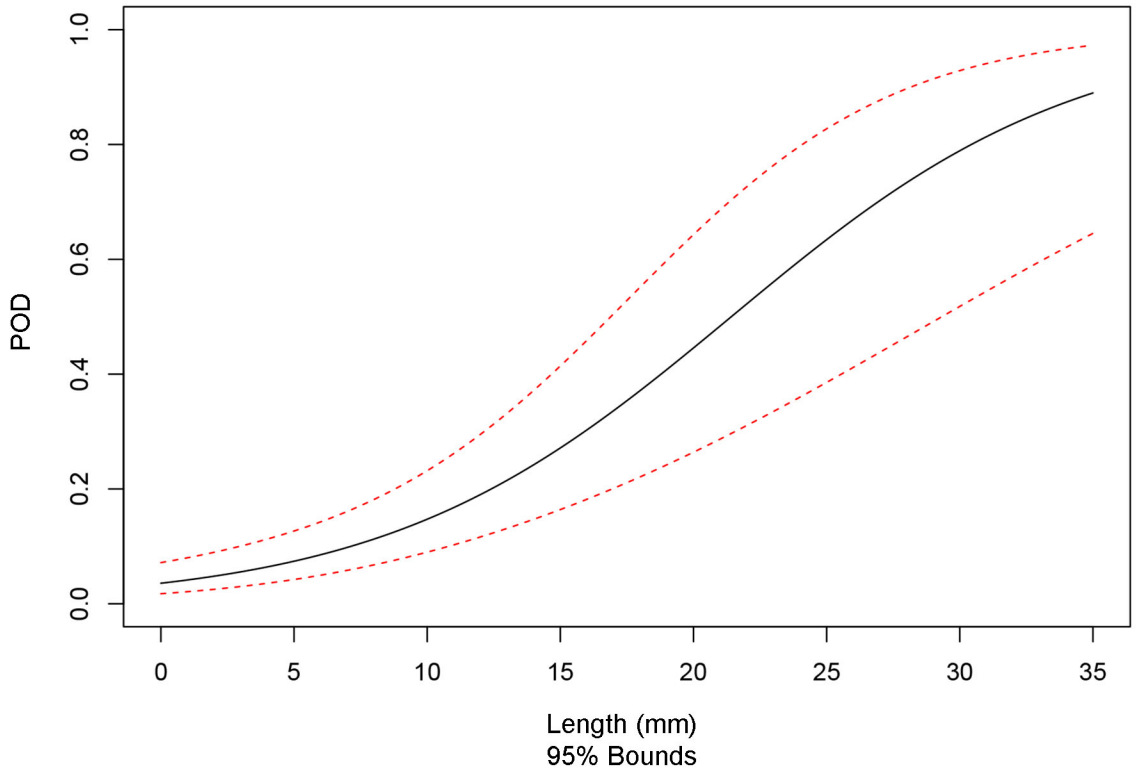

Figure 5.22. Aggregate Probability of Detection Curve versus Length for PAUT Techniques 108-PA1 and 126-PA1 (Blind), and for All Flaw Orientations (tolerance = 10 mm)

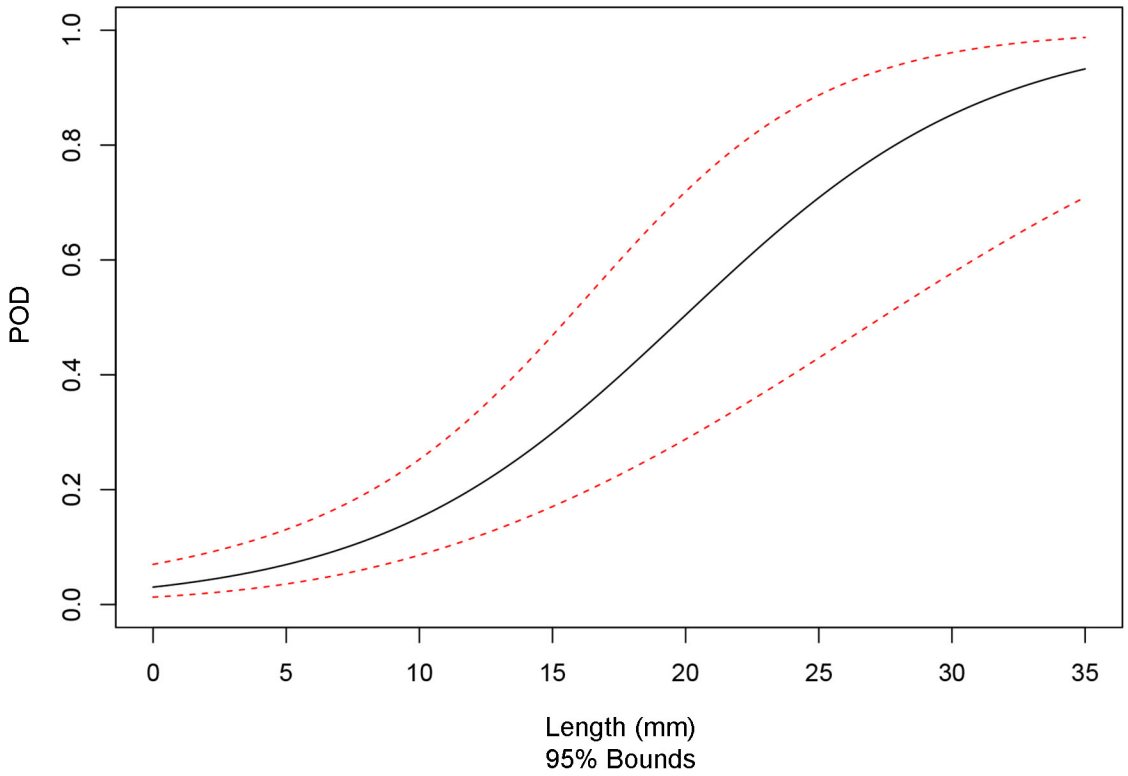

Figure 5.23. Aggregate Probability of Detection Curve versus Length for PAUT Techniques 108-PA1 and 126-PA1 (Blind), and for All Flaw Orientations (tolerance = 15 mm)

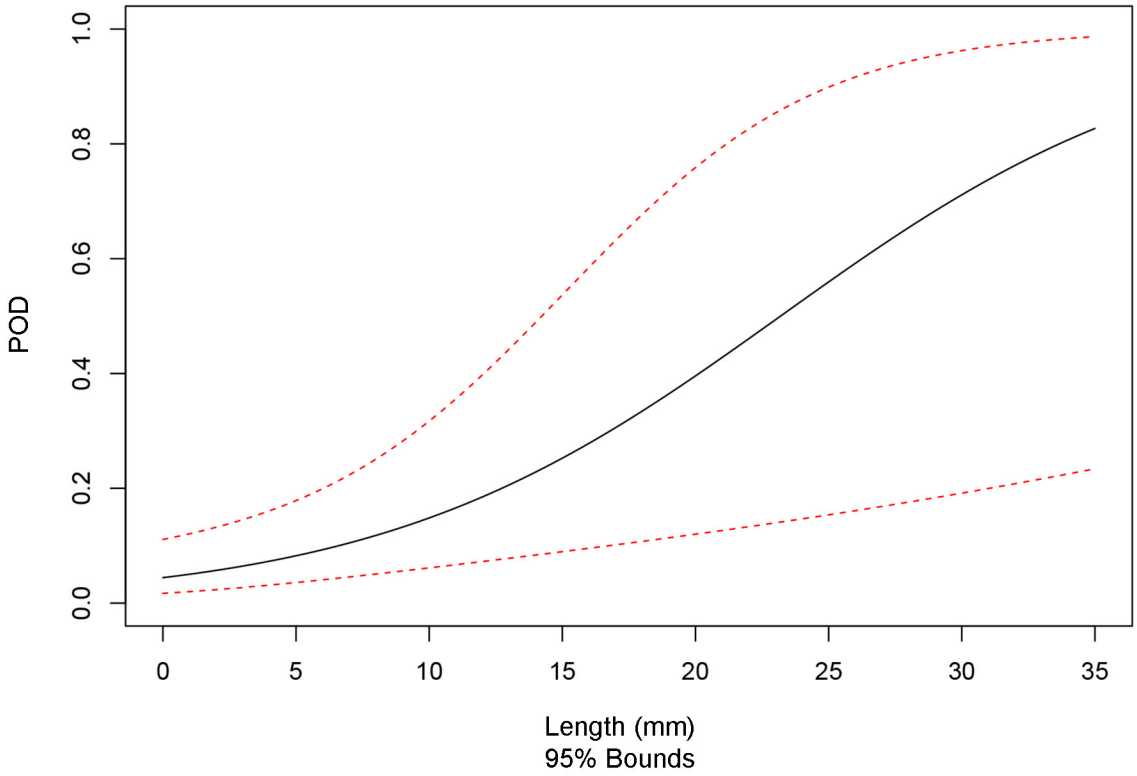

Figure 5.24. Aggregate Probability of Detection Curve versus Length for PAUT Techniques 108-PA0 and 126-PA0 (Quickblind), and for All Flaw Orientations (tolerance = 10 mm and 15 mm)

5.1.9.3 Summary of Detection Analysis Results for Axial Flaws

This section presents the detection performance results obtained from the axial flaw population as POD versus depth and length. The data is presented in tabular form and as plots of POD curves, as is done for detection performance data collected from the population of all flaws in Section 5.1.9.2.

Summary of Detection Performance as a Function of Flaw Depth

This section summarizes detection performance results obtained from the axial flaw population as POD versus depth. Table 5.13 and Table 5.14 provide the POD values at discrete flaw sizes (i.e., at 0 mm, 5 mm, 10 mm, 15 mm, 30 mm, and 60 mm) for scoring tolerances of 10 mm and 15 mm, respectively. A column for NOBS and FCR is also included in the tables. In this case, NOBS represents the total number of axial flaws in the test blocks inspected by a given technique. Comparison of Table 5.13 and Table 5.14 illustrates how aggregate detection performance (i.e., for 108-PA1 + 126-PA1) and detection performance for technique 108-PA1 is impacted by the increase in tolerance from 10 mm to 15 mm. As the tables show, the increase in scoring tolerance results in a decrease in the FCR. Further, an increase in the POD is observed for flaw depths of 10 mm, 15 mm, and 30 mm.

Plots of aggregate POD curves versus flaw depth (i.e., for 108-PA1 + 126-PA1) for axial flaws and for scoring tolerances of 10 mm and 15 mm are provided in Figure 5.25 and Figure 5.26, respectively. The solid black line represents the regression fit to the data and the red dashed lines represent 95% confidence bounds for the regression fit. The change in shape from Figure 5.25 and Figure 5.26 indicates an overall increase in detection performance.

Table 5.13. Summary of POD versus Flaw Depth for Axially Oriented Flaws (tolerance = 10 mm)

	NOBS	FCR	0 mm	5 mm	10 mm	15 mm	30 mm	60 mm
108-PA1	9	0.76	3	6	11	21	72	100
126-PA1	9	1.88	5	9	18	32	82	100
108-PA1 + 126-PA1 (Blind)	18	1.32	3	7	14	27	79	100

Table 5.14. Summary of POD versus Flaw Depth for Axially Oriented Flaws (tolerance = 15 mm)

	NOBS	FCR	0 mm	5 mm	10 mm	15 mm	30 mm	60 mm
108-PA1	9	0.00	1	4	13	33	94	100
126-PA1	9	1.95	5	10	18	32	82	100
108-PA1 + 126-PA1 (Blind)	18	0.98	3	7	17	36	91	100

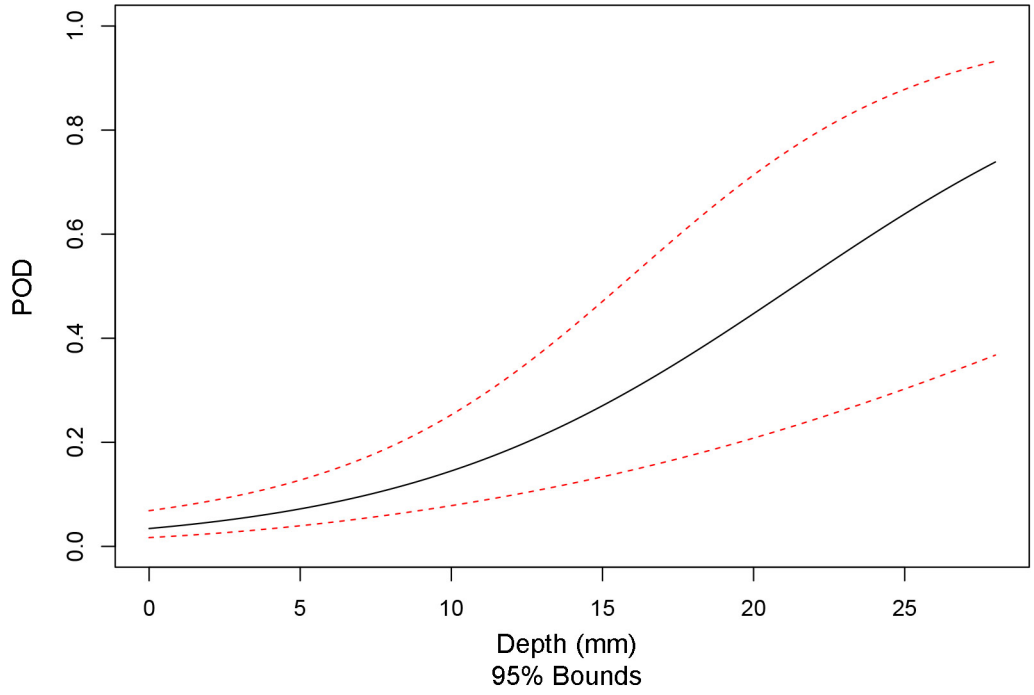

Figure 5.25. Aggregate Probability of Detection Curve versus Depth for PAUT Techniques 108-PA1 and 126-PA1 (Blind) for Axial Flaws (tolerance = 10 mm)

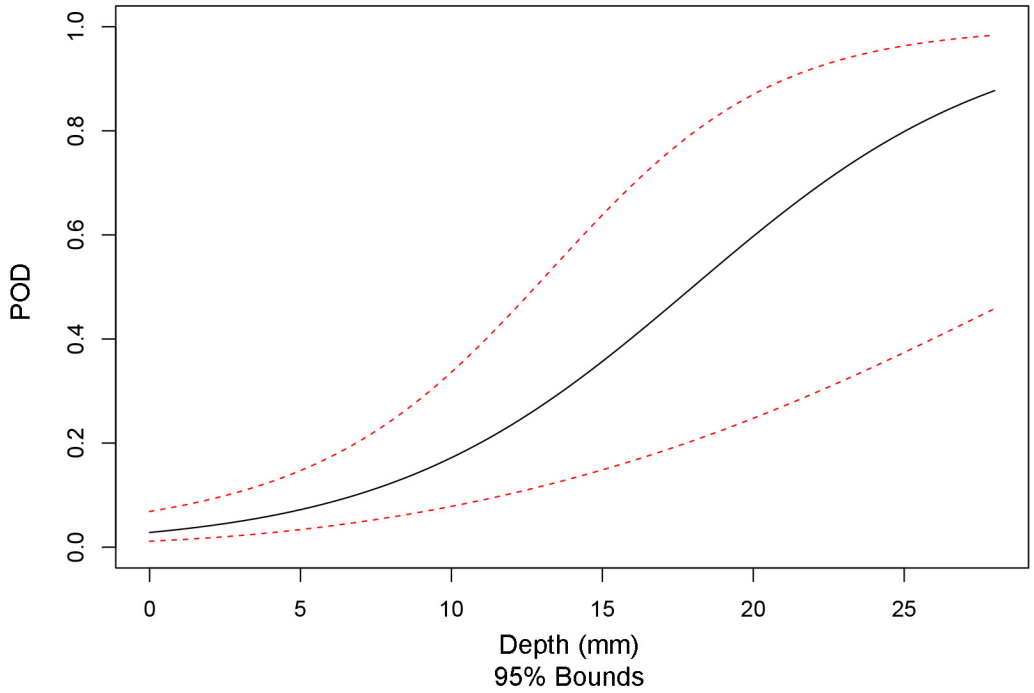

Figure 5.26. Aggregate Probability of Detection Curve versus Depth for PAUT Techniques 108-PA1 and 126-PA1 (Blind) for Axial Flaws (tolerance = 15 mm)

Summary of Detection Performance as a Function of Flaw Length

This section summarizes detection performance results obtained from the axial flaw population as POD versus length. Table 5.15 and Table 5.16 provide the POD values at discrete flaw sizes (i.e., at 0 mm, 5 mm, 10 mm, 15 mm, 30 mm, and 60 mm) for scoring tolerances of 10 mm and 15 mm, respectively. A column for NOBS and FCR is also included in the tables. In this case, NOBS represents the total number of axial flaws in the test blocks inspected by a given technique. Comparison of Table 5.15 and Table 5.16 illustrates how aggregate detection performance (i.e., for 108-PA1 + 126-PA1) and detection performance for 108-PA1 is impacted by the increase in tolerance from 10 mm to 15 mm. As the tables show, the increase in scoring tolerance results in a decrease in the FCR. Further, an increase in the POD is observed for all flaw depth values.

Plots of aggregate POD curves versus flaw length (i.e., for 108-PA1 + 126-PA1) for axial flaws and for scoring tolerances of 10 mm and 15 mm are provided in Figure 5.27 and Figure 5.28, respectively. The solid black line represents the regression fit to the data and the red dashed lines represent 95% confidence bounds for the regression fit. The change in shape from Figure 5.27 and Figure 5.28 indicates an overall increase in detection performance.

Table 5.15. Summary of POD versus Flaw Length for Axially Oriented Flaws (tolerance = 10 mm)

	NOBS	FCR	0 mm	5 mm	10 mm	15 mm	30 mm	60 mm
108-PA1	9	0.76	2	5	12	24	80	100
126-PA1	9	1.88	5	9	16	27	71	99
108-PA1 + 126-PA1 (Blind)	18	1.32	4	7	14	26	76	100

Table 5.16. Summary of POD versus Flaw Length for Axially Oriented Flaws (tolerance = 15 mm)

	NOBS	FCR	0 mm	5 mm	10 mm	15 mm	30 mm	60 mm
108-PA1	9	0.00	1	4	12	34	96	100
126-PA1	9	1.95	5	10	16	27	71	99
108-PA1 + 126-PA1 (Blind)	18	0.98	3	7	16	32	88	100

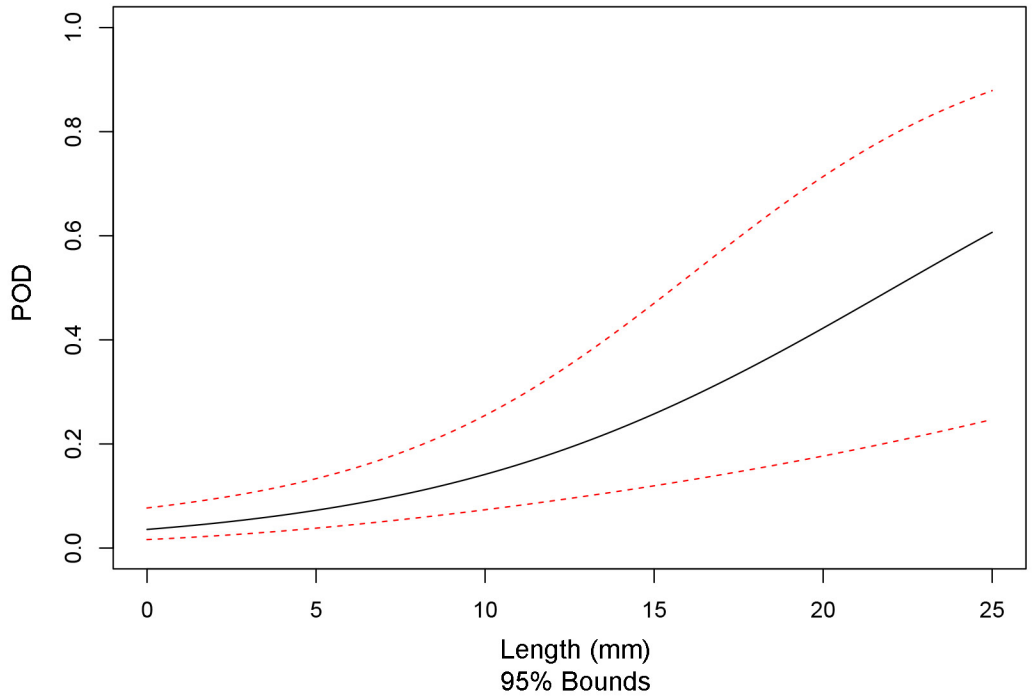

Figure 5.27. Aggregate Probability of Detection Curve versus Length for PAUT Techniques 108-PA1 and 126-PA1 (Blind) for Axial Flaws (tolerance = 10 mm)

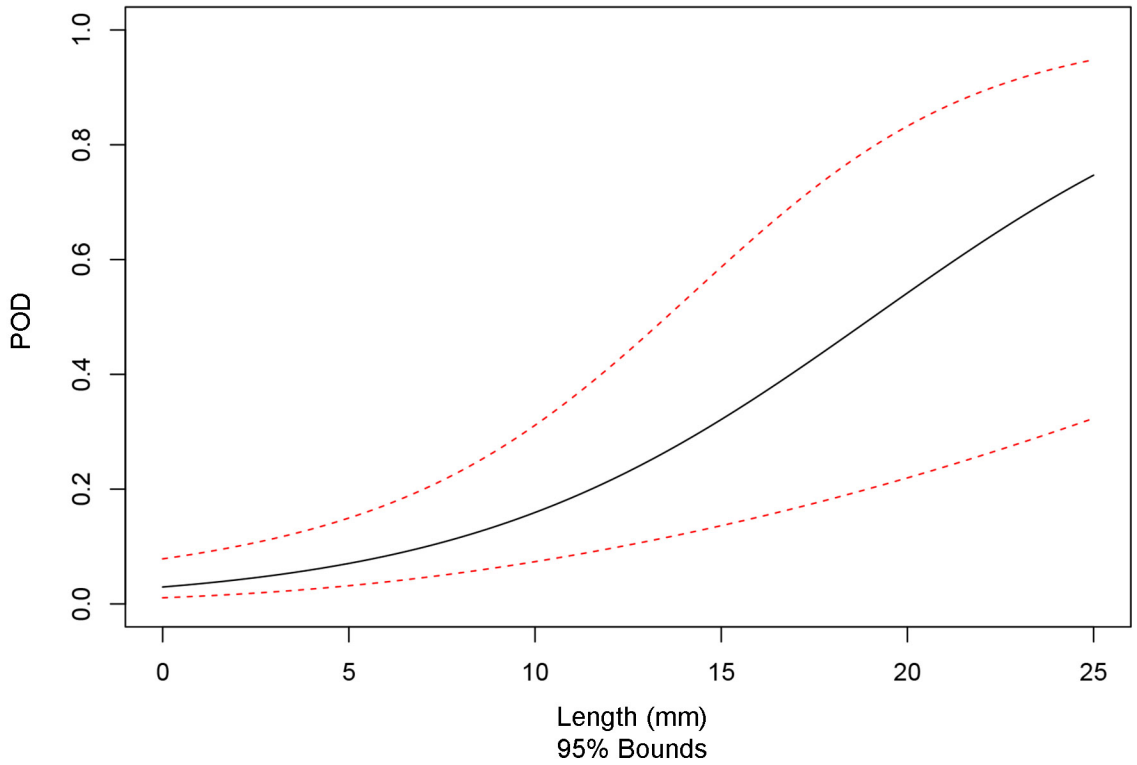

Figure 5.28. Aggregate Probability of Detection Curve versus Length for PAUT Techniques 108-PA1 and 126-PA1 (Blind) for Axial Flaws (tolerance = 15 mm)

5.1.9.4 Summary of Detection Analysis Results for Circumferential Flaws

This section presents the detection performance results obtained from the circumferential flaw population as POD versus depth and length. The data is presented in tabular form and as plots of POD curves, as is done for detection performance data collected from the population of all flaws in Section 5.1.9.2 and the population of axial flaws in Section 5.1.9.3.

Summary of Detection Performance as a Function of Flaw Depth

This section summarizes detection performance results obtained from the circumferential flaw population as POD versus depth. Table 5.17 and Table 5.18 provide the POD values at discrete flaw sizes (i.e., at 0 mm, 5 mm, 10 mm, 15 mm, 30 mm, and 60 mm) for scoring tolerances of 10 mm and 15 mm, respectively. A column for NOBS and FCR is also included in the tables. In this case, NOBS represents the total number of axial flaws in the test blocks inspected by a given technique. Comparison of Table 5.17 and Table 5.18 illustrates that detection performance for circumferential flaws is mostly unaffected for any techniques by the increase in tolerance from 10 mm to 15 mm. This is anticipated considering the positioning error is only associated with axial flaws. Differences in Table 5.17 and Table 5.18 are observed in FCR; however, this is because false calls are irrespective of the orientation of flaws in the test block.

Plots of aggregate POD curves versus flaw depth (i.e., for 108-PA1 + 126-PA1) for circumferential flaws and for scoring tolerances of 10 mm and 15 mm are provided in Figure 5.29 and Figure 5.30, respectively. The solid black line represents the regression fit to the data and the red dashed lines represent 95%

confidence bounds for the regression fit. As can be seen from Figure 5.29 and Figure 5.30, there is no visible change in the POD curve as a consequence of the increase in tolerance from 10 mm to 15 mm. This is anticipated considering the positioning error is only associated with axial flaws.

Table 5.17. Summary of POD versus Flaw Depth for Circumferentially Oriented Flaws (tolerance = 10 mm)

	NOBS	FCR	0 mm	5 mm	10 mm	15 mm	30 mm	60 mm
108-PA1	10	0.76	3	8	19	39	93	100
126-PA1	10	1.88	7	13	24	40	86	100
108-PA1 + 126-PA1 (Blind)	20	1.32	5	11	24	45	93	100

Table 5.18. Summary of POD versus Flaw Depth for Circumferentially Oriented Flaws (tolerance = 15 mm)

	NOBS	FCR	0 mm	5 mm	10 mm	15 mm	30 mm	60 mm
108-PA1	10	0.00	2	5	14	35	95	100
126-PA1	10	1.95	7	14	24	40	86	100
108-PA1 + 126-PA1 (Blind)	20	0.98	4	10	23	44	94	100

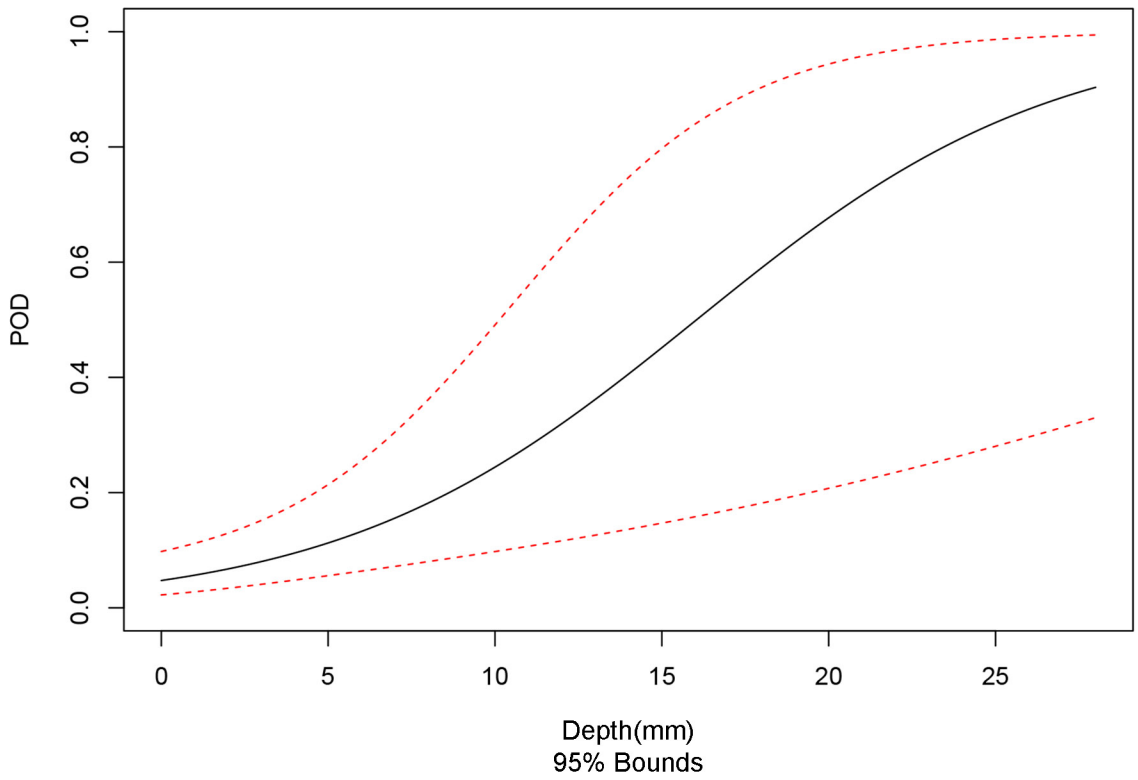

Figure 5.29. Aggregate Probability of Detection Curve versus Depth for PAUT Techniques 108-PA1 and 126-PA1 (Blind) for Circumferential Flaws (tolerance = 10 mm)

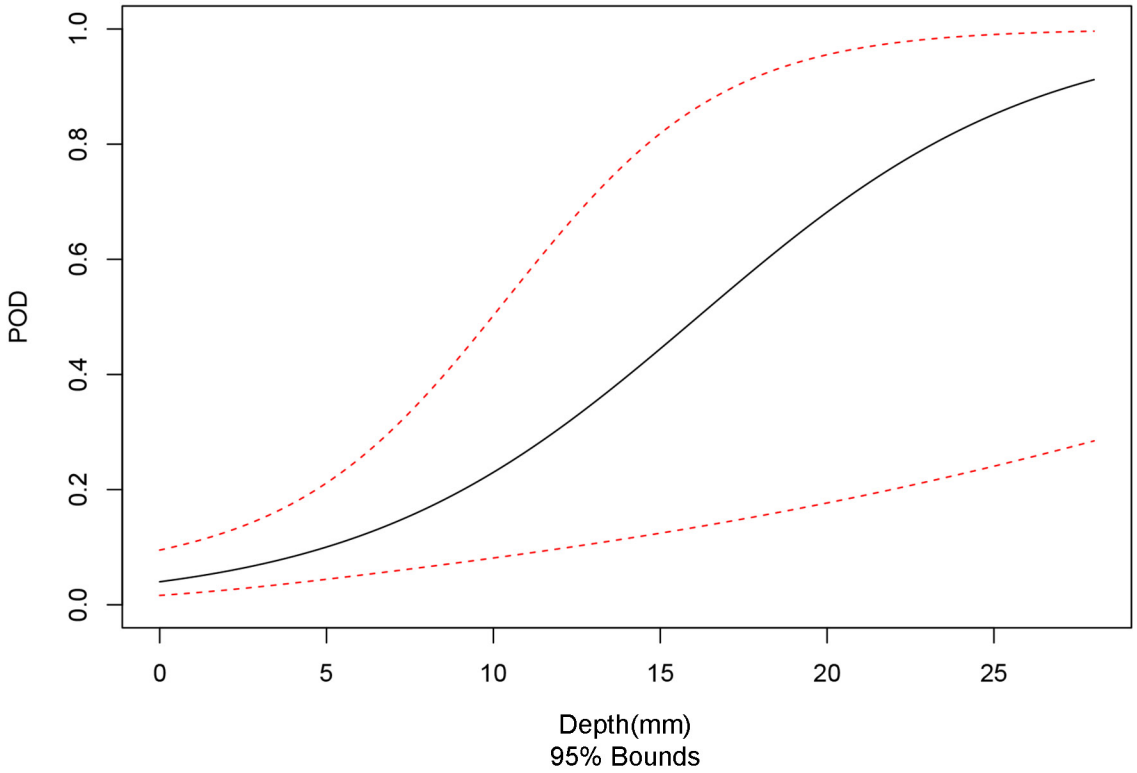

Figure 5.30. Aggregate Probability of Detection Curve versus Depth for PAUT Techniques 108-PA1 and 126-PA1 (Blind) for Circumferential Flaws (tolerance = 15 mm)

Summary of Detection Performance as a Function of Flaw Length

This section summarizes detection performance results obtained from the circumferential flaw population as POD versus length. Table 5.19 and Table 5.20 provide the POD values at discrete flaw sizes (i.e., at 0 mm, 5 mm, 10 mm, 15 mm, 30 mm, and 60 mm) for scoring tolerances of 10 mm and 15 mm, respectively. A column for NOBS and FCR is also included in the tables. In this case, NOBS represents the total number of axial flaws in the test blocks inspected by a given technique. Comparison of Table 5.19 and Table 5.20 illustrates that detection performance for circumferential flaws is mostly unaffected for any techniques by the increase in tolerance from 10 mm to 15 mm. This is anticipated considering the positioning error is only associated with axial flaws. Differences in Table 5.19 and Table 5.20 are observed in FCR; however, this is because false calls are irrespective of the orientation of flaws in the test block.

Plots of aggregate POD curves versus flaw length (i.e., for 108-PA1 + 126-PA1) for circumferential flaws and for scoring tolerances of 10 mm and 15 mm are provided in Figure 5.31 and Figure 5.32, respectively. The solid black line represents the regression fit to the data and the red dashed lines represent 95% confidence bounds for the regression fit. As can be seen from Figure 5.31 and Figure 5.32, there is no visible change in the POD curve as a consequence of the increase in tolerance from 10 mm to 15 mm. This is anticipated considering the positioning error is only associated with axial flaws.

Table 5.19. Summary of POD versus Flaw Length for Circumferentially Oriented Flaws (tolerance = 10 mm)

	NOBS	FCR	0 mm	5 mm	10 mm	15 mm	30 mm	60 mm
108-PA1	10	0.76	2	5	11	22	78	100
126-PA1	10	1.88	6	10	18	29	74	99
108-PA1 + 126-PA1 (Blind)	20	1.32	4	7	15	28	80	100

Table 5.20. Summary of POD versus Flaw Length for Circumferentially Oriented Flaws (tolerance = 15 mm)

	NOBS	FCR	0 mm	5 mm	10 mm	15 mm	30 mm	60 mm
108-PA1	10	0.00	0	2	5	14	84	100
126-PA1	10	1.95	6	10	18	29	73	99
108-PA1 + 126-PA1 (Blind)	20	0.98	3	6	13	26	81	100

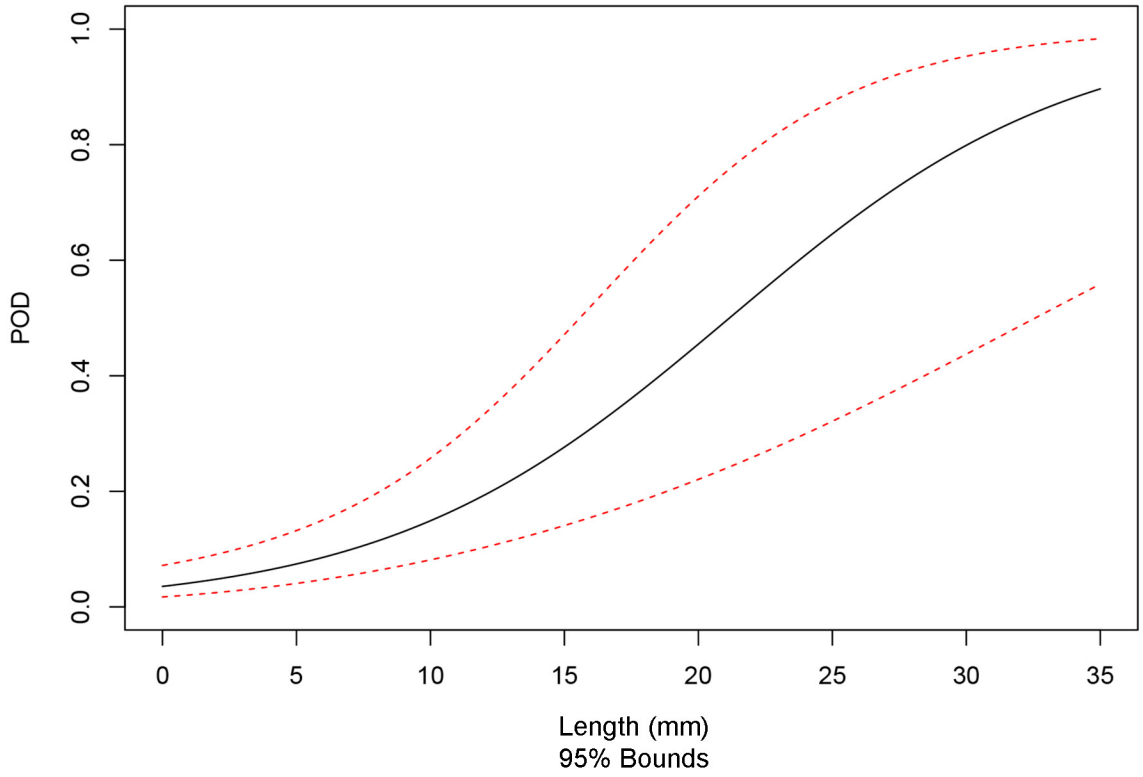

Figure 5.31. Aggregate Probability of Detection Curve versus Length for PAUT Techniques 108-PA1 and 126-PA1 (Blind) for Circumferential Flaws (tolerance = 10 mm)

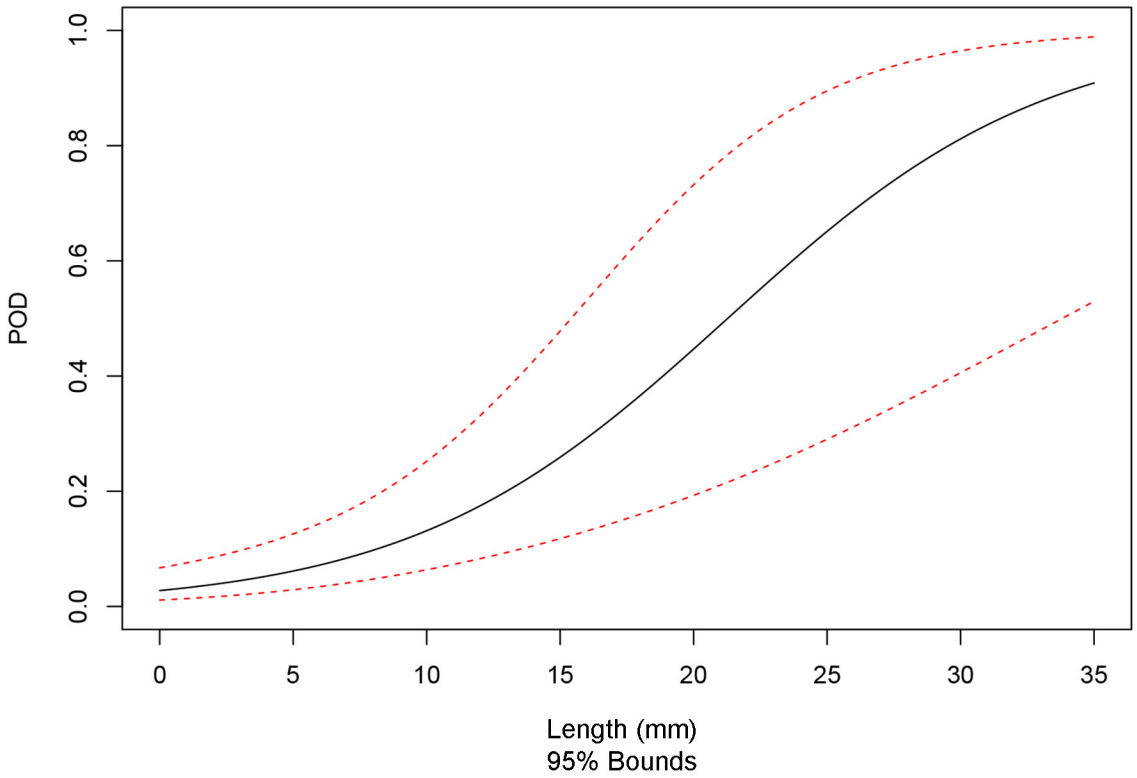

Figure 5.32. Aggregate Probability of Detection Curve versus Length for PAUT Techniques 108-PA1 and 126-PA1 (Blind) for Circumferential Flaws (tolerance = 15 mm)

5.1.10 Depth Sizing Performance Analysis

This section presents the results of the depth sizing performance analysis of PAUT techniques applied to LBDMW test blocks in PARENT. Results are presented as tabulations of bias and RMSE and as plots of depth sizing regression curves. The following sections include tabulated summaries of depth sizing performance for PAUT techniques for scoring tolerances of 10 mm and 15 mm to account for the positioning error observed for axial flaws in test block P33. Summaries of depth sizing results are provided for the total flaw population, the axial flaw population, and the circumferential flaw population.

Linear regression was used to analyze depth sizing data. The formulas for the regression analysis curves, computing RMSE, sizing bias, and sizing StDev are defined in Section 3.4 and in Eqs. (3.7)–(3.11), specifically.

5.1.10.1 Summary of Depth Sizing Analysis Results for All Flaws

This section presents the results of the depth sizing performance analysis of PAUT techniques applied to the total detected flaw population. Tabulation of depth sizing bias and RMSE for PAUT techniques are provided in Table 5.21 and Table 5.22 for scoring tolerances of 10 mm and 15 mm, respectively. The NOBS column refers to the sample size used for depth sizing analysis. It is equal to the number of detections.

Aggregate depth sizing regression plots are provided in Figure 5.33, Figure 5.34, and Figure 5.35. Symbols “A” and “C” are used to represent axially oriented flaws and circumferentially oriented flaws,

respectively. The symbol “D” in Figure 5.35 refers to flaws with a diagonal orientation. The designation of diagonal orientation is used to denote flaws that do not have a dominant orientation based on dimensions. In this case, flaws in the Quickblind test blocks P15, P16, and P17 were denoted as diagonal. Figure 5.33 and Figure 5.34 provide aggregate regression plots for PAUT techniques 108-PA1 and 126-PA1 for scoring tolerances of 10 mm and 15 mm, respectively. Figure 5.35 provides the aggregate regression plot for PAUT techniques 108-PA0 and 126-PA0 for scoring tolerances of 10 mm and 15 mm. In this case, the data is the same for a tolerance of 10 mm and 15 mm.

Table 5.21. Summary of Depth Sizing Error for PAUT Techniques for All Flaw Orientations (tolerance = 10 mm)

	NOBS	Bias	RMSE
108-PA0	2	−14.0	14.4
108-PA1	7	−2.8	5.0
126-PA0	2	−7.1	7.1
126-PA1	8	2.6	12.5
108-PA0 and 126-PA0 (Quickblind)	4	−10.6	11.3
108-PA1 and 126-PA1 (Blind)	15	0.1	9.7
108-PA0 + 126-PA0 + 108-PA1 + 126-PA1 (Blind + Quickblind)	19	−2.2	10.1

Table 5.22. Summary of Depth Sizing Error for PAUT Techniques for All Flaw Orientations (tolerance = 15 mm)

	NOBS	Bias	RMSE
108-PA0	2	−14.0	14.4
108-PA1	9	−3.0	4.9
126-PA0	2	−7.1	7.1
126-PA1	8	2.6	12.5
108-PA0 and 126-PA0 (Quickblind)	4	−10.6	11.3
108-PA1 and 126-PA1 (Blind)	17	−0.4	9.2
108-PA0 + 126-PA0 + 108-PA1 + 126-PA1 (Blind + Quickblind)	21	−2.3	9.7

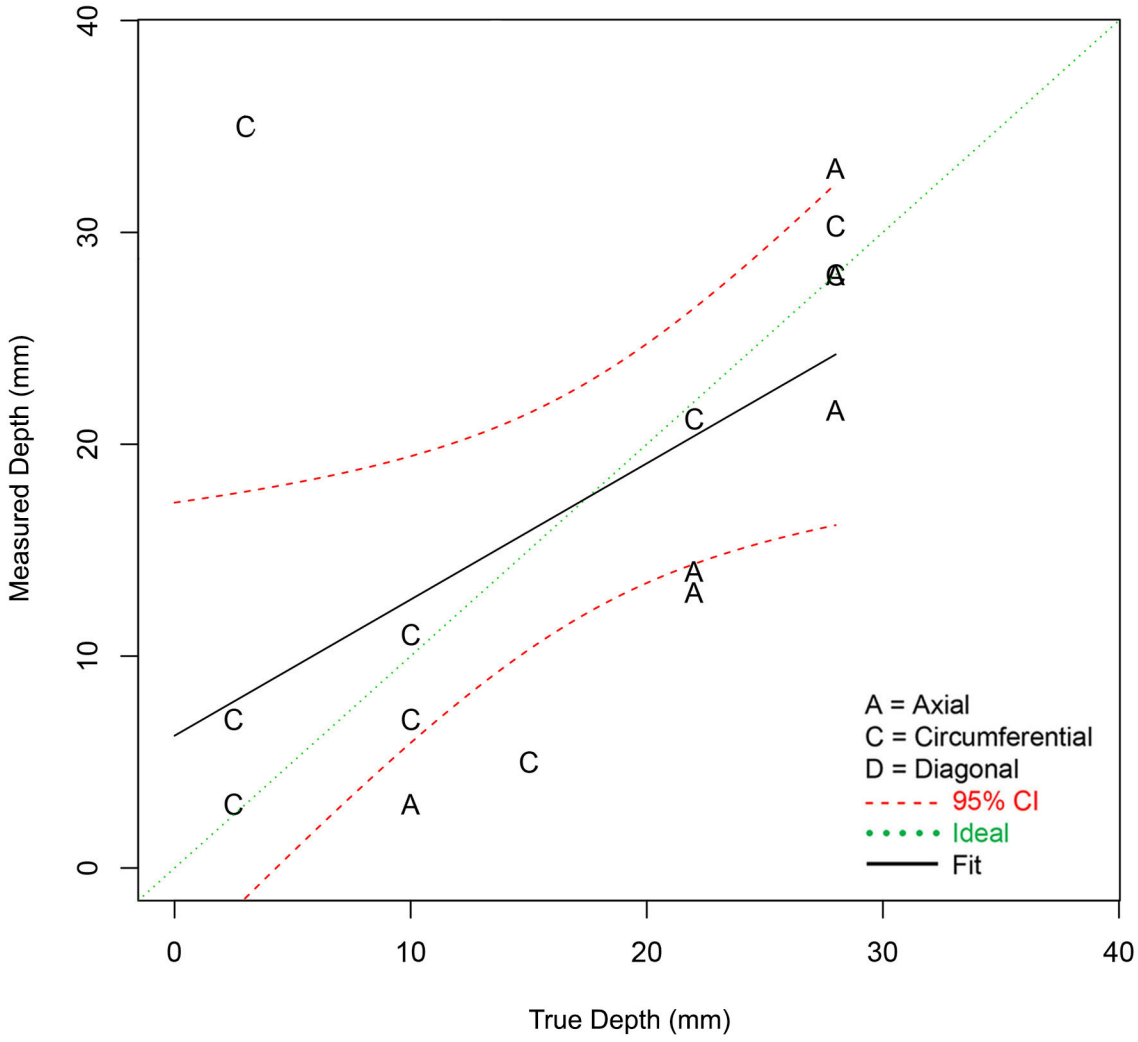

Figure 5.33. Aggregate Depth Sizing Regression Fit for PAUT Techniques 108-PA1 and 126-PA1 for All Flaw Orientations (tolerance = 10 mm)

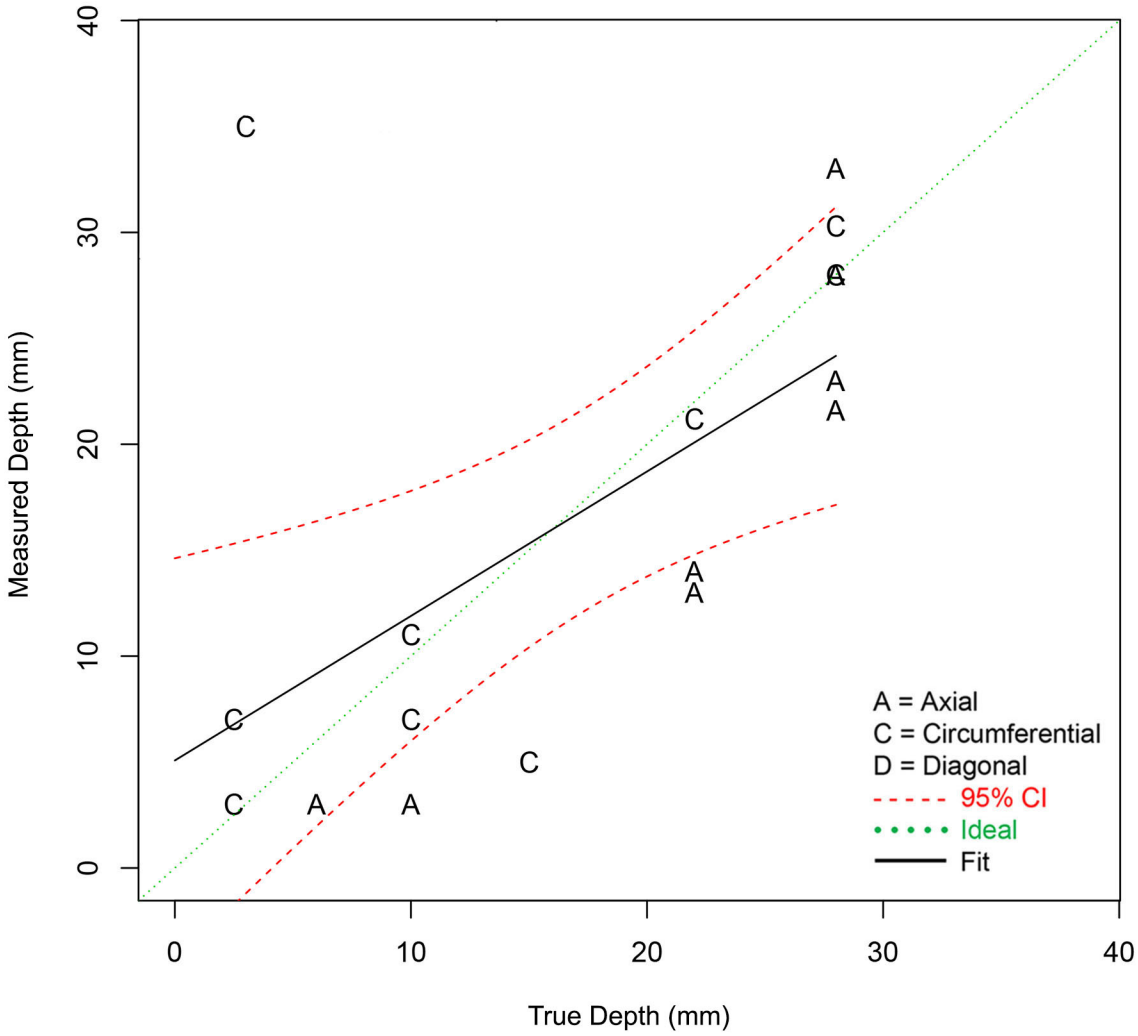

Figure 5.34. Aggregate Depth Sizing Regression Fit for PAUT Techniques 108-PA1 and 126-PA1 for All Flaw Orientations (tolerance = 15 mm)

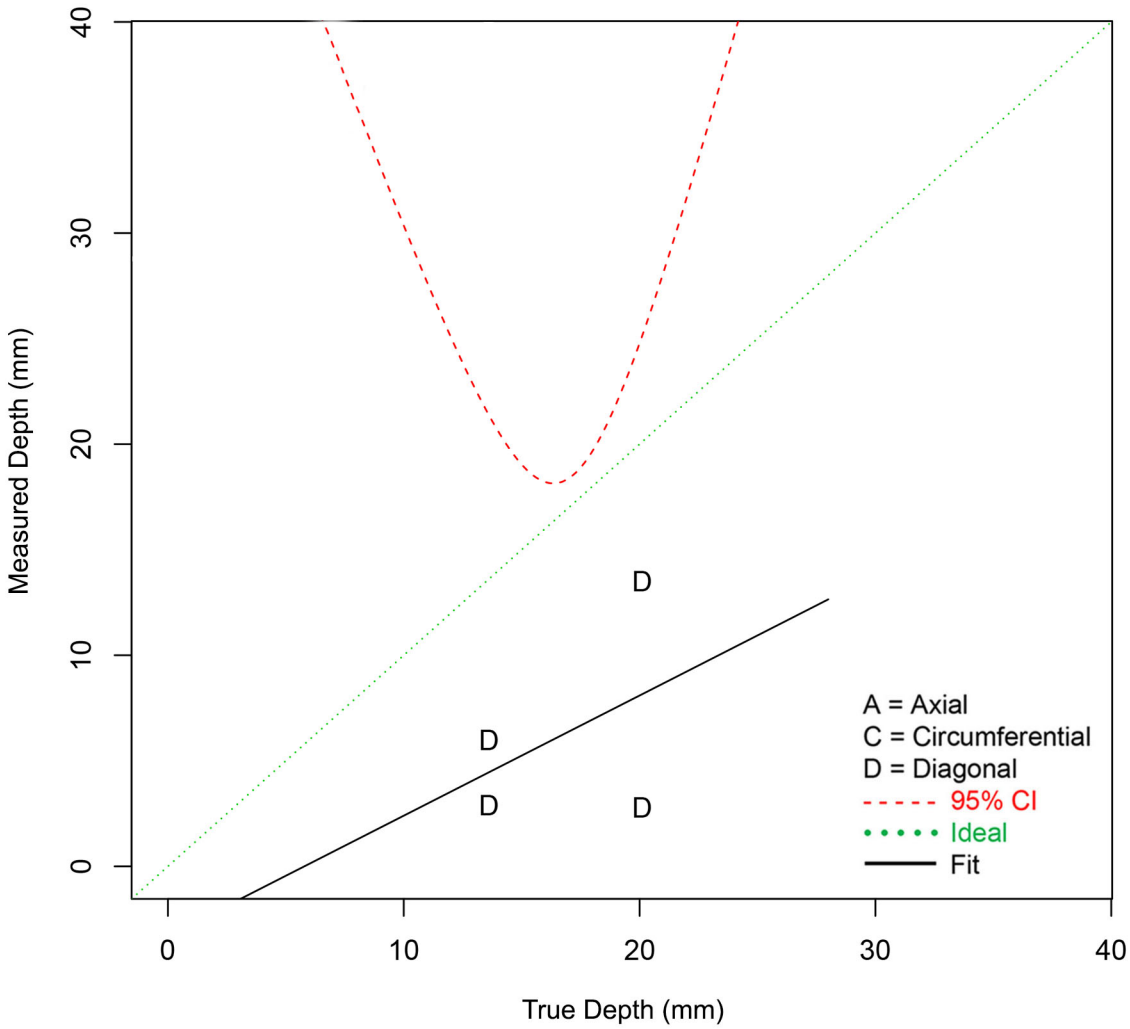

Figure 5.35. Aggregate Depth Sizing Regression Fit for PAUT Techniques 108-PA0 and 126-PA0 for All Flaw Orientations (tolerance = 10 mm and 15 mm)

5.1.10.2 Summary of Depth Sizing Analysis Results for Axial Flaws

This section presents the results of the depth sizing performance analysis of PAUT techniques applied to the population of detected axial flaws. Tabulation of depth sizing bias and RMSE for PAUT techniques are provided in Table 5.23 and Table 5.24 for scoring tolerances of 10 mm and 15 mm, respectively. In this case, NOBS is equal to the number of detected axial flaws.

Aggregate depth sizing regression plots are provided in Figure 5.36 and Figure 5.37 for the population of detected axial flaws for scoring tolerances of 10 mm and 15 mm, respectively.

Table 5.23. Summary of Depth Sizing Error for PAUT Techniques for Axial Flaws (tolerance = 10 mm)

	NOBS	Bias	RMSE
108-PA1	3	−7.5	7.5
126-PA1	3	−1.0	5.4
108-PA1 + 126-PA1 (Blind)	6	−4.2	6.6

Table 5.24. Summary of Depth Sizing Error for PAUT Techniques for Axial Flaws (tolerance = 15 mm)

	NOBS	Bias	RMSE
108-PA1	5	−6.1	6.4
126-PA1	3	−1.0	5.4
108-PA1 + 126-PA1 (Blind)	8	−4.2	6.1

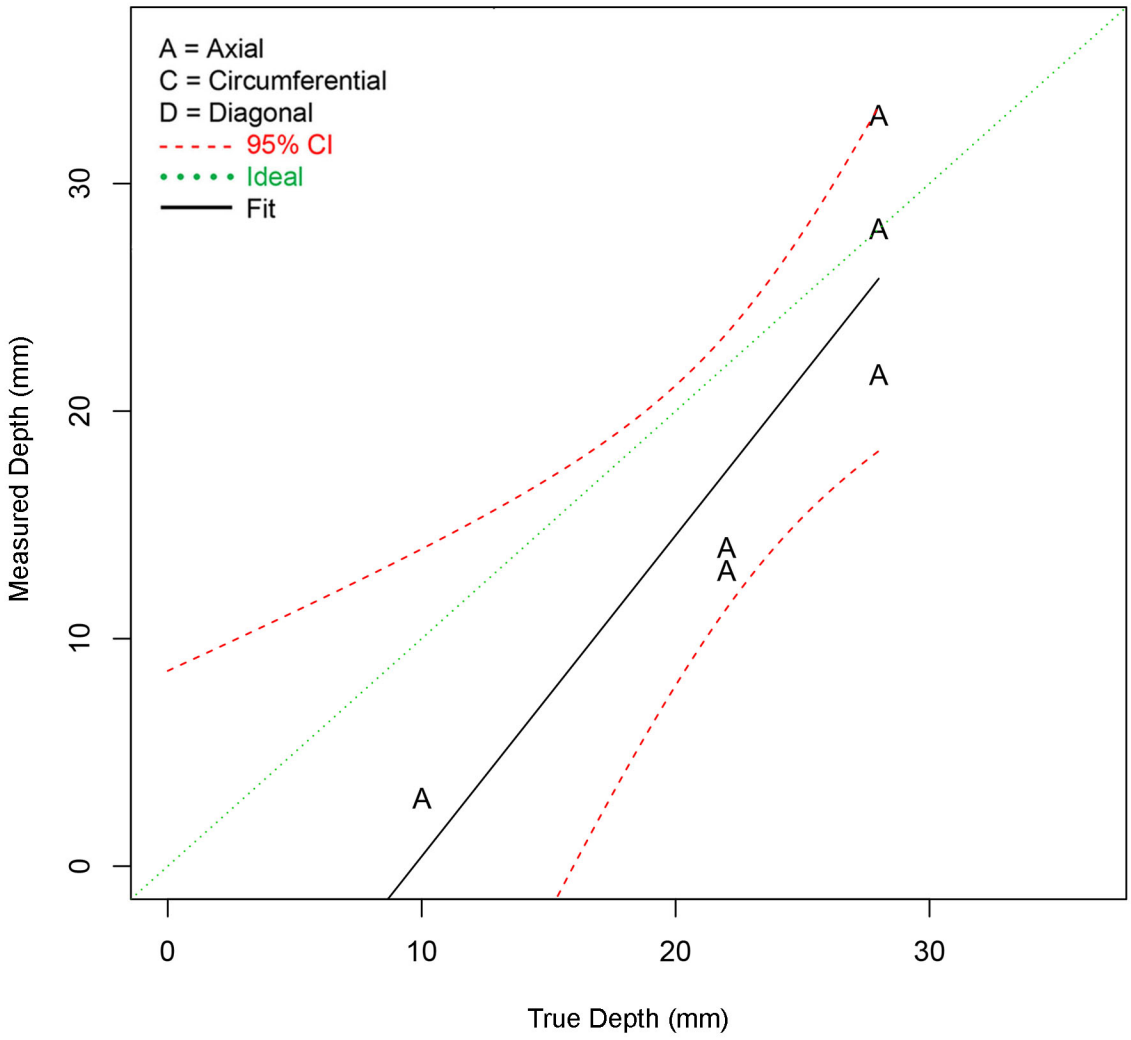

Figure 5.36. Aggregate Depth Sizing Regression Fit for PAUT Techniques 108-PA1 and 126-PA1 for Axial Flaws (tolerance = 10 mm)

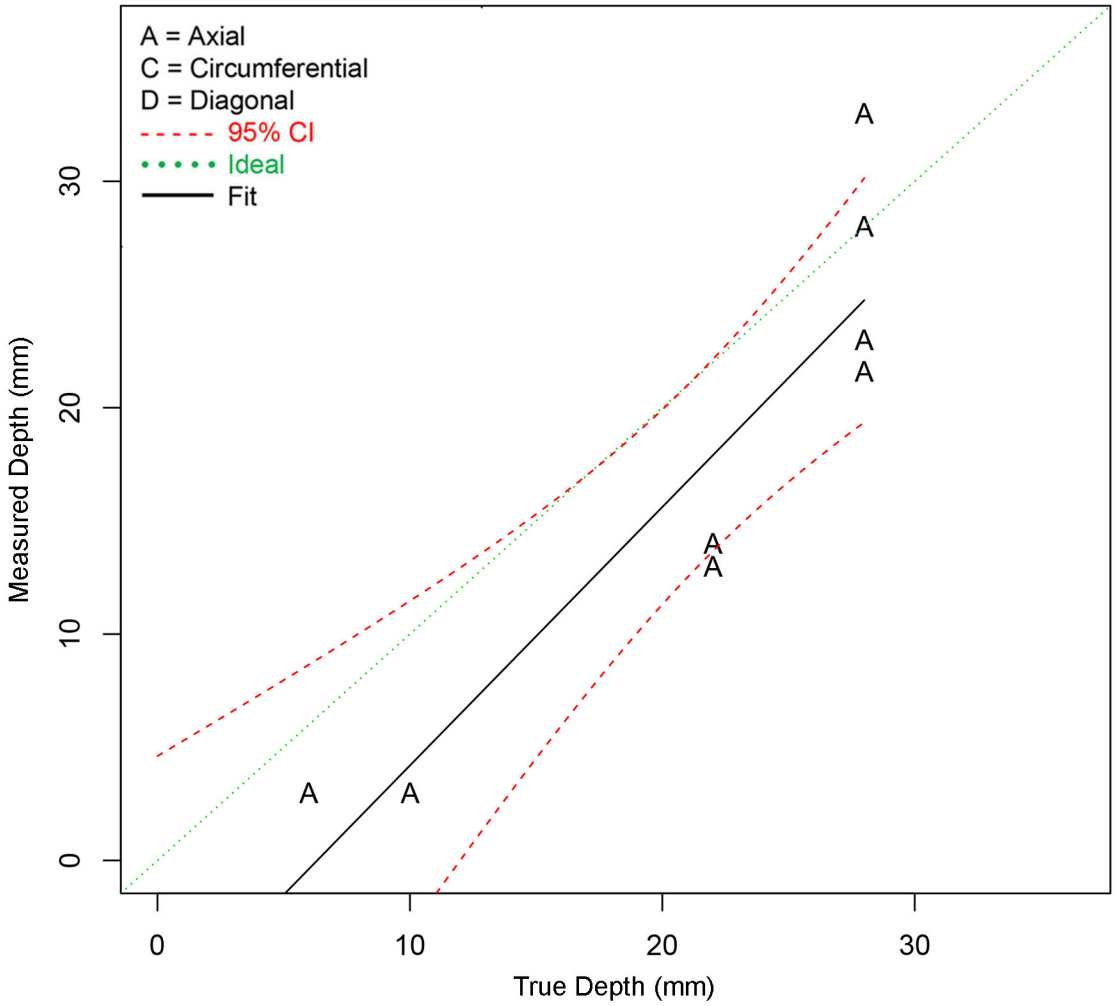

Figure 5.37. Aggregate Depth Sizing Regression Fit for PAUT Techniques 108-PA1 and 126-PA1 for Axial Flaws (tolerance = 15 mm)

5.1.10.3 Summary of Depth Sizing Analysis Results for Circumferential Flaws

This section presents the results of the depth sizing performance analysis of PAUT techniques applied to the population of detected circumferential flaws. Tabulation of depth sizing bias and RMSE for PAUT techniques are provided in Table 5.25 and Table 5.26 for scoring tolerances of 10 mm and 15 mm, respectively. In this case, NOBS is equal to the number of detected circumferential flaws. Table 5.25 and Table 5.26 indicate no changes as a result of the increase in scoring tolerance from 10 mm to 15 mm, which is expected because the number of circumferential flaw detections is not impacted by the scoring tolerance change.

The aggregate depth sizing regression plot is provided in Figure 5.38 and represents the depth sizing regression curve for scoring tolerances of 10 mm and 15 mm.

Table 5.25. Summary of Length Sizing Error for PAUT Techniques for Circumferential Flaws (tolerance = 10 mm)

	NOBS	Bias	RMSE
108-PA1	4	0.8	1.3
126-PA1	5	4.7	15.2
108-PA1 + 126-PA1 (Blind)	9	2.9	11.4

Table 5.26. Summary of Length Sizing Error for PAUT Techniques for Circumferential Flaws (tolerance = 15 mm)

	NOBS	Bias	RMSE
108-PA1	4	0.8	1.3
126-PA1	5	4.7	15.2
108-PA1 + 126-PA1 (Blind)	9	2.9	11.4

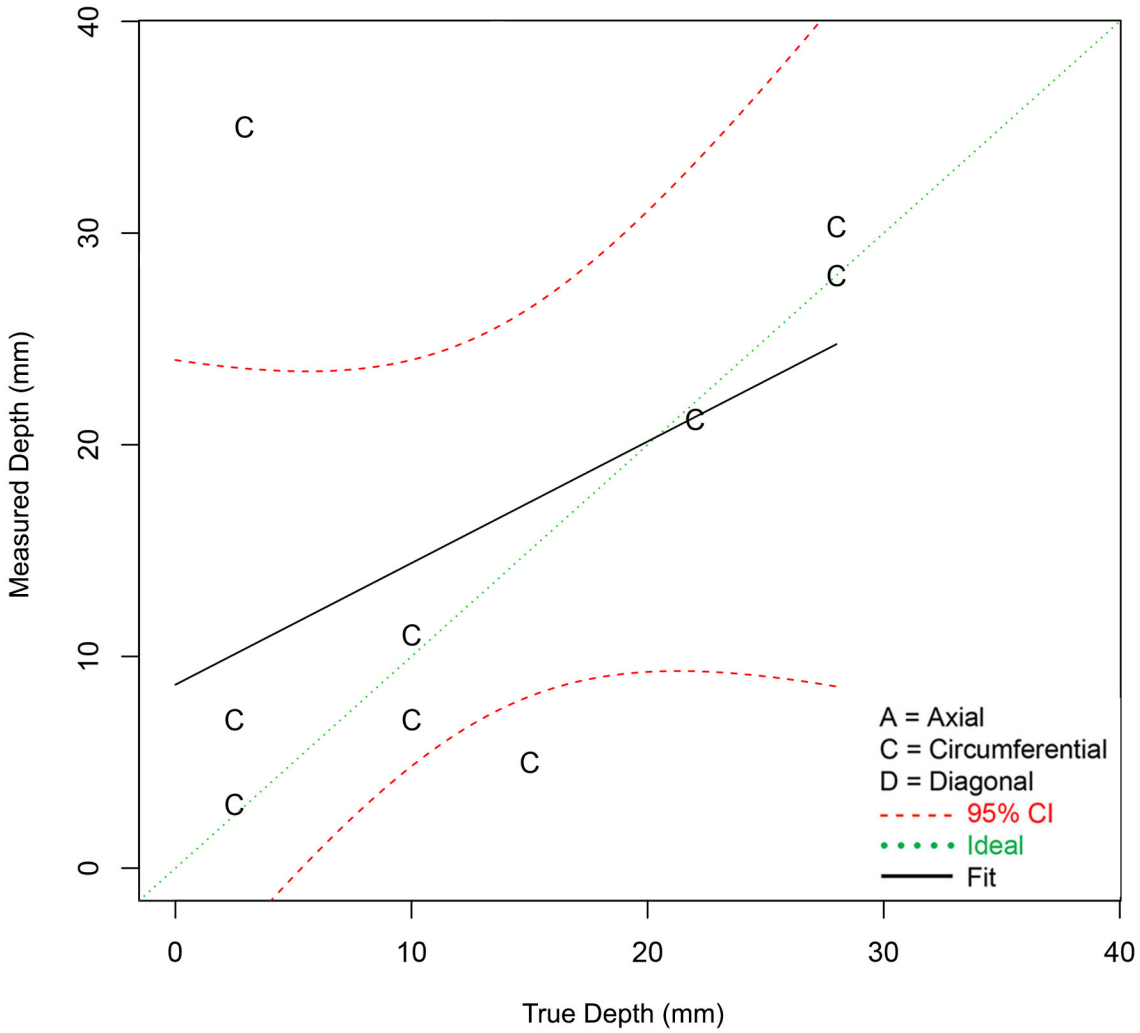

Figure 5.38. Aggregate Depth Sizing Regression Fit for PAUT Techniques 108-PA1 and 126-PA1 for Circumferential Flaws (tolerance = 10 mm and 15 mm)

5.1.11 Length Sizing Performance Analysis

This section presents the results of the length sizing performance analysis of PAUT techniques applied to LBDMW test blocks in PARENT. Results are presented as tabulations of bias and RMSE and as plots of length sizing regression curves. The following sections include tabulated summaries of length sizing performance for PAUT techniques for scoring tolerances of 10 mm and 15 mm to account for the positioning error observed for axial flaws in test block P33. Summaries of length sizing results are provided for the total flaw population, the axial flaw population, and the circumferential flaw population.

Linear regression was used to analyze length sizing data. The formulas for the regression analysis curves, computing RMSE, sizing bias, and sizing StDev are defined in Section 3.4 and in Eqs. (3.7)–(3.11), specifically.

5.1.11.1 Summary of Length Sizing Analysis Results for All Flaws

This section presents the results of the length sizing performance analysis of PAUT techniques applied to the total detected flaw population. Tabulation of length sizing bias and RMSE for PAUT techniques are provided in Table 5.27 and Table 5.28 for scoring tolerances of 10 mm and 15 mm, respectively. The NOBS column refers to the sample size used for length sizing analysis. It is equal to the number of detections.

Aggregate length sizing regression plots are provided in Figure 5.39, Figure 5.40, and Figure 5.41 for the total detected flaw population. Symbols "A" and "C" are used to represent axially oriented flaws and circumferentially oriented flaws, respectively. The symbol "D" in Figure 5.41 refers to flaws with a diagonal orientation. The designation of diagonal orientation is used to denote flaws that do not have a dominant orientation based on dimensions. In this case, flaws in the Quickblind test blocks P15, P16, and P17 were denoted as diagonal. Figure 5.39 and Figure 5.40 provide aggregate regression plots for PAUT techniques 108-PA1 and 126-PA1 for scoring tolerances of 10 mm and 15 mm, respectively. Figure 5.41 provides the aggregate regression plot for PAUT techniques 108-PA0 and 126-PA0 for scoring tolerances of 10 mm and 15 mm. In this case, the data is the same for a tolerance of 10 mm and 15 mm.

Table 5.27. Summary of Length Sizing Error for PAUT Techniques for All Flaw Orientations (tolerance = 10 mm)

	NOBS	Bias	RMSE
108-PA0	2	−6.0	6.7
108-PA1	7	−0.4	7.2
126-PA0	2	5.0	5.4
126-PA1	7	6.6	10.3
108-PA0 and 126-PA0 (Quickblind)	4	−0.5	6.1
108-PA1 and 126-PA1 (Blind)	14	3.1	8.9
108-PA0 + 126-PA0 + 108-PA1 + 126-PA1 (Blind + Quickblind)	18	2.3	8.3

Table 5.28. Summary of Length Sizing Error for PAUT Techniques for All Flaw Orientations (tolerance = 15 mm)

	NOBS	Bias	RMSE
108-PA0	2	−6.0	6.7
108-PA1	9	1.8	8.7
126-PA0	2	5.0	5.4
126-PA1	7	6.6	10.3
108-PA0 and 126-PA0 (Quickblind)	4	−0.5	6.1
108-PA1 and 126-PA1 (Blind)	16	3.9	9.5
108-PA0 + 126-PA0 + 108-PA1 + 126-PA1 (Blind + Quickblind)	20	3.0	8.9

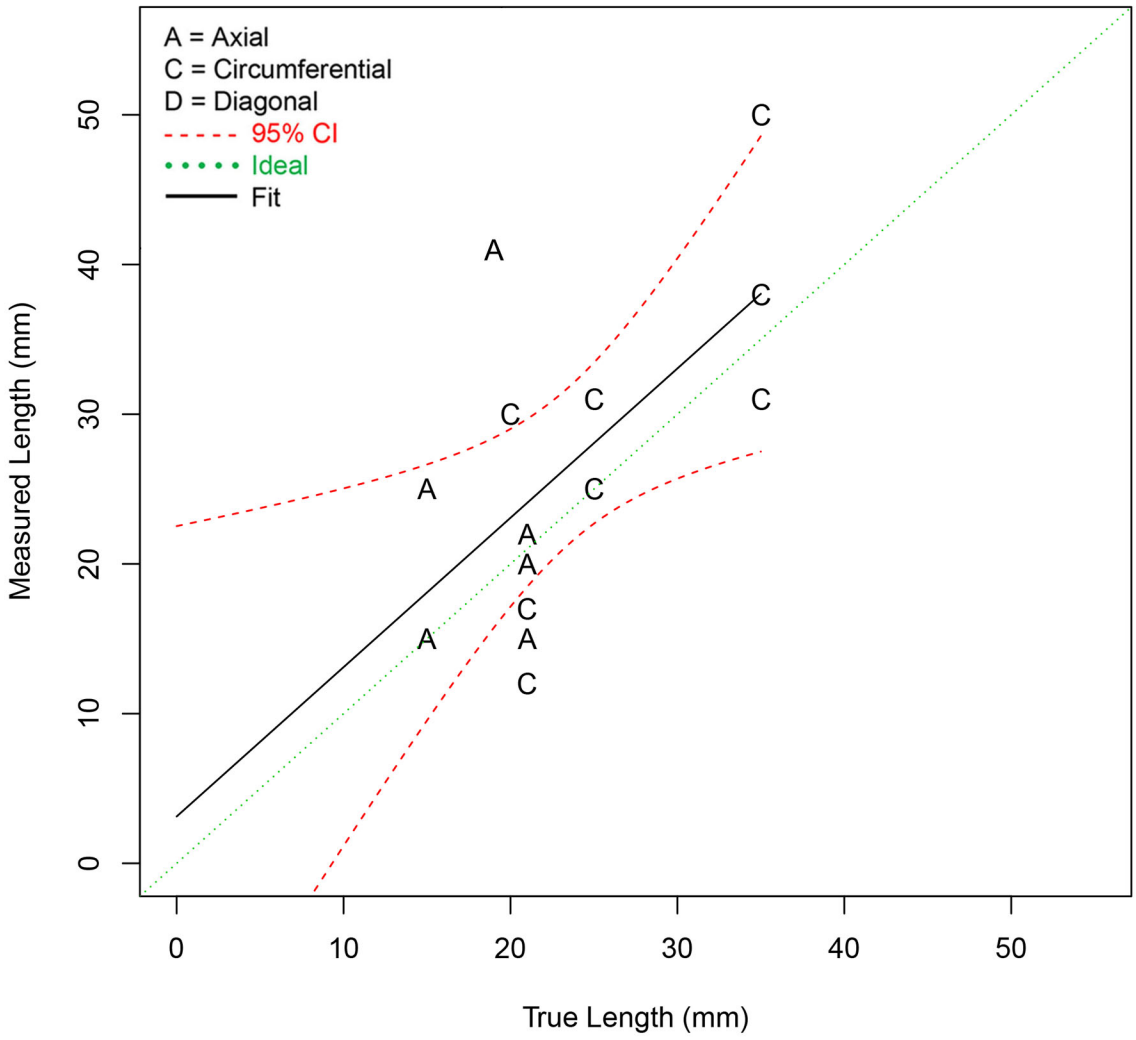

Figure 5.39. Aggregate Length Sizing Regression Fit for PAUT Techniques 108-PA1 and 126-PA1 for All Flaw Orientations (tolerance = 10 mm)

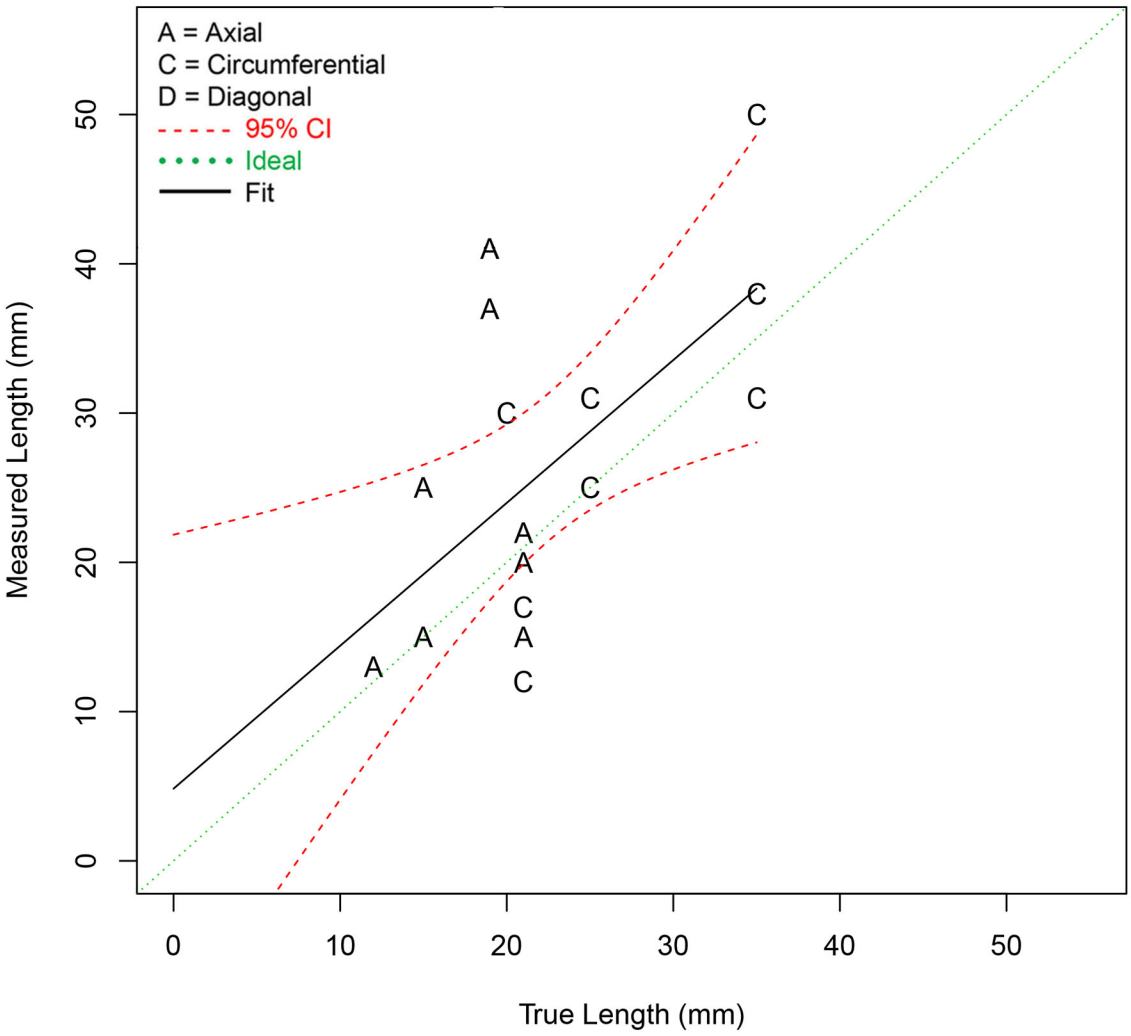

Figure 5.40. Aggregate Length Sizing Regression Fit for PAUT Techniques 108-PA1 and 126-PA1 for All Flaw Orientations (tolerance = 15 mm)

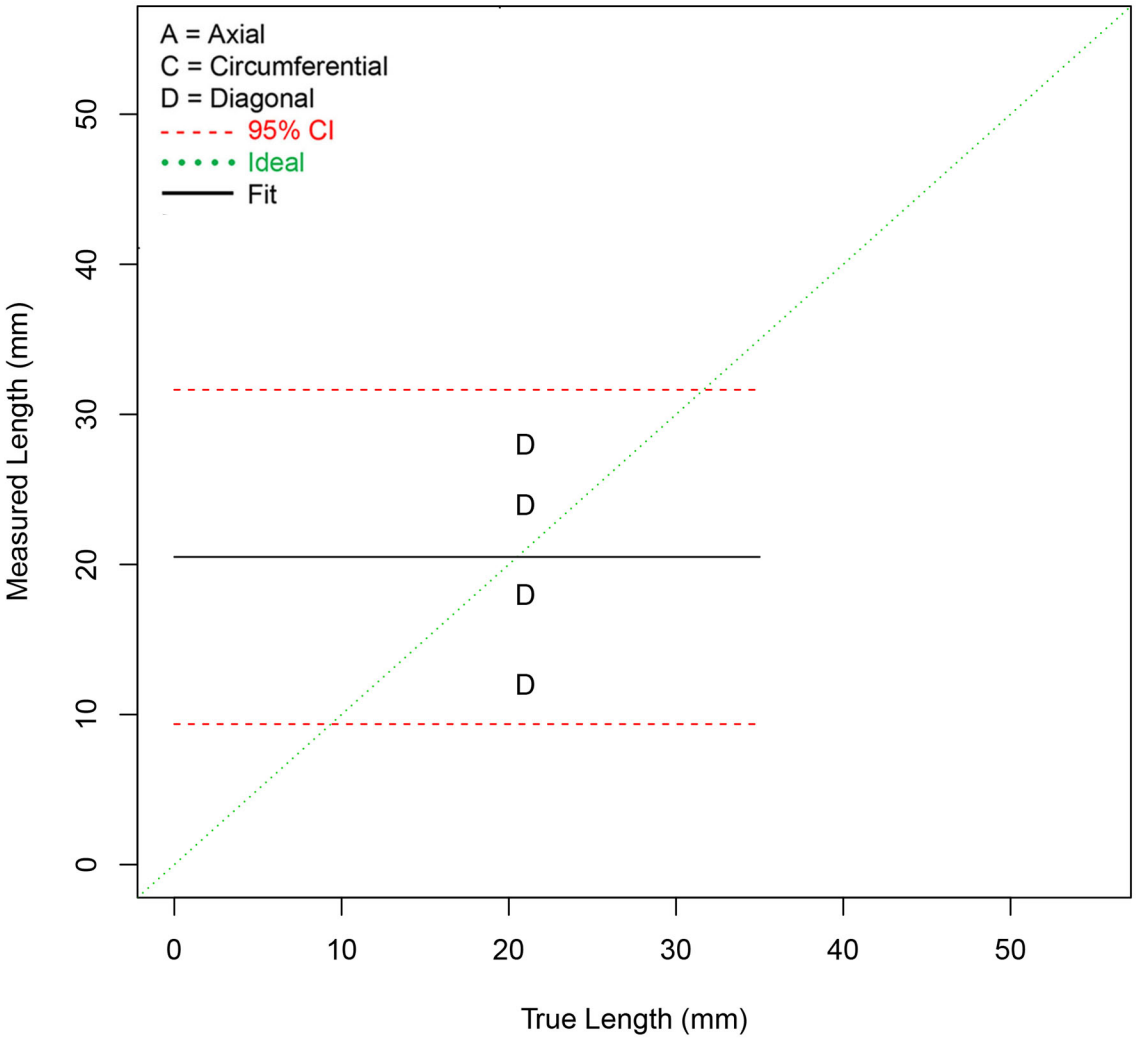

Figure 5.41. Aggregate Length Sizing Regression Fit for PAUT Techniques 108-PA0 and 126-PA0 for All Flaw Orientations (tolerance = 10 mm and 15 mm)

5.1.11.2 Summary of Length Sizing Analysis Results for Axial Flaws

This section presents the results of the length sizing performance analysis of PAUT techniques applied to the population of detected axial flaws. The algorithm for length sizing error analysis is normally performed by comparing the longest dimension of the flaw with the longest dimension of the associated indication. This algorithm is adequate for the majority of flaw and indication pairs in which the indication has the same orientation as the associated flaw. However, the inspections of P33 by PAUT techniques resulted in some indications with orientations that do not match the orientation of their associated flaws. This can be observed by reviewing Figure 5.2, which depicts the indication plot for technique 126-PA1. This plot shows several indications that have orientations that appear to be different than their associated flaws. In this case, it is of interest to perform length sizing error analysis by comparing the axial dimension of the flaw to the axial dimension of the associated indication in addition to the standard length sizing analysis. In the tables and figures below, results are presented for standard length sizing error analysis and for axial dimension length sizing analysis. Tabulation of length sizing bias and RMSE for PAUT techniques is provided in Table 5.29 and Table 5.30 for standard length sizing analysis for scoring tolerances of 10 mm and 15 mm, respectively. Length sizing bias and RMSE are tabulated in Table 5.31

and Table 5.32 for axial dimension length sizing analysis for tolerances of 10 mm and 15 mm, respectively. In this case, NOBS is equal to the number of detected axial flaws. These tables do indicate that the length sizing error results based on the axial dimension analysis does result in a smaller RMSE value.

The aggregate length sizing regression plots are provided in Figure 5.42 and Figure 5.43 for standard length sizing analysis for tolerances of 10 mm and 15 mm, respectively, and in Figure 5.44 and Figure 5.45 for axial dimension length sizing analysis for tolerances of 10 mm and 15 mm, respectively. In all plots, the confidence bounds are fairly large and there is significant scatter in the data points.

Table 5.29. Summary of Length Sizing Error for PAUT Techniques for Axial Flaws (tolerance = 10 mm)

	NOBS	Bias	RMSE
108-PA1	3	−1.7	3.5
126-PA1	3	10.3	14.0
108-PA1 + 126-PA1 (Blind)	6	4.3	10.2

Table 5.30. Summary of Length Sizing Error for PAUT Techniques for Axial Flaws (tolerance = 15 mm)

	NOBS	Bias	RMSE
108-PA1	5	2.8	8.5
126-PA1	3	10.3	14.0
108-PA1 + 126-PA1 (Blind)	8	5.6	10.9

Table 5.31. Summary of Axial Dimension Length Sizing Error for PAUT Techniques for Axial Flaws (tolerance = 10 mm)

	NOBS	Bias	RMSE
108-PA1	3	−1.7	3.5
126-PA1	3	−10.3	10.6
108-PA1 + 126-PA1 (Blind)	6	−6.0	7.9

Table 5.32. Summary of Axial Dimension Length Sizing Error for PAUT Techniques for Axial Flaws (tolerance = 15 mm)

	NOBS	Bias	RMSE
108-PA1	5	2.8	8.5
126-PA1	3	−10.3	10.6
108-PA1 + 126-PA1 (Blind)	8	−2.1	9.4

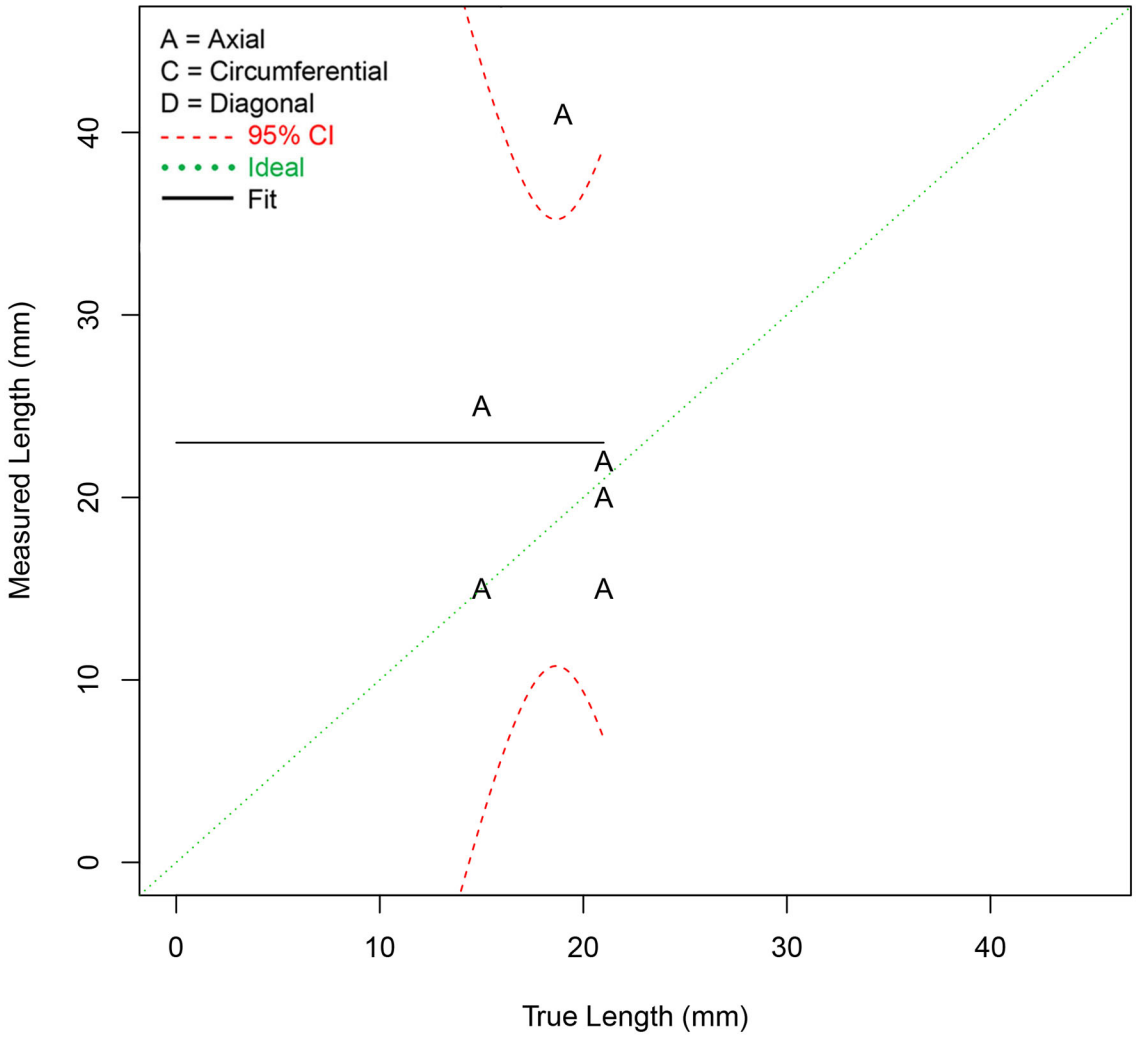

Figure 5.42. Aggregate Length Sizing Regression Fit for PAUT Techniques 108-PA1 and 126-PA1 for Axial Flaws (tolerance = 10 mm)

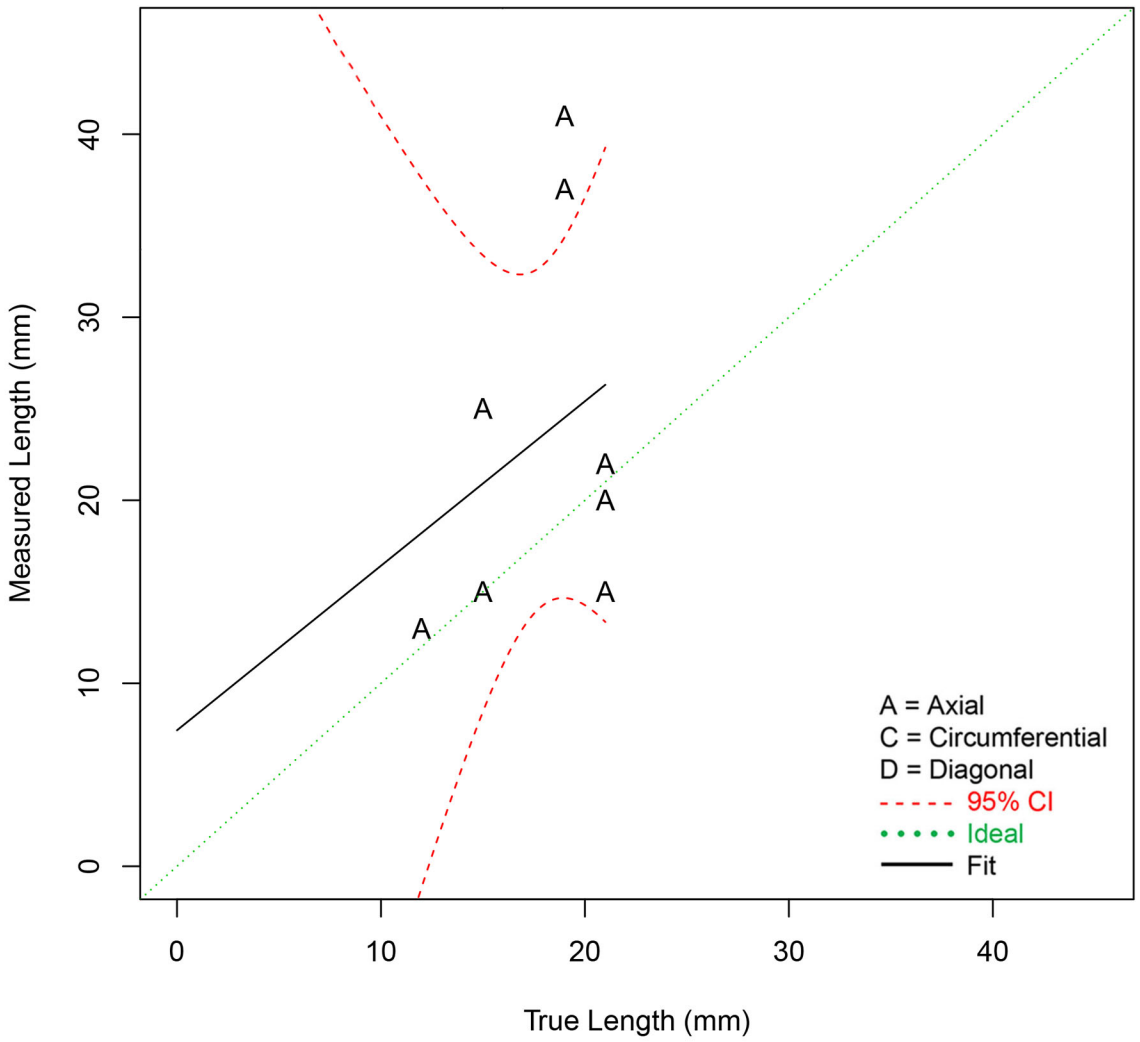

Figure 5.43. Aggregate Length Sizing Regression Fit for PAUT Techniques 108-PA1 and 126-PA1 for Axial Flaws (tolerance = 15 mm)

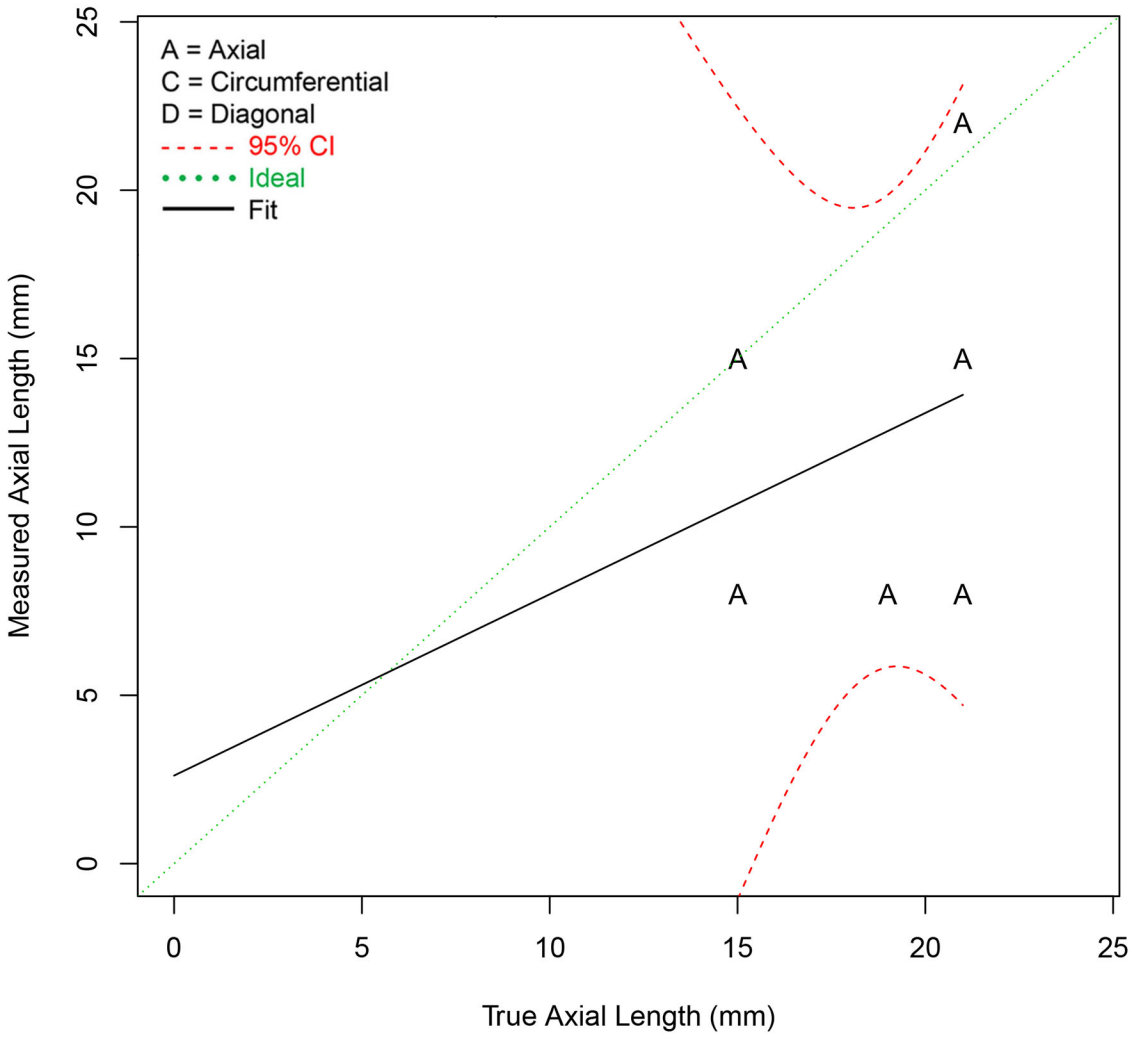

Figure 5.44. Aggregate Axial Dimension Length Sizing Regression Fit for PAUT Techniques 108-PA1 and 126-PA1 for Axial Flaws (tolerance = 10 mm)

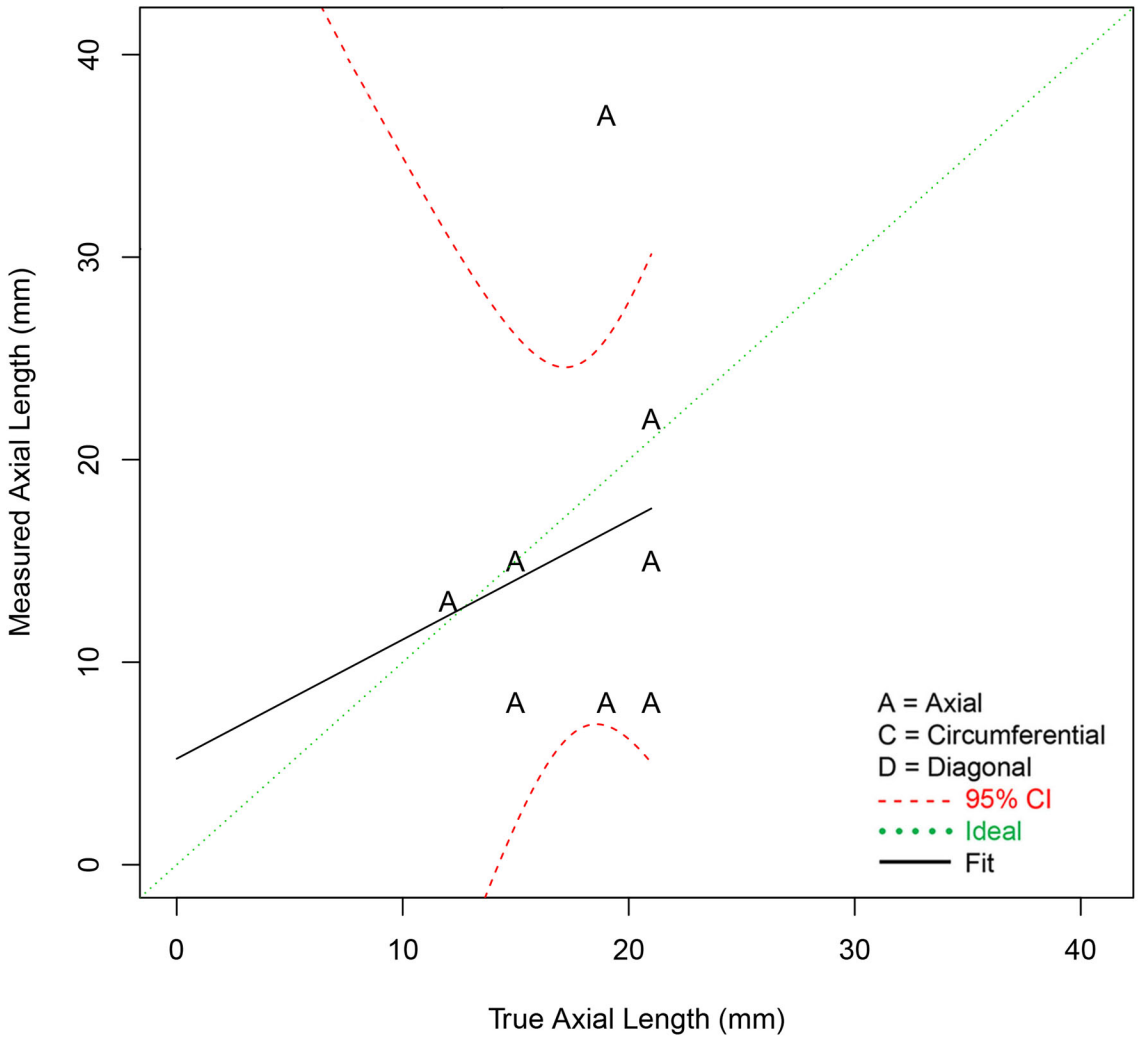

Figure 5.45. Aggregate Axial Dimension Length Sizing Regression Fit for PAUT Techniques 108-PA1 and 126-PA1 for Axial Flaws (tolerance = 15 mm)

5.1.11.3 Summary of Length Sizing Analysis Results for Circumferential Flaws

This section presents the results of the length sizing performance analysis of PAUT techniques applied to the population of detected circumferential flaws. Tabulation of length sizing bias and RMSE for PAUT techniques are provided in Table 5.33 and Table 5.34 for scoring tolerances of 10 mm and 15 mm, respectively. In this case, NOBS is equal to the number of detected circumferential flaws. Table 5.33 and Table 5.34 indicate no changes as a result of the increase in scoring tolerance from 10 mm to 15 mm, which is expected because the number of circumferential flaw detections is not impacted by the scoring tolerance change.

The aggregate length sizing regression plot is provided in Figure 5.46 and represents the length sizing regression curve for scoring tolerances of 10 mm and 15 mm.

Table 5.33. Summary of Length Sizing Error for PAUT Techniques for Circumferential Flaws (tolerance = 10 mm)

	NOBS	Bias	RMSE
108-PA1	4	0.5	9.0
126-PA1	4	3.8	6.3
108-PA1 + 126-PA1 (Blind)	8	2.1	7.8

Table 5.34. Summary of Length Sizing Error for PAUT Techniques for Circumferential Flaws (tolerance = 15 mm)

	NOBS	Bias	RMSE
108-PA1	4	0.5	9.0
126-PA1	4	3.8	6.3
108-PA1 + 126-PA1 (Blind)	8	2.1	7.8

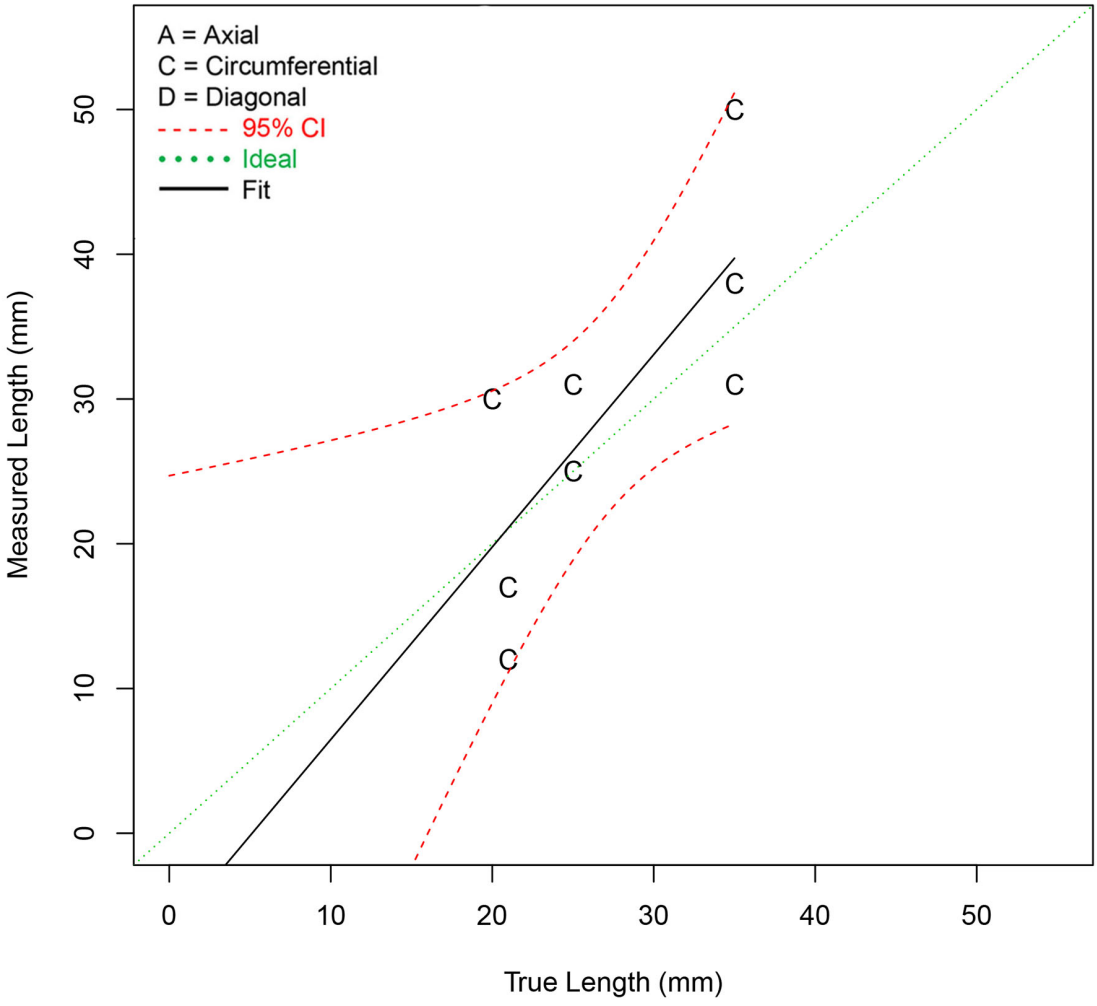

Figure 5.46. Aggregate Length Sizing Regression Fit for PAUT Techniques 108-PA1 and 126-PA1 for Circumferential Flaws (tolerance = 10 mm and 15 mm)

5.1.11.4 Summary of Length Sizing Analysis Results for Diagonal Flaws

This section presents the results of the length sizing performance analysis of PAUT techniques applied to the population of detected diagonal flaws. The algorithm for length sizing error analysis is normally performed by comparing the longest dimension of the flaw with the longest dimension of the associated indication. This algorithm is adequate for the majority of flaws, which have a clear axial or circumferential orientation. However, the Quickblind test blocks have flaws that were intended to be axially oriented but are reported to have a diagonal orientation based on destructive analysis, which indicated a flaw morphology with comparable axial and circumferential dimensions. In this case, it is of interest to perform length size error analysis by comparing the axial dimension of the flaw to the axial dimension of the associated indication, in addition to performing length sizing error analysis by comparing the largest flaw dimension to the largest dimension of the associated indication. In the tables and figures below, results are presented for standard length sizing error analysis, for axial dimension length sizing analysis, and for circumferential dimension length sizing analysis. Tabulation of length sizing bias and RMSE for PAUT techniques is provided in Table 5.35, Table 5.36, and Table 5.37 for standard length sizing analysis, axial dimension length sizing analysis, and circumferential dimension length sizing analysis, respectively. In this case, NOBS is equal to the number of detected diagonal flaws. Table 5.35 and Table 5.36 indicate that the length sizing error results based on the standard analysis and based on the axial dimension analysis are comparable. However, the results obtained in Table 5.37 for the circumferential dimension analysis are significantly different with much greater RMSE and a negative bias of large magnitude.

The aggregate length sizing regression plots are provided in Figure 5.47, Figure 5.48, and Figure 5.49 for standard length sizing analysis, axial dimension length sizing analysis, and circumferential dimension length sizing analysis, respectively. From these plots, it appears that the flaws produce responses that are indicative of axially oriented flaws as the reported measurements for circumferential dimensions are near zero. This indicates that although the destructive analysis of flaws in Quickblind test blocks revealed a flaw morphology with significant extent in both the axial and circumferential dimensions, the flaws respond to interrogation with PAUT techniques as axially oriented flaws.

Table 5.35. Summary of Length Sizing Error for PAUT Techniques for Diagonal Flaws (tolerance = 10 mm and 15 mm)

	NOBS	Bias	RMSE
108-PA0	2	−6.0	6.7
126-PA0	2	5.0	5.4
108-PA0 + 126-PA0 (Quickblind)	4	−0.5	6.1

Table 5.36. Summary of Axial Dimension Length Sizing Error for PAUT Techniques for Diagonal Flaws (tolerance = 10 mm and 15 mm)

	NOBS	Bias	RMSE
108-PA0	2	−3.5	3.5
126-PA0	2	7.5	8.7
108-PA0 + 126-PA0 (Quickblind)	4	2.0	6.7

Table 5.37. Summary of Circumferential Dimension Length Sizing Error for PAUT Techniques for Diagonal Flaws (tolerance = 10 mm and 15 mm)

	NOBS	Bias	RMSE
108-PA0	2	−14.5	15.9
126-PA0	2	−15.5	16.4
108-PA0 + 126-PA0 (Quickblind)	4	−15.0	16.2

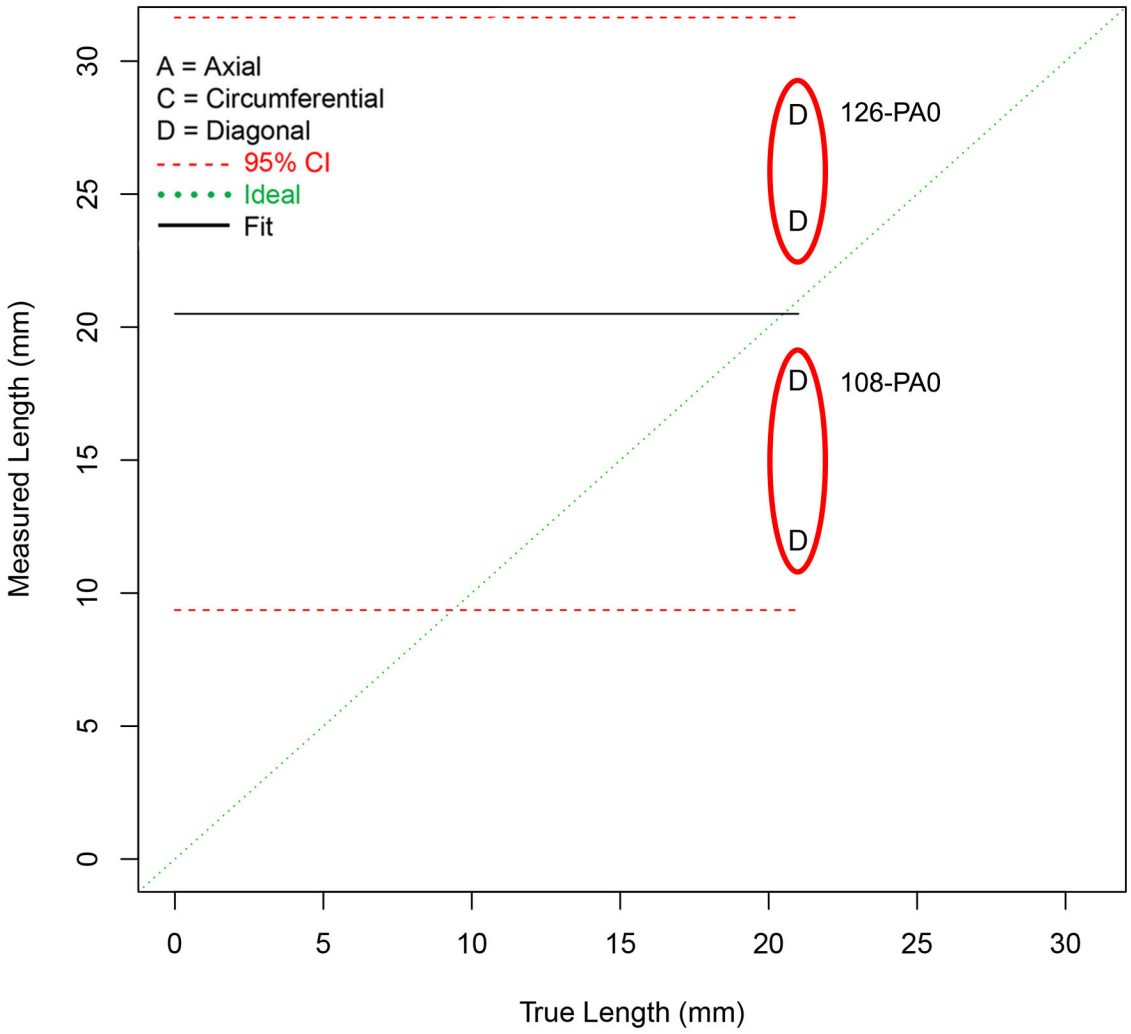

Figure 5.47. Aggregate Length Sizing Regression Fit for PAUT Techniques 108-PA0 and 126-PA0 for Diagonal Flaws (tolerance = 10 mm)

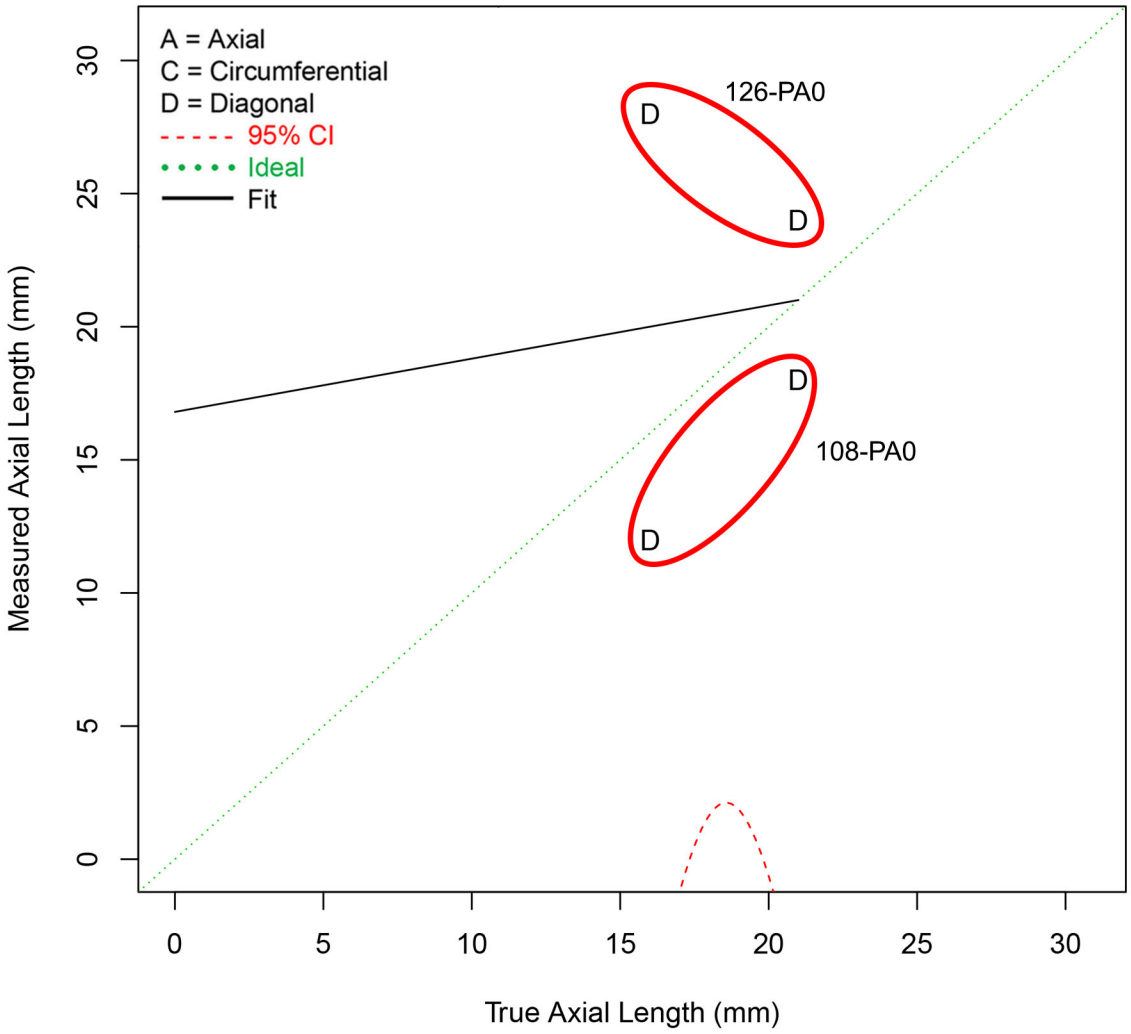

Figure 5.48. Aggregate Axial Dimension Length Sizing Regression Fit for PAUT Techniques 108-PA0 and 126-PA0 for Diagonal Flaws (tolerance = 10 mm)

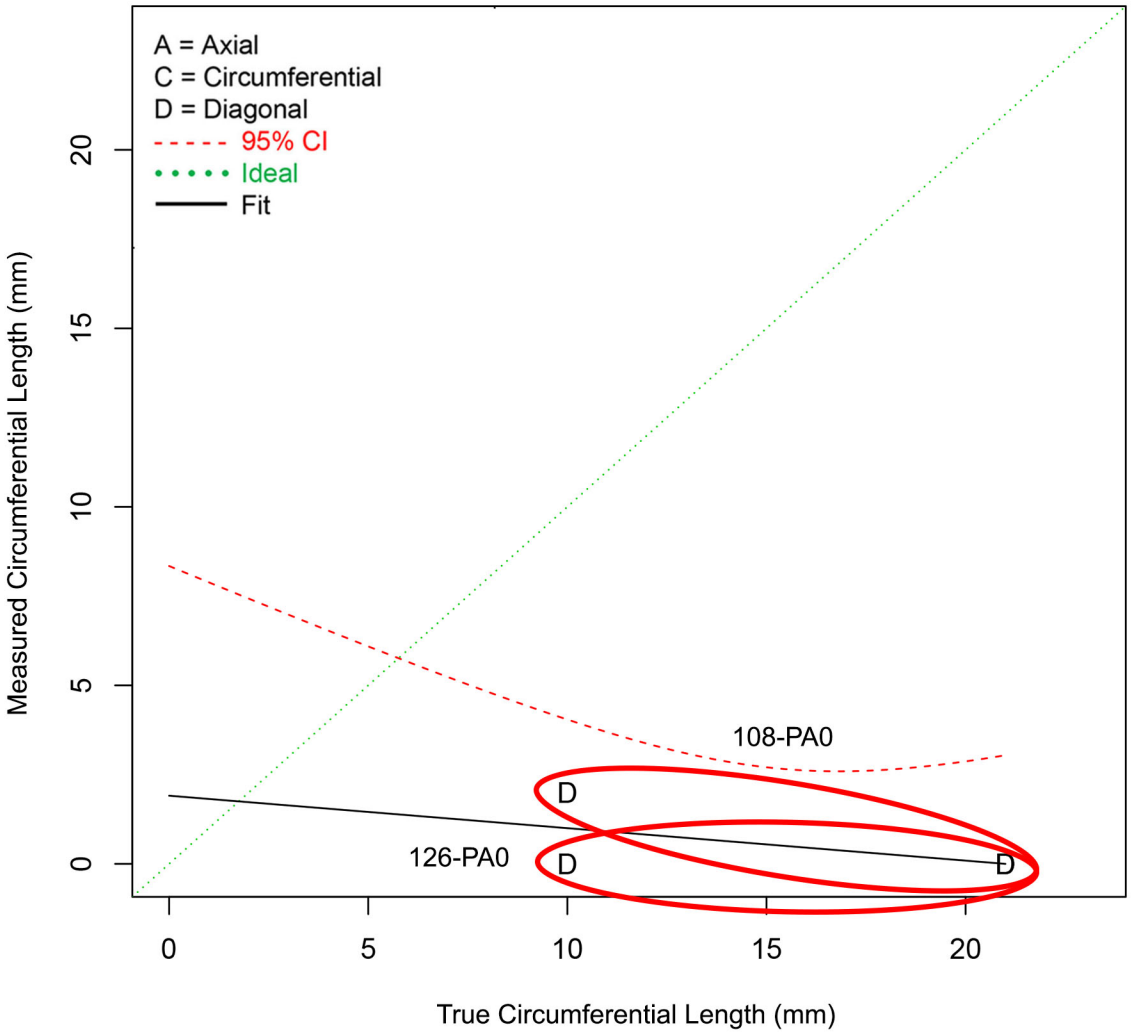

Figure 5.49. Aggregate Circumferential Dimension Length Sizing Regression Fit for PAUT Techniques 108-PA0 and 126-PA0 for Diagonal Flaws (tolerance = 10 mm)

5.2 Conventional UT Technique Analysis

Conventional UT technique analysis was performed in an attempt to enhance the amount of inspection data available for comparisons of results between inspections performed on Quickblind test blocks and inspections performed on test blocks in the regular portion of blind testing. This section includes a summary of some of the procedures in PARENT blind testing that incorporated conventional UT techniques and provides a review of the performance of procedures incorporating conventional UT techniques. This is followed by a summary of the inspections that are included in the conventional UT technique analysis, the results of detection performance analysis of conventional UT techniques, and the results of depth sizing and length sizing performance analysis of conventional UT techniques.

5.2.1 Summary of Conventional UT Techniques to be Analyzed

Table 5.38 summarizes procedures in PARENT blind testing incorporating conventional UT techniques. The six procedure IDs are UT.134.1, UT.PAUT.108, UT.PAUT.126, UT.108, UT.126, and UT.134.2.

Procedures UT.134.1, UT.PAUT.108, UT.PAUT.126 were incorporated in the Quickblind test and procedures UT.108, UT.134.2, and UT.126 were incorporated in the Blind test. General descriptions of these techniques are provided in Sections 3.2 and 3.3 of the PARENT Blind test report (Meyer and Heasler 2017). Summaries of individual procedures are provided in Appendix B of Meyer and Heasler (2017) with information obtained from procedure datasheets that were filled out by participating teams and which are included in Appendix C of Meyer and Heasler (2017).

5.2.1.1 Summary of UT.134.1

Procedure UT.134.1 consisted only of technique 134-UT0. Technique 134-UT0 was utilized for detection, characterization, length sizing, depth sizing, and positioning. The technique was manually scanned, not encoded, and accessed the component O.D. The technique was applied at a frequency of 1.5 MHz at longitudinal wave angles of 35° and 45° and at a frequency of 2.0 MHz at a longitudinal wave angle of 33°.

5.2.1.2 Summary of UT.PAUT.108

Procedure UT.PAUT.108 consisted of techniques 108-UT0 and 108-PA0. Both techniques were utilized for detection, characterization, length sizing, depth sizing, and positioning. In addition, both techniques were manually scanned, accessed the component O.D, and were not encoded. Technique 108-PA0 was applied at 2.0 MHz in a sectorial scan from 0° to 85°. Technique 108-UT0 was applied as linear scans at frequencies from 1.0 MHz to 2.0 MHz at the angles specified in Table 5.38.

5.2.1.3 Summary of UT.PAUT.126

Procedure UT.PAUT.126 consisted of techniques 126-UT0 and 126-PA0. Both techniques were utilized for detection, characterization, length sizing, depth sizing, and positioning. In addition, both techniques were manually scanned and accessed the component O.D. Technique 126-PA0 was encoded and technique 126-UT0 was not encoded. Both techniques were applied as linear scans at angles specified in Table 5.38. Technique 126-PA0 was applied at a frequency of 1.5 MHz and technique 126-UT0 was applied at a frequency of 2.0 MHz.

5.2.1.4 Summary of UT.108

Procedure UT.108 consisted only of technique 108-UT1. Technique 108-UT1 was utilized for detection, characterization, length sizing, depth sizing, and positioning. The technique was manually scanned, not encoded, and accessed the component O.D. The technique was applied at frequencies of 1.5 MHz and 2.0 MHz at longitudinal mode angles of 30°, 45°, and 60°.

5.2.1.5 Summary of UT.126

Procedure UT.126 consisted only of technique 126-UT1. Technique 126-UT1 was utilized for detection, characterization, length sizing, depth sizing, and positioning. The technique was manually scanned, not encoded, and accessed the component O.D. The technique was applied in base metal at frequencies of 1.0 to 1.5 MHz and at a shear mode angle of 45°. It was applied in weld or butter material at frequencies of 1.0 to 2.0 MHz at longitudinal mode angles of 30°, 45°, and 60°.

5.2.1.6 Summary of UT.134.2

Procedure UT.134.2 consisted only of technique 134-UT1. Technique 134-UT1 was utilized for detection, characterization, length sizing, depth sizing, and positioning. The technique was manually scanned, not encoded, and accessed the component O.D. The technique was applied at frequencies of 1.0 to 5.0 MHz and at longitudinal mode angles of 35°, 45°, 60°, and 70°.

Table 5.38. Summary of Procedures Incorporating Conventional UT Techniques

Procedure ID	Technique ID	Manual or Automated	Encoded (Y/N)	Exam Surface	Probe Frequency (MHz)/Inspection Angle (Deg.)	Technique Comment
UT.134.1	134-UT0	Manual	N	O.D.	1.5 MHz/L35° 1.5 MHz/L45° 2.0 MHz/L33°	Detection, characterization, length, depth, positioning
UT.PAUT.126	126-UT0	Manual	N	O.D.	2.0 MHz/L45° 2.0 MHz/L60°	Detection, characterization, length, depth, positioning
	126-PA0	Manual	Y	O.D.	Circ. Scan 1.5 MHz/L25° 1.5 MHz/L35° 1.5 MHz/L45° 1.5 MHz/L55°	Detection, characterization, length, depth, positioning
UT.PAUT.108	108-UT0	Manual	N	O.D.	1.0 MHz/L45° 1.0 MHz/L60° 1.5 MHz/L35° 1.5 MHz/L45° 2.0 MHz/L33° 2.0 MHz/L45	Detection, characterization, length, depth, positioning
	108-PA0	Manual	N	O.D.	2.0 MHz/L0°~L85°	Detection, characterization, length, depth, positioning
UT.108	108-UT1	Manual	N	O.D.	1.5 MHz/L30° 1.5 MHz/L45° 1.5 MHz/L60° 2.0 MHz/L30° 2.0 MHz/L45° 2.0 MHz/L60°	Detection, characterization, length, depth, positioning
UT.134.2	134-UT1	Manual	N	O.D.	1~5 MHz L35°, L45°, L60°, L70° CW/CCW scan for circ. flaws Raster scan for axial flaws	Detection, characterization, length, depth, positioning

Procedure ID	Technique ID	Manual or Automated	Encoded (Y/N)	Exam Surface	Probe Frequency (MHz)/Inspection Angle (Deg.)	Technique Comment
UT.126	126-UT1	Manual	N	O.D.	1~1.5 MHz/S45° base metal 1~2.25 MHz/L30°, L45°, L60° weld or butter material CW/CCW scan for circ. flaws Raster scan for axial flaws	Detection, characterization, length, depth, positioning

5.2.2 Review of Conventional UT Performance in PARENT Blind Testing

This section provides a review of performance data for procedures that incorporated conventional UT techniques in PARENT blind testing. This review is provided so that results of analysis of performance of conventional UT techniques can be conveniently compared to the results obtained from these procedures. A summary of the overall detection and false call performance for procedures incorporating conventional UT techniques on LBDMW test blocks with O.D. access in PARENT blind testing is provided in Table 5.39. The procedures implemented in the Quickblind study (UT.PAUT.108, UT.PAUT.126, and UT.134.1) detected all flaws, while the procedures implemented in the regular portion of blind testing (UT.108, UT.126, and UT.134.2) exhibited lower PODs.

POD as a function of flaw depth is summarized in Table 5.40. This table includes data for each of the procedures in Table 5.38, as well as aggregate POD data. Table 5.41 provides a summary of POD versus flaw length for each procedure in Table 5.38 and aggregate POD results for procedures implemented in the blind and Quickblind studies, respectively. Finally, summaries of sizing analyses results are provided in Table 5.42 and Table 5.43 for depth sizing error and length sizing error, respectively.

Table 5.39. Summary of Overall Detection and False Call Performance for Procedures Incorporating Conventional UT Techniques on LBDMW Test Blocks with O.D. Access in PARENT Blind Testing

	NOBS	POD, %	FCP, %	FCR, #/m	Access	LBDMW
UT.108	19	62	2	0.8	O.D.	P13, P33
UT.126	19	34	6	2.3	O.D.	P13, P33
UT.134.1 (Quickblind)	3	100	0	0.0	O.D.	P15, P16, P17, P45
UT.134.2	19	66	4	1.7	O.D.	P13, P33
UT.PAUT.108 (Quickblind)	3	100	0	0.0	O.D.	P15, P16, P17, P45
UT.PAUT.126 (Quickblind)	3	100	7	2.9	O.D.	P15, P16, P17, P45

UT = conventional UT

Table 5.40. Probability of Detection versus Depth for Procedures Incorporating Conventional UT Techniques on LBDMW Test Blocks with O.D. Access in PARENT Blind Testing

	NOBS	0 mm	5 mm	10 mm	15 mm	30 mm
UT.108	19	3	8	16	30	79
UT.126	19	7	11	15	20	40
UT.134.2	19	6	14	28	49	91
UT.134.1 (Quickblind)	3	2	10	35	73	93
UT.PAUT.108 (Quickblind)	3	2	8	25	55	97
UT.PAUT.126 (Quickblind)	3	9	20	39	61	94
UT.108 + UT.126 + UT.134.2	57	5	10	19	32	74
UT.108 + UT.126 + UT.134.2 + UT.134.1 (Blind + Quickblind)	60	5	10	19	34	79
UT.PAUT.108 + UT.PAUT.126 (Quickblind)	6	5	19	49	80	99

UT = conventional UT

Table 5.41. Probability of Detection versus Length for Procedures Incorporating Conventional UT Techniques on LBDMW Test Blocks with O.D. Access in PARENT Blind Testing

	NOBS	0 mm	5 mm	10 mm	15 mm	30 mm
UT.108	19	2	5	11	23	80
UT.126	19	7	9	13	18	39
UT.134.2	19	6	11	20	33	80
UT.134.1 (Quickblind)	3	1	3	12	35	95
UT.PAUT.108 (Quickblind)	3	1	4	12	31	94
UT.PAUT.126 (Quickblind)	3	8	16	30	48	91
UT.108 + UT.126 + UT.134.2	57	5	8	15	25	70
UT.108 + UT.126 + UT.134.2 + UT.134.1 (Blind + Quickblind)	60	4	8	14	26	75
UT.PAUT.108 + UT.PAUT.126 (Quickblind)	6	4	12	29	55	97

UT = conventional UT

Table 5.42. Depth Sizing Results Summary for Procedures Incorporating Conventional UT Techniques on LBDMW Test Blocks with O.D. Access in PARENT Blind Testing

	NOBS	Bias, mm	RMSE, mm
UT.108	4	−0.3	9.0
UT.126	4	0.6	6.8
UT.134.2	8	−8.9	11.4
UT.134.1 (Quickblind)	3	−6.2	11.3
UT.PAUT.108 (Quickblind)	3	−9.1	11.4
UT.PAUT.126 (Quickblind)	3	−3.5	6.2
UT.108 + UT.126 + UT.134.2	16	−4.4	9.8
UT.108 + UT.126 + UT.134.2 + UT.134.1 (Blind + Quickblind)	19	−4.7	9.9
UT.PAUT.108 + UT.PAUT.126 (Quickblind)	6	−6.3	9.2

UT = conventional UT

Table 5.43. Length Sizing Results Summary for Procedures Incorporating Conventional UT Techniques on LBDMW Test Blocks with O.D. Access in PARENT Blind Testing

	NOBS	Bias, mm	RMSE, mm
UT.108	4	4.9	8.1
UT.126	4	12.3	17.1
UT.134.2	8	6.8	20.0
UT.134.1 (Quickblind)	3	6.6	8.2
UT.PAUT.108 (Quickblind)	3	−9.0	11.1
UT.PAUT.126 (Quickblind)	3	−0.7	6.4
UT.108 + UT.126 + UT.134.2	18	6.9	15.9
UT.108 + UT.126 + UT.134.2 + UT.134.1 (Blind + Quickblind)	21	4.7	15.4
UT.PAUT.108 + UT.PAUT.126 (Quickblind)	6	−4.2	9.0

UT = conventional UT

5.2.3 Conventional UT Inspections of Test Block P33

Figure 5.50 shows indication plots for procedure UT.108 and technique 108-UT1 examination of test block P33. The only technique applied in procedure UT.108 was technique 108-UT1 so their results are represented by the same indication plots. Figure 5.50 shows that 9 of 18 flaws were missed by procedure UT.108 and technique 108-UT1 and that only 1 of 2 subsurface flaws were detected. Also, Figure 5.50 indicates some positioning error for axial flaws that resulted in indications 02 and 07 being recorded outside of the tolerance boundary for nearby flaws. These are marked with the label “Probable Detection.” As a consequence, detection and sizing analysis is performed with a tolerance of 10 mm and a tolerance of 15 mm, respectively.

Figure 5.51 shows indication plots for procedure UT.126 and technique 126-UT1 examinations of test block P33. The only technique applied in procedure UT.126 was technique 126-UT1 so their results are represented by the same indication plots. Figure 5.51 shows that 14 of 18 flaws were missed by procedure UT.126 and technique 126-UT1 and that both of the subsurface flaws were detected. Also, Figure 5.51 indicates that there were five false calls and large length sizing error associated with indication 08.

Figure 5.52 shows indication plots for procedure UT.134.2 and technique 134-UT1 examinations of test block P33. The only technique applied in procedure UT.134.2 was technique 134-UT1 so their results are represented by the same indication plots. Figure 5.52 shows that 10 of 18 flaws were missed by procedure UT.134.2 and technique 134-UT1 and that both of the subsurface flaws were missed. Also, Figure 5.52 indicates that there were four false calls.

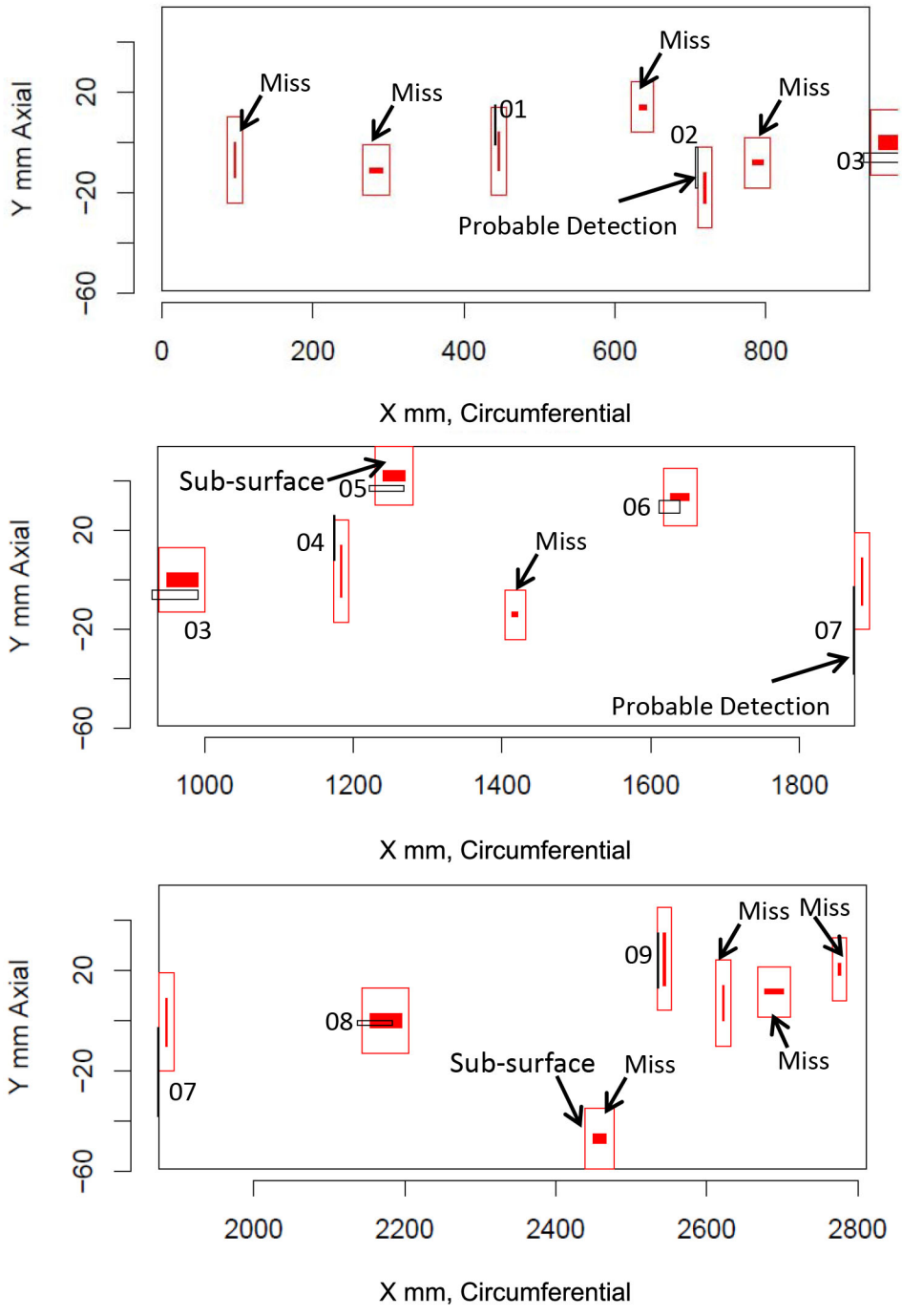

Figure 5.50. Indication Plot for Procedure UT.108 and Technique 108-UT1 Applied to Test Block P33 in PARENT Blind Testing (X–Y view)

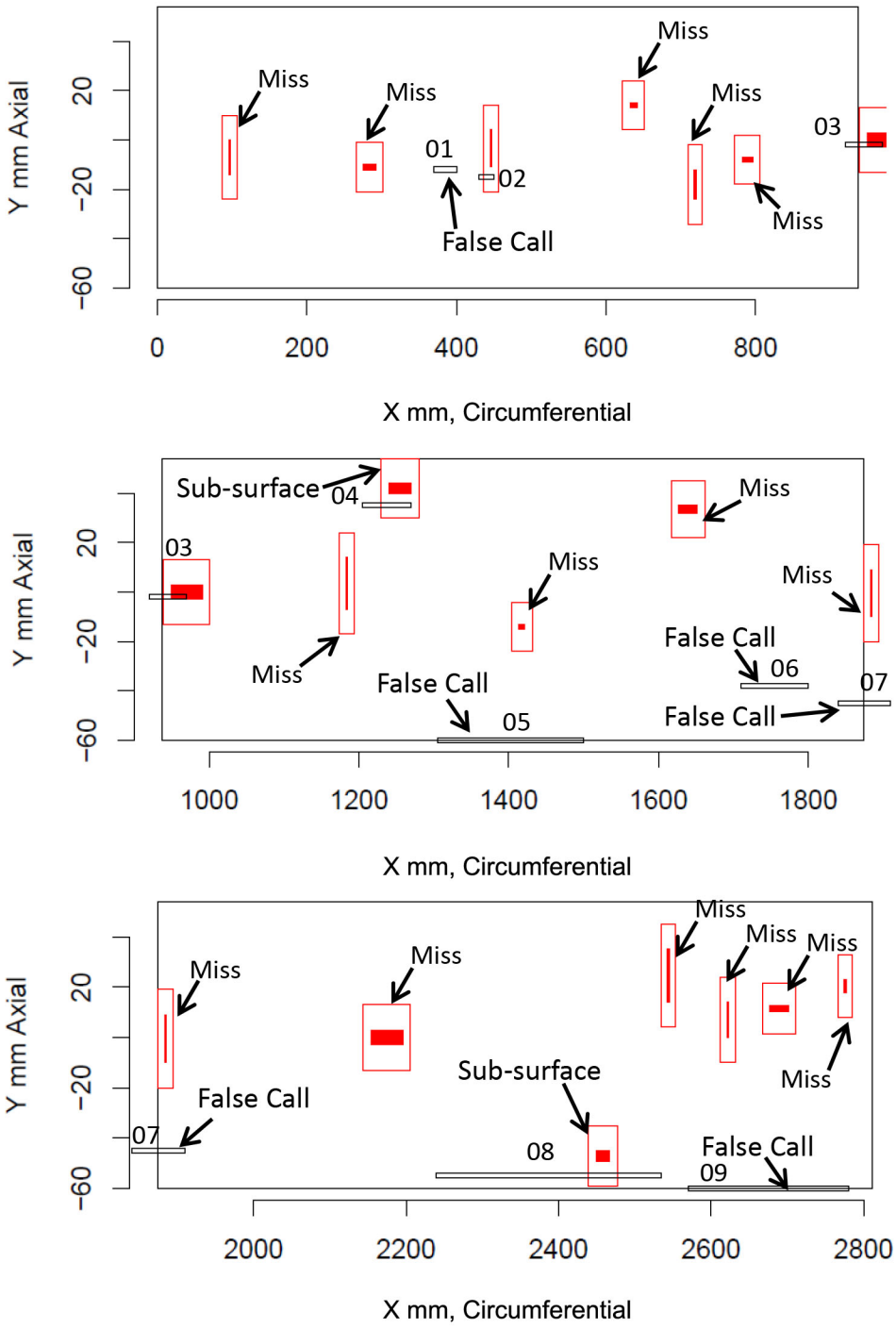

Figure 5.51. Indication Plot for Procedure UT.126 and Technique 126-UT1 Applied to Test Block P33 in PARENT Blind Testing (X–Y view)

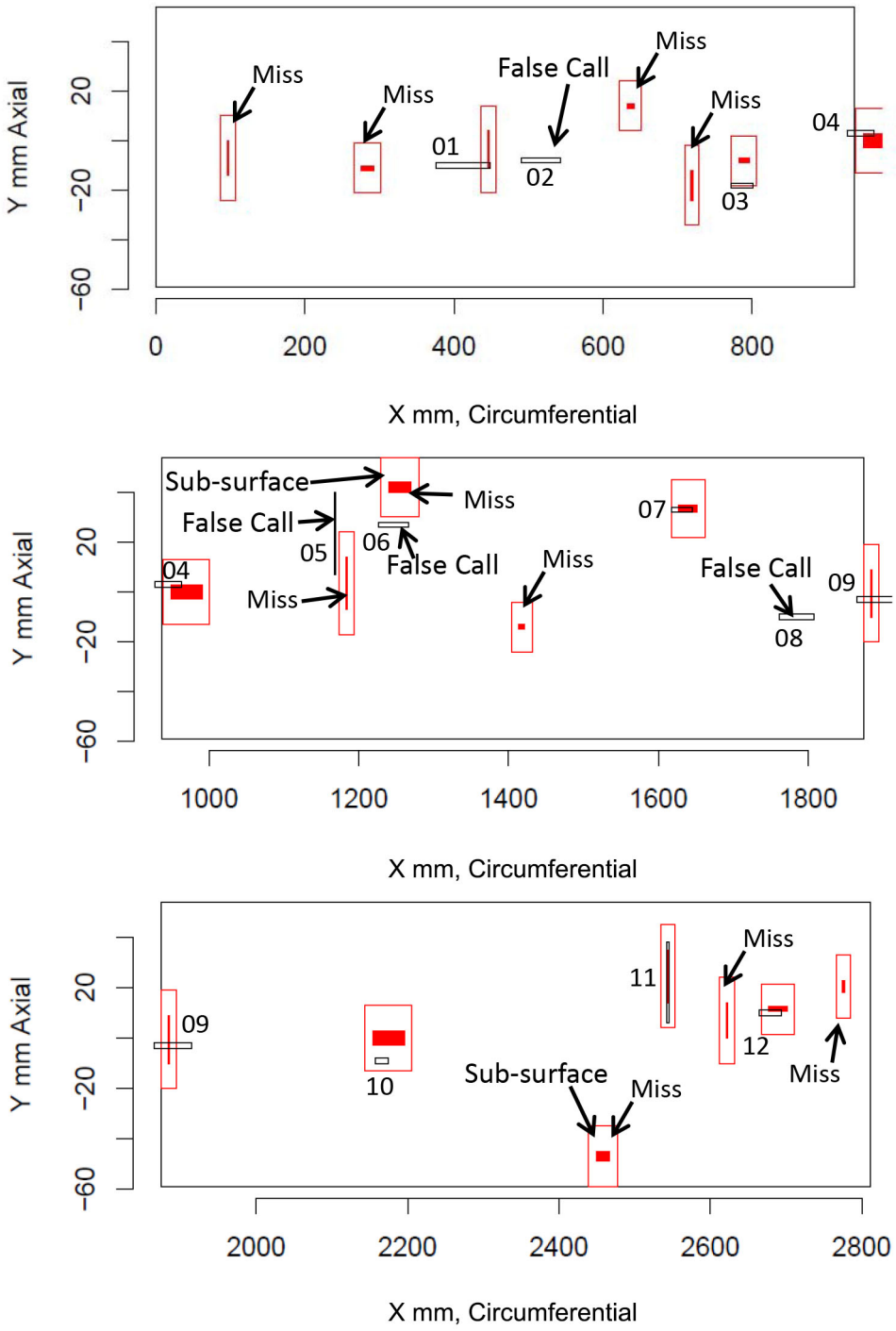

Figure 5.52. Indication Plot for Procedure UT.134.2 and Technique 134-UT1 Applied to Test Block P33 in PARENT Blind Testing (X–Y view)

5.2.4 Conventional UT Inspections of Test Block P13

Figure 5.53, Figure 5.54, and Figure 5.55 show indication plots for procedure UT.108 and technique 108-UT1, for procedure UT.126 and technique 126-UT1, and for procedure UT.134.2 and technique 134-UT1, respectively, for examinations of test block P13, which contained one flaw. Figure 5.53 and Figure 5.54 show that the flaw was not detected by procedure UT.108, technique 108-UT1, procedure UT.126, or technique 126-UT1. Further, Figure 5.54 shows that procedure UT.126 and technique 126-UT1 reported two false calls in P13. Figure 5.55 shows that the flaw was detected by procedure UT.134.2 and technique 134-UT1, but a false call was also reported.

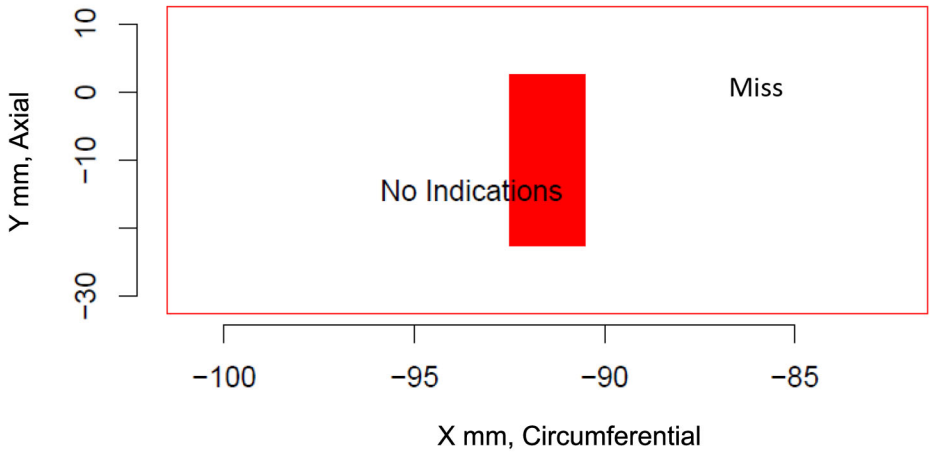

Figure 5.53. Indication Plot for Procedure UT.108 and Technique 108-UT1 Applied to Test Block P13 in PARENT Blind Testing (X–Y view)

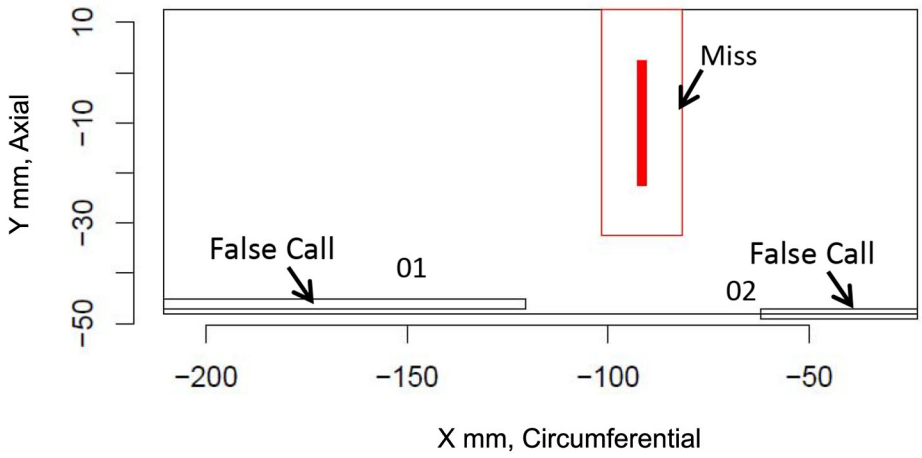

Figure 5.54. Indication Plot for Procedure UT.126 and Technique 126-UT1 Applied to Test Block P13 in PARENT Blind Testing (X–Y view)

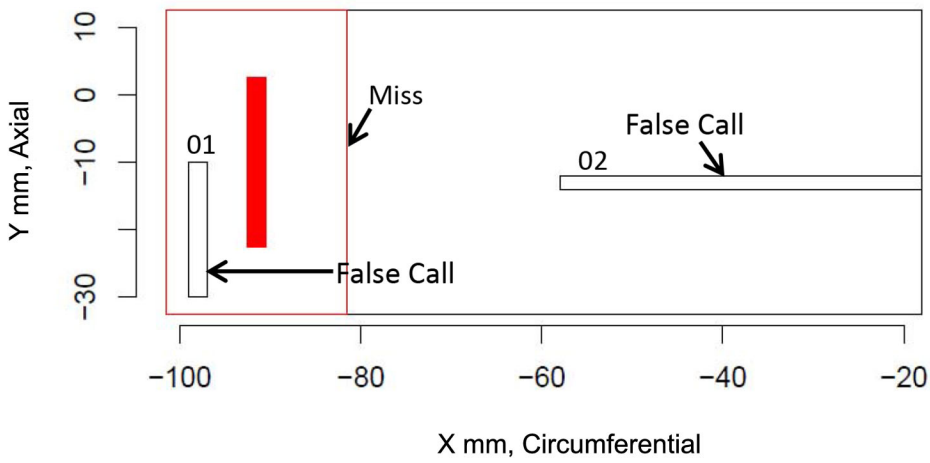

Figure 5.55. Indication Plot for Procedure UT.134.2 and Technique 134-UT1 Applied to Test Block P13 in PARENT Blind Testing (X–Y view)

5.2.5 Conventional UT Inspections of Test Block P15 (Quickblind)

Figure 5.56, Figure 5.57, and Figure 5.58 show indication plots for technique 108-UT0, for technique 126-UT0, and for procedure UT.134.1 and technique 134-UT0, respectively, for examinations of Quickblind test block P15 which contained one flaw. Figure 5.5 shows the indication plot for procedure UT.PAUT.108 and technique 108-PA0 and Figure 5.6 shows the indication plot for procedure UT.PAUT.126 and technique 126-PA0. Figure 5.5 and Figure 5.6 show that the flaw was detected by procedure UT.PAUT.108, technique 108-PA0, procedure UT.PAUT.126, and technique 126-PA0. Figure 5.56 shows that the flaw was detected by technique 108-UT0 while Figure 5.57 shows that the flaw was missed by technique 126-UT0. Further, Figure 5.57 shows that technique 126-UT0 reported a false call. Finally, Figure 5.58 shows that the flaw was detected by procedure UT.134.1 and technique 134-UT0.

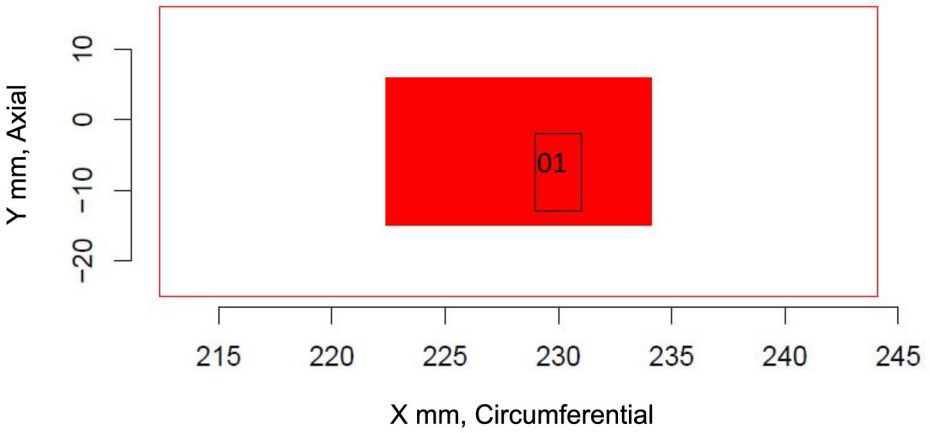

Figure 5.56. Indication Plot for Technique 108-UT0 Applied to Quickblind Test Block P15 in PARENT Blind Testing (X–Y view)

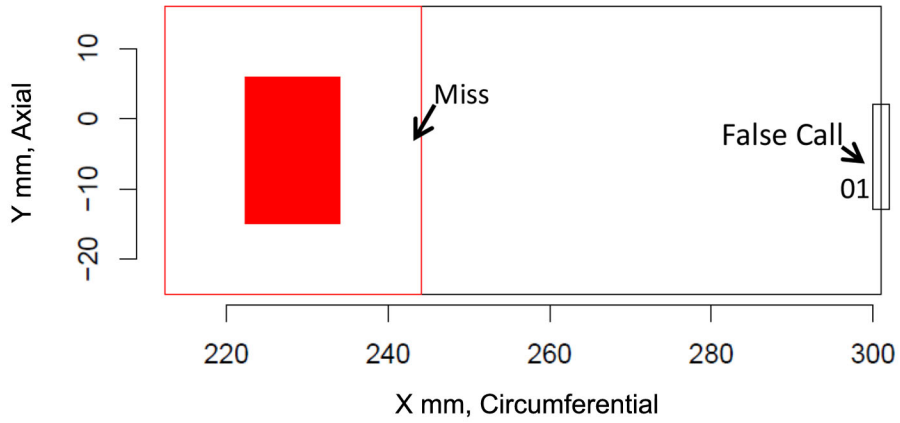

Figure 5.57. Indication Plot for Technique 126-UT0 Applied to Quickblind Test Block P15 in PARENT Blind Testing (X–Y view)

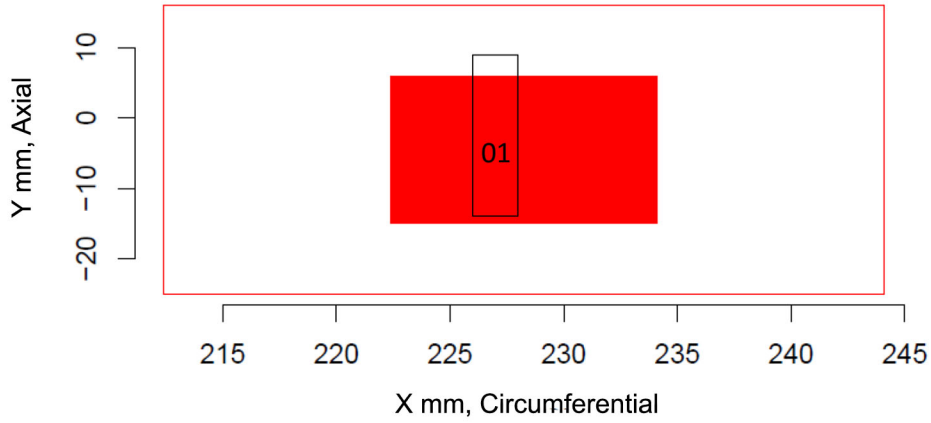

Figure 5.58. Indication Plot for Procedure UT.134.1and Technique 134-UT0 Applied to Quickblind Test Block P15 in PARENT Blind Testing (X–Y view)

5.2.6 Conventional UT Inspections of Test Block P16 (Quickblind)

Figure 5.59, Figure 5.60, and Figure 5.61 show indication plots for technique 108-UT0, for technique 126-UT0, and for procedure UT.134.1 and technique 134-UT0, respectively, for examinations of Quickblind test block P16, which contained one flaw. Figure 5.7 shows the indication plot for procedure UT.PAUT.108, Figure 5.8 shows the indication plot technique 108-PA0, and Figure 5.9 shows the indication plot for procedure UT.PAUT.126 and technique 126-PA0. Figure 5.7, Figure 5.8, and Figure 5.9 show that the flaw was detected by procedure UT.PAUT.108, technique 108-PA0, procedure UT.PAUT.126, and technique 126-PA0. Figure 5.59 and Figure 5.60 show that the flaw was also detected by techniques 108-UT0 and 126-UT0; however, Figure 5.9 and Figure 5.60 also show that a false call was reported for procedure UT.PAUT.126, technique 126-PA0, and technique 126-UT0. Finally, Figure 5.61 shows that the flaw was detected by procedure UT.134.1 and technique 134-UT0.

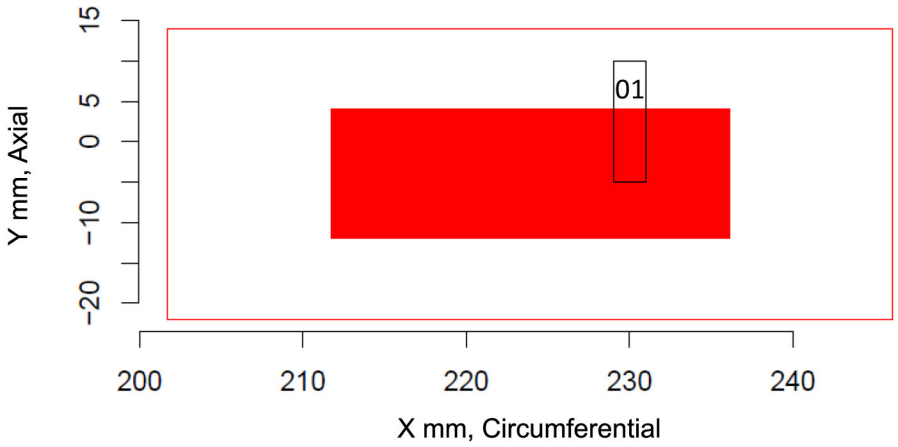

Figure 5.59. Indication Plot for Technique 108-UT0 Applied to Quickblind Test Block P16 in PARENT Blind Testing (X–Y view)

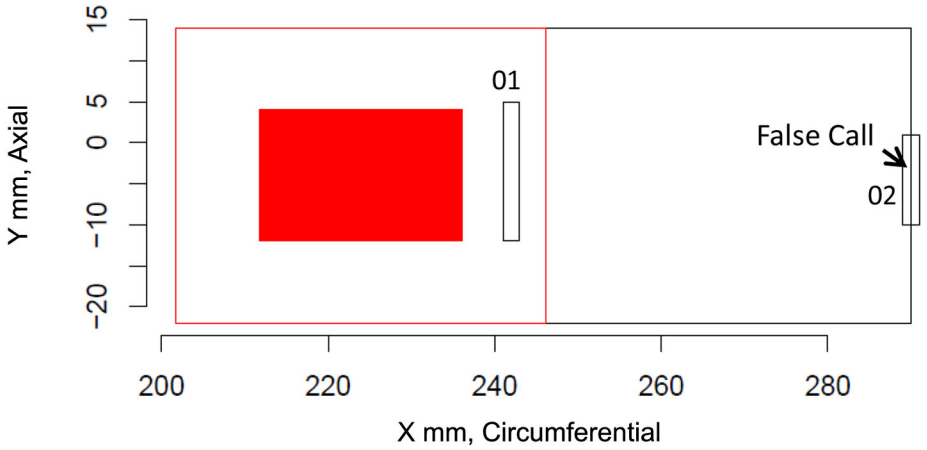

Figure 5.60. Indication Plot for Technique 126-UT0 Applied to Quickblind Test Block P16 in PARENT Blind Testing (X–Y view)

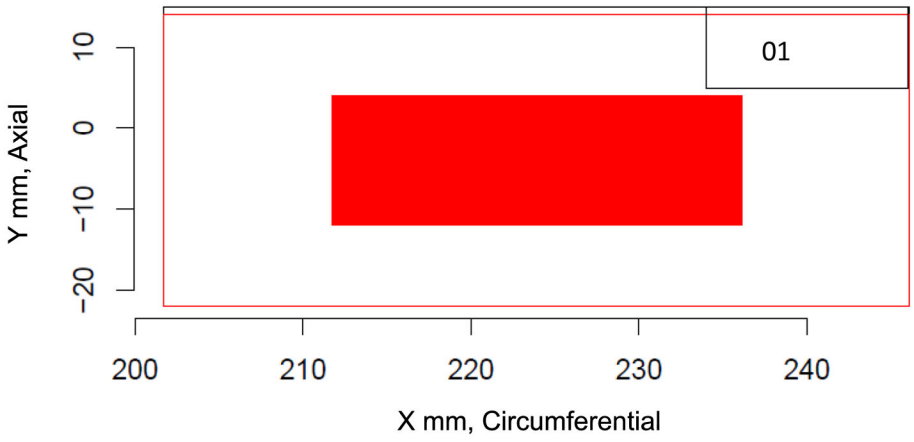

Figure 5.61. Indication Plot for Procedure UT.134.1 and Technique 134-UT0 Applied to Quickblind Test Block P16 in PARENT Blind Testing (X–Y view)

5.2.7 Conventional UT Inspections of Test Block P17 (Quickblind)

Figure 5.62, Figure 5.63, and Figure 5.64 show indication plots for technique 108-UT0, for technique 126-UT0, and for procedure UT.134.1 and technique 134-UT0, respectively, for examinations of Quickblind test block P17, which contained one flaw. Figure 5.10 shows the indication plot for procedure UT.PAUT.108, Figure 5.11 shows the indication plot technique 108-PA0, and Figure 5.12 shows the indication plot for procedure UT.PAUT.126 and technique 126-PA0. Figure 5.10 and Figure 5.11 show that the flaw was detected by procedure UT.PAUT.108 but not by technique 108-PA0. Figure 5.12 shows that the flaw was detected by procedure UT.PAUT.126 and technique 126-PA0; however, a false call was also reported. Figure 5.62 and Figure 5.63 show that the flaw was detected by techniques 108-UT0 and 126-UT0, but a false call was also reported for technique 126-UT0. Finally, Figure 5.64 shows that the flaw was detected by procedure UT.134.1 and technique 134-UT0.

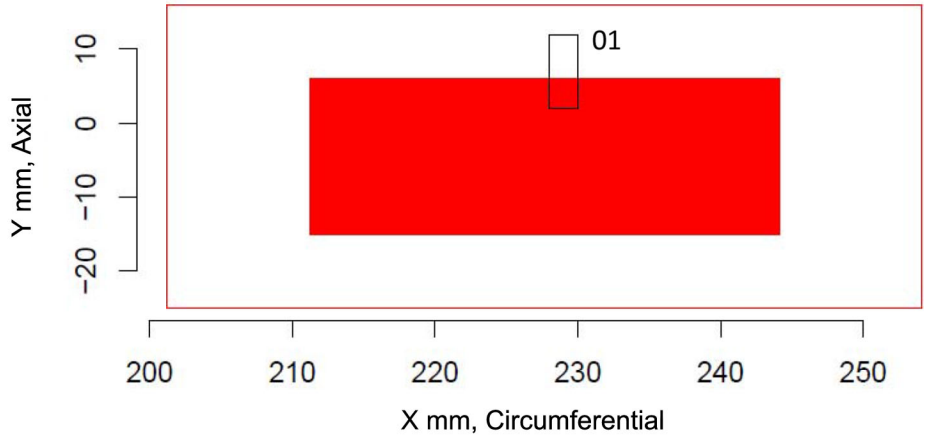

Figure 5.62. Indication Plot for Technique 108-UT0 Applied to Quickblind Test Block P17 in PARENT Blind Testing (X–Y view)

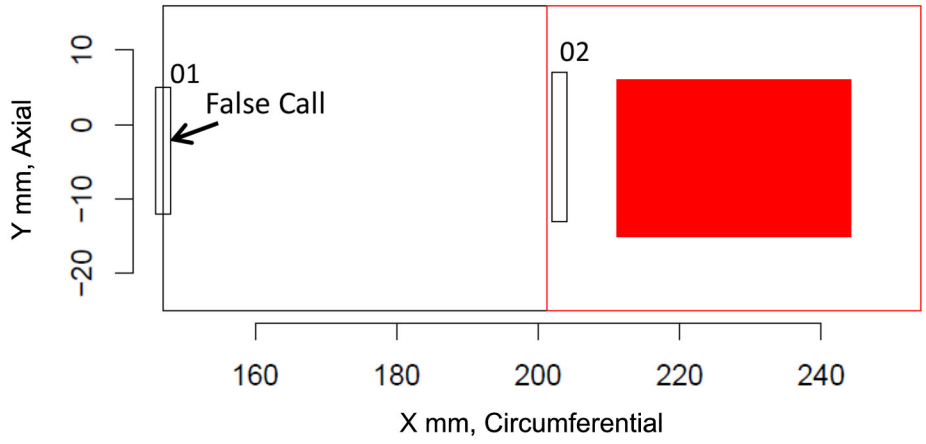

Figure 5.63. Indication Plot for Technique 126-UT0 Applied to Quickblind Test Block P17 in PARENT Blind Testing (X–Y view)

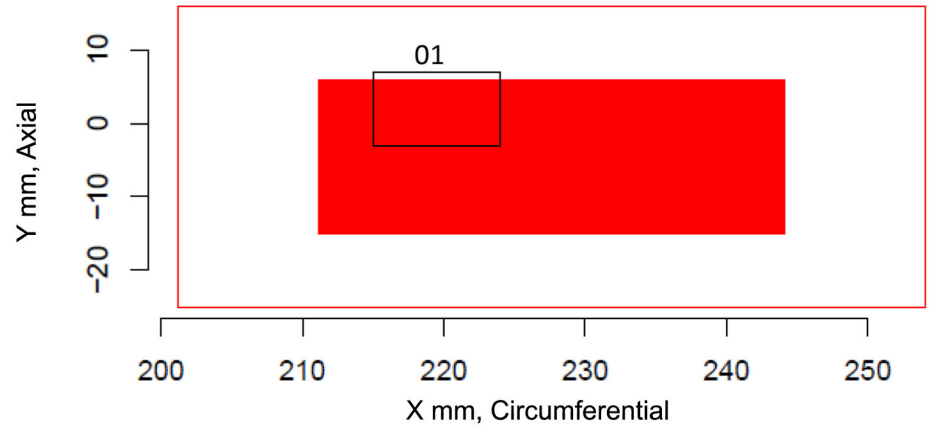

Figure 5.64. Indication Plot for Procedure UT.134.1 and Technique 134-UT0 Applied to Quickblind Test Block P17 in PARENT Blind Testing (X–Y view)

5.2.8 Conventional UT Inspections of Test Block P45 (Quickblind)

Figure 5.65, Figure 5.66, and Figure 5.67 show indication plots for technique 108-UT0, for technique 126-UT0, and for procedure UT.134.1 and technique 134-UT0, respectively, for examinations of Quickblind test block P45 which did not contain any flaws. Figure 5.13 shows the indication plot for procedure UT.PAUT.108 and technique 108-PA0 and Figure 5.14 shows the indication plot for procedure UT.PAUT.126 and technique 126-PA0. Figure 5.13 shows that no indications were reported for procedure UT.PAUT.108 and technique 108-PA0. However, Figure 5.14 shows that two false calls were reported for UT.PAUT.126 and technique 126-PA0. Figure 5.65 shows that no indications were reported for technique 108-UT0 while Figure 5.66 shows that two false calls were reported for 126-UT0. Finally, Figure 5.67 shows that no indications were reported for procedure UT.134.1 and technique 134-UT0.

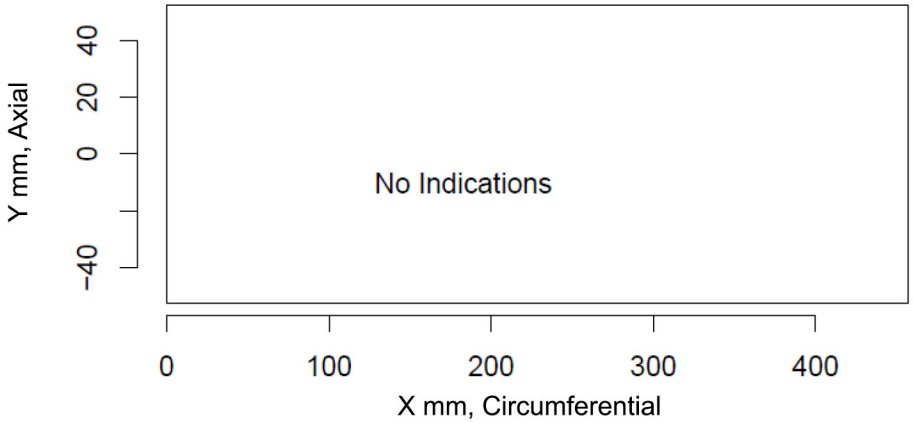

Figure 5.65. Indication Plot for Technique 108-UT0 and Technique 108-PA0 Applied to Quickblind Test Block P45 in PARENT Blind Testing (X–Y view)

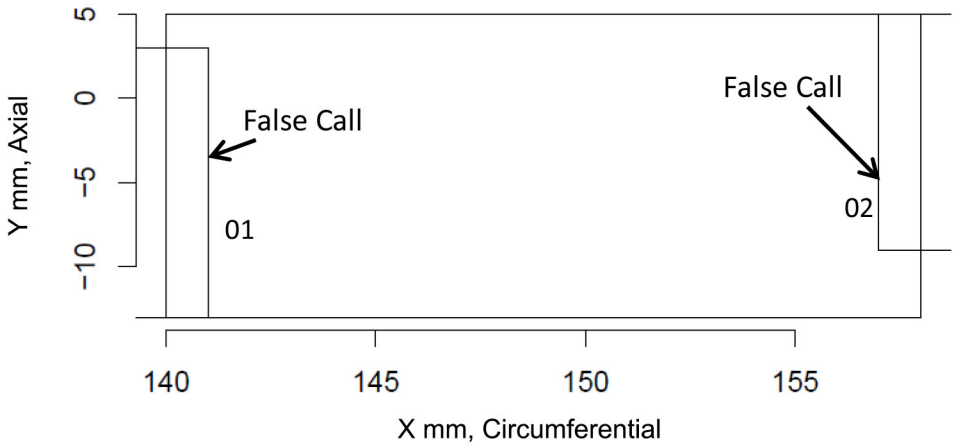

Figure 5.66. Indication Plot for Technique 126-UT0 Applied to Quickblind Test Block P45 in PARENT Blind Testing (X–Y view)

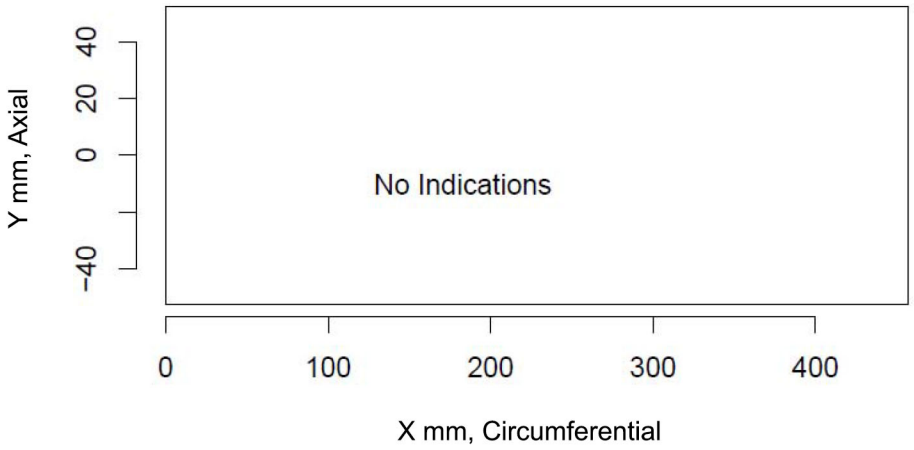

Figure 5.67. Indication Plot for Procedure UT.134.1and Technique 134-UT0 Applied to Quickblind Test Block P45 in PARENT Blind Testing (X–Y view)

5.2.9 Detection Performance Analysis

This section presents the results of the detection performance analysis of conventional UT techniques applied to the O.D. surface of LBDMW test blocks in PARENT. Results are presented as tables of POD at several discrete flaw sizes (depth and length) and as plots of POD curves as a function of flaw size. The tables also include tabulation of the FCR. The following section includes a tabulated summary of overall detection performance for conventional UT techniques for scoring tolerances of 10 mm and 15 mm to account for the positioning error observed for axial flaws in test block P33. This summary is followed by sections presenting the detection performance results obtained from the total flaw population, the axial flaw population, and the circumferential flaw population as a function of depth and length. In these sections, results are also presented for scoring tolerances of 10 mm and 15 mm.

5.2.9.1 Overall Detection Analysis Results

This section provides tabulated summaries of the overall detection performance of conventional UT techniques in PARENT for scoring tolerances of 10 mm (Table 5.44) and 15 mm (Table 5.45). In these tables, NOBS for overall detection performance refers to the total number of flaws in the inspected test blocks. POD in these tables is not expressed as a function of any parameter, but is simply the overall POD obtained by dividing the detected flaws by NOBS. The FCR is the number of observed false calls per unit length. The FCP is calculated from Eq. (3.6) (Section 3.3).

The impact of increasing the tolerance from 10 mm and 15 mm on the detection performance of 108-UT1 is evident in Table 5.44 and Table 5.45. These tables reveal that the overall POD increases from 37% to 47%, and the FCR and FCP experience reductions as the tolerance is increased from 10 mm to 15 mm.

Table 5.44. Overall Detection Performance by Conventional UT Techniques Applied to the O.D. Surface of LBDMW Blocks with a Tolerance = 10 mm

	NOBS	POD, %	FCP, %	FCR, #/m
108-UT0	3	100	0	0.0
108-UT1	19	37	2	0.8
126-UT0	3	67	8	3.5
126-UT1	19	21	6	2.6
134-UT0	3	100	0	0.0
134-UT1	19	42	5	2.3
All	66	41	4	1.6

Table 5.45. Overall Detection Performance by Conventional UT Techniques applied to the O.D. Surface of LBDMW Blocks with a Tolerance = 15 mm

	NOBS	POD, %	FCP, %	FCR, #/m
108-UT0	3	100	0	0.0
108-UT1	19	47	0	0.0
126-UT0	3	67	8	3.5
126-UT1	19	21	7	2.7
134-UT0	3	100	0	0.0
134-UT1	19	42	6	2.3
All	66	44	4	1.4

5.2.9.2 Summary of Detection Analysis Results for All Flaws

This section presents the detection performance results obtained from the total flaw population as POD versus depth and length. A logistic regression model was used to relate POD to flaw size, S. Flaw size represents either depth or length. The logistic regression model is defined by Eqs. and (Section 4.9.2). Estimates produced by the algorithm are maximum-likelihood estimates. Detection performance is presented in a tabular format with POD values provided at discrete flaw sizes (i.e., at 0 mm, 5 mm, 10 mm, 15 mm, etc.). The values of POD at these discrete flaw sizes are the values estimated by the logistic regression model expressed by Eqs. and . In tabulated summaries, NOBS refers to the total number of flaws in the test blocks inspected by a given technique. The value of POD at 0 mm [POD(0)] is

the value of the regression fit at S = 0 mm. The value of the regression fit at 0 mm is influenced by the measured FCP, which is calculated from the FCR by Eq.(3.6).

Summary of Detection Performance as a Function of Flaw Depth

This section summarizes detection performance results obtained from the total flaw population as POD versus depth. Table 5.46 and Table 5.47 provide the POD values at discrete flaw sizes (i.e., at 0 mm, 5 mm, 10 mm, 15 mm, 30 mm, and 60 mm) for scoring tolerances of 10 mm and 15 mm, respectively. A column for NOBS and FCR is also included in the tables. Comparison of Table 5.46 and Table 5.47 illustrate how aggregate detection performance (i.e., for 108-UT1 + 126-UT1 + 134-UT1 [Blind], and for 108-UT0 + 126-UT0 + 134-UT0 + 108-UT1 + 126-UT1 + 134-UT1 [Blind + Quickblind]) and detection performance for 108-UT1 is impacted by the increase in tolerance from 10 mm to 15 mm. As the tables show, the increase in scoring tolerance results in a decrease in the FCR, which is anticipated considering the positioning error that results in misses of axial flaws for a scoring tolerance of 10 mm. Further, a modest increase in the POD is observed, especially for flaw depths of 10 mm and greater.

Plots of aggregate POD curves versus flaw depth for scoring tolerances of 10 mm and 15 mm are provided in Figure 5.68 and Figure 5.69 (i.e., for 108-UT0 + 126-UT0 + 134-UT0 + 108-UT1 + 126-UT1 + 134-UT1 [Blind + Quickblind]), respectively and in Figure 5.70 and Figure 5.71 (i.e., for 108-UT1 + 126-UT1 + 134-UT1 [Blind]), respectively. Finally, the plot in Figure 5.72 is of the aggregate POD for 108-UT0 + 126-UT0 + 134-UT0 (Quickblind) data. The POD for Quickblind data is the same for 10 mm and 15 mm tolerance values. The solid black line represents the regression fit to the data and the red dashed lines represent 95% confidence bounds for the regression fit.

Table 5.46. Summary of POD (%) versus Flaw Depth for All Flaw Orientations (tolerance = 10 mm)

	NOBS	FCR	0 mm	5 mm	10 mm	15 mm	30 mm	60 mm
108-UT0	3	0.00	2	8	25	55	98	100
108-UT1	19	0.76	3	8	16	30	84	100
126-UT0	3	3.46	11	16	23	32	65	96
126-UT1	19	2.64	7	11	15	20	44	88
134-UT0	3	0.00	2	8	25	55	98	100
134-UT1	19	2.25	6	14	28	49	93	100
108-UT0 + 126-UT0 + 134-UT0 (Quick - blind)	19	1.02	4	13	34	64	99	100
108-UT1 + 126-UT1 + 134-UT1 (Blind)	57	1.88	5	10	19	32	79	100
108-UT0 + 126-UT0 + 134-UT0 + 108-UT1 + 126-UT1 + 134-UT1 (Blind + Quickblind)	66	1.55	5	10	21	36	86	100

Table 5.47. Summary of POD (%) versus Flaw Depth for All Flaw Orientations (tolerance = 15 mm)

	NOBS	FCR	0 mm	5 mm	10 mm	15 mm	30 mm	60 mm
108-UT0	3	0.00	2	8	25	55	98	100
108-UT1	19	0.00	2	7	19	43	96	100
126-UT0	3	3.50	11	17	24	33	65	96
126-UT1	19	2.74	8	11	15	20	44	88
134-UT0	3	0.00	2	8	25	55	98	100
134-UT1	19	2.34	6	14	28	49	93	100
108-UT0 + 126-UT0 + 134-UT0 (Quick - blind)	19	1.03	4	13	34	64	99	100
108-UT1 + 126-UT1 + 134-UT1 (Blind)	57	1.69	5	10	20	36	85	100
108-UT0 + 126-UT0 + 134-UT0 + 108-UT1 + 126-UT1 + 134-UT1 (Blind + Quickblind)	66	1.44	5	11	22	40	90	100

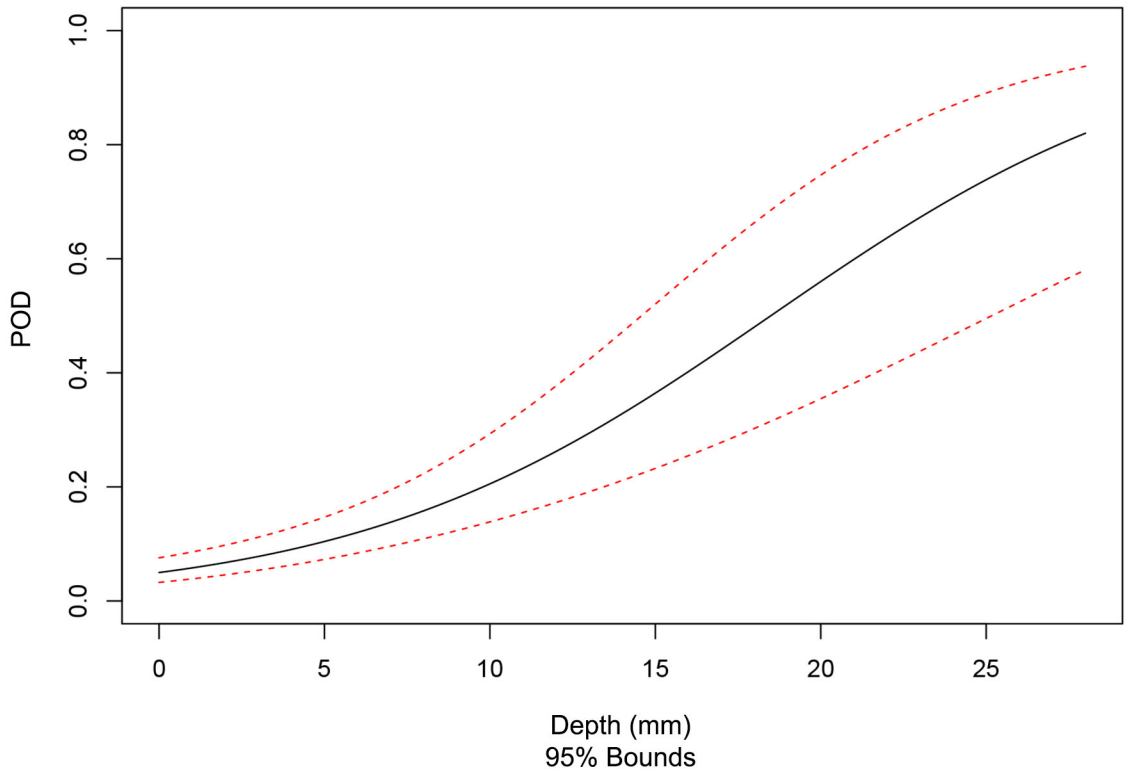

Figure 5.68. Aggregate Probability of Detection Curve versus Depth for Conventional UT Techniques 108-UT0, 126-UT0, 134-UT0, 108-UT1, 126-UT1, and 134-UT1 (Blind + Quickblind) and for All Flaw Orientations (tolerance = 10 mm)

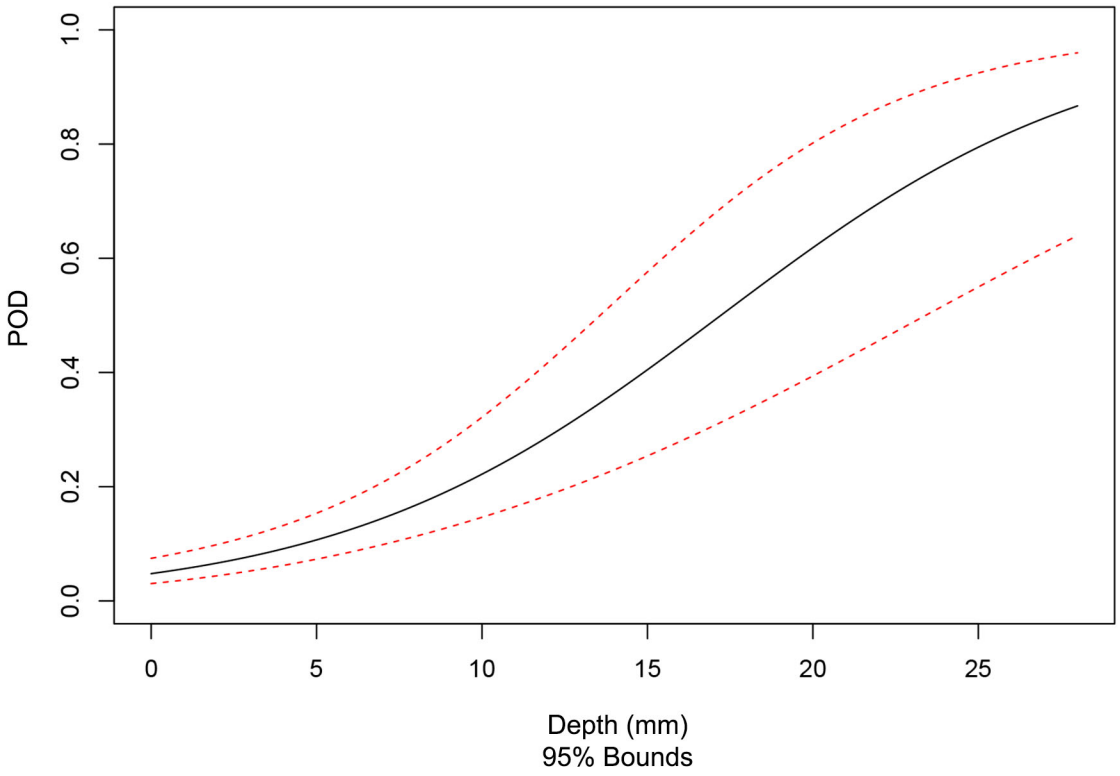

Figure 5.69. Aggregate Probability of Detection Curve versus Depth for Conventional UT Techniques 108-UT0, 126-UT0, 134-UT0, 108-UT1, 126-UT1, and 134-UT1 (Blind + Quickblind) and for All Flaw Orientations (tolerance = 15 mm)

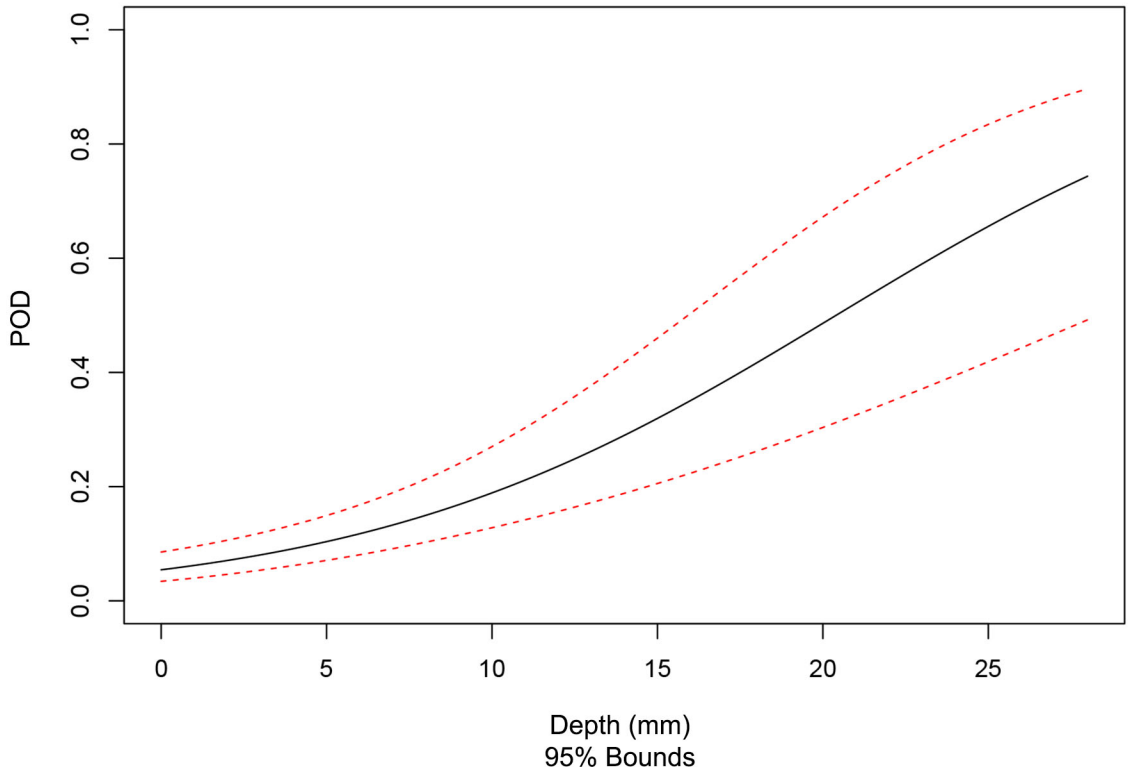

Figure 5.70. Aggregate Probability of Detection Curve versus Depth for Conventional UT Techniques 108-UT1, 126-UT1, and 134-UT1 (Blind) and for All Flaw Orientations (tolerance = 10 mm)

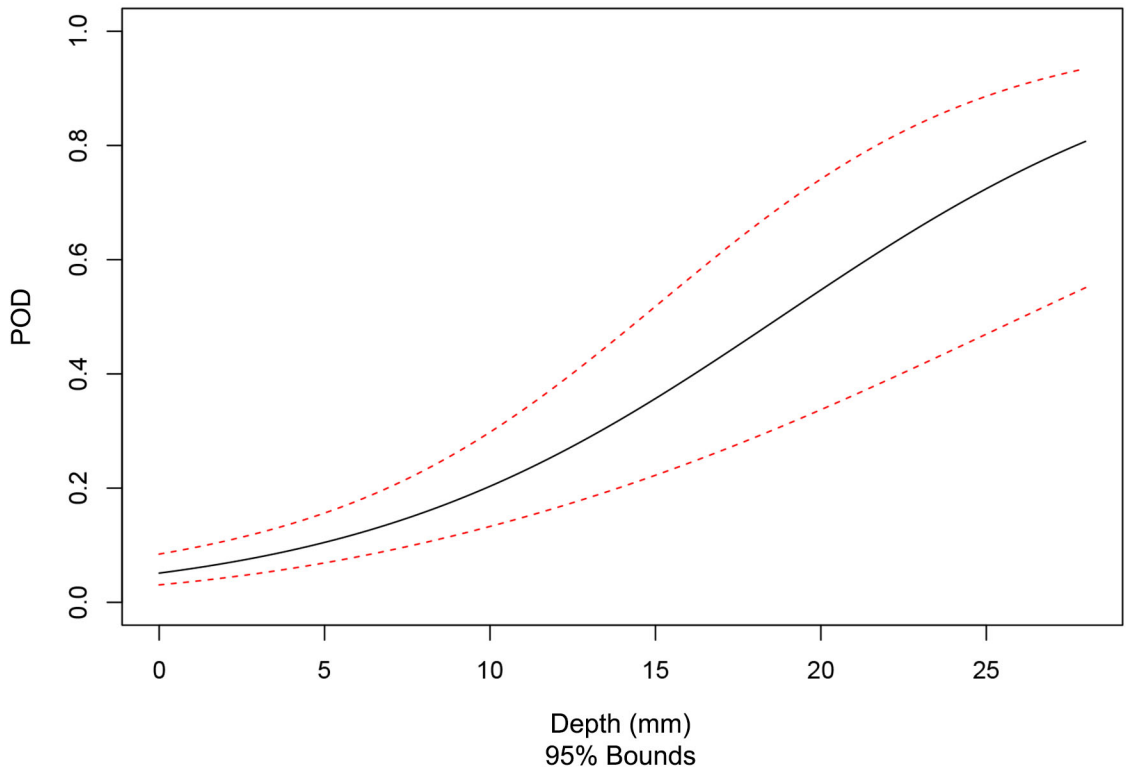

Figure 5.71. Aggregate Probability of Detection Curve versus Depth for Conventional UT Techniques 108-UT1, 126-UT1, and 134-UT1 (Blind) **and for All Flaw Orientations (tolerance = 15 mm)**

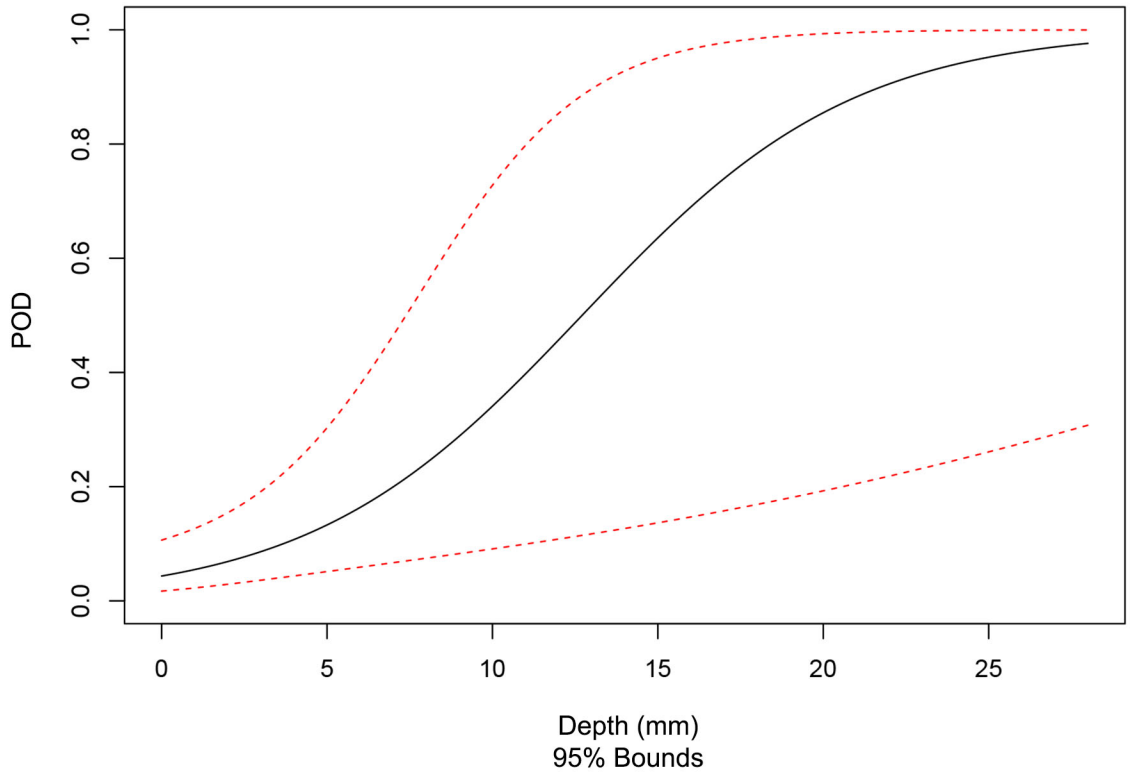

Figure 5.72. Aggregate Probability of Detection Curve versus Depth for Conventional UT Techniques 108-UT0, 126-UT0, and 134-UT0 (Quickblind) and for All Flaw Orientations (tolerance = 10 mm and 15 mm).

Summary of Detection Performance as a Function of Flaw Length

This section summarizes detection performance results obtained from the total flaw population as POD versus length. Table 5.48 and Table 5.49 provide the POD values at discrete flaw sizes (i.e., at 0 mm, 5 mm, 10 mm, 15 mm, 30 mm, and 60 mm) for scoring tolerances of 10 mm and 15 mm, respectively. A column for NOBS and FCR is also included in the tables. Comparison of Table 5.48 and Table 5.49 illustrate how aggregate detection performance (i.e., for 108-UT1 + 126-UT1 + 134-UT1 [Blind], and for 108-UT0 + 126-UT0 + 134-UT0 + 108-UT1 + 126-UT1 + 134-UT1 [Blind + Quickblind]) and detection performance for 108-UT1 is impacted by the increase in tolerance from 10 mm to 15 mm. As the tables show, the increase in scoring tolerance results in a decrease in the FCR, which is anticipated considering the positioning error that results in misses of axial flaws for a scoring tolerance of 10 mm. Further, a modest increase in the POD is observed, especially for flaw lengths of 15 mm and greater.

Plots of aggregate POD curves versus flaw length for scoring tolerances of 10 mm and 15 mm are provided in Figure 5.73 and Figure 5.74 (i.e., for 108-UT0 + 126-UT0 + 134-UT0 + 108-UT1 + 126-UT1 + 134-UT1 [Blind + Quickblind]), respectively, and in Figure 5.75 and Figure 5.76 (i.e., for 108-UT1 + 126-UT1 + 134-UT1 [Blind]), respectively. Finally, the plot in Figure 5.77 is of the aggregate POD for 108-UT0 + 126-UT0 + 134-UT0 (Quickblind) data. The POD for Quickblind data is the same for 10 mm and 15 mm tolerance values. The solid black line represents the regression fit to the data and the red dashed lines represent 95% confidence bounds for the regression fit.

Table 5.48. Summary of POD (%) versus Flaw Length for All Flaw Orientations (tolerance = 10 mm)

	NOBS	FCR	0 mm	5 mm	10 mm	15 mm	30 mm	60 mm
108-UT0	3	0.00	1	4	12	31	94	100
108-UT1	19	0.76	2	5	11	23	80	100
126-UT0	3	3.46	9	15	23	33	70	98
126-UT1	19	2.64	7	9	13	18	39	85
134-UT0	3	0.00	1	4	12	31	94	100
134-UT1	19	2.25	6	11	20	33	80	100
108-UT0 + 126-UT0 + 134-UT0 (Quickblind)	19	1.02	3	8	21	44	95	100
108-UT1 + 126-UT1 + 134-UT1 (Blind)	57	1.88	5	8	15	25	70	99
108-UT0 + 126-UT0 + 134-UT0 + 108-UT1 + 126-UT1 + 134-UT1 (Blind + Quickblind)	66	1.55	4	8	15	28	80	100

Table 5.49. Summary of POD versus Flaw Length for All Flaw Orientations (tolerance = 15 mm)

	NOBS	FCR	0 mm	5 mm	10 mm	15 mm	30 mm	60 mm
108-UT0	3	0.00	1	4	12	31	94	100
108-UT1	19	0.00	1	3	10	27	93	100
126-UT0	3	3.50	10	15	23	33	70	98
126-UT1	19	2.74	7	10	13	18	39	84
134-UT0	3	0.00	1	4	12	31	94	100
134-UT1	19	2.34	6	11	20	33	80	100
108-UT0 + 126-UT0 + 134-UT0 (Quickblind)	19	1.03	3	8	21	44	95	100
108-UT1 + 126-UT1 + 134-UT1 (Blind)	57	1.69	4	8	15	27	74	99
108-UT0 + 126-UT0 + 134-UT0 + 108-UT1 + 126-UT1 + 134-UT1 (Blind + Quickblind)	66	1.44	4	8	16	30	83	100

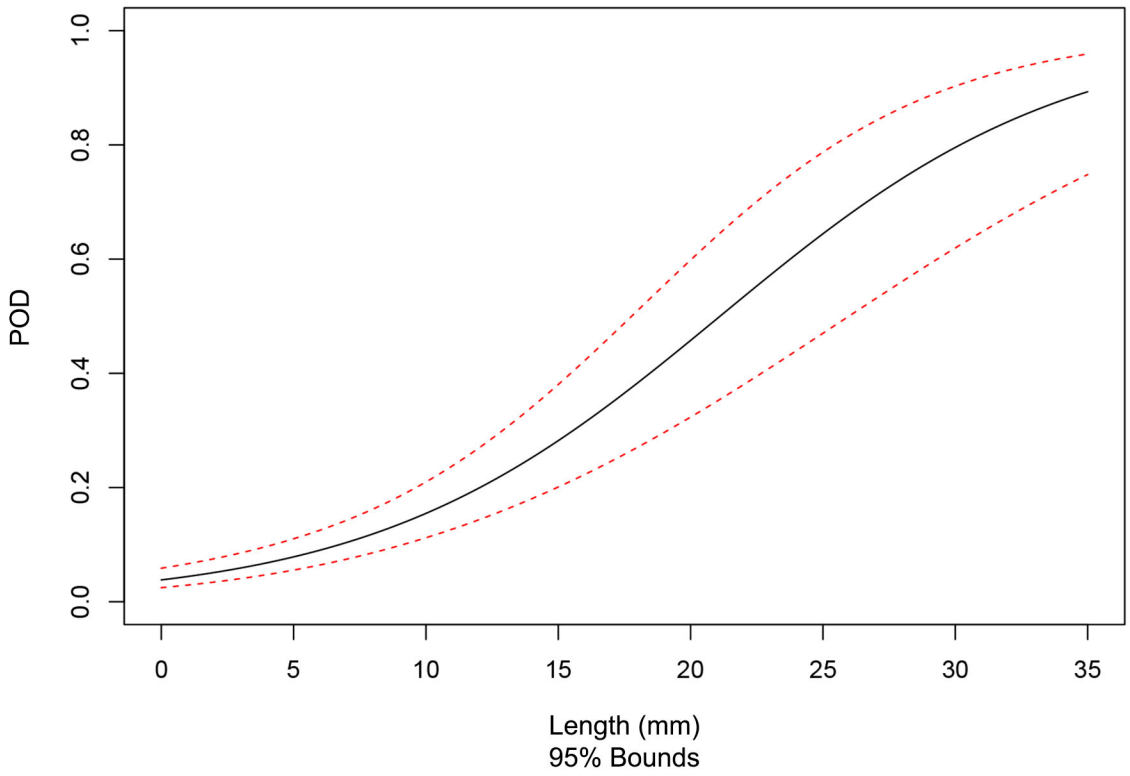

Figure 5.73. Aggregate Probability of Detection Curve versus Length for Conventional UT Techniques 108-UT0, 126-UT0, 134-UT0, 108-UT1, 126-UT1, and 134-UT1 (Blind + Quickblind) and for All Flaw Orientations (tolerance = 10 mm)

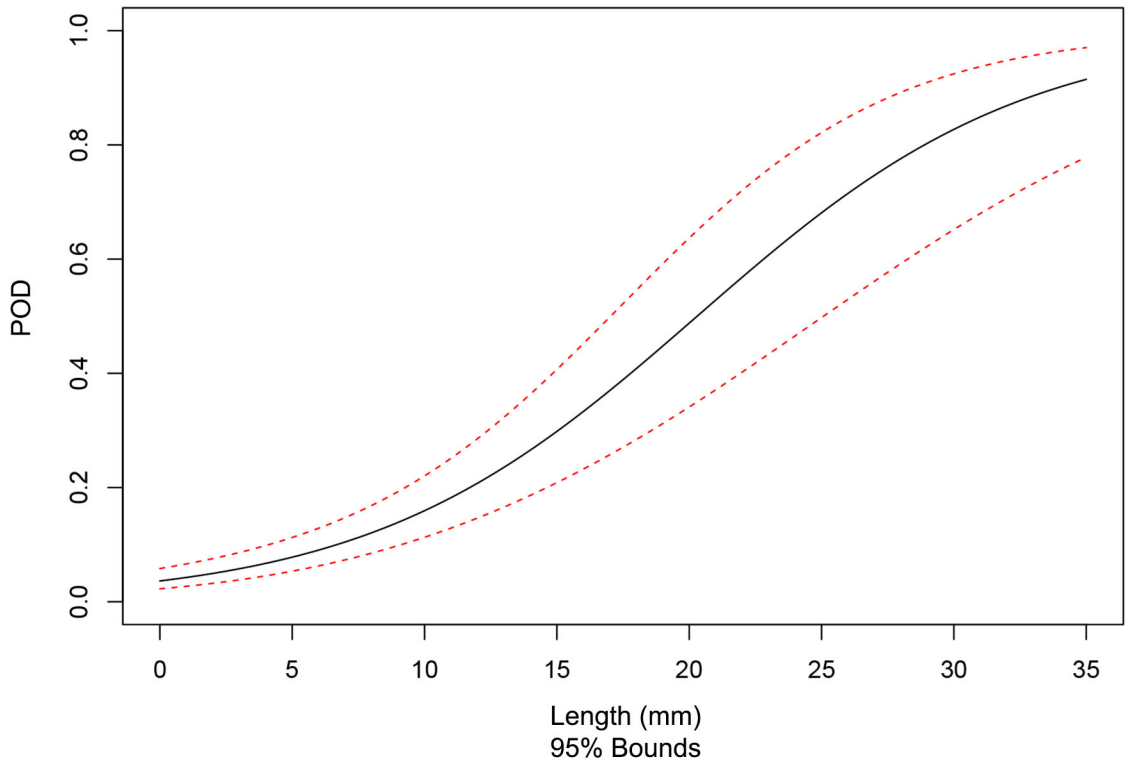

Figure 5.74. Aggregate Probability of Detection Curve versus Length for Conventional UT Techniques 108-UT0, 126-UT0, 134-UT0, 108-UT1, 126-UT1, and 134-UT1 (Blind + Quickblind) and for All Flaw Orientations (tolerance = 15 mm)

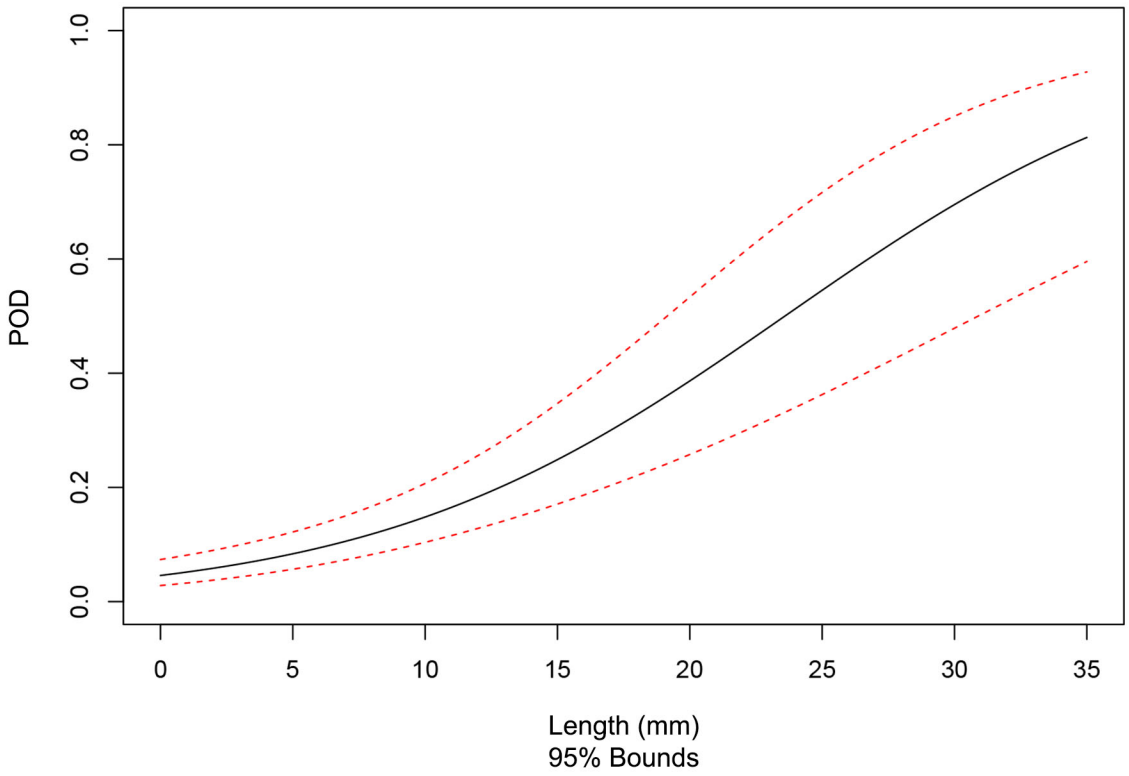

Figure 5.75. Aggregate Probability of Detection Curve versus Length for conventional UT Techniques 108-UT1, 126-UT1, and 134-UT1 (Blind) and for All Flaw Orientations (tolerance = 10 mm).

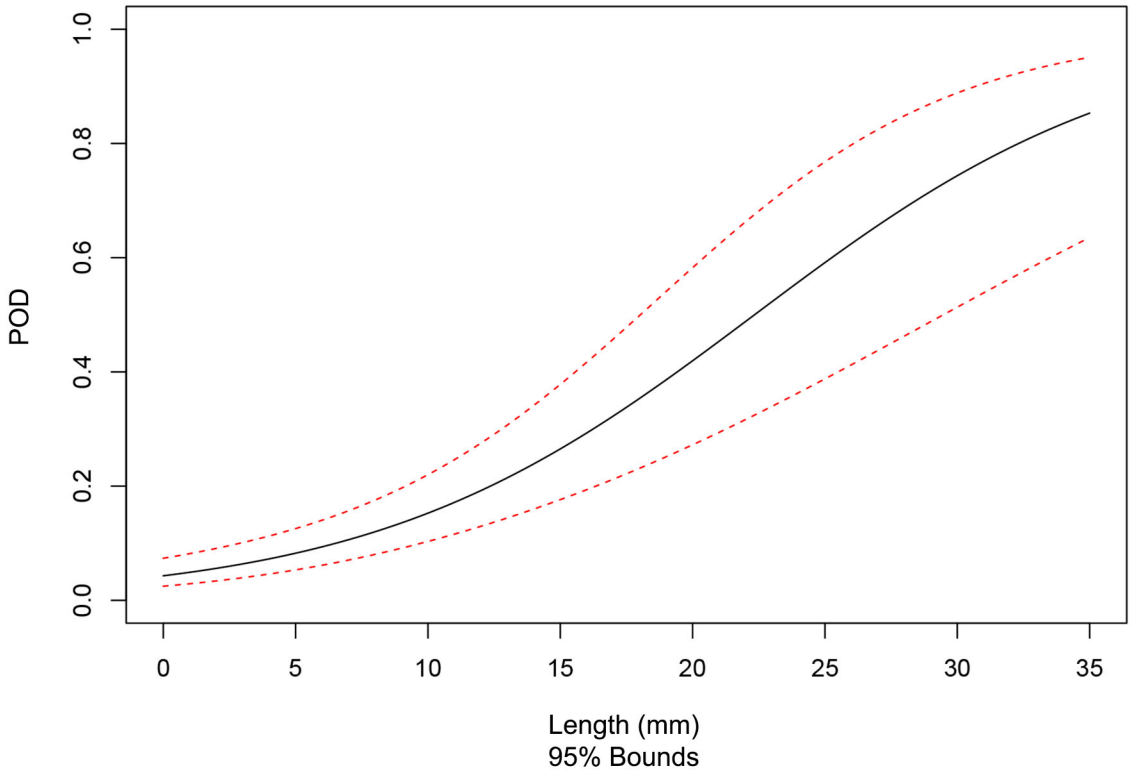

Figure 5.76. Aggregate Probability of Detection Curve versus Length for Conventional UT Techniques 108-UT1, 126-UT1, and 134-UT1 (Blind) and for All Flaw Orientations (tolerance = 15 mm)

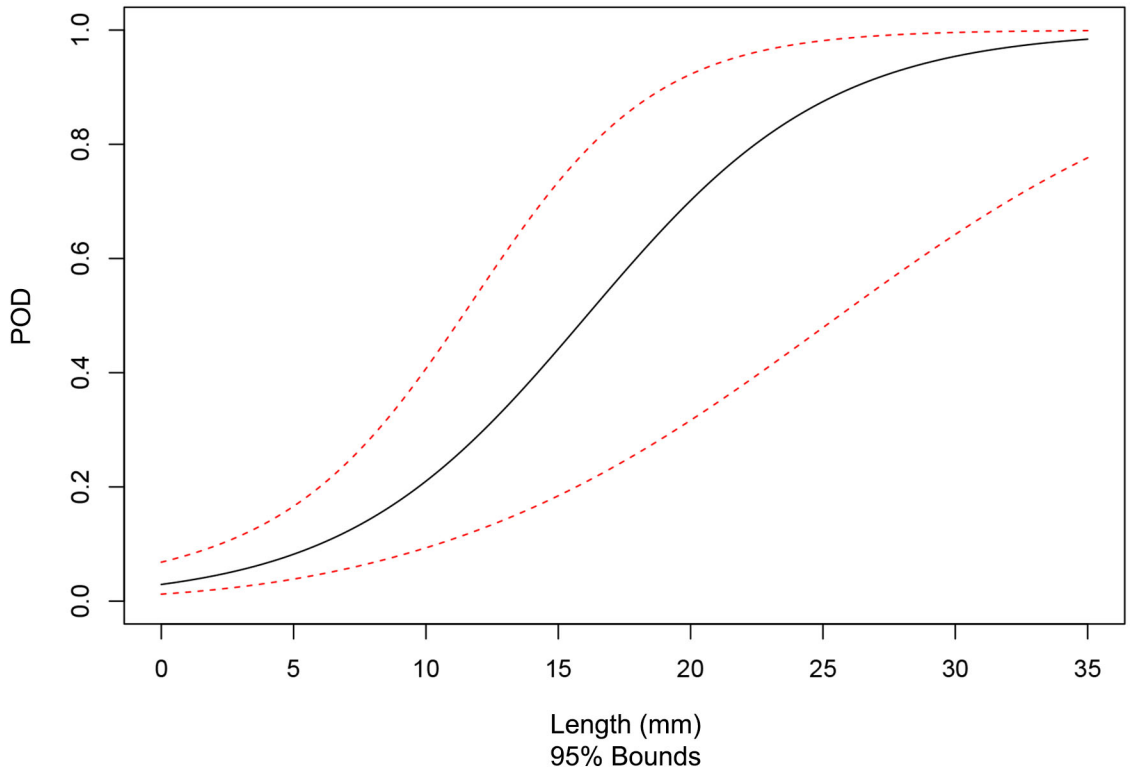

Figure 5.77. Aggregate Probability of Detection Curve versus Length for Conventional UT Techniques 108-UT0, 126-UT0, and 134-UT0 (Quickblind) and for All Flaw Orientations (tolerance = 10 mm and 15 mm)

5.2.9.3 Summary of Detection Analysis Results for Axial Flaws

This section presents the detection performance results obtained from the axial flaw population as POD versus depth and length. The data is presented in tabular form and as plots of POD curves, as is done for detection performance data collected from the population of all flaws in Section 5.2.9.2.

Summary of Detection Performance as a Function of Flaw Depth

This section summarizes detection performance results obtained from the axial flaw population as POD versus depth. Table 5.50 and Table 5.51 provide the POD values at discrete flaw sizes (i.e., at 0 mm, 5 mm, 10 mm, 15 mm, 30 mm, and 60 mm) for scoring tolerances of 10 mm and 15 mm, respectively. A column for NOBS and FCR is also included in the tables. In this case, NOBS represents the total number of axial flaws in the test blocks inspected by a given technique. Comparison of Table 5.50 and Table 5.51 illustrates how aggregate detection performance (i.e., for 108-UT1 + 126-UT1 + 134-UT1) and detection performance for 108-UT1 is impacted by the increase in tolerance from 10 mm to 15 mm. As the tables show, the increase in scoring tolerance results in a decrease in the FCR, which is anticipated considering the positioning error that results in several misses of axial flaws for a scoring tolerance of 10 mm. Further, an increase in the POD is observed for all flaw depth values of 10 mm, 15 mm, and 30 mm.

Plots of aggregate POD curves versus flaw depth (i.e., for 108-UT1 + 126-UT1 + 134-UT1) for axial flaws and for scoring tolerances of 10 mm and 15 mm are provided in Figure 5.78 and Figure 5.79, respectively. The solid black line represents the regression fit to the data and the red dashed lines

represent 95% confidence bounds for the regression fit. The change in shape from Figure 5.25 and Figure 5.26 is modest but indicates an overall increase in detection performance.

Table 5.50. Summary of POD versus Flaw Depth for Axially Oriented Flaws (tolerance = 10 mm)

	NOBS	FCR	0 mm	5 mm	10 mm	15 mm	30 mm	60 mm
108-UT1	9	0.76	3	6	11	21	72	100
126-UT1	9	2.64	7	9	12	17	37	83
134-UT1	9	2.25	6	12	22	37	84	100
108-UT1 + 126-UT1 + 134-UT1 (Blind)	27	1.88	5	9	15	25	68	99

Table 5.51. Summary of POD versus Flaw Depth for Axially Oriented Flaws (tolerance = 15 mm)

	NOBS	FCR	0 mm	5 mm	10 mm	15 mm	30 mm	60 mm
108-UT1	9	0.00	1	4	13	33	94	100
126-UT1	9	2.74	7	9	13	17	37	82
134-UT1	9	2.34	6	12	22	37	83	100
108-UT1 + 126-UT1 + 134-UT1 (Blind)	27	1.69	5	9	17	29	78	100

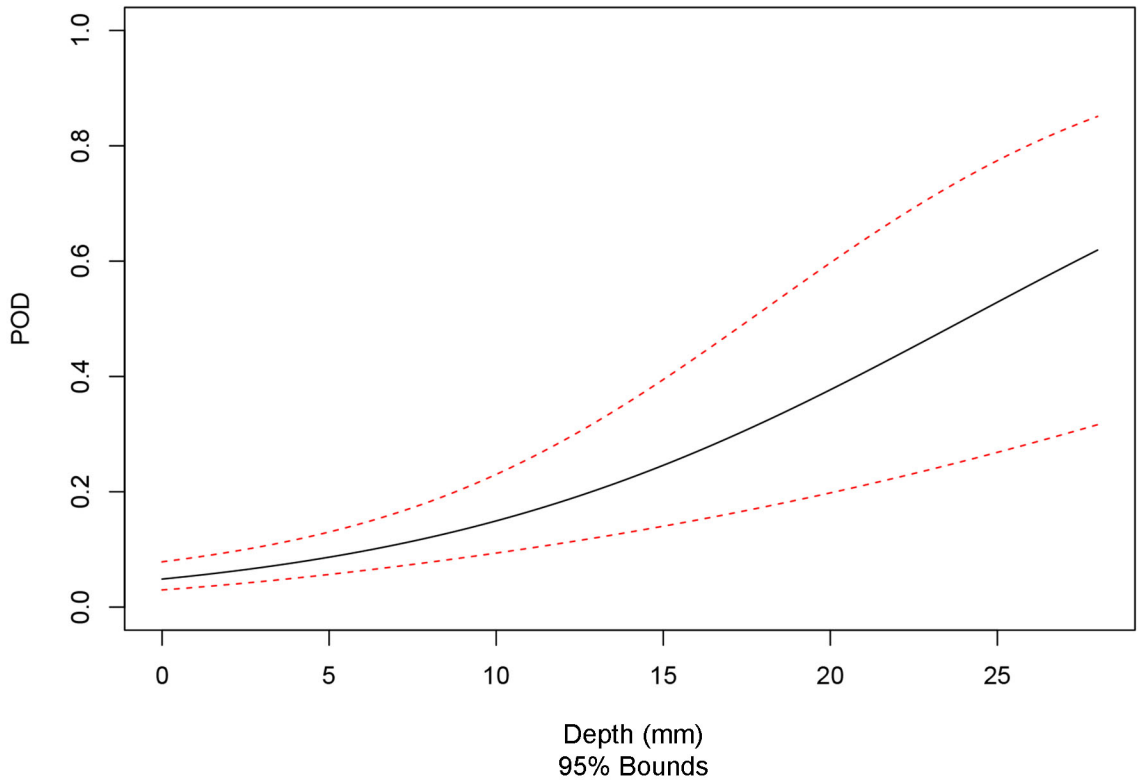

Figure 5.78. Aggregate Probability of Detection Curve versus Depth for Conventional UT Techniques 108-UT1, 126-UT1, and 134-UT1 (Blind) for Axial Flaws (tolerance = 10 mm)

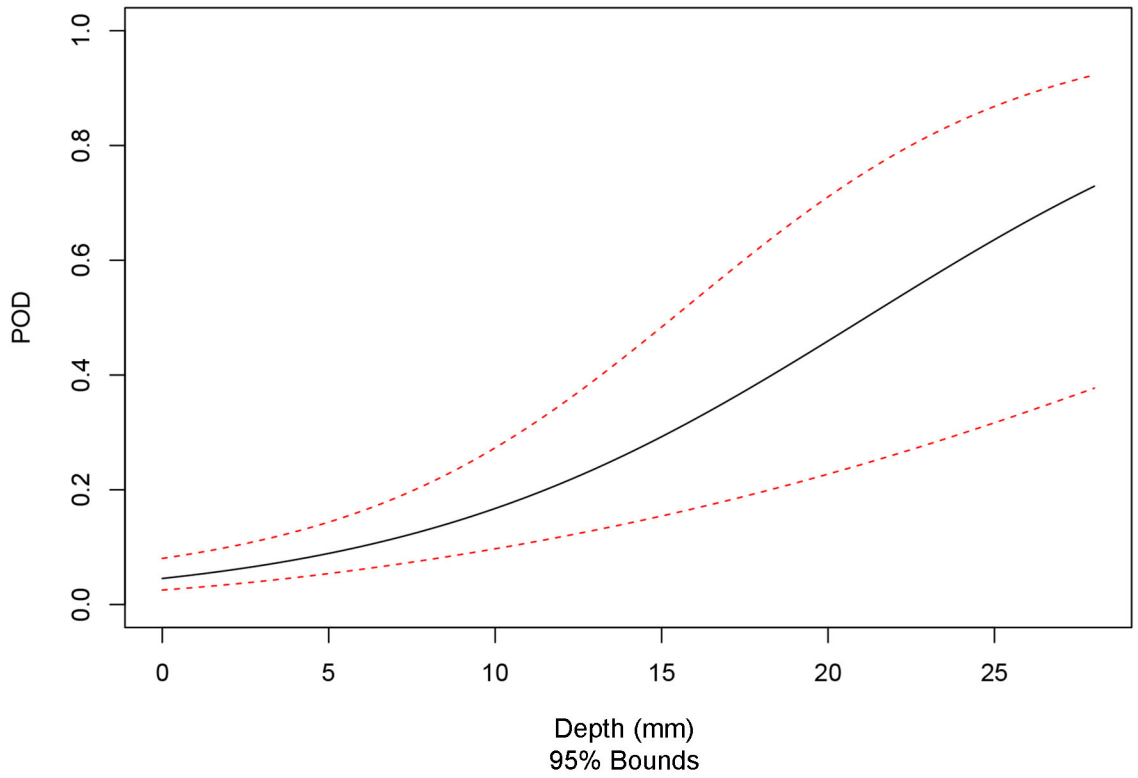

Figure 5.79. Aggregate Probability of Detection Curve versus Depth for Conventional UT Techniques 108-UT1, 126-UT1, and 134-UT1 (Blind) for Axial Flaws (tolerance = 15 mm)

Summary of Detection Performance as a Function of Flaw Length

This section summarizes detection performance results obtained from the axial flaw population as POD versus length. Table 5.52 and Table 5.53 provide the POD values at discrete flaw sizes (i.e., at 0 mm, 5 mm, 10 mm, 15 mm, 30 mm, and 60 mm) for scoring tolerances of 10 mm and 15 mm, respectively. A column for NOBS and FCR is also included in the tables. In this case, NOBS represents the total number of axial flaws in the test blocks inspected by a given technique. Comparison of Table 5.52 and Table 5.53 illustrates how aggregate detection performance (i.e., for 108-UT1 + 126-UT1 + 134-UT1) and detection performance for 108-UT1 is impacted by the increase in tolerance from 10 mm to 15 mm. As the tables show, the increase in scoring tolerance results in a decrease in the FCR, which is anticipated considering the positioning error that results in several misses of axial flaws for a scoring tolerance of 10 mm. Further, an increase in the POD is observed for flaw lengths of 10 mm, 15 mm, and 30 mm.

Plots of aggregate POD curves versus flaw length (i.e., for 108-UT1 + 126-UT1 + 134-UT1) for axial flaws and for scoring tolerances of 10 mm and 15 mm are provided in Figure 5.80 and Figure 5.81, respectively. The solid black line represents the regression fit to the data and the red dashed lines represent 95% confidence bounds for the regression fit. The change in shape from Figure 5.80 and Figure 5.81 indicates an overall increase in detection performance.

Table 5.52. Summary of POD versus Flaw Length for Axially Oriented Flaws (tolerance = 10 mm)

	NOBS	FCR	0 mm	5 mm	10 mm	15 mm	30 mm	60 mm
108-UT1	9	0.76	2	5	12	24	80	100
126-UT1	9	2.64	7	9	11	13	24	57
134-UT1	9	2.25	6	12	22	38	86	100
108-UT1 + 126-UT1 + 134-UT1 (Blind)	27	1.88	5	9	15	25	69	99

Table 5.53. Summary of POD versus Flaw Length for Axially Oriented Flaws (tolerance = 15 mm)

	NOBS	FCR	0 mm	5 mm	10 mm	15 mm	30 mm	60 mm
108-UT1	9	0.00	1	4	12	34	96	100
126-UT1	9	2.74	7	9	11	13	24	55
134-UT1	9	2.34	6	12	23	39	86	100
108-UT1 + 126-UT1 + 134-UT1 (Blind)	27	1.69	4	9	17	29	79	100

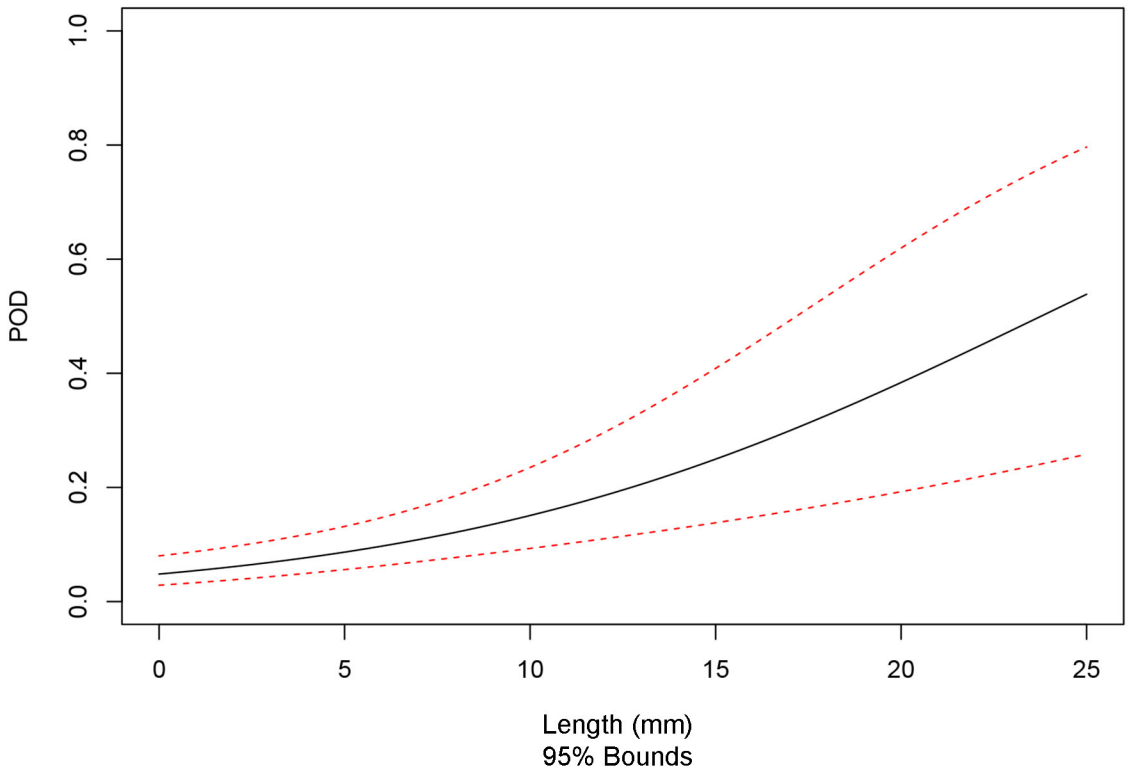

Figure 5.80. Aggregate Probability of Detection Curve versus Length for Conventional UT Techniques 108-UT1, 126-UT1, and 134-UT1 (Blind) for Axial Flaws (tolerance = 10 mm)

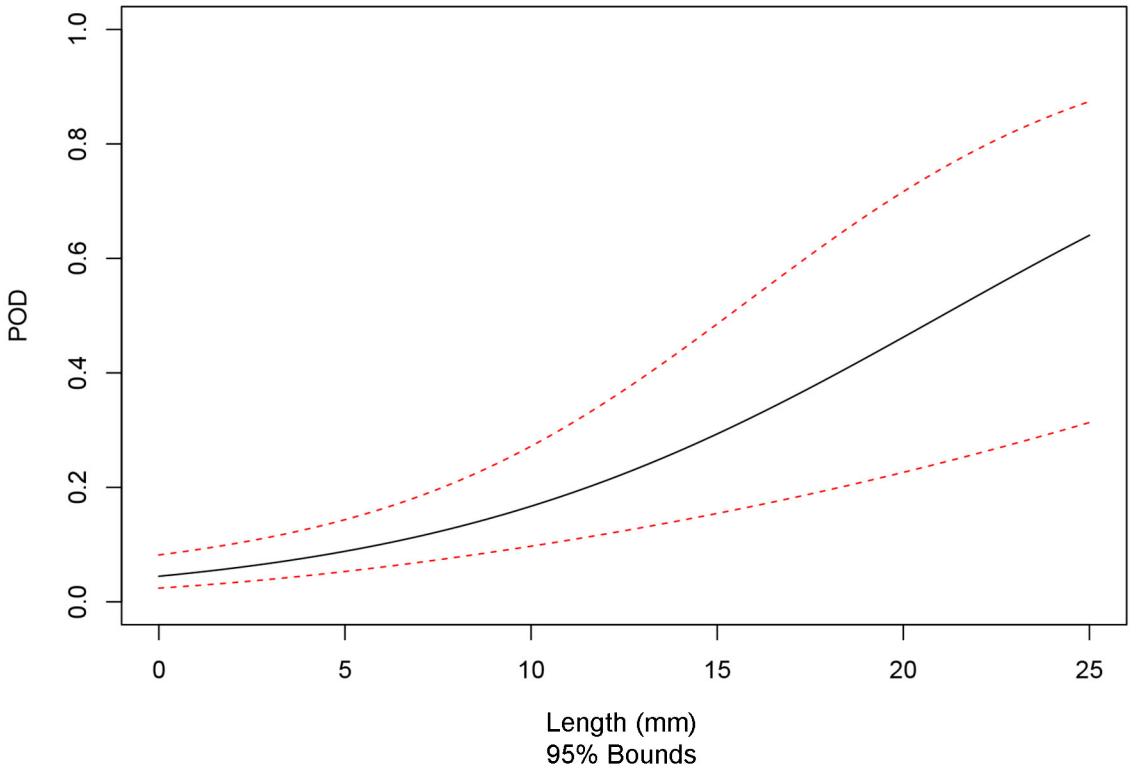

Figure 5.81. Aggregate Probability of Detection Curve versus Length for Conventional UT Techniques 108-UT1, 126-UT1, and 134-UT1 (Blind) for Axial Flaws (tolerance = 15 mm)

5.2.9.4 Summary of Detection Analysis Results for Circumferential Flaws

This section presents the detection performance results obtained from the circumferential flaw population as POD versus depth and length. The data is presented in tabular form and as plots of POD curves, as is done for detection performance data collected from the population of all flaws in Section 5.2.9.2 and the population of axial flaws in Section 5.2.9.3.

Summary of Detection Performance as a Function of Flaw Depth

This section summarizes detection performance results obtained from the circumferential flaw population as POD versus depth. Table 5.54 and Table 5.55 provide the POD values at discrete flaw sizes (i.e., at 0 mm, 5 mm, 10 mm, 15 mm, 30 mm, and 60 mm) for scoring tolerances of 10 mm and 15 mm, respectively. A column for NOBS and FCR is also included in the tables. In this case, NOBS represents the total number of axial flaws in the test blocks inspected by a given technique. Comparison of Table 5.54 and Table 5.55 illustrates that detection performance for circumferential flaws is mostly unaffected for any techniques by the increase in tolerance from 10 mm to 15 mm. This is anticipated considering the positioning error is only associated with axial flaws. Differences in Table 5.54 and Table 5.55 are observed in FCR; however, this is because false calls are irrespective of the orientation of flaws in the test block.

Plots of aggregate POD curves versus flaw depth (i.e., for 108-UT1 + 126-UT1 + 134-UT1) for circumferential flaws and for scoring tolerances of 10 mm and 15 mm are provided in Figure 5.82 and Figure 5.83, respectively. The solid black line represents the regression fit to the data and the red dashed

lines represent 95% confidence bounds for the regression fit. As can be seen from Figure 5.82 and Figure 5.83, there is no visible change in the POD curve as a consequence of the increase in tolerance from 10 mm to 15 mm. This is anticipated considering the positioning error is only associated with axial flaws.

Table 5.54. Summary of POD versus Flaw Depth for Circumferentially Oriented Flaws (tolerance = 10 mm)

	NOBS	FCR	0 mm	5 mm	10 mm	15 mm	30 mm	60 mm
108-UT1	10	0.76	3	8	19	39	93	100
126-UT1	10	2.64	8	12	18	26	58	96
134-UT1	10	2.25	6	15	33	58	97	100
108-UT1 + 126-UT1 + 134-UT1 (Blind)	30	1.88	5	12	24	44	91	100

Table 5.55. Summary of POD versus Flaw Depth for Circumferentially Oriented Flaws (tolerance = 15 mm)

	NOBS	FCR	0 mm	5 mm	10 mm	15 mm	30 mm	60 mm
108-UT1	10	0.00	2	5	14	35	95	100
126-UT1	10	2.74	8	12	18	26	58	95
134-UT1	10	2.34	6	15	33	58	97	100
108-UT1 + 126-UT1 + 134-UT1 (Blind)	30	1.69	5	11	24	43	92	100

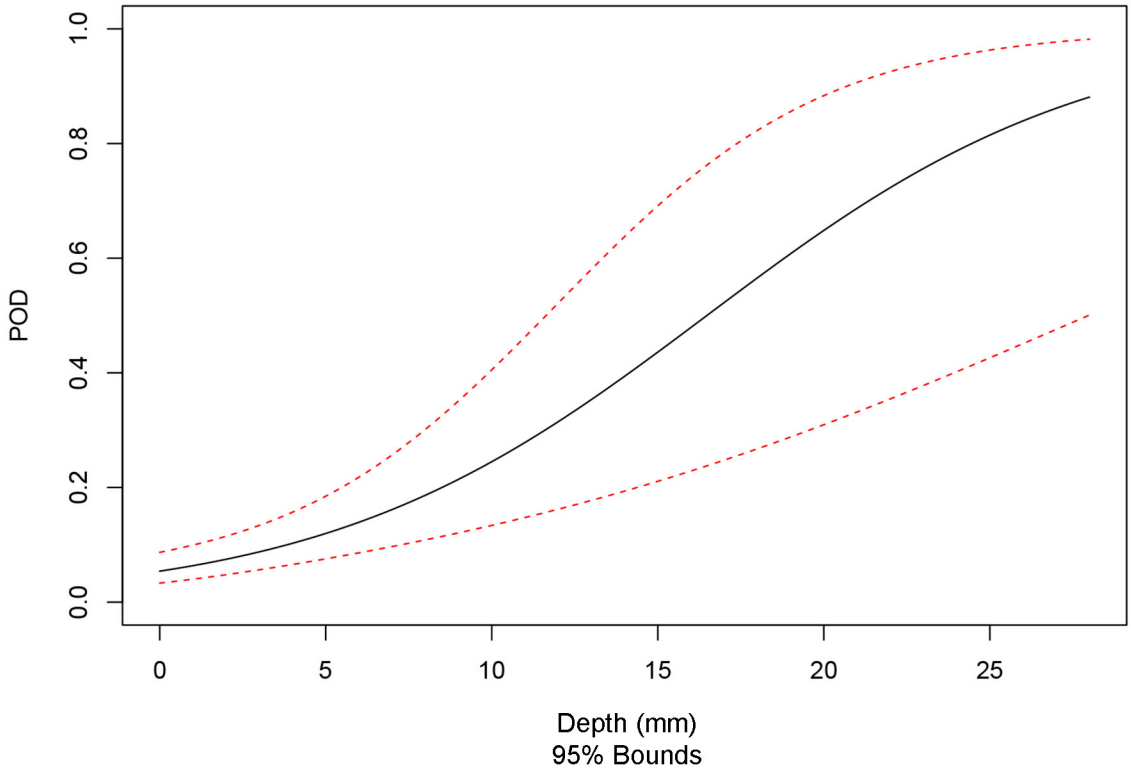

Figure 5.82. Aggregate Probability of Detection Curve versus Depth for Conventional UT Techniques 108-UT1, 126-UT1, and 134-UT1 (Blind) for Circumferential Flaws (tolerance = 10 mm)

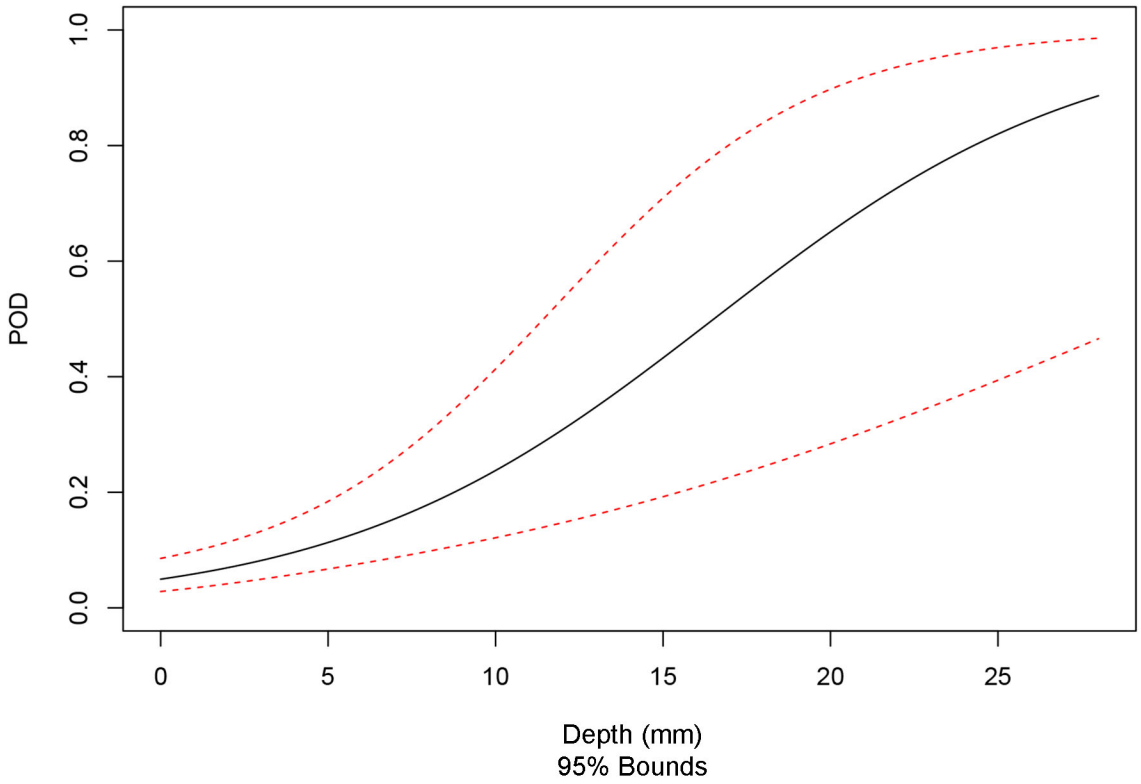

Figure 5.83. Aggregate Probability of Detection Curve versus Depth for Conventional UT Techniques 108-UT1, 126-UT1, and 134-UT1 (Blind) for Circumferential Flaws (tolerance = 15 mm)

Summary of Detection Performance as a Function of Flaw Length

This section summarizes detection performance results obtained from the circumferential flaw population as POD versus length. Table 5.56 and Table 5.57 provide the POD values at discrete flaw sizes (i.e., at 0 mm, 5 mm, 10 mm, 15 mm, 30 mm, and 60 mm) for scoring tolerances of 10 mm and 15 mm, respectively. A column for NOBS and FCR is also included in the tables. In this case, NOBS represents the total number of axial flaws in the test blocks inspected by a given technique. Comparison of Table 5.56 and Table 5.57 illustrates that detection performance for circumferential flaws is mostly unaffected for any techniques by the increase in tolerance from 10 mm to 15 mm. This is anticipated considering the positioning error is only associated with axial flaws. Differences in Table 5.56 and Table 5.57 are observed in FCR; however, this is because false calls are irrespective of the orientation of flaws in the test block.

Plots of aggregate POD curves versus flaw length (i.e., for 108-UT1 + 126-UT1 + 134-UT1) for circumferential flaws and for scoring tolerances of 10 mm and 15 mm are provided in Figure 5.84 and Figure 5.85, respectively. The solid black line represents the regression fit to the data and the red dashed lines represent 95% confidence bounds for the regression fit. As can be seen from Figure 5.84 and Figure 5.85, there is no visible change in the POD curve as a consequence of the increase in tolerance from 10 mm to 15 mm. This is anticipated considering the positioning error is only associated with axial flaws.

Table 5.56. Summary of POD versus Flaw Length for Circumferentially Oriented Flaws (tolerance = 10 mm)

	NOBS	FCR	0 mm	5 mm	10 mm	15 mm	30 mm	60 mm
108-UT1	10	0.76	2	5	11	22	78	100
126-UT1	10	2.64	7	10	15	21	48	92
134-UT1	10	2.25	6	10	17	28	70	99
108-UT1 + 126-UT1 + 134-UT1 (Blind)	30	1.88	5	8	15	25	69	99

Table 5.57. Summary of POD versus Flaw Length for Circumferentially Oriented Flaws (tolerance = 15 mm)

	NOBS	FCR	0 mm	5 mm	10 mm	15 mm	30 mm	60 mm
108-UT1	10	0.00	0	2	5	14	84	100
126-UT1	10	2.74	7	10	15	21	48	92
134-UT1	10	2.34	6	10	17	28	70	99
108-UT1 + 126-UT1 + 134-UT1 (Blind)	30	1.69	4	8	14	24	70	99

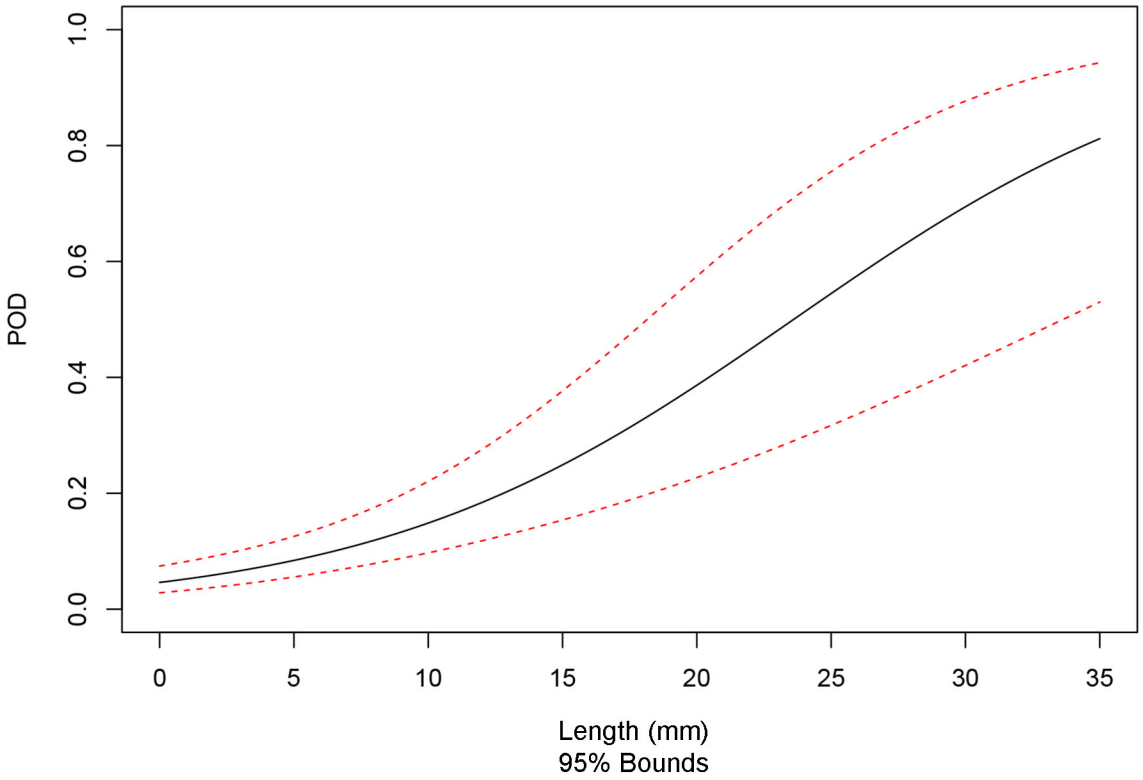

Figure 5.84. Aggregate Probability of Detection Curve versus Length for Conventional UT Techniques 108-UT1, 126-UT1, and 134-UT1 (Blind) for Circumferential Flaws (tolerance = 10 mm)

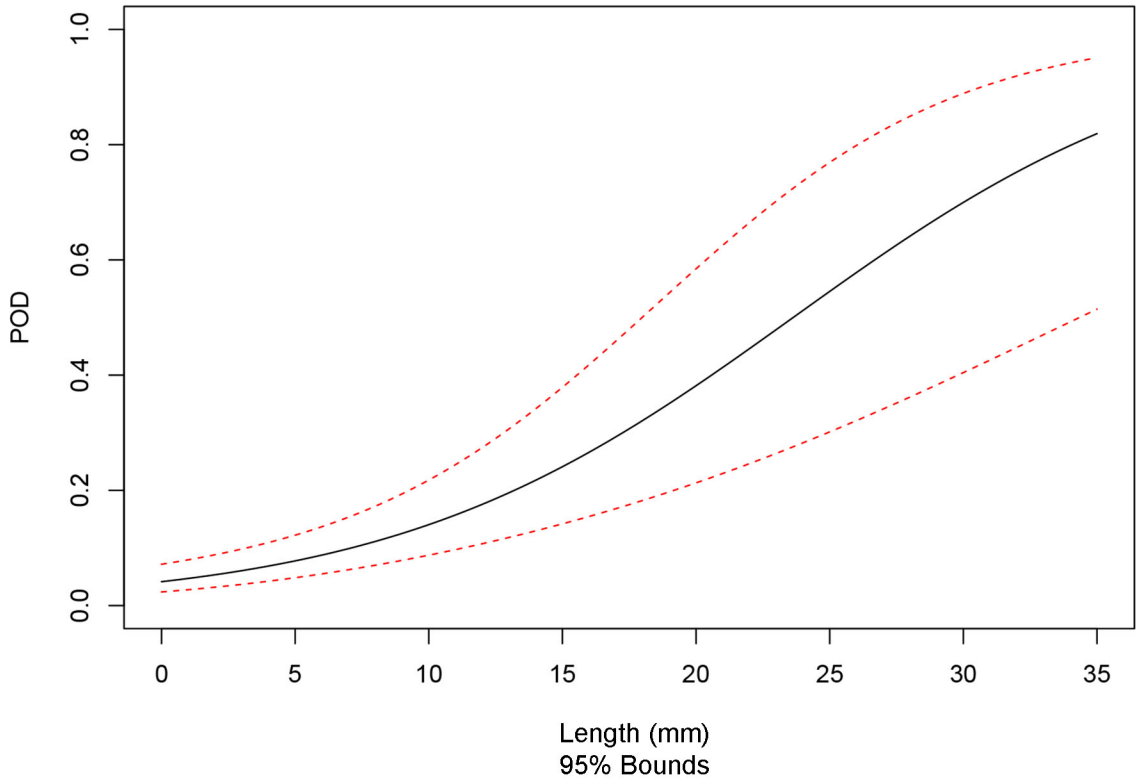

Figure 5.85. Aggregate Probability of Detection Curve versus Length for Conventional UT Techniques 108-UT1, 126-UT1, and 134-UT1 (Blind) for Circumferential Flaws (tolerance = 15 mm)

5.2.10 Depth Sizing Performance Analysis

This section presents the results of the depth sizing performance analysis of conventional UT techniques applied to LBDMW test blocks in PARENT. Results are presented as tabulations of bias and RMSE and as plots of depth sizing regression curves. The following sections include tabulated summaries of depth sizing performance for conventional UT techniques. Depth sizing was not attempted for all axial flaws detected in test block P33; as a result, positioning error did not influence the depth sizing results, and scoring tolerances of 10 mm and 15 mm produced identical results. Summaries of depth sizing results are provided for the total flaw population, the axial flaw population, and the circumferential flaw population.

Linear regression was used to analyze depth sizing data. The formulas for the regression analysis curves, computing RMSE, sizing bias, and sizing StDev are defined in Section 3.4 and in Eqs. (3.7)–(3.11), specifically.

5.2.10.1 Summary of Depth Sizing Analysis Results for All Flaws

This section presents the results of the depth sizing performance analysis of conventional UT techniques applied to the total detected flaw population. Tabulation of depth sizing bias and RMSE for conventional UT techniques are provided in Table 5.58. The NOBS column is the sample size used for depth sizing analysis. It is equal to the number of detections.

Aggregate depth sizing regression plots are provided in Figure 5.86 and Figure 5.87. Symbols “A” and “C” are used to represent axially oriented flaws and circumferentially oriented flaws, respectively. The symbol “D” in Figure 5.87 refers to flaws with a diagonal orientation. The designation of diagonal orientation is used to denote flaws that do not have a dominant orientation based on dimensions. In this case, flaws in the Quickblind test blocks P15, P16, and P17 were denoted as diagonal. Figure 5.86 provides aggregate regression plots for conventional UT Techniques 108-UT1, 126-UT1, and 134-UT1. Figure 5.87 provides the aggregate regression plot for conventional UT techniques 108-UT0, 126-UT0, and 134-UT0.

Table 5.58. Summary of Depth Sizing Error for Conventional UT Techniques for All Flaw Orientations

	NOBS	Bias	RMSE
108-UT0	3	−9.0	11.3
108-UT1	4	−0.3	9.0
126-UT0	2	−1.5	5.3
126-UT1	4	0.6	6.8
134-UT0	3	−6.5	10.0
134-UT1	8	−8.9	11.4
108-UT0 + 126-UT0 + 134-UT0 (Quickblind)	8	−6.2	9.6
108-UT1 + 126-UT1 + 134-UT1 (Blind)	16	−4.4	9.8
108-UT0 + 126-UT0 + 134-UT0 + 108-UT1 + 126-UT1 + 134-UT1 (Blind + Quickblind)	24	−5.0	9.8

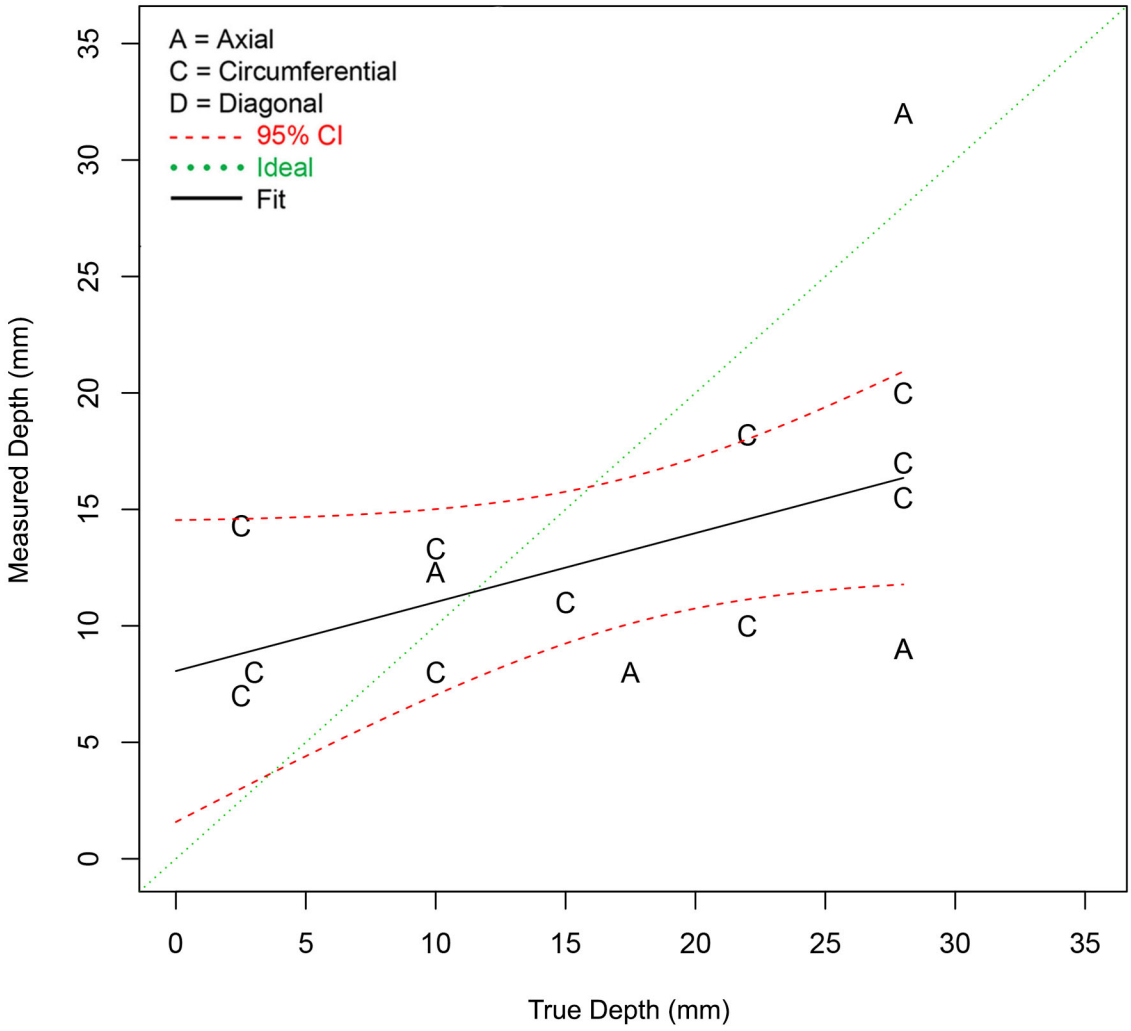

Figure 5.86. Aggregate Depth Sizing Regression Fit for Conventional UT Techniques 108-UT1, 126-UT1, and 134-UT1 for All Flaw Orientations

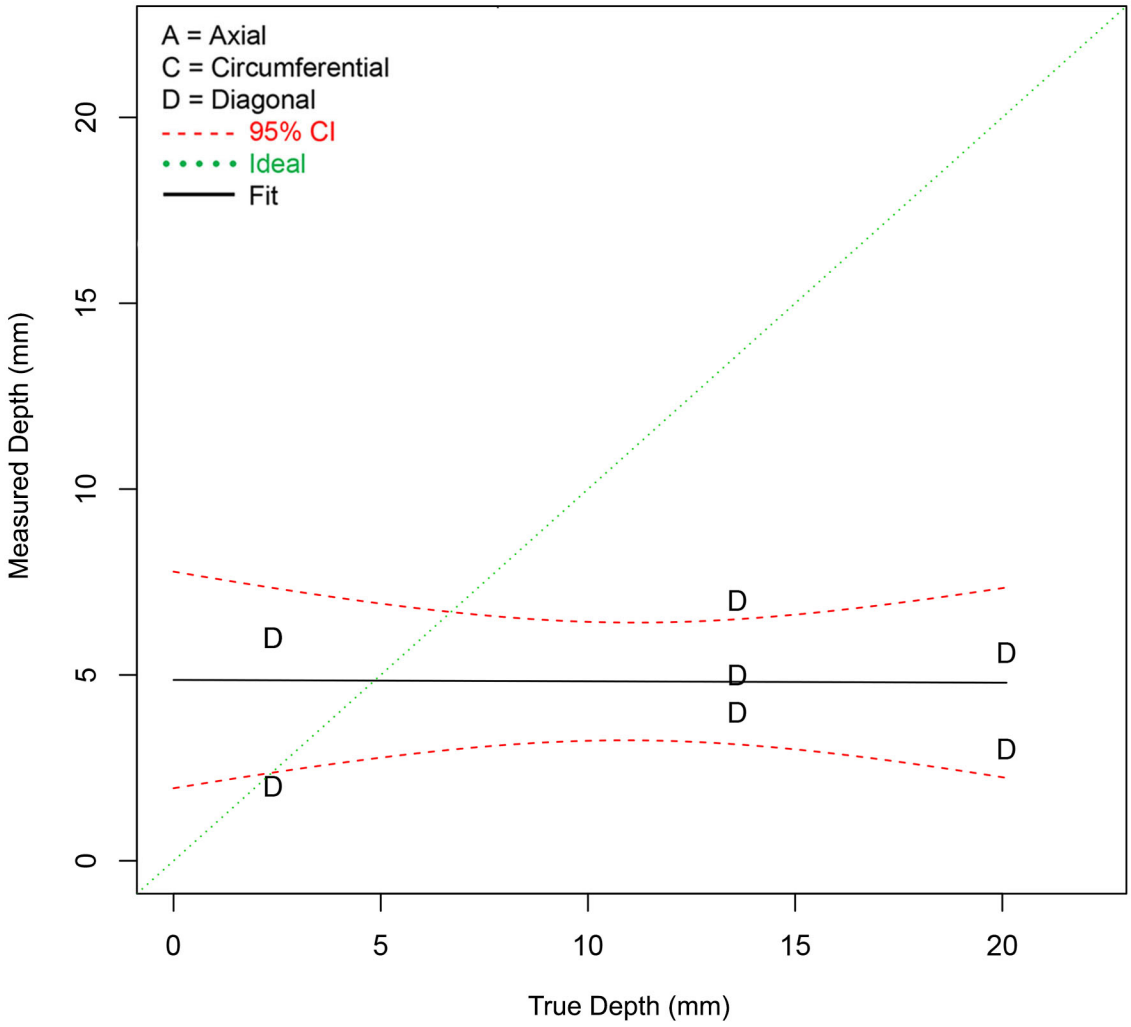

Figure 5.87. Aggregate Depth Sizing Regression Fit for Conventional UT Techniques 108-UT0, 126-UT0, and 134-UT0 for All Flaw Orientations

5.2.10.2 Summary of Depth Sizing Analysis Results for Axial Flaws

This section presents the results of the depth sizing performance analysis of conventional UT techniques applied to the population of detected axial flaws. Tabulation of depth sizing bias and RMSE for conventional UT techniques are provided in Table 5.59. In this case, NOBS is equal to the number of detected axial flaws. An aggregate depth sizing regression plot is provided in Figure 5.88.

Table 5.59. Summary of Depth Sizing Error for Conventional UT Techniques for Axial Flaws

	NOBS	Bias	RMSE
108-UT1	0		
126-UT1	1	4.0	4.0
134-UT1	4	−11.3	14.3
108-UT1 + 126-UT1 + 134-UT1 (Blind)	5	−8.2	12.9

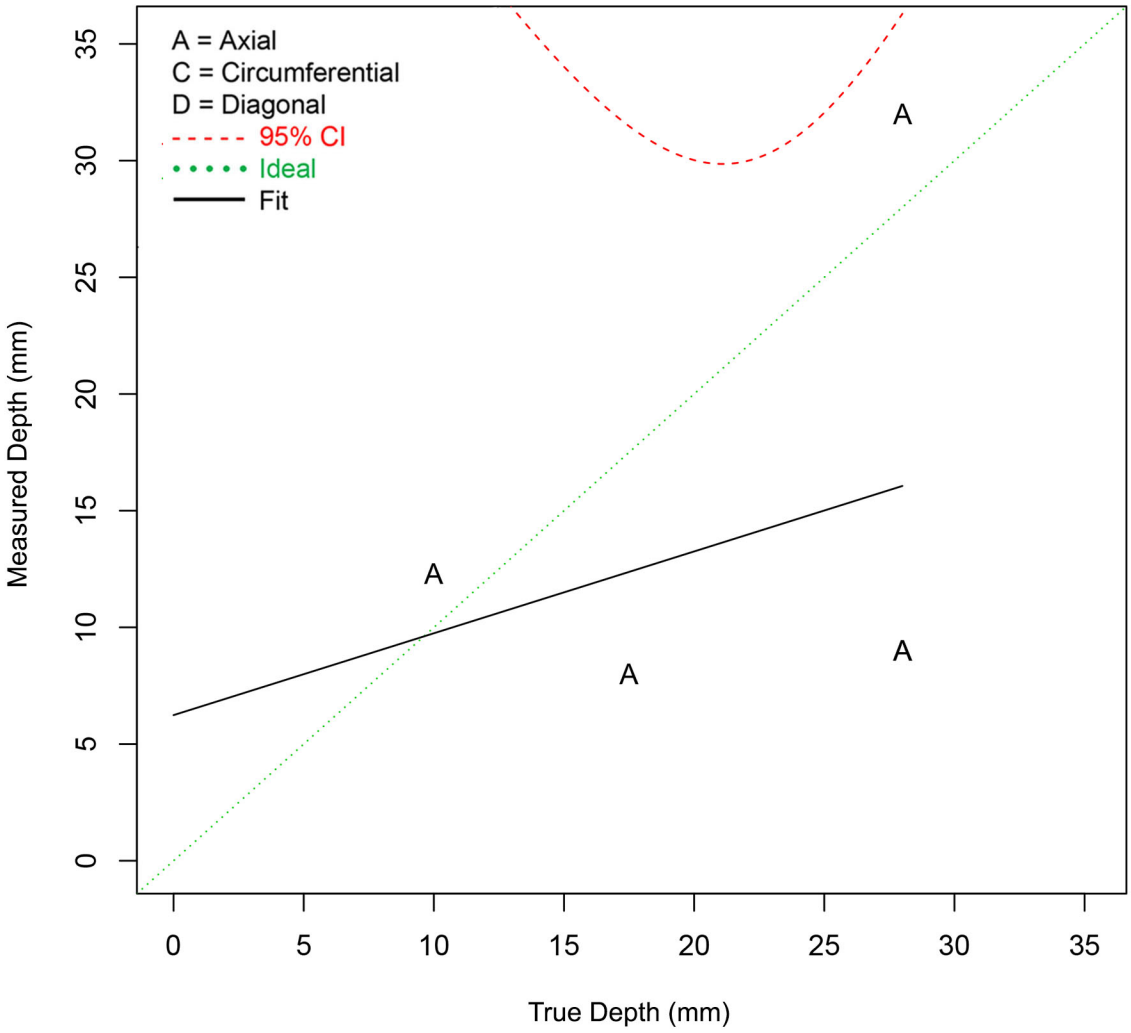

Figure 5.88. Aggregate Depth Sizing Regression Fit for Conventional UT Techniques 108-UT1, 126-UT1, and 134-UT1 for Axial Flaws

5.2.10.3 Summary of Depth Sizing Analysis Results for Circumferential Flaws

This section presents the results of the depth sizing performance analysis of conventional UT techniques applied to the population of detected circumferential flaws. Tabulation of depth sizing bias and RMSE for conventional UT techniques is provided in Table 5.60. In this case, NOBS is equal to the number of detected circumferential flaws. The aggregate depth sizing regression plot is provided in Figure 5.89.

Table 5.60. Summary of Depth Sizing Error for Conventional UT Techniques for Circumferential Flaws

	NOBS	Bias	RMSE
108-UT1	4	−0.3	9.0
126-UT1	3	−0.5	7.4
134-UT1	4	−6.5	7.5
108-UT1 + 126-UT1 + 134-UT1 (Blind)	11	−2.6	8.1

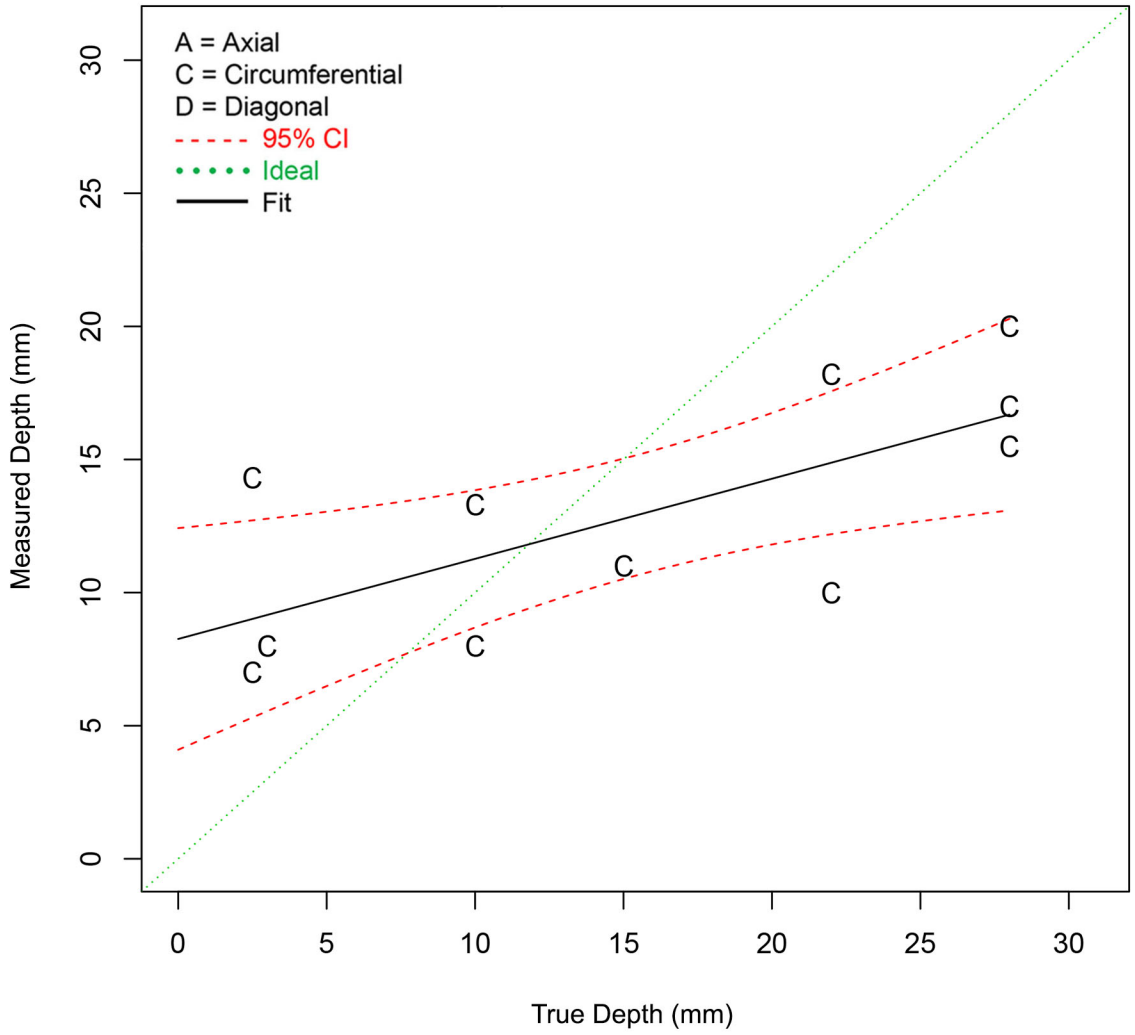

Figure 5.89. Aggregate Depth Sizing Regression Fit for Conventional UT Techniques 108-UT1, 126-UT1, and 134-UT1 for Circumferential Flaws

5.2.11 Length Sizing Performance Analysis

This section presents the results of the length sizing performance analysis of conventional UT techniques applied to LBDMW test blocks in PARENT. Results are presented as tabulations of bias and RMSE and as plots of length sizing regression curves. The following sections include tabulated summaries of length sizing performance for conventional UT techniques for scoring tolerances of 10 mm and 15 mm to

account for the positioning error observed for axial flaws in test block P33. Summaries of length sizing results are provided for the total flaw population, the axial flaw population, and the circumferential flaw population.

Linear regression was used to analyze length sizing data. The formulas for the regression analysis curves, computing RMSE, sizing bias, and sizing StDev are defined in Section 3.4 and in Eqs. (3.7)–(3.11), specifically.

5.2.11.1 Summary of Length Sizing Analysis Results for All Flaws

This section presents the results of the length sizing performance analysis of conventional UT techniques applied to the total detected flaw population. Tabulation of length sizing bias and RMSE for conventional UT techniques are provided in Table 5.61 and Table 5.62 for scoring tolerances of 10 mm and 15 mm, respectively. The NOBS column is the sample size used for length sizing analysis. It is equal to the number of detections.

Aggregate length sizing regression plots are provided in Figure 5.90, Figure 5.91, and Figure 5.92 for the total detected flaw population. Symbols "A" and "C" are used to represent axially oriented flaws and circumferentially oriented flaws, respectively. The symbol "D" in Figure 5.92 refers to flaws with a diagonal orientation. The designation of diagonal orientation is used to denote flaws that do not have a dominant orientation based on dimensions. In this case, flaws in the Quickblind test blocks P15, P16, and P17 were denoted as diagonal. Figure 5.90 and Figure 5.91 provide aggregate regression plots for conventional UT techniques 108-UT1, 126-UT1, and 134-UT1 for scoring tolerances of 10 mm and 15 mm, respectively. Figure 5.92 provides the aggregate regression plot for conventional UT techniques 108-UT0, 126-UT0, and 134-UT0 for scoring tolerances of 10 mm and 15 mm. In this case, the data is the same for a tolerance of 10 mm and 15 mm.

Table 5.61. Summary of Length Sizing Error for Conventional UT Techniques for All Flaw Orientations (tolerance = 10 mm)

	NOBS	Bias	RMSE
108-UT0	3	−11.3	12.4
108-UT1	7	4.9	8.1
126-UT0	2	−6.0	6.3
126-UT1	3	12.3	17.1
134-UT0	3	−9.0	12.2
134-UT1	8	6.8	20.0
108-UT0 + 126-UT0 + 134-UT0 (Quickblind)	8	−9.1	11.1
108-UT1 + 126-UT1 + 134-UT1 (Blind)	18	6.9	15.9
108-UT0 + 126-UT0 + 134-UT0 + 108-UT1 + 126-UT1 + 134-UT1 (Blind + Quickblind)	26	2.0	14.6

Table 5.62. Summary of Length Sizing Error for Conventional UT Techniques for All Flaw Orientations (tolerance = 15 mm)

	NOBS	Bias	RMSE
108-UT0	3	−11.3	12.4
108-UT1	9	6.0	9.0
126-UT0	2	−6.0	6.3
126-UT1	3	12.3	17.1
134-UT0	3	−9.0	12.2
134-UT1	8	6.8	20.0
108-UT0 + 126-UT0 + 134-UT0 (Quickblind)	8	−9.1	11.1
108-UT1 + 126-UT1 + 134-UT1 (Blind)	20	7.2	15.5
108-UT0 + 126-UT0 + 134-UT0 + 108-UT1 + 126-UT1 + 134-UT1 (Blind + Quickblind)	28	2.6	14.4

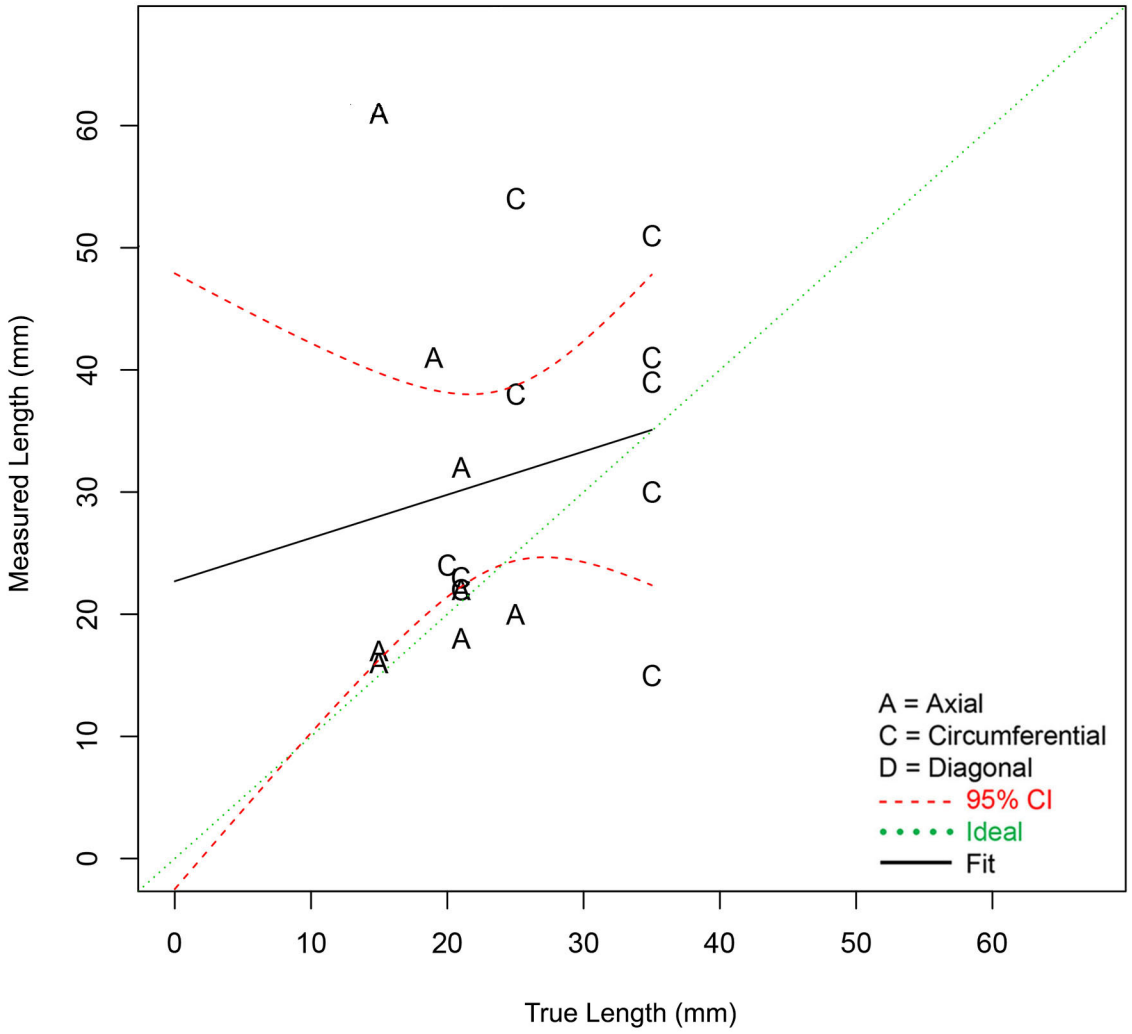

Figure 5.90. Aggregate Length Sizing Regression Fit for Conventional UT Techniques 108-UT1, 126-UT1, and 134-UT1 for All Flaw Orientations (tolerance = 10 mm)

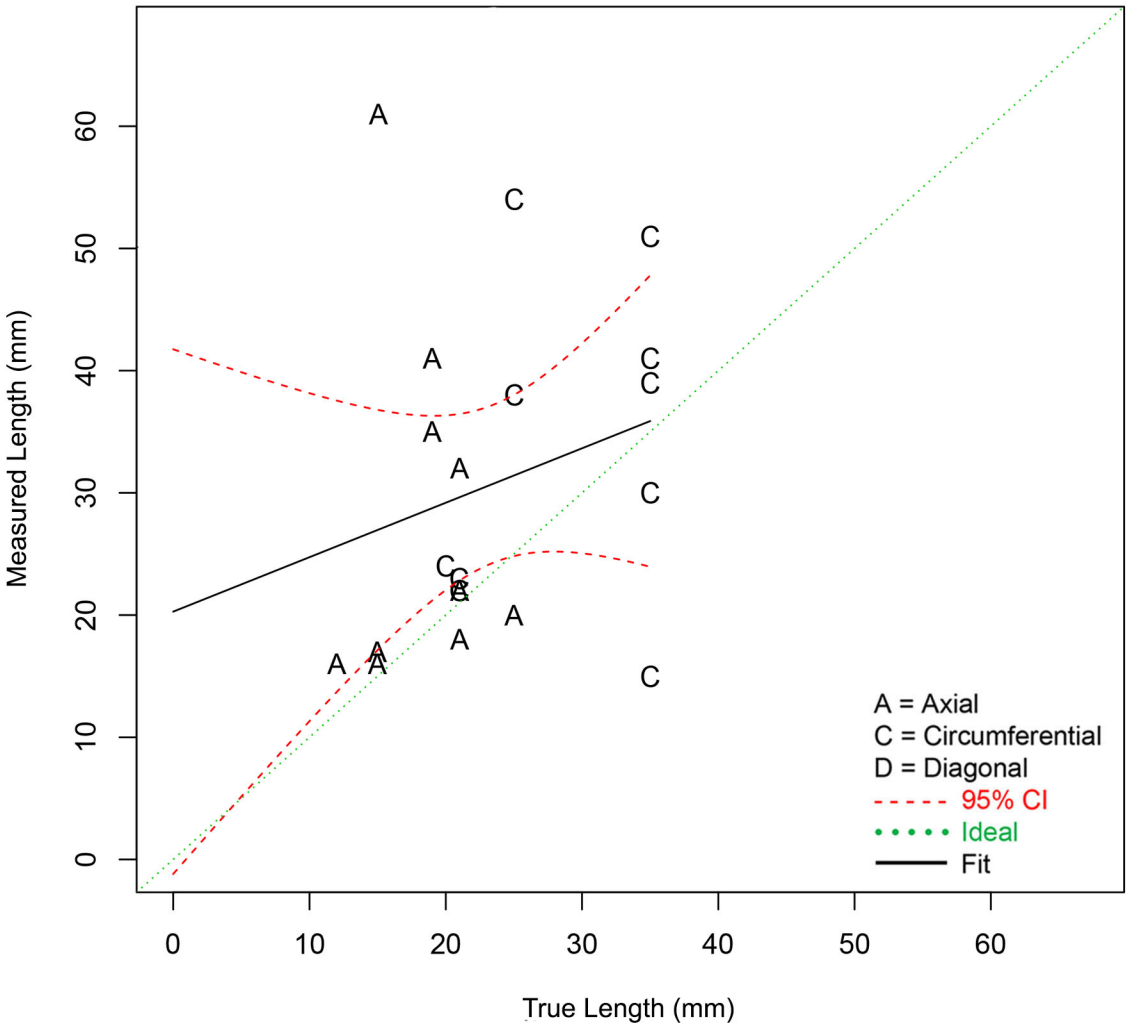

Figure 5.91. Aggregate Length Sizing Regression Fit for Conventional UT Techniques 108-UT1, 126-UT1, and 134-UT1 for All Flaw Orientations (tolerance = 15 mm)

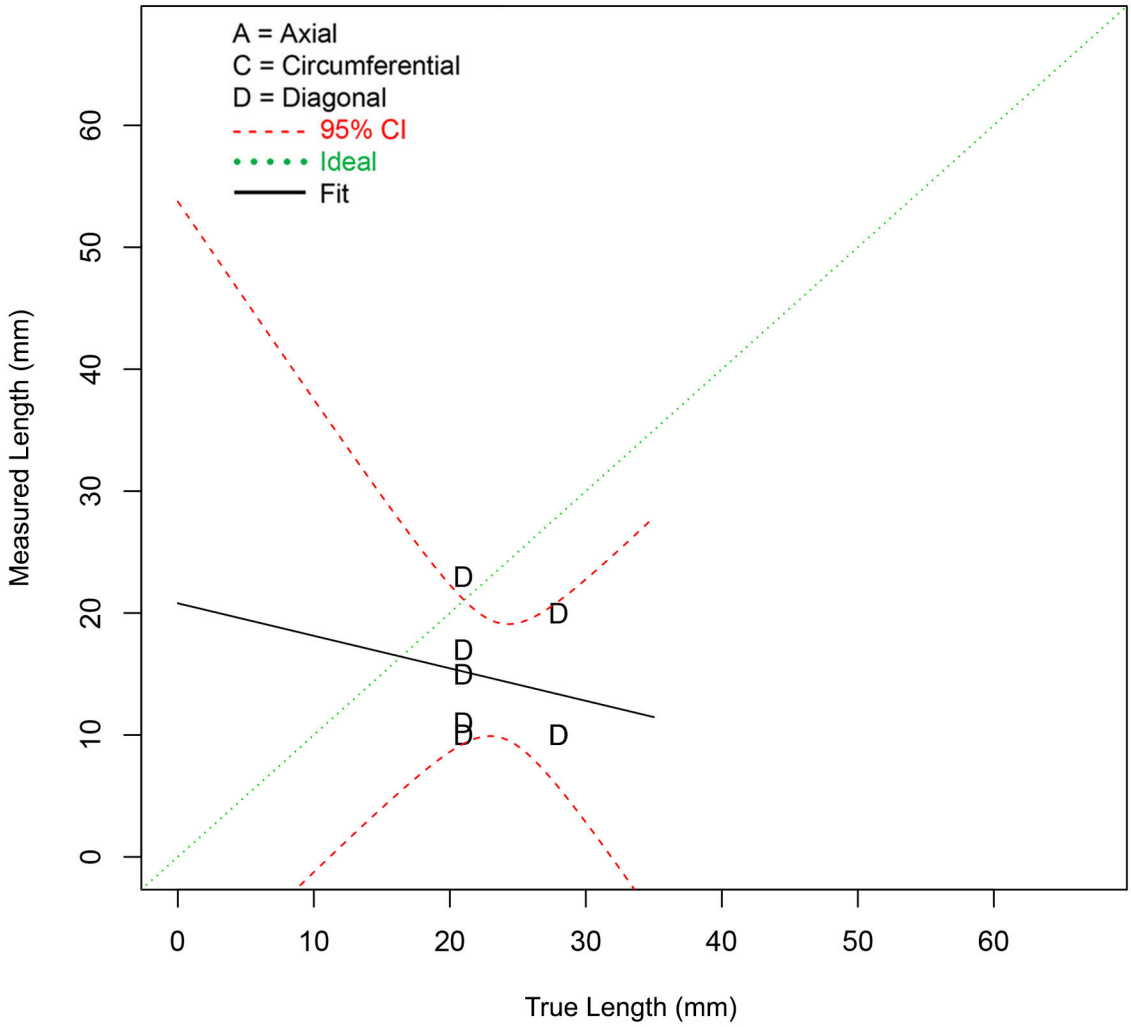

Figure 5.92. Aggregate Length Sizing Regression Fit for Conventional UT Techniques 108-UT0, 126-UT0, and 134-UT0 for All Flaw Orientations (tolerance = 10 mm and 15 mm)

5.2.11.2 Summary of Length Sizing Analysis Results for Axial Flaws

This section presents the results of the length sizing performance analysis of conventional UT techniques applied to the population of detected axial flaws. The algorithm for length sizing error analysis is normally performed by comparing the longest dimension of the flaw with the longest dimension of the associated indication. This algorithm is adequate for the majority of flaw and indication pairs in which the indication has the same orientation as the associated flaw. However, the inspections of P33 by conventional UT techniques resulted in some indications with orientations that do not match the orientation of their associated flaws. This can be observed by reviewing Figure 5.51 and Figure 5.52, which depict the indication plots for techniques 126-UT1 and 134-UT1. In these instances, both techniques produce an indication (indication 02 for 126-UT1 and indication 01 for 134-UT1) with a circumferential orientation that is associated with an axially oriented flaw. Also, technique 134-UT1 has another indication (indication 09) that is also circumferentially oriented and associated with an axial flaw.

In this case, it is of interest to perform length size error analysis by comparing the axial dimension of the flaw to the axial dimension of the associated indication in addition to the standard length sizing analysis.

In the tables and figures below, results are presented for standard length sizing error analysis and for axial dimension length sizing analysis. Tabulation of length sizing bias and RMSE for conventional UT techniques are provided in Table 5.63 and Table 5.64 for standard length sizing analysis for tolerances of 10 mm and 15 mm, respectively. Length sizing bias and RMSE are tabulated in Table 5.65 and Table 5.66 for axial dimension length sizing analysis for tolerances of 10 mm and 15 mm, respectively. In this analysis, NOBS is equal to the number of detected axial flaws. Table 5.63 and Figure 5.65, indicate that the length sizing error results based on the axial dimension analysis does result in a smaller RMSE and a bias with lower magnitude.

The aggregate length sizing regression plots are provided in Figure 5.93 and Figure 5.94 for standard length sizing analysis for tolerances of 10 mm and 15 mm, respectively, and in Figure 5.95 and Figure 5.96 for axial dimension length sizing analysis for tolerances of 10 mm and 15 mm, respectively. In all plots, the confidence bounds are fairly large; however, the slope of the regression curve does change from negative to positive when the length sizing analysis is performed based on comparison of axial dimensions, rather than largest dimensions.

Table 5.63. Summary of Length Sizing Error for Conventional UT Techniques for Axial Flaws (tolerance = 10 mm)

	NOBS	Bias	RMSE
108-UT1	3	−0.3	1.9
126-UT1	1	2.0	2.0
134-UT1	4	18.5	26.2
108-UT1 + 126-UT1 + 134-UT1 (Blind)	8	9.4	18.6

Table 5.64. Summary of Length Sizing Error for Conventional UT Techniques for Axial Flaws (tolerance = 15 mm)

	NOBS	Bias	RMSE
108-UT1	5	3.8	7.5
126-UT1	1	2.0	2.0
134-UT1	4	18.5	26.2
108-UT1 + 126-UT1 + 134-UT1 (Blind)	10	9.5	17.4

Table 5.65. Summary of Axial Dimension Length Sizing Error for Conventional UT Techniques for Axial Flaws (tolerance = 10 mm)

	NOBS	Bias	RMSE
108-UT1	3	−0.3	1.9
126-UT1	1	−15.0	15.0
134-UT1	4	−7.0	13.5
108-UT1 + 126-UT1 + 134-UT1 (Blind)	8	−5.5	11.0

Table 5.66. Summary of Axial Dimension Length Sizing Error for Conventional UT Techniques for Axial Flaws (tolerance = 15 mm)

	NOBS	Bias	RMSE
108-UT1	5	3.8	7.5
126-UT1	1	−15.0	15.0
134-UT1	4	−7.0	13.5
108-UT1 + 126-UT1 + 134-UT1 (Blind)	10	−2.4	11.1

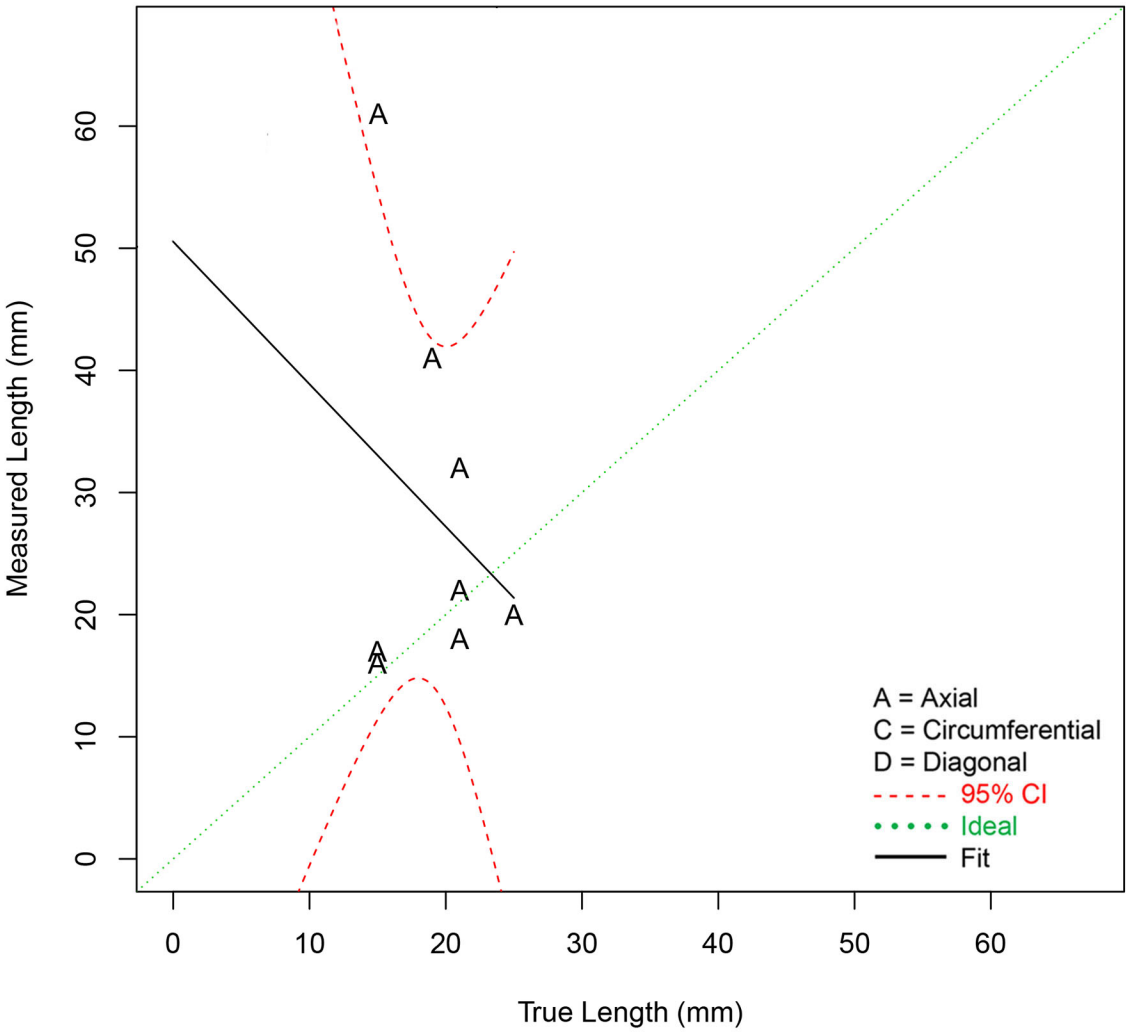

Figure 5.93. Aggregate Length Sizing Regression Fit for Conventional UT Techniques 108-UT1, 126-UT1, and 134-UT1 for Axial Flaws (tolerance = 10 mm)

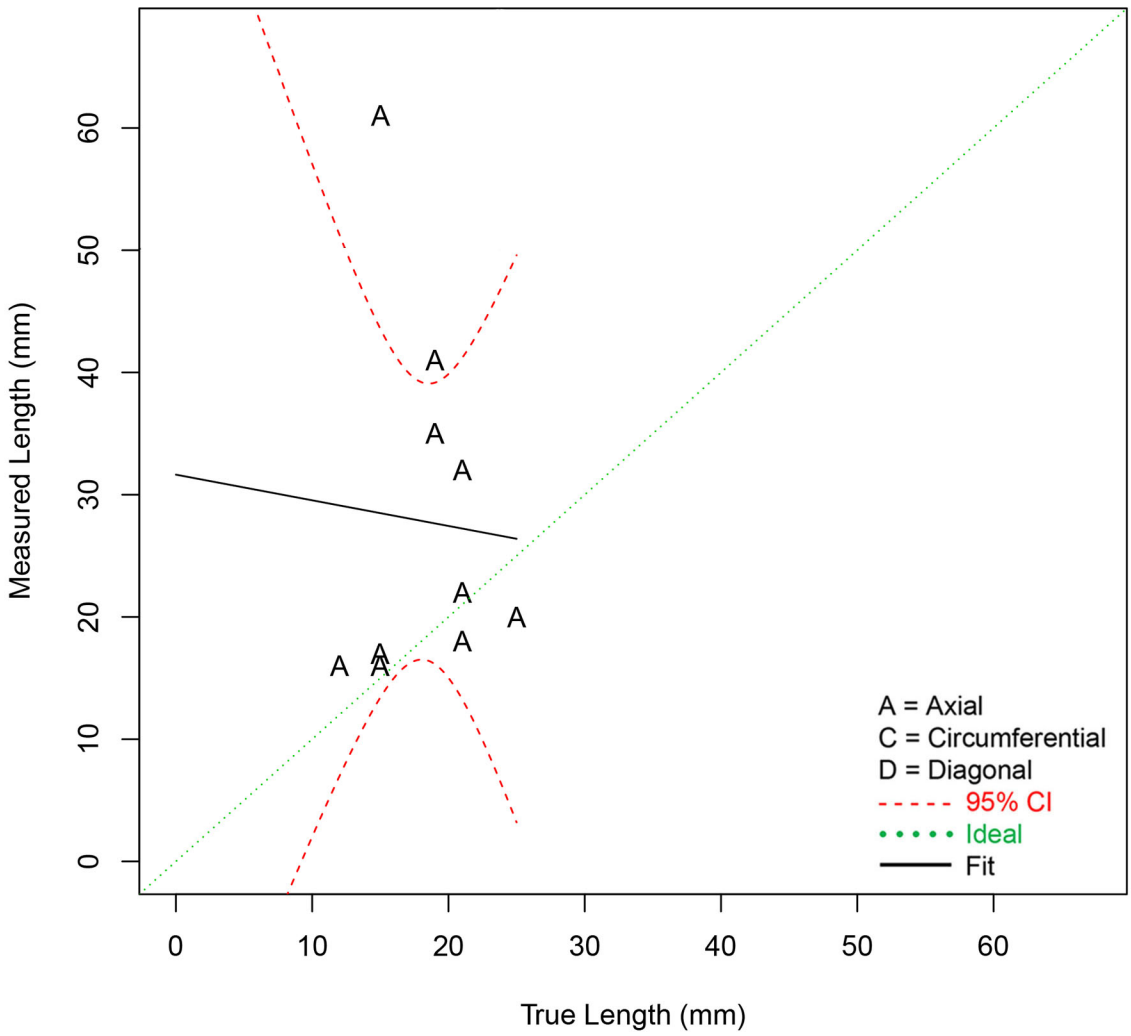

Figure 5.94. Aggregate Length Sizing Regression Fit for Conventional UT Techniques 108-UT1, 126-UT1, and 134-UT1 for Axial Flaws (tolerance = 15 mm)

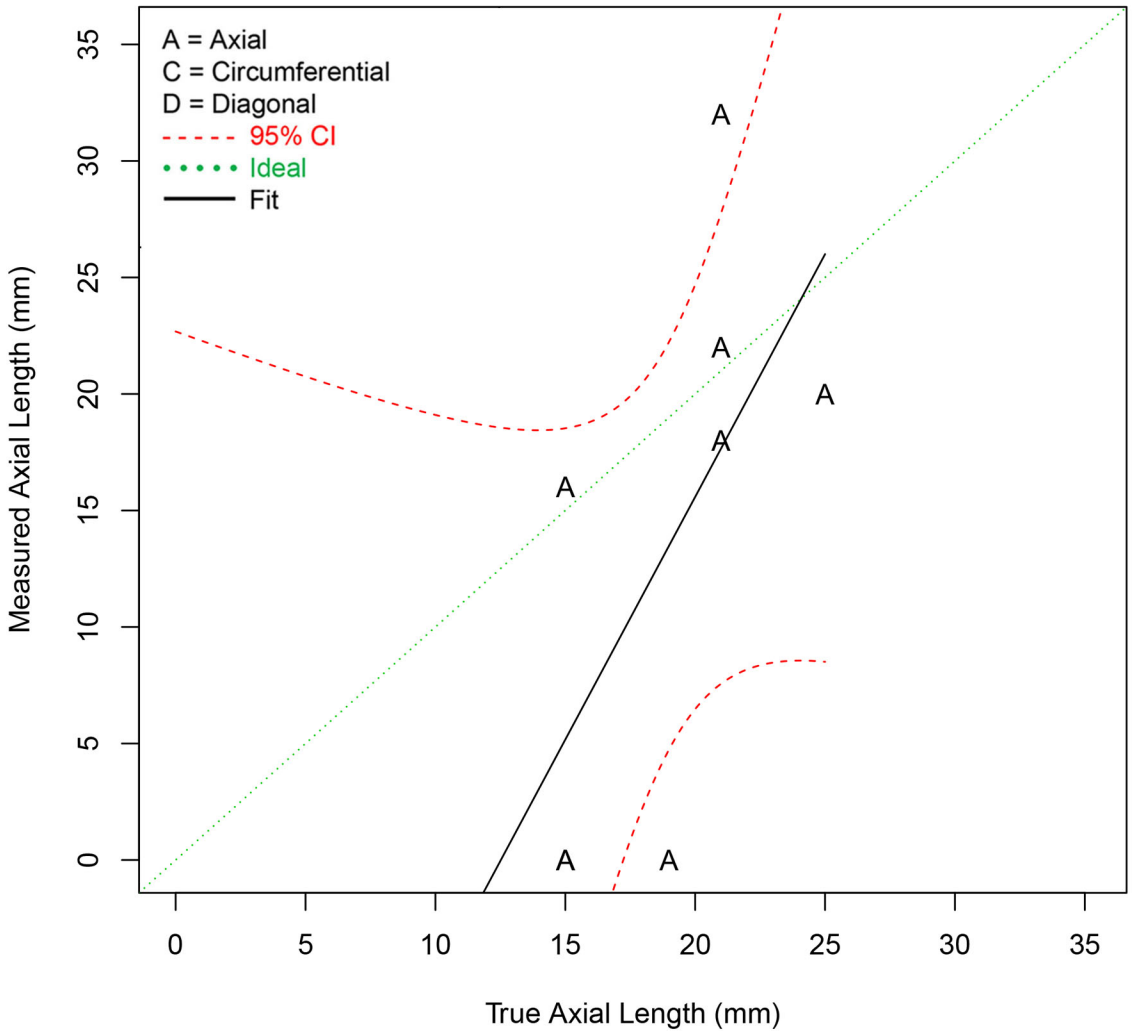

Figure 5.95. Aggregate Axial Dimension Length Sizing Regression Fit for Conventional UT Techniques 108-UT1, 126-UT1, and 134-UT1 for Axial Flaws (tolerance = 10 mm)

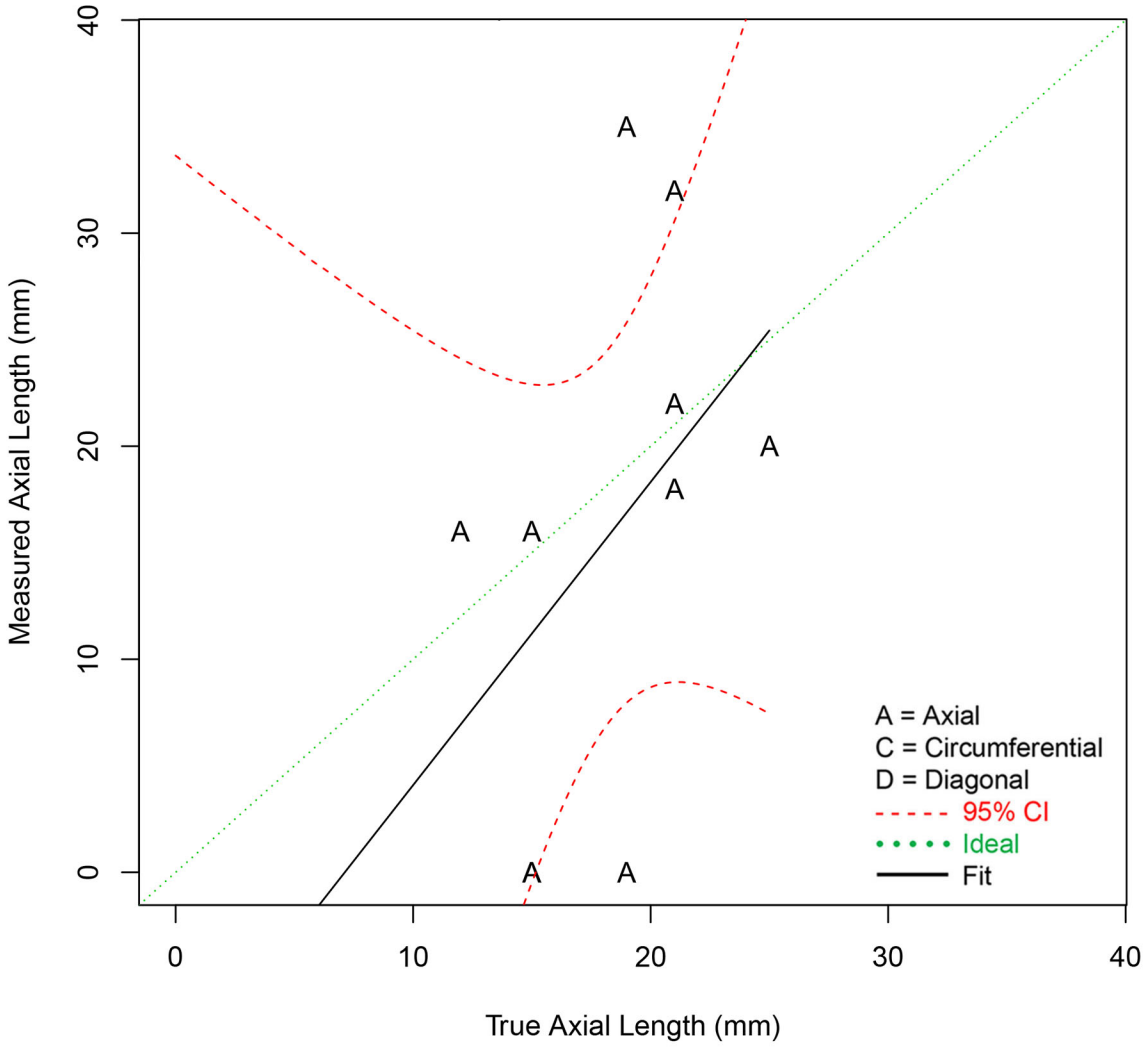

Figure 5.96. Aggregate Axial Dimension Length Sizing Regression Fit for Conventional UT Techniques 108-UT1, 126-UT1, and 134-UT1 for Axial Flaws (tolerance = 15 mm)

5.2.11.3 Summary of Length Sizing Analysis Results for Circumferential Flaws

This section presents the results of the length sizing performance analysis of conventional UT techniques applied to the population of detected circumferential flaws. The standard algorithm for length sizing analysis is used for circumferential flaws because all indications associated with circumferential flaws have a circumferential orientation. Further, because positioning error on test block P33 is only associated with axial flaws, the analysis results for 10 mm are identical to the results for 15 mm. Tabulation of length sizing bias and RMSE for conventional UT techniques are provided in Table 5.67 for the circumferential flaws. In this analysis, NOBS is equal to the number of detected circumferential flaws. The aggregate length sizing regression plots are provided in Figure 5.97 for standard length sizing analysis.

Table 5.67. Summary of Length Sizing Error for conventional UT Techniques for Circumferential Flaws

	NOBS	Bias	RMSE
108-UT1	4	8.8	10.5
126-UT1	2	17.5	20.9
134-UT1	4	−5.0	10.5
108-UT1 + 126-UT1 + 134-UT1 (Blind)	10	5.0	13.3

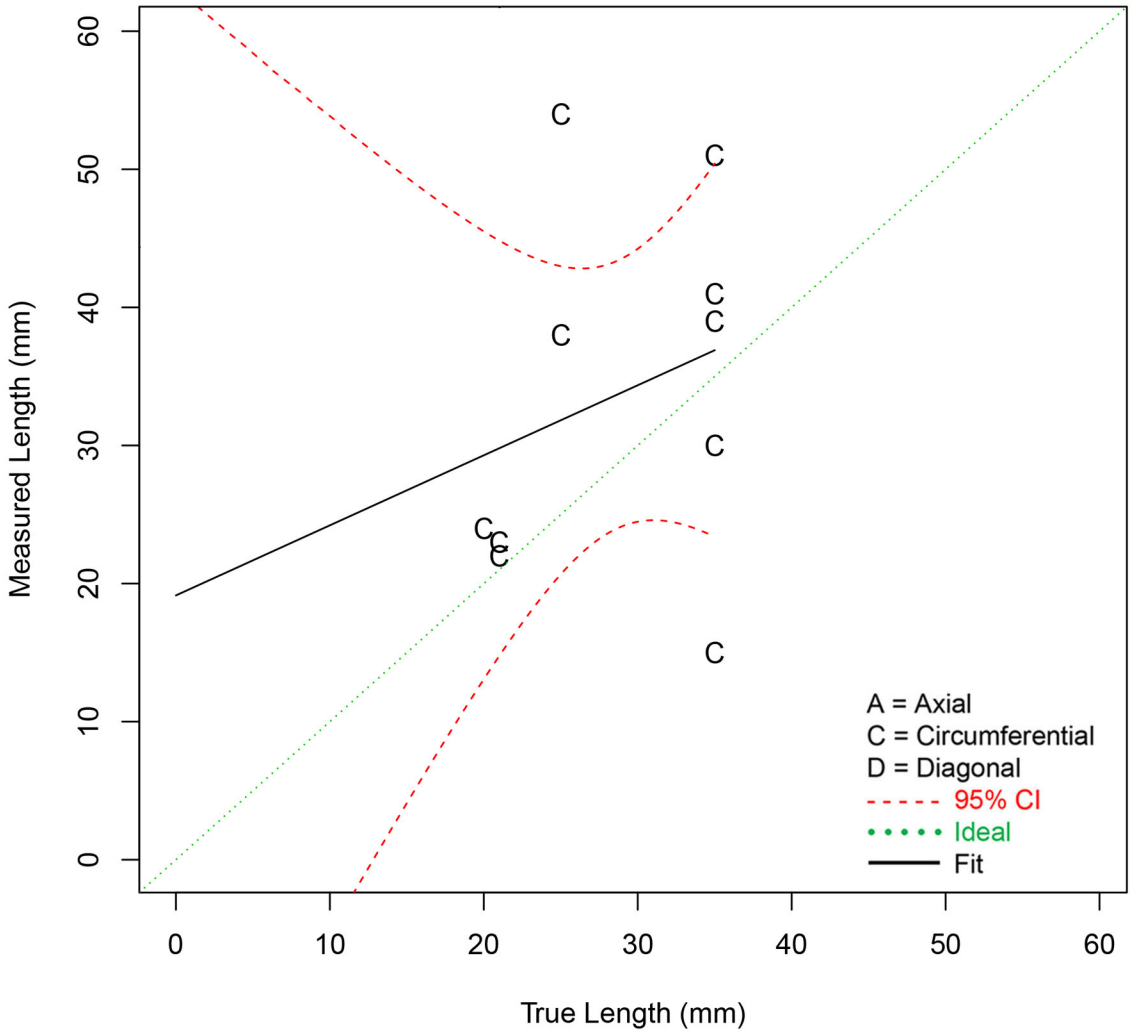

Figure 5.97. Aggregate Length Sizing Regression Fit for Conventional UT Techniques 108-UT1, 126-UT1, and 134-UT1 for Circumferential Flaws

5.2.11.4 Summary of Length Sizing Analysis Results for Diagonal Flaws

This section presents the results of the length sizing performance analysis of conventional UT techniques applied to the population of detected diagonal flaws. The algorithm for length sizing error analysis is normally performed by comparing the longest dimension of the flaw with the corresponding dimension of the associated indication. This algorithm is adequate for the majority of flaws, which have a clear axial or

circumferential orientation. However, the Quickblind test blocks have flaws that were intended to be axially oriented but are reported to have a diagonal orientation based on destructive analysis, which indicated a flaw morphology with comparable axial and circumferential dimensions. In this case, it is of interest to perform length sizing error analysis by comparing the axial dimension of the flaw to the axial dimension of the associated indication, in addition to performing length sizing error analysis by the standard method. In the tables and figures below, results are presented for standard length sizing error analysis, for axial dimension length sizing analysis, and for circumferential dimension length sizing analysis. Tabulation of length sizing bias and RMSE for PAUT techniques are provided in Table 5.68, Table 5.69, and Table 5.70 for standard length sizing analysis, axial dimension length sizing analysis, and circumferential dimension length sizing analysis, respectively. In this case, NOBS is equal to the number of detected diagonal flaws. Table 5.68 and Table 5.69 indicate that the length sizing error results based on the standard analysis are larger than length sizing error based on the axial dimension length sizing analysis. However, the results obtained in Table 5.70 for the circumferential dimension analysis are significantly different with much greater RMSE and a negative bias of large magnitude, which is consistent with results for PAUT techniques in Section 5.1.11.4.

The aggregate length sizing regression plots are provided in Figure 5.98, Figure 5.99, and Figure 5.100 for standard length sizing analysis, axial dimension length sizing analysis, and circumferential dimension length sizing analysis, respectively. From these plots, it appears that the flaws produce responses that are indicative of axially oriented flaws as the reported measurements for circumferential dimensions are near zero. This is also consistent with results for PAUT techniques in Section 5.1.11.4. Thus, it appears that flaws in Quickblind test blocks are producing PAUT and conventional UT responses consistent with axially oriented flaws.

Table 5.68. Summary of Length Sizing Error for Conventional UT Techniques for Diagonal Flaws

	NOBS	Bias	RMSE
108-UT0	3	−11.3	12.4
126-UT0	2	−6.0	6.3
134-UT0	3	−9.0	12.2
108-UT0+ 126-UT0 + 134-UT0 (Quickblind)	8	−9.1	11.1

Table 5.69. Summary of Axial Dimension Length Sizing Error for Conventional UT Techniques for Diagonal Flaws

	NOBS	Bias	RMSE
108-UT0	3	−7.3	8.6
126-UT0	2	0.0	1.0
134-UT0	3	−5.0	7.3
108-UT0+ 126-UT0 + 134-UT0 (Quickblind)	8	−4.6	6.9

Table 5.70. Summary of Circumferential Dimension Length Sizing Error for Conventional UT Techniques for Diagonal Flaws

	NOBS	Bias	RMSE
108-UT0	3	−19.7	21.0
126-UT0	2	−24.5	24.7
134-UT0	3	−14.3	14.9
108-UT0+ 126-UT0 + 134-UT0 (Quickblind)	8	−18.9	20.0

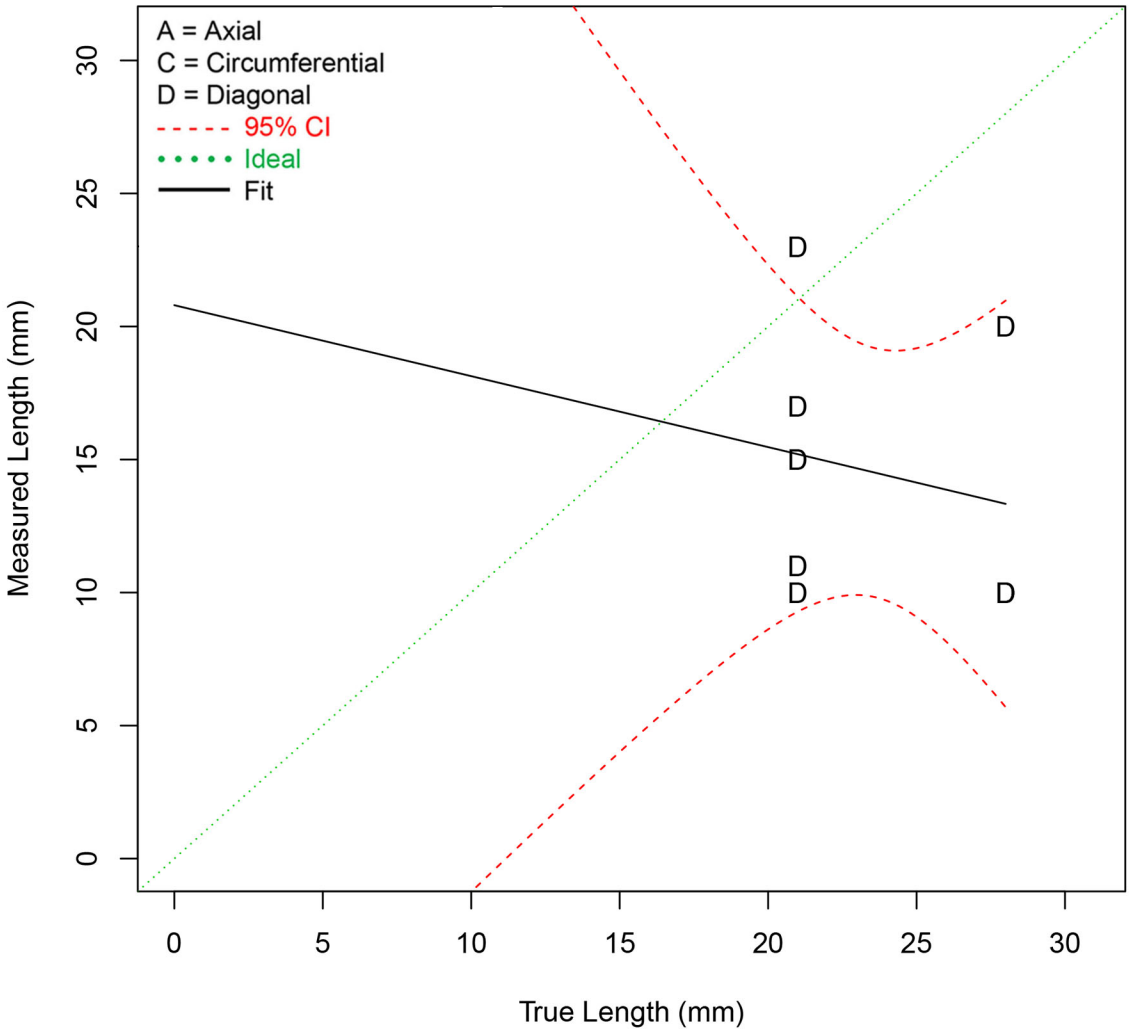

Figure 5.98. Aggregate Length Sizing Regression Fit for Conventional UT Techniques 108-UT0, 126-UT0, and 134-UT0 for Diagonal Flaws

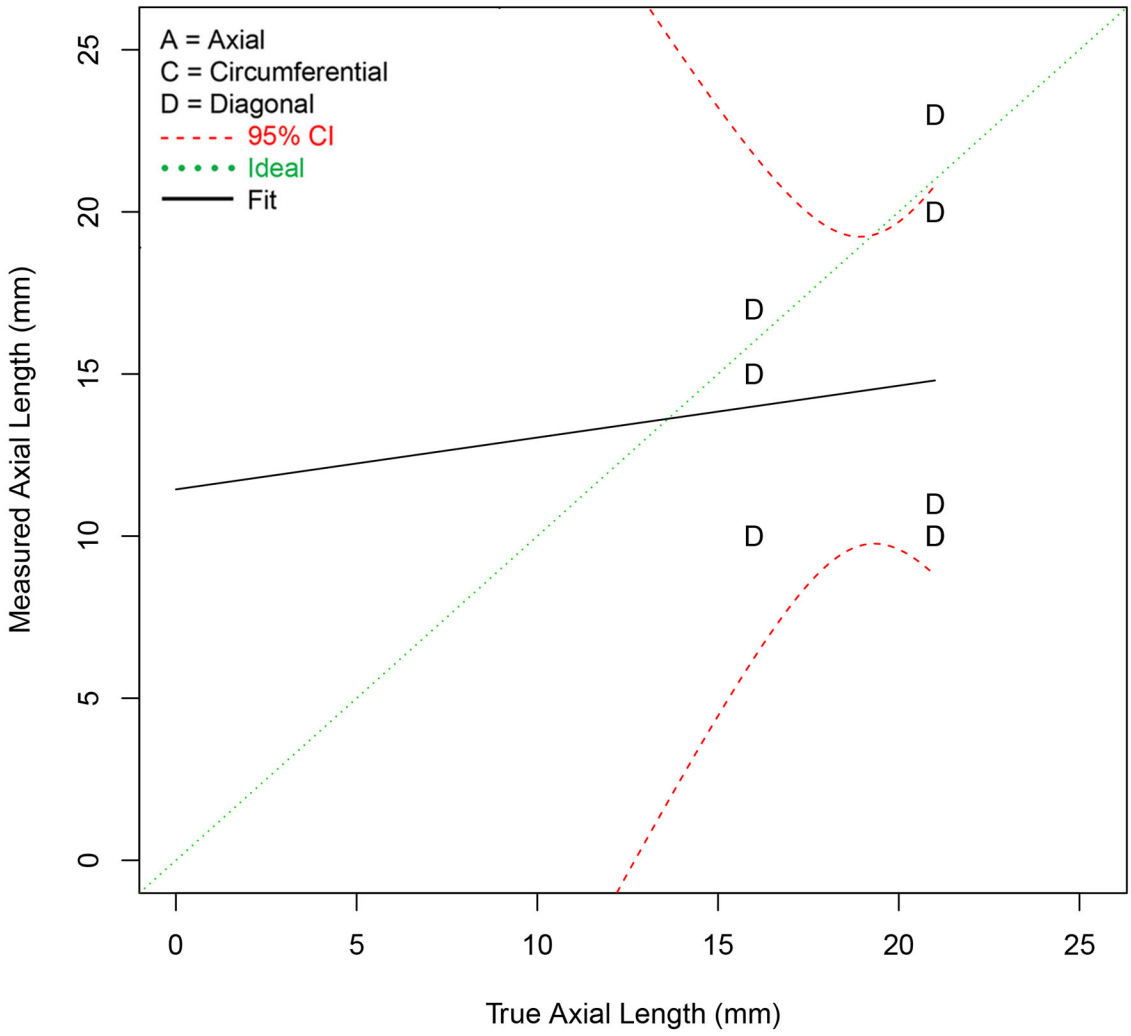

Figure 5.99. Aggregate Axial Dimension Length Sizing Regression Fit for Conventional UT Techniques 108-UT0, 126-UT0, and 134-UT0 for Diagonal Flaws

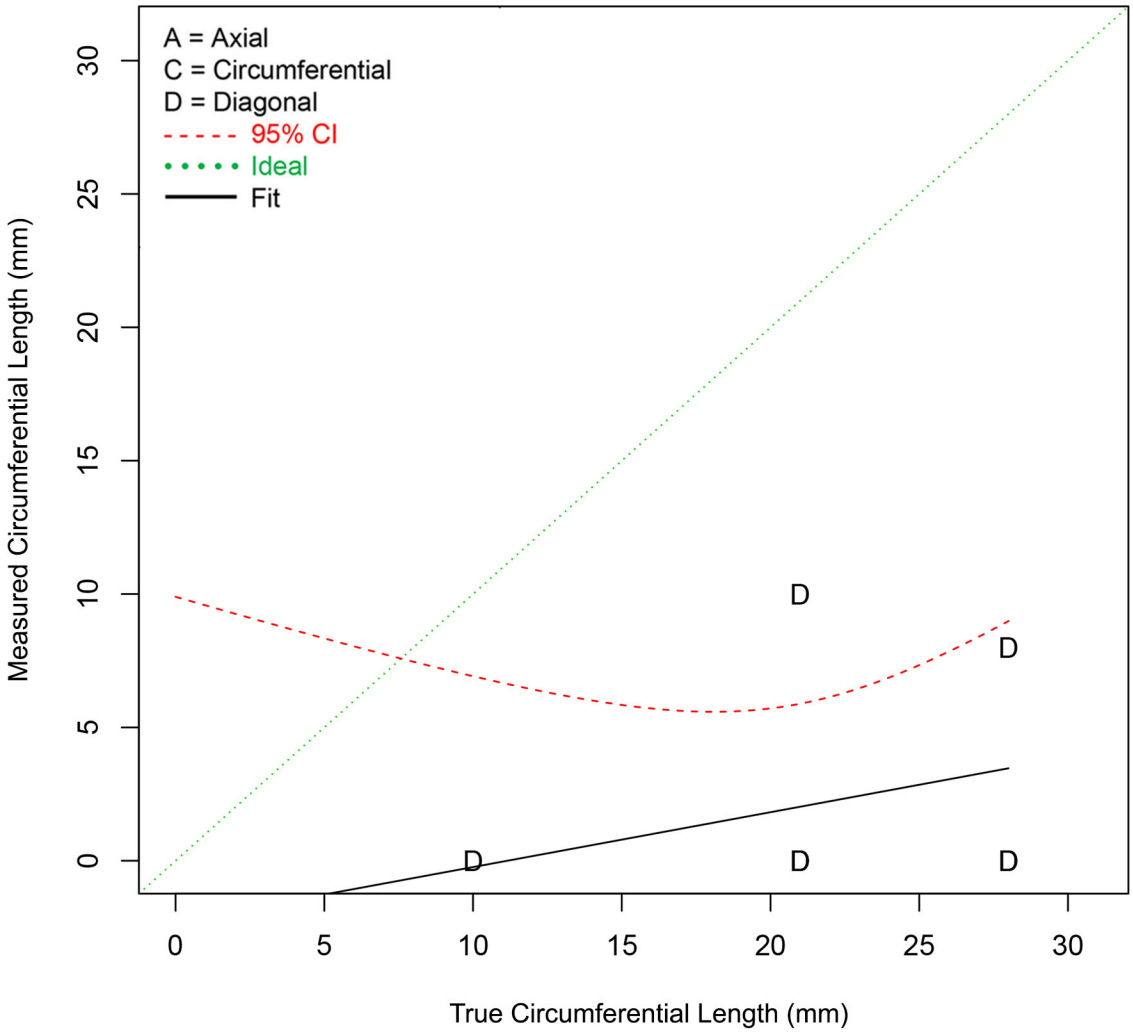

Figure 5.100. Aggregate Circumferential Dimension Length Sizing Regression Fit for Conventional UT Techniques 108-UT0, 126-UT0, and 134-UT0 for Diagonal Flaws

5.3 Blind and Quickblind Comparison Summary

The analysis of PAUT and conventional UT technique data was performed with the objective of comparing results between the Quickblind and Blind testing. A comparison of Quickblind and Blind test results from procedures UT.PAUT.113, UT.ECT.144, and UT.ECT.106 is summarized in Section 6.3 of NUREG/CR-7235 (Meyer and Heasler 2017). Overall, a distinguishing trend in performance for Quickblind and Blind testing could not be identified with the exception of bias observed in length sizing. In this case, the results indicated that length sizing bias was significantly more negative for Quickblind testing relative to Blind testing. In this section, Quickblind and Blind performance results are compared for PAUT and conventional UT techniques. A detection performance comparison is provided in Section 5.3.1 followed by depth sizing and length sizing performance comparisons in Sections 5.3.2 and 5.3.3, respectively.

5.3.1 Detection Performance Comparison Summary

A summary of Quickblind and Blind detection performance is provided in Table 5.71 and Table 5.72 as POD as a function of depth and length, respectively, for PAUT techniques. Similarly, a summary of Quickblind and Blind detection performance for conventional UT techniques is provided in Table 5.73 and Table 5.74 as a function of depth and length, respectively. As anticipated, the POD obtained from Quickblind testing exceeds the POD from Blind testing for all scenarios with the exception of POD as a function of length for PAUT techniques, as represented in Table 5.72.

Table 5.71. Summary Comparison of Blind and Quickblind Results for PAUT Techniques for POD (%) versus Flaw Depth for All Flaw Orientations (tolerance = 15 mm)

	NOBS	FCR	0 mm	5 mm	10 mm	15 mm	30 mm	60 mm
108-PA0 + 126-PA0 (Quickblind)	6	1.45	4	14	39	71	99	100
108-PA1 + 126-PA1 (Blind)	38	1.32	5	10	20	36	87	100
PAUT (from Table 5.8, NUREG/CR-7235) tolerance = 10 mm	38	1.51	5	10	21	37	82	-

Table 5.72. Summary Comparison of Blind and Quickblind Results for PAUT Techniques for POD (%) versus Flaw Length for All Flaw Orientations (tolerance = 15 mm)

	NOBS	FCR	0 mm	5 mm	10 mm	15 mm	30 mm	60 mm
108-PA0 + 126-PA0 (Quickblind)	6	1.46	4	8	15	25	71	99
108-PA1 + 126-PA1 (Blind)	38	0.98	3	7	15	30	85	100
PAUT (from Table 5.14, NUREG/CR-7235) tolerance = 10 mm	38	1.51	4	8	16	28	78	-

Table 5.73. Summary Comparison of Blind and Quickblind Results for Conventional UT Techniques for POD (%) versus Flaw Depth for All Flaw Orientations (tolerance = 15 mm)

	NOBS	FCR	0 mm	5 mm	10 mm	15 mm	30 mm	60 mm
108-UT0 + 126-UT0 + 134-UT0 (Quickblind)	9	1.03	4	13	34	64	99	100
108-UT1 + 126-UT1 + 134-UT1 (Blind)	57	1.69	5	10	20	36	85	100
UT (from Table 5.8, NUREG/CR-7235) tolerance = 10 mm	57	1.88	5	10	19	32	74	-

Table 5.74. Summary Comparison of Blind and Quickblind Results for Conventional UT Techniques for POD (%) versus Flaw Length for All Flaw Orientations (tolerance = 15 mm)

	NOBS	FCR	0 mm	5 mm	10 mm	15 mm	30 mm	60 mm
108-UT0 + 126-UT0 + 134-UT0 (Quickblind)	19	1.03	3	8	21	44	95	100
108-UT1 + 126-UT1 + 134-UT1 (Blind)	57	1.69	4	8	15	27	74	99
UT (from Table 5.14, NUREG/CR-7235) tolerance = 10 mm	57	1.88	5	8	15	25	70	-

5.3.2 Depth Sizing Performance Comparison Summary

A summary of Quickblind and Blind depth sizing performance is provided in Table 5.75 and Table 5.76 for PAUT techniques and conventional UT techniques, respectively. Blind depth sizing results are presented in both tables for all flaws, for axial flaws, and for circumferential flaws. The tables do not indicate a clear distinguishing trend in depth sizing performance for Blind and Quickblind results.

Table 5.75. Summary Comparison of Blind and Quickblind Depth Sizing Results for PAUT Techniques (tolerance = 15 mm)

	NOBS	Bias	RMSE
108-PA0 +126-PA0 (Quickblind)	4	−10.6	11.3
108-PA1 + 126-PA1 (Blind) [All Flaws]	17	−0.4	9.2
108-PA1 + 126-PA1 (Blind) [Axial Flaws]	8	−4.2	6.1
108-PA1 + 126-PA1 (Blind) [Circumferential Flaws]	9	2.9	11.4
PAUT (from Table 5.20, NUREG/CR-7235) [All Flaws]	15	0.1	9.7

Table 5.76. Summary Comparison of Blind and Quickblind Depth Sizing Results for Conventional UT Techniques (tolerance = 15 mm)

	NOBS	Bias	RMSE
108-UT0 + 126-UT0 + 134-UT0 (Quickblind)	8	−6.2	9.6
108-UT1 + 126-UT1 + 134-UT1 (Blind) [All Flaws]	16	−4.4	9.8
108-UT1 + 126-UT1 + 134-UT1 (Blind) [Axial Flaws]	5	−8.2	12.9
108-UT1 + 126-UT1 + 134-UT1 (Blind) [Circumferential Flaws]	11	−2.6	8.1
UT (from Table 5.20, NUREG/CR-7235) [All Flaws]	16	−4.4	9.8

5.3.3 Length Sizing Performance Comparison Summary

A summary of Quickblind and Blind length performance is provided in Table 5.77 and Table 5.78 for PAUT techniques and in Table 5.79 and Table 5.80 for conventional UT techniques. Table 5.77 and Table 5.79 provide length sizing results obtained by the standard analysis method while Table 5.78 and Table 5.80 provide axial dimension length sizing results. Overall, it appears that length sizing RMSE obtained from Quickblind testing is consistently lower than length sizing RMSE obtained in Blind testing.

The length sizing bias is significantly more negative for Quickblind results relative to Blind results for the standard method of length sizing analysis. However, when length sizing analysis is performed based on measurements of axial dimensions, the gap in bias between Quickblind results and Blind results becomes much smaller or even reverses (Table 5.78).

Table 5.77. Summary Comparison of Length Sizing Error for PAUT Techniques by Standard Method (tolerance = 15 mm)

	NOBS	Bias	RMSE
108-PA0 and 126-PA0 (Quickblind)	4	−0.5	6.1
108-PA1 + 126-PA1 (Blind)	16	3.9	9.5
PAUT (from Table 5.26, NUREG/CR-7235)	14	3.1	8.9

Table 5.78. Summary Comparison of Axial Dimension Length Sizing Error for PAUT Techniques (tolerance = 15 mm)

	NOBS	Bias	RMSE
108-PA0 + 126-PA0 (Quickblind)	4	2.0	6.7
108-PA1 + 126-PA1 (Blind)	8	−2.1	9.4

Table 5.79. Summary Comparison of Length Sizing Error for Conventional UT Techniques by Standard Method (tolerance = 15 mm)

	NOBS	Bias	RMSE
108-UT0 + 126-UT0 + 134-UT0 (Quickblind)	8	−9.1	11.1
108-UT1 + 126-UT1 + 134-UT1 (Blind)	20	7.2	15.5
UT (from Table 5.26, NUREG/CR-7235)	18	6.9	15.9

Table 5.80. Summary Comparison of Axial Dimension Length Sizing Error for Conventional UT Techniques (tolerance = 15 mm)

	NOBS	Bias	RMSE
108-UT0+ 126-UT0 + 134-UT0 (Quickblind)	8	−4.6	6.9
108-UT1 + 126-UT1 + 134-UT1 (Blind)	10	−2.4	11.1

6.0 BMI Analysis

The objective of this effort is to pool J-groove weld surface inspection data from the Program for Inspection of Nickel Alloy Components (PINC) with PARENT to enhance overall sample size of J-groove weld surface inspection data to obtain an estimate of detection and length sizing performance that has greater representativeness. In this case, however, the analysis is restricted to ECT procedures. In PINC, variations of potential drop testing and a phased-array UT procedure were applied to inspect bottom-mounted instrumentation (BMI) specimens from the J-groove weld surface. However, data collected by potential drop or PAUT procedures is not included in this analysis, because only ECT procedures were employed in PARENT. Thus, there is no additional potential drop or PAUT data from PARENT to pool with PINC data. Two test blocks were utilized in both the PINC and PARENT studies. These test blocks included PINC test block 5.1 (PARENT alias P25) and PINC test block 5.3 (PARENT alias P26). The true state defined for these test blocks in PINC was slightly different than the true state defined in PARENT. Thus, a true state is defined for these test blocks in this effort so that the evaluation of PINC and PARENT data is consistent. The following sections include a summary of the ECT techniques employed for J-groove weld surface inspections in PINC and PARENT, a discussion of how the true states in PINC test block 5.1 (PARENT alias P25) and PINC test block 5.3 (PARENT alias P26) are defined in this effort, the results of detection performance analysis, and the results of length sizing performance analysis.

6.1 Summary of BMI Inspection Procedures

Summaries of procedures used for J-groove weld surface inspections of BMI test blocks for PINC and PARENT are included in Table 6.1 and Table 6.2. All of the procedures summarized in these tables are ECT procedures with frequencies ranging from 100 kHz to 500 kHz. The tables also indicate which procedures were automated and which were applied manually, and summarizes which test blocks were inspected by each procedure. Table 6.2 also indicates that procedures used in PARENT were encoded. Table 6.1 and Table 6.2 indicate that two ECT array procedures were employed in PINC and one ECT array procedure was employed in PARENT.

Table 6.1. Summary of Procedures Used for J-groove Surface Weld Inspections in BMI Test Blocks in PINC

Team	Detection Technique	Manual or Automated	Test Block Inspections
373	ECT 300 kHz	Automatic	5.1, 5.2, 5.3, 5.6, 5.7, 5.8, 5.9, 5.10, 5.11, 5.12, 5.13, 5.14, 5.15, 5.16
38	Array ECT 100 kHz	Manual	5.6, 5.7, 5.8, 5.9, 5.10, 5.11, 5.12, 5.13, 5.14, 5.15, 5.16
70	ECT 400 kHz	Automatic	5.6, 5.7, 5.8, 5.9, 5.10, 5.11, 5.12, 5.13, 5.14, 5.15, 5.16
99	Array ECT 200 kHz	Automatic	5.1, 5.2, 5.3, 5.6, 5.7, 5.8, 5.9, 5.10, 5.11, 5.12

Table 6.2. Summary of Procedures Used for J-groove Surface Weld Inspections in BMI Test Blocks in PARENT

Team	Procedure ID	Manual or Automated	Encoded (Y/N)	Probe Frequency/Description	Test Block Inspections
124	ECT.124	Automated	Y	100 kHz Probe with ferrite core driven both in driver pick-up and differential modes	P6, P8, P9, P25, and P26
108	ECT.108	Automated	Y	32-channel array 500 kHz Pancake coil probe Flexible array	P6, P8, P9, P25, and P26

6.2 True State of PINC Test Block 5.1/PARENT Test Block P25

PINC test blocks 5.1 and 5.3 were reutilized in PARENT with aliases P25 and P26, respectively. To ensure consistency in the evaluation of procedures used in PINC and PARENT, the true state defined for test blocks 5.1 and 5.3 in PINC were reviewed in comparison to the true states used for PARENT (i.e., P25 and P26). A cross-sectional view of test block 5.1 (P25) is provided in Figure 6.1. An illustration of the true state used for J-groove weld surface examination evaluations is provided in Figure 6.2. In Figure 6.2, Flaw 05 is emphasized with red color, because it represented the true state used in test block 5.1 for J-groove weld surface examinations in PINC.

An illustration of the true state used for test block P25 in PARENT is provided in Figure 6.3 in which flaws used to define the true state for J-groove weld surface examinations are highlighted with red color. A comparison of Figure 6.2 and Figure 6.3 shows differences in defined true states for the test block in the PINC and PARENT studies. One obvious difference is that the true state defined for PARENT includes one additional flaw (Flaw 01) in comparison to the true state defined for PINC. Another important difference is associated with the coordinate system used to define the locations and dimensions of flaws and indications. In PINC, the coordinate system is defined such that the azimuthal dimension increases in the clockwise direction; in PARENT, it is defined to increase in the counter clockwise direction. Additional differences in true state can be observed from the tabular representations of the true state of test block 5.1 in PINC and test block P25 in PARENT, provided in Table 6.3 and Table 6.4. A review of these tables shows that besides the update to the azimuthal dimensions ($\Theta 1$ and $\Theta 2$) for Flaw 05 due to the change in the coordinate system definition, there were also some updates to the r1, r2, Z1, and Z2 dimensions. The updates to these dimensions are made on the basis of additional measurements conducted to refine the understanding of the true state between PINC and PARENT studies. Thus, the more recent definitions of r1, r2, Z1, and Z2 for Flaw 05 used in PARENT were considered more accurate and were also utilized for the reanalysis of PINC data in this effort.

Thus, while the true state illustrated in Figure 6.3 and defined in Table 6.4 for the analysis of P25 in PARENT was reutilized for the analysis of PARENT data in this effort, a new true state was defined for the reanalysis of PINC data. The updated true state used for analyzing J-groove weld surface data collected from test block 5.1 in PINC is illustrated in Figure 6.4 and summarized in Table 6.5.

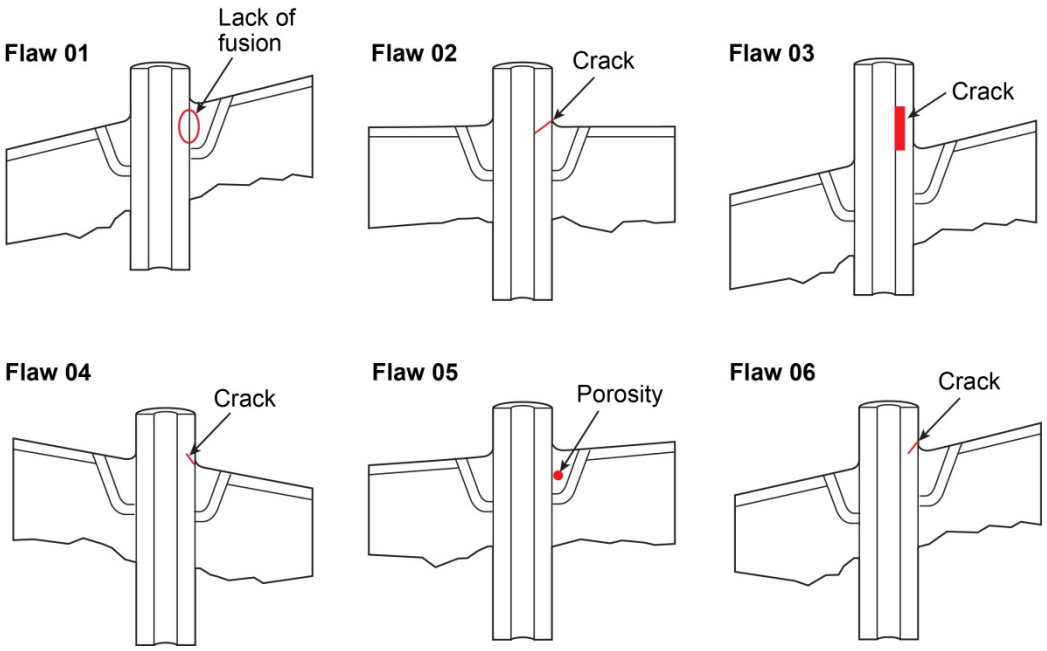

Figure 6.1. Cross-Sectional View of PINC Test Block 5.1 (PARENT Test Block P25) Illustrating the Location of Flaws in the Test Block

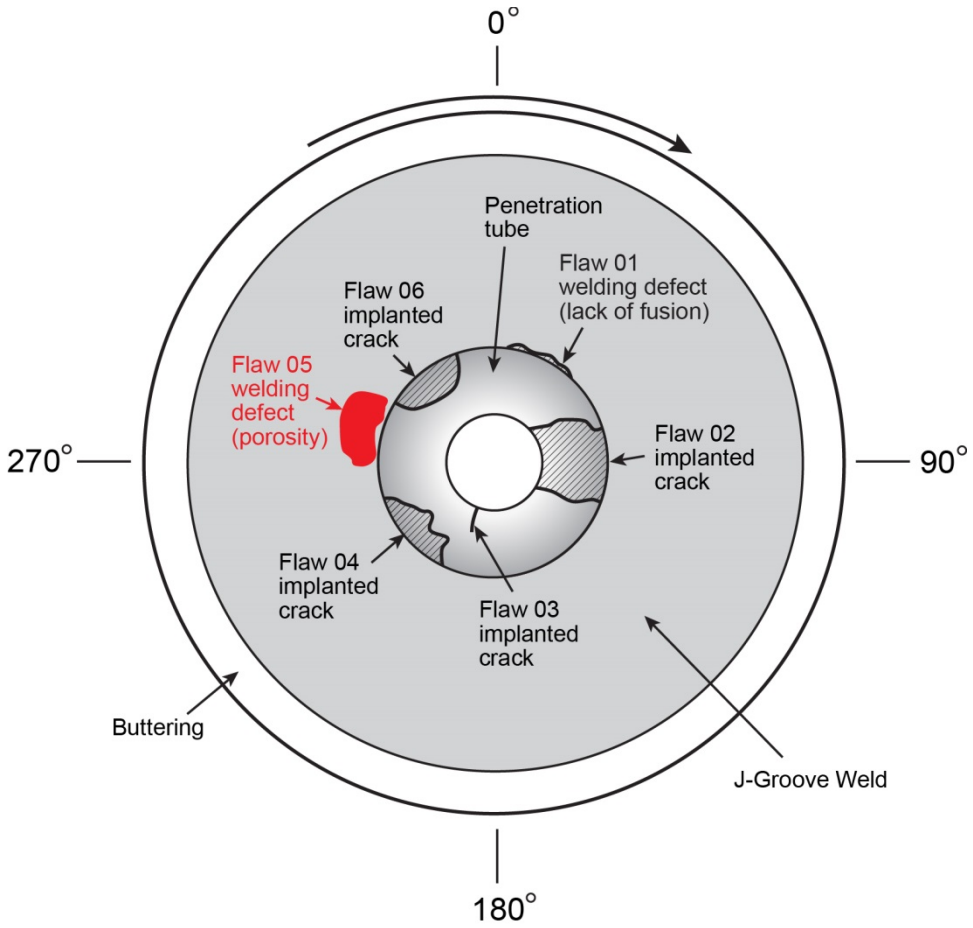

Figure 6.2. Top View Illustration of the True State Used for J-groove Weld Surface Testing of PINC Test Block 5.1 (PARENT Test Block P25) in PINC. The true state used in PINC is emphasized with red shading of Flaw 05.

Table 6.3. Definition of True State for Test Block 5.1 Utilized in PINC

Flaw	Θ1, °	Θ2, °	r1, mm	r2, mm	Z1, mm	Z2, mm	SB*	Orient
5	268	304	20	23.6	1	10	No	Circ.

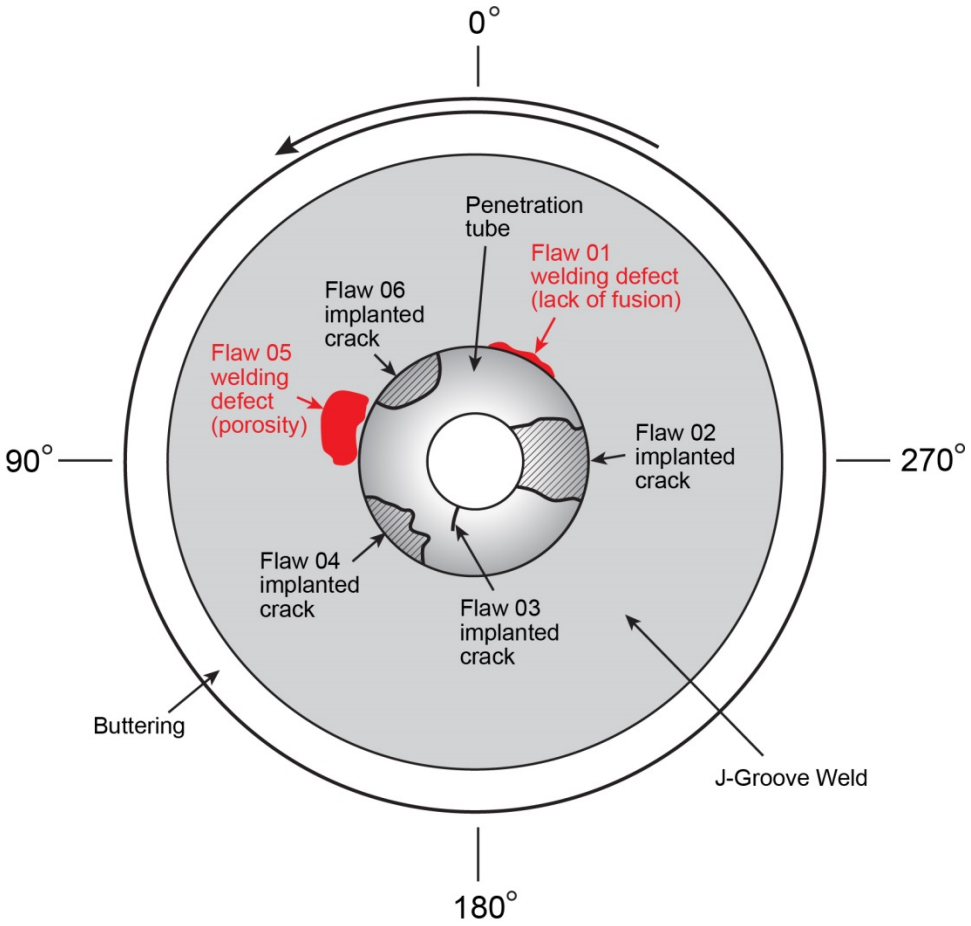

Figure 6.3. Top View Illustration of the True State Used for J-groove Weld Surface Testing of PARENT Test Block P25 (PINC Test Block 5.1). The true state used in PARENT is emphasized with red shading of Flaw 01 and Flaw 05.

Table 6.4. Definition of True State for Test Block P25 Utilized in PARENT

Flaw	Θ1, °	Θ2, °	r1, mm	r2, mm	Z1, mm	Z2, mm	SB*	Orient
1	314.0	356.3	14.9	15.7	14.5	17.2	No	Circ.
5	54.2	93.9	19.3	23.7	9.4	13.8	No	Circ.

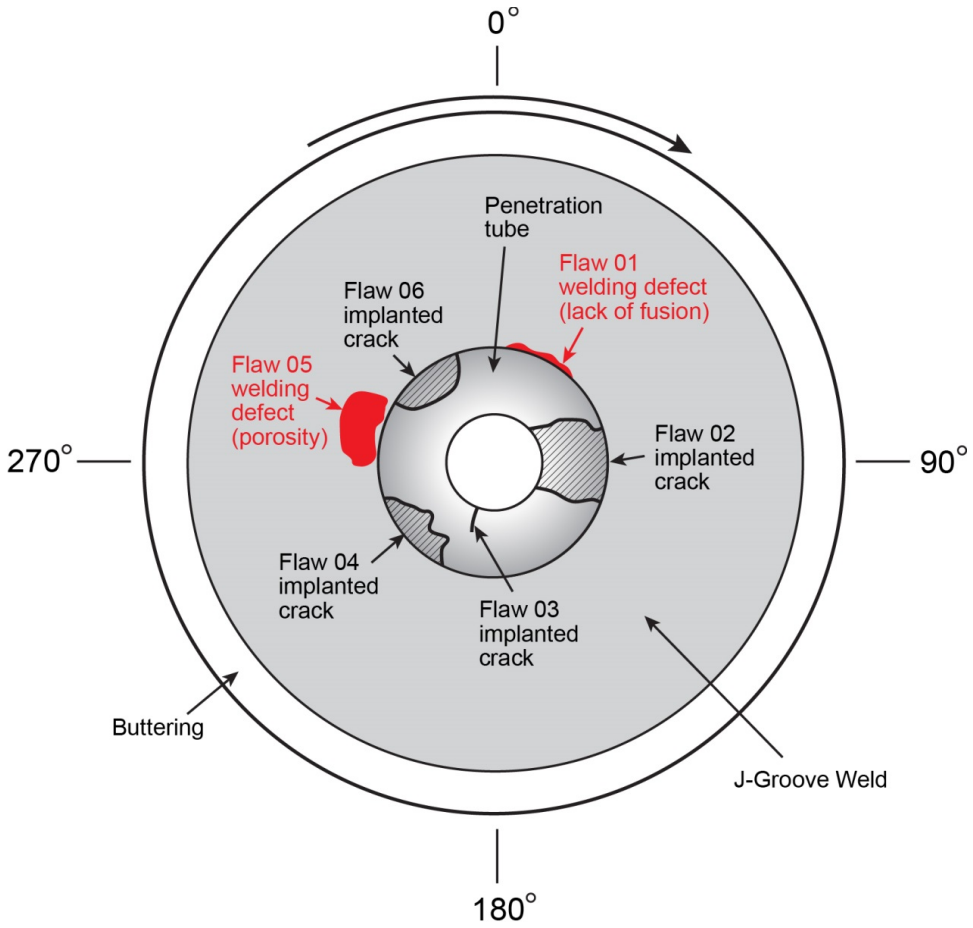

Figure 6.4. Top View Illustration of the Updated True State Used for Analysis of PINC Data Collected from J-groove Weld Surface Examinations of PINC Test Block 5.1 in This Effort

Table 6.5. Tabulated Summary of the Updated True State Used for Analysis of PINC Data Collected from J-groove Weld Surface Examinations of PINC Test Block 5.1 in This Effort

Flaw	Θ1, °	Θ2, °	r1, mm	r2, mm	Z1, mm	Z2, mm	SB*	Orient
1	3.7	46.0	14.9	15.7	14.5	17.2	No	Circ.
5	266.1	305.8	19.3	23.7	9.4	13.8	No	Circ.

6.3 True State of PINC Test Block 5.3/PARENT Test Block P26

A cross-sectional view of test block 5.3 (P26) is provided in Figure 6.5. An illustration of the true state used for J-groove weld surface examination evaluations is provided in Figure 6.6 and summarized in Table 6.6. In Figure 6.6, Flaws 03 and 06 are emphasized in red color because they were defined as the true state of 5.3 in PINC for J-groove weld surface examinations.

An illustration of the true state used for test block P26 in PARENT is provided in Figure 6.7 in which flaws used to define the true state for J-groove weld surface examinations are highlighted with red color. The true state defined for test block P26 in PARENT is also summarized in Table 6.7. As with test block

5.1 (P25), a comparison of Figure 6.6 and Figure 6.7 shows differences in defined true states for the test block in the PINC and PARENT studies. One difference is that the true state defined for PARENT includes two additional flaws (Flaw 02 and Flaw 05) in comparison to the true state defined for PINC. Also, as with test block 5.1 (P25), the coordinate system was defined such that the azimuthal dimension increased in the clockwise direction in PINC and was defined to increase in the counter clockwise direction in PARENT. Additional differences in true state can be observed from the tabular representations of the true state of test block 5.3 in PINC and test block P26 in PARENT, provided in Table 6.6 and Table 6.7. A review of these tables shows that besides the update to the azimuthal dimensions ($\Theta 1$ and $\Theta 2$) for Flaws 03 and 06 due to the change in the coordinate system definition, there were also some updates to the r1, r2, Z1, and Z2 dimensions. The updates to these dimensions are made on the basis of additional measurements conducted to refine the understanding of the true state between PINC and PARENT studies. Thus, the more recent definitions of r1, r2, Z1, and Z2 for Flaws 03 and 06 used in PARENT were considered more accurate and were also utilized for the reanalysis of PINC data in this effort.

Thus, while the true state illustrated in Figure 6.7 and defined in Table 6.7 for the analysis of P26 in PARENT was reutilized for the analysis of PARENT data in this effort, a new true state was defined for the reanalysis of PINC data. The updated true state used for analyzing J-groove weld surface data collected from test block 5.3 in PINC is illustrated in Figure 6.8 and summarized in Table 6.8.

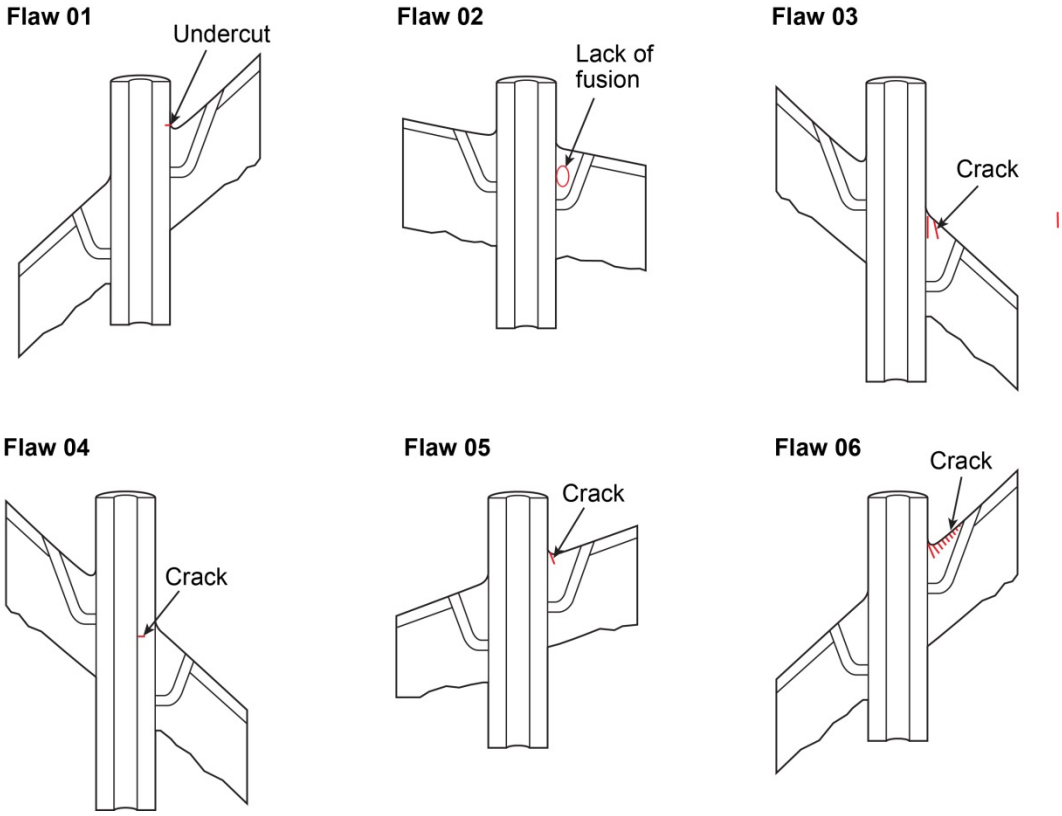

Figure 6.5. Cross-Sectional View of PINC Test Block 5.3 (PARENT Test Block P26) Illustrating the Location of Flaws in the Test Block

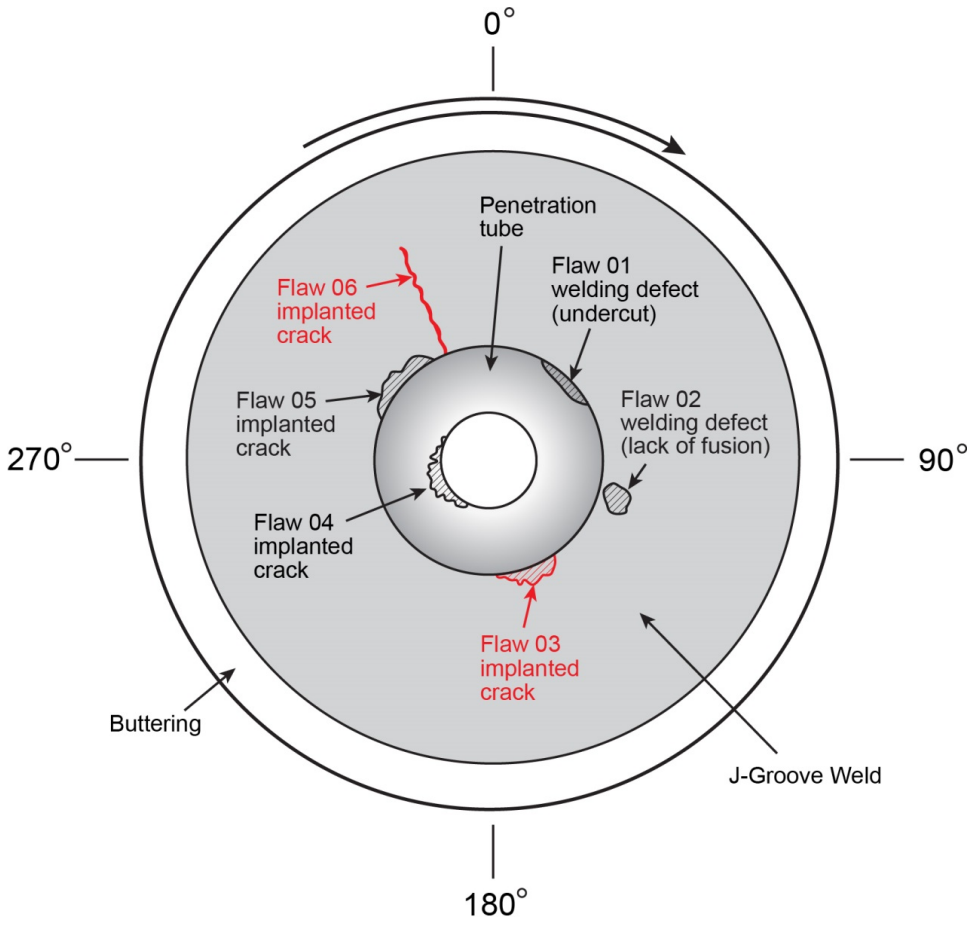

Figure 6.6. Top View Illustration of the True State Used for J-groove Weld Surface Testing of PINC Test Block 5.3 (PARENT Test Block P26) in PINC. The true state used in PINC is emphasized with red shading of Flaw 03.

Table 6.6. Definition of True State for Test Block 5.3 Utilized in PINC

Flaw	Θ1, °	Θ2, °	r1, mm	r2, mm	Z1, mm	Z2, mm	SB*	Orient
3	130	160	19.1	27.7	0	8	Yes	Circ.
6	338	338	19.1	30	0	10	Yes	Axial

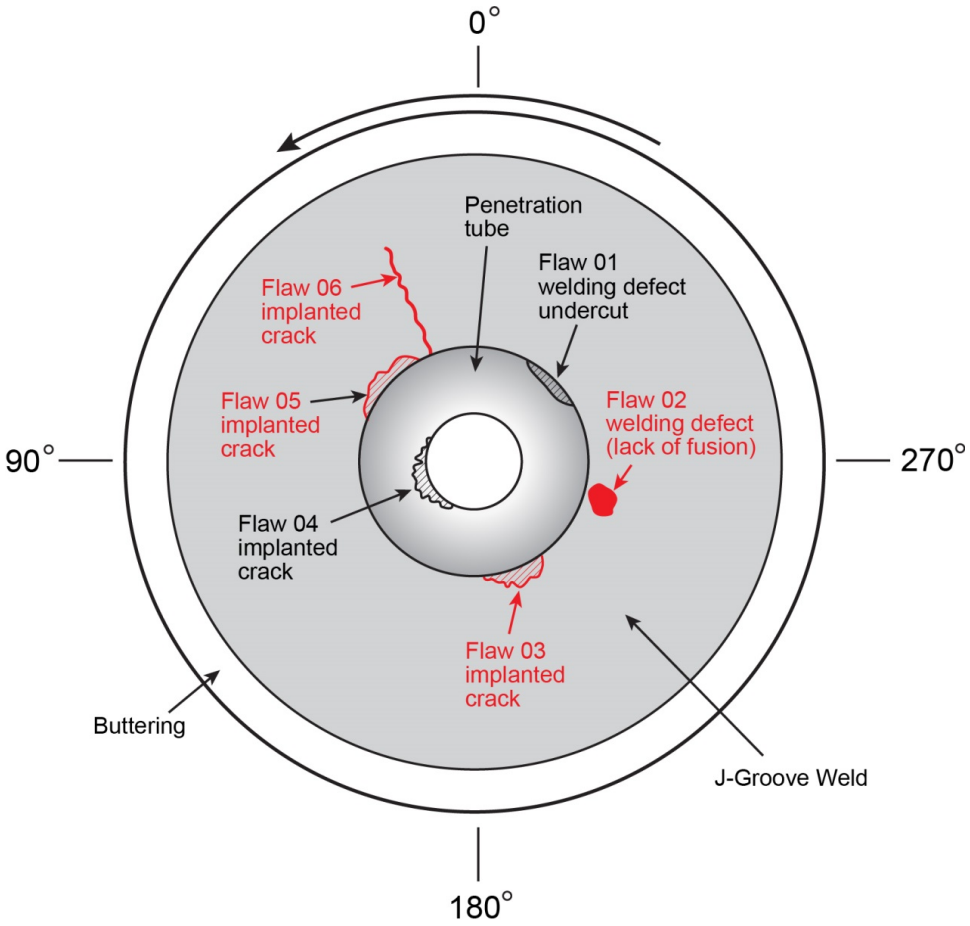

Figure 6.7. Top View Illustration of the True State Used for J-groove Weld Surface Testing of PARENT Test Block P26 (PINC Test Block 5.3). The true state used in PARENT is emphasized with red shading of Flaw 02, Flaw 03, Flaw 05, and Flaw 06.

Table 6.7. Definition of True State for Test Block P26 Utilized in PARENT

Flaw	Θ1, °	Θ2, °	r1, mm	r2, mm	Z1, mm	Z2, mm	SB*	Orient
2	244.1	273.9	24.1	25.2	10.8	16.7	No	Circ.
3	199.1	230	19.9	30.6	−6.1	2	Yes	Diag.
5	45.6	92.4	22.7	23.2	−6.3	4.4	Yes	Circ.
6	22	22	22.7	64.7	0	9.9	Yes	Axial

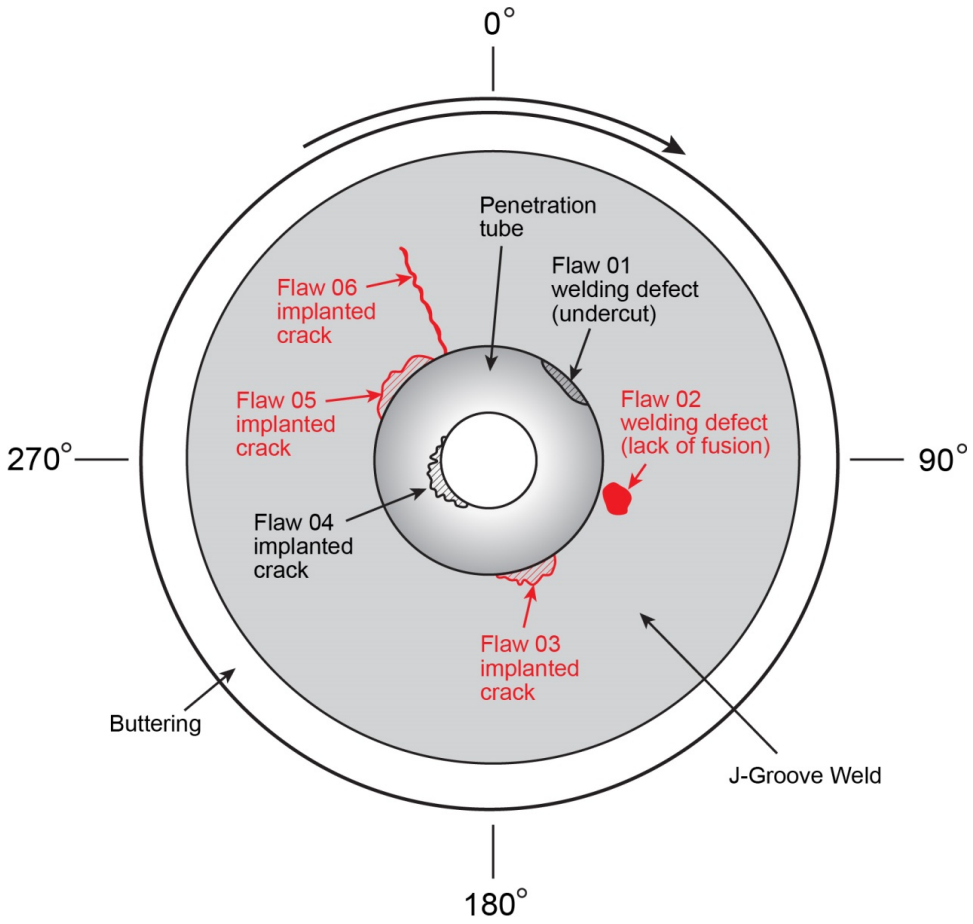

Figure 6.8. Top View Illustration of the Updated True State Used for Analysis of PINC Data Collected from J-groove Weld Surface Examinations of PINC Test Block 5.3 in This Effort

Table 6.8. Tabulated Summary of the Updated True State Used for Analysis of PINC Data Collected from J-groove Weld Surface Examinations of PINC Test Block 5.3 in This Effort

Flaw	Θ1, °	Θ2, °	r1, mm	r2, mm	Z1, mm	Z2, mm	SB*	Orient
2	86.1	115.9	24.1	25.2	10.8	16.7	No	Circ.
3	130	160.9	19.9	30.6	−6.1	2	Yes	Diag.
5	267.6	314.4	22.7	23.2	−6.3	4.4	Yes	Circ.
6	338	338	22.7	64.7	0	9.9	Yes	Axial

6.4 Indication Plots for BMI Examinations

This section includes the indication plots for examinations of the surface of J-groove welds of BMI test blocks in PINC and PARENT for convenience. The indication plots are organized by team (i.e., PINC team 38, PINC team 99, PINC team 373, PINC team 70, PARENT team 108, and PARENT team 124) in the following sections. All of the flaws represented are surface-breaking with the exception of the two flaws in PINC test block 5.1 (PARENT test block P25) and one of the flaws in PINC test block 5.3 (PARENT test block P26). Non-surface-breaking flaws are excluded from the analysis because all of the

techniques analyzed are ECT techniques. The teams are not penalized for missing non-surface-breaking flaws and are not credited if they do detect them.

6.4.1 Indication Plots for PINC Team 38 Examinations (100 kHz, Array Probe)

Indication plots for examinations performed by PINC team 38 on the surface of J-groove weld regions in BMI test blocks in PINC are provided in Figure 6.9 through Figure 6.19. These plots indicate the occurrence of multiple false calls for nearly all examined test blocks including blank test blocks 5.8, 5.11, and 5.12. Further, missed flaws can be observed for every non-blank test block with the exception of test block 5.16.

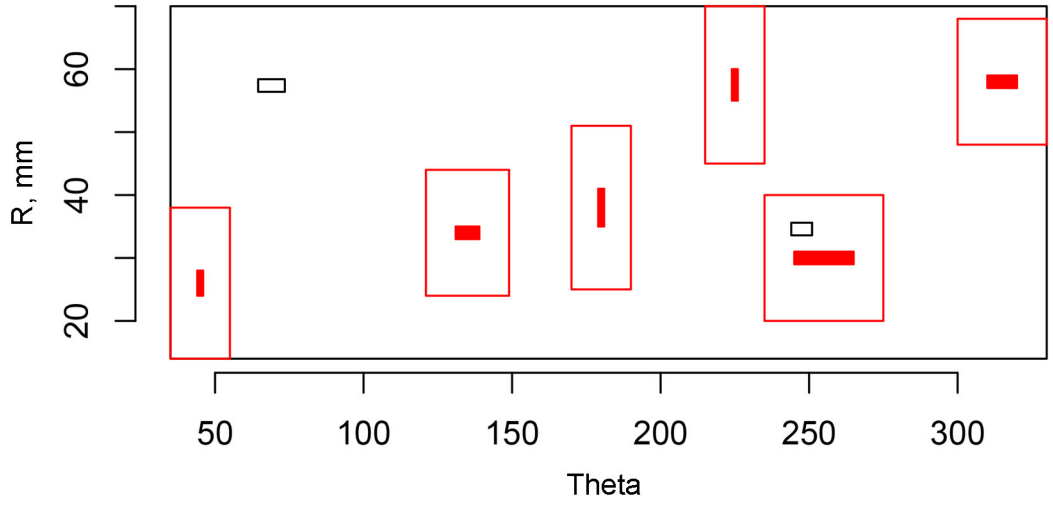

Figure 6.9. Indication Plot for PINC Team 38 (100 kHz, Array Probe) Applied to Test Block 5.6 in PINC (theta – R view)

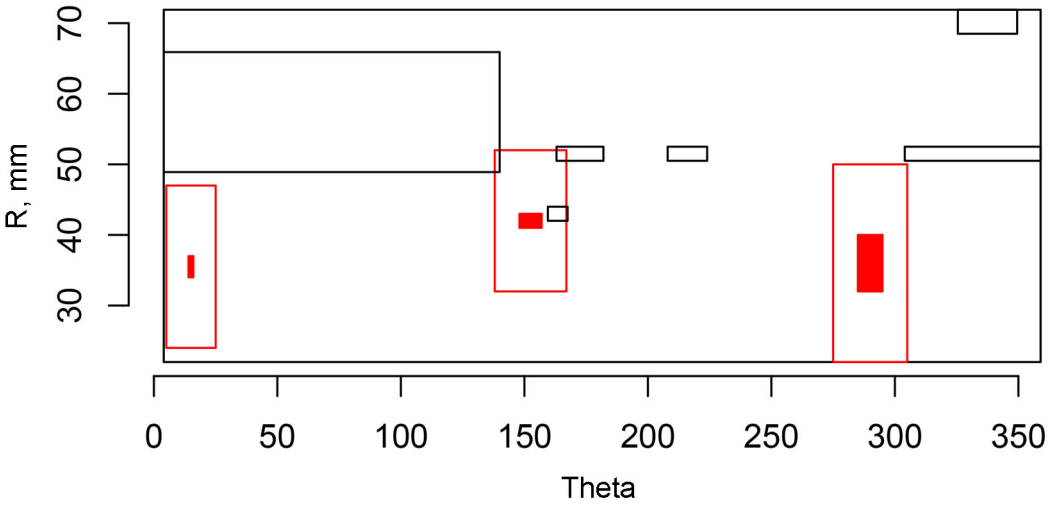

Figure 6.10. Indication Plot for PINC Team 38 (100 kHz, Array Probe) Applied to Test Block 5.7 in PINC (theta – R view)

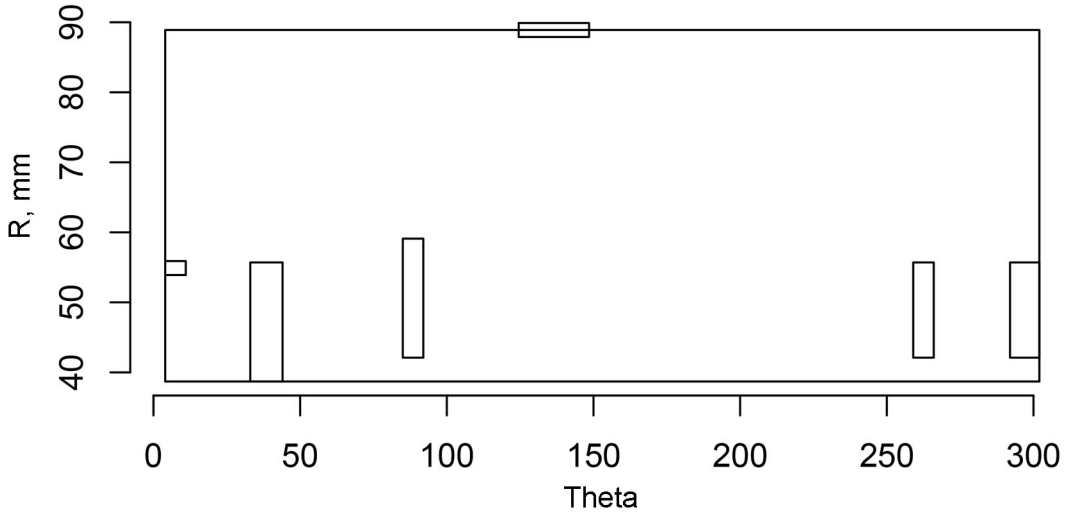

Figure 6.11. Indication Plot for PINC Team 38 (100 kHz, Array Probe) Applied to Test Block 5.8 in PINC (theta – R view)

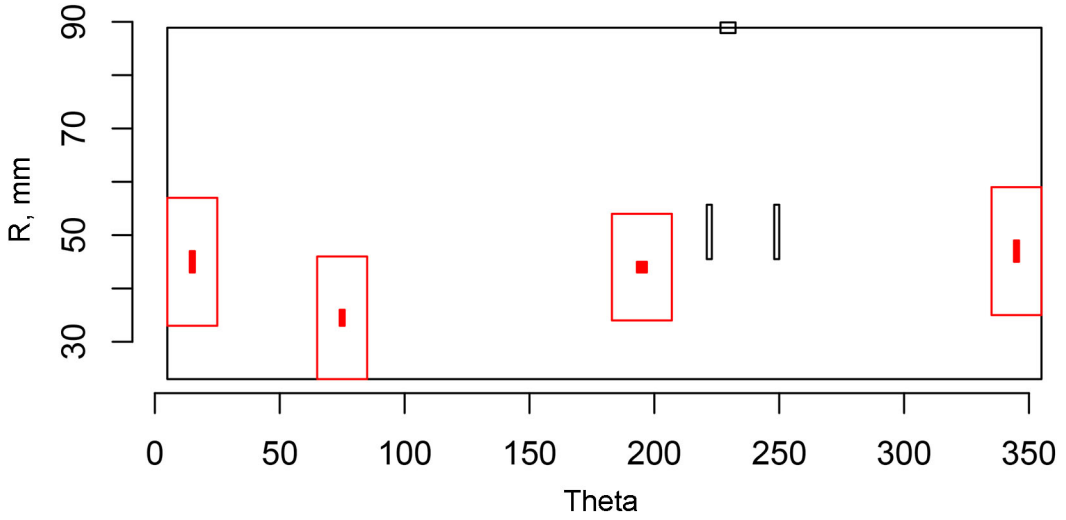

Figure 6.12. Indication Plot for PINC Team 38 (100 kHz, Array Probe) Applied to Test Block 5.9 in PINC (theta – R view)

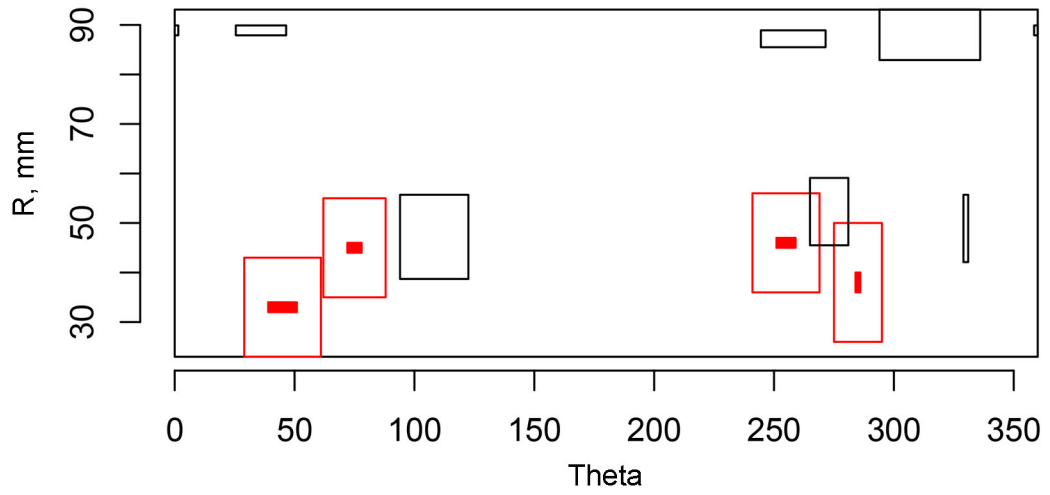

Figure 6.13. Indication Plot for PINC Team 38 (100 kHz, Array Probe) Applied to Test Block 5.10 in PINC (theta – R view)

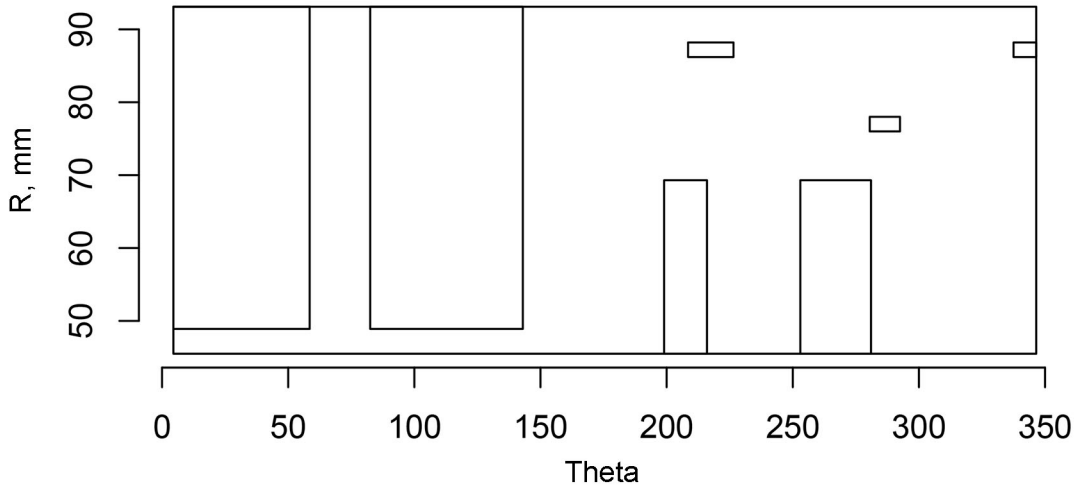

Figure 6.14. Indication Plot for PINC Team 38 (100 kHz, Array Probe) Applied to Test Block 5.11 in PINC (theta – R view)

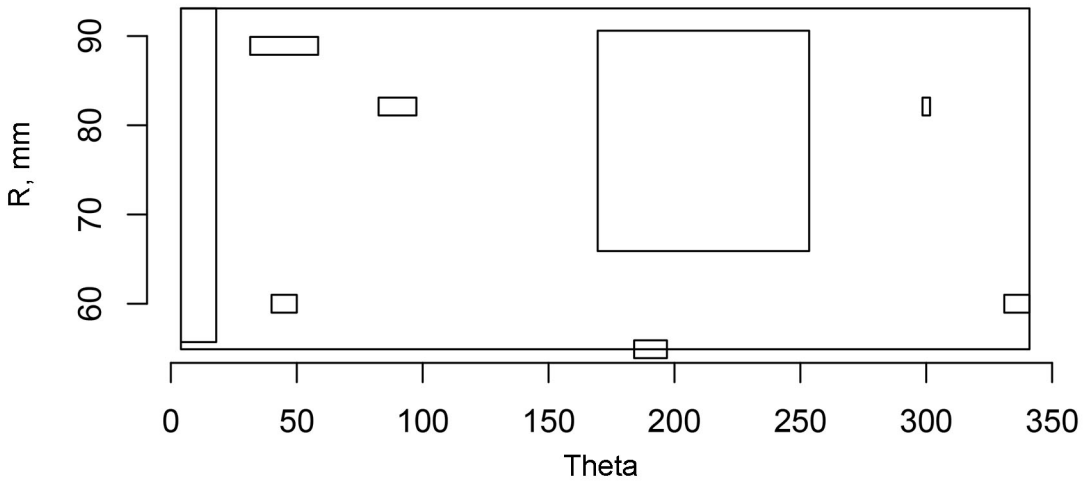

Figure 6.15. Indication Plot for PINC Team 38 (100 kHz, Array Probe) Applied to Test Block 5.12 in PINC (theta – R view)

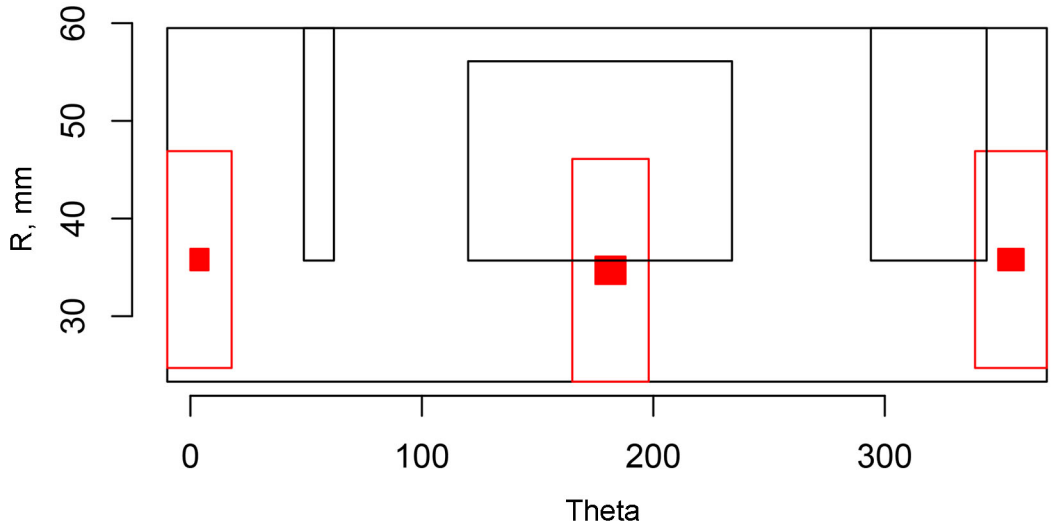

Figure 6.16. Indication Plot for PINC Team 38 (100 kHz, Array Probe) Applied to Test Block 5.13 in PINC (theta – R view)

Figure 6.17. Indication Plot for PINC Team 38 (100 kHz, Array Probe) Applied to Test Block 5.14 in PINC (theta – R view)

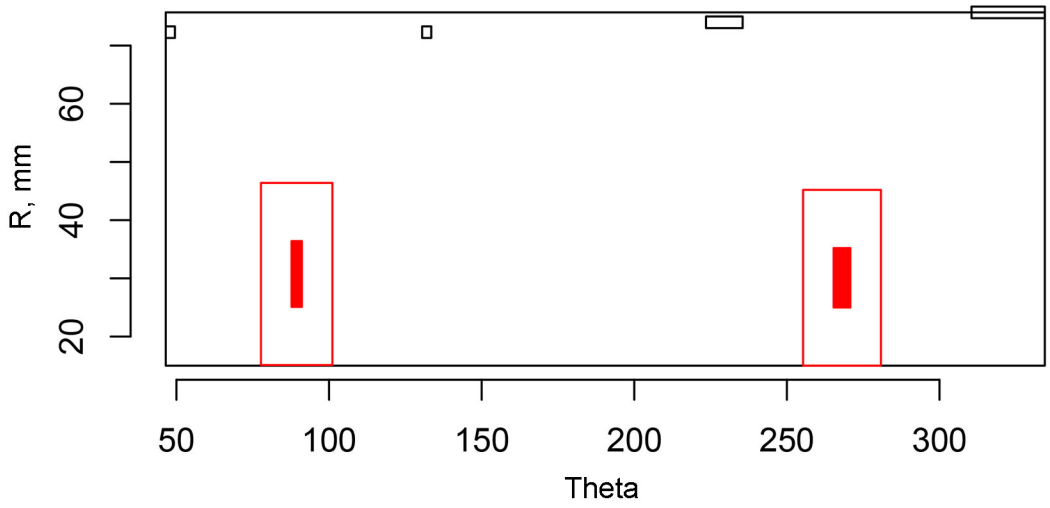

Figure 6.18. Indication Plot for PINC Team 38 (100 kHz, Array Probe) Applied to Test Block 5.15 in PINC (theta – R view)

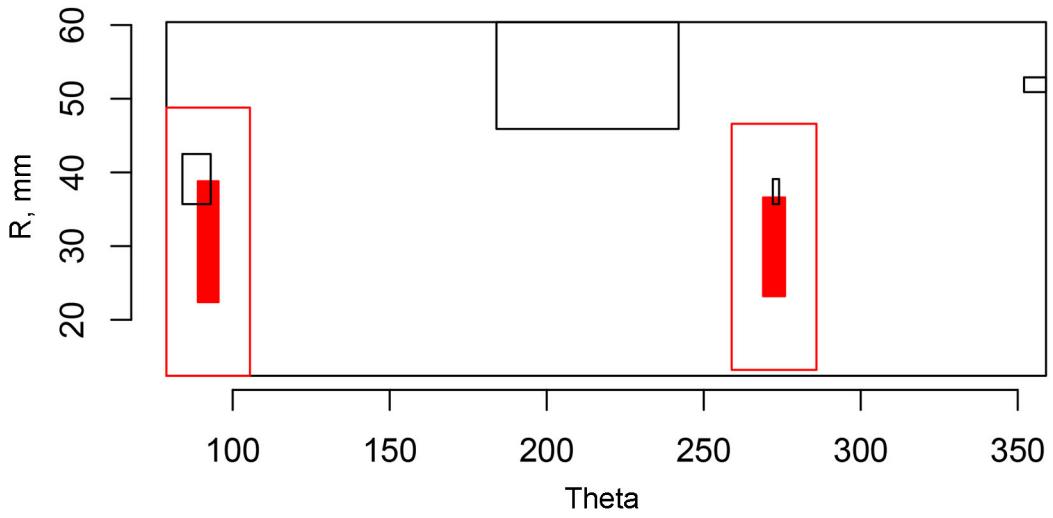

Figure 6.19. Indication Plot for PINC Team 38 (100 kHz, Array Probe) Applied to Test Block 5.16 in PINC (theta – R view)

6.4.2 Indication Plots for PINC Team 99 Examinations (200 kHz, Array Probe)

Indication plots for examinations performed by PINC team 99 on the surface of J-groove weld regions in BMI test blocks in PINC are provided in Figure 6.20 through Figure 6.29. These plots indicate the occurrence of multiple false calls for several of the examined test blocks. False calls are also observed in blank test blocks 5.8 and 5.12. All of the flaws in test blocks 5.1, 5.2, and 5.7 are detected and only one flaw is missed in test block 5.6. Three or more missed flaws were observed for examinations of test blocks 5.3, 5.9, and 5.10.

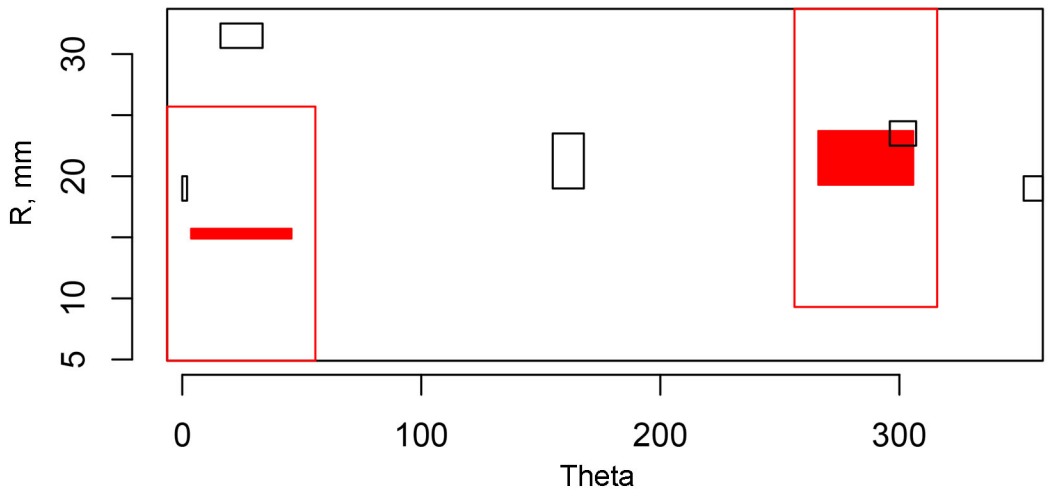

Figure 6.20. Indication Plot for PINC Team 99 (200 kHz, Array Probe) Applied to Test Block 5.1 in PINC (theta – R view)

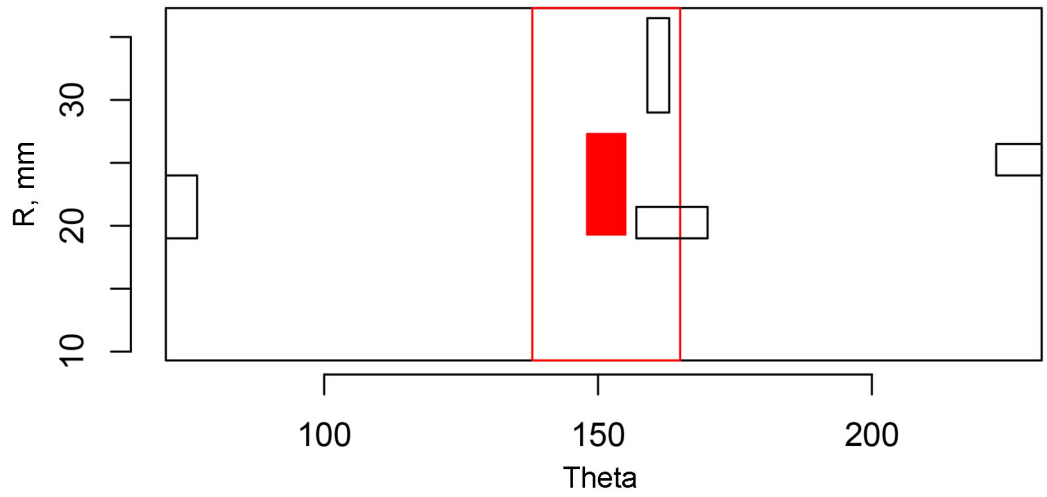

Figure 6.21. Indication Plot for PINC Team 99 (200 kHz, Array Probe) Applied to Test Block 5.2 in PINC (theta – R view)

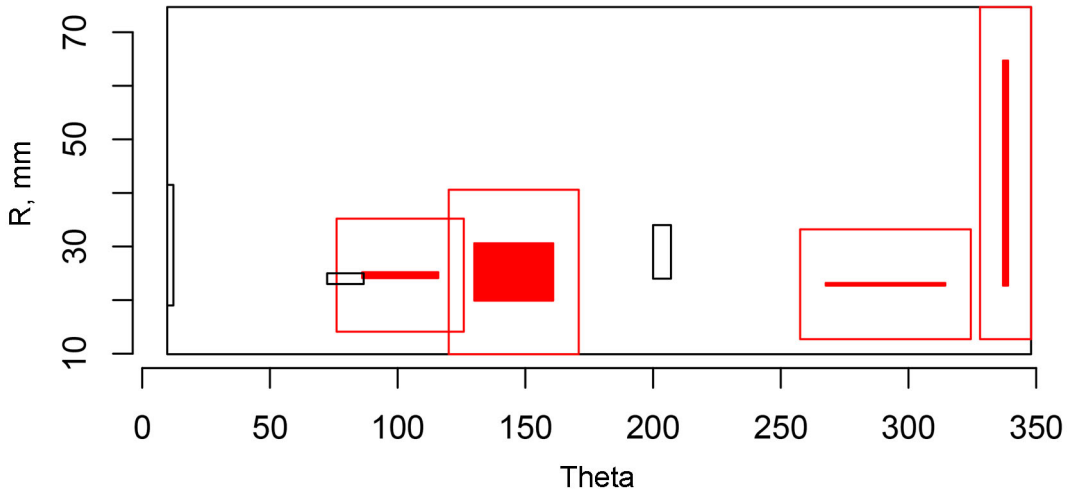

Figure 6.22. Indication Plot for PINC Team 99 (200 kHz, Array Probe) Applied to Test Block 5.3 in PINC (theta – R view)

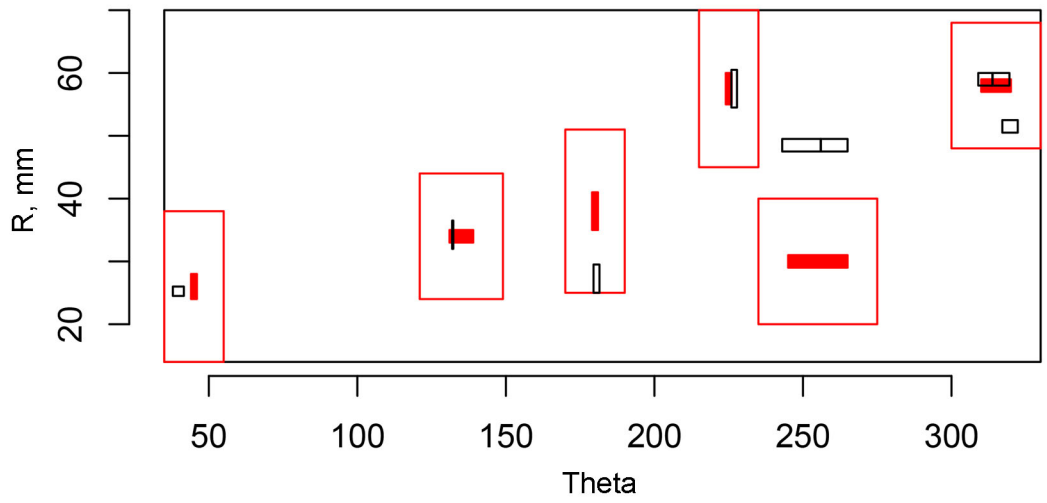

Figure 6.23. Indication Plot for PINC Team 99 (200 kHz, Array Probe) Applied to Test Block 5.6 in PINC (theta – R view)

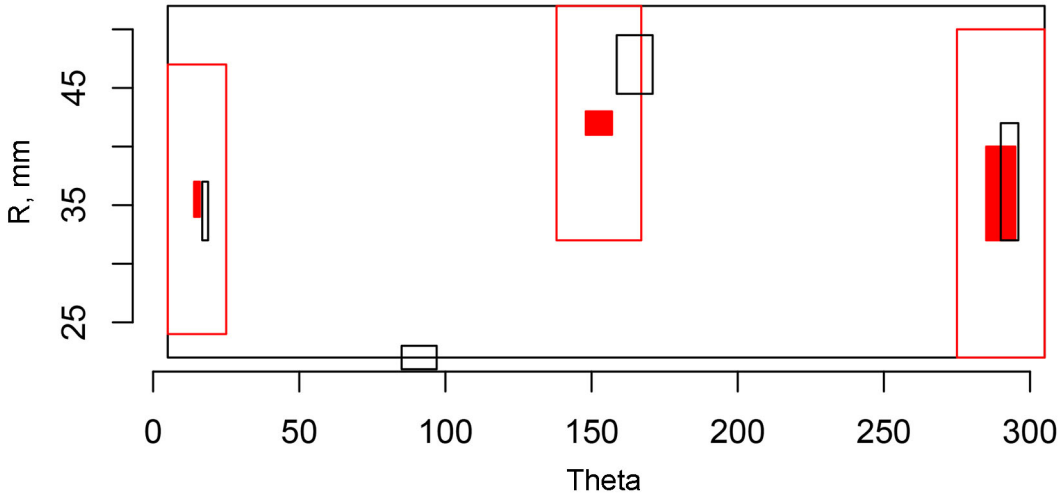

Figure 6.24. Indication Plot for PINC Team 99 (200 kHz, Array Probe) Applied to Test Block 5.7 in PINC (theta – R view)

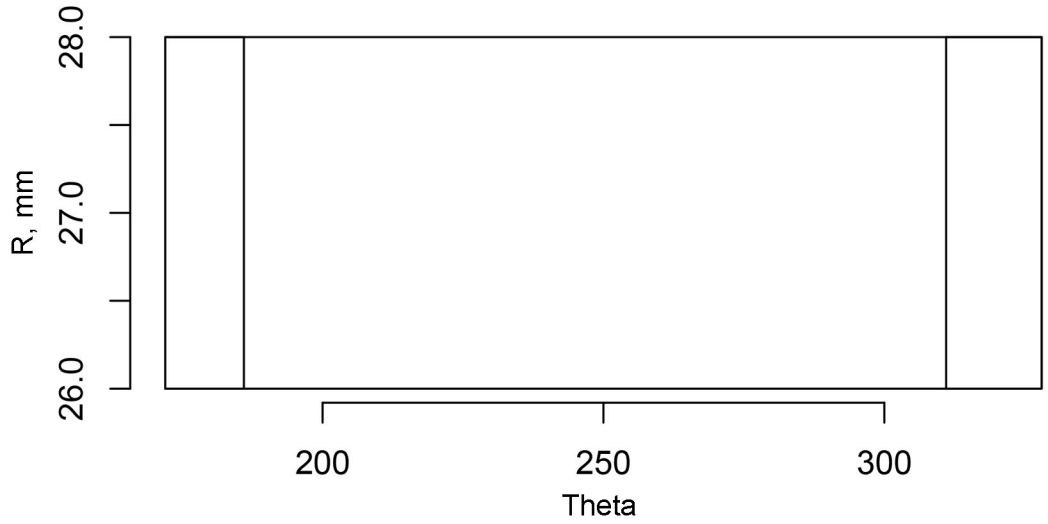

Figure 6.25. Indication Plot for PINC Team 99 (200 kHz, Array Probe) Applied to Test Block 5.8 in PINC (theta – R view)

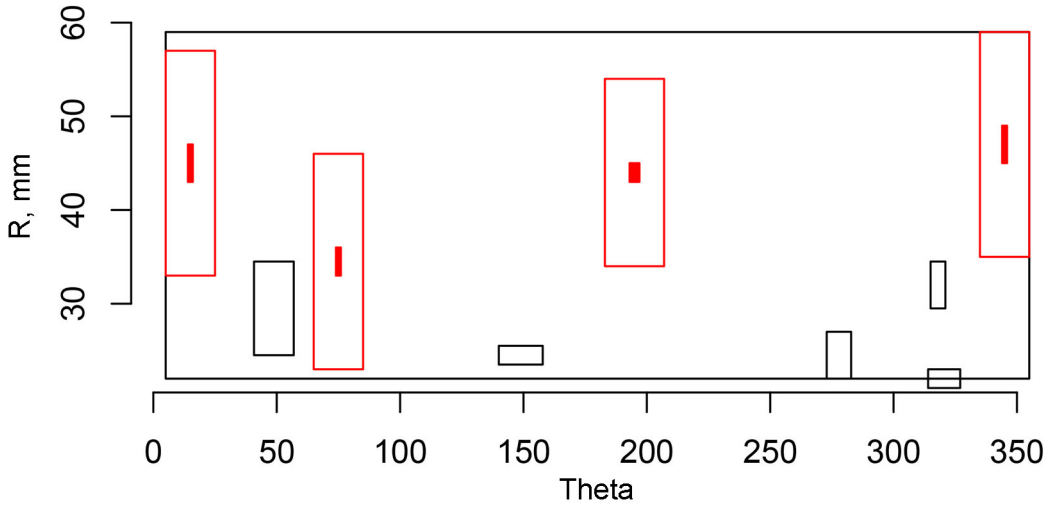

Figure 6.26. Indication Plot for PINC Team 99 (200 kHz, Array Probe) Applied to Test Block 5.9 in PINC (theta – R view)

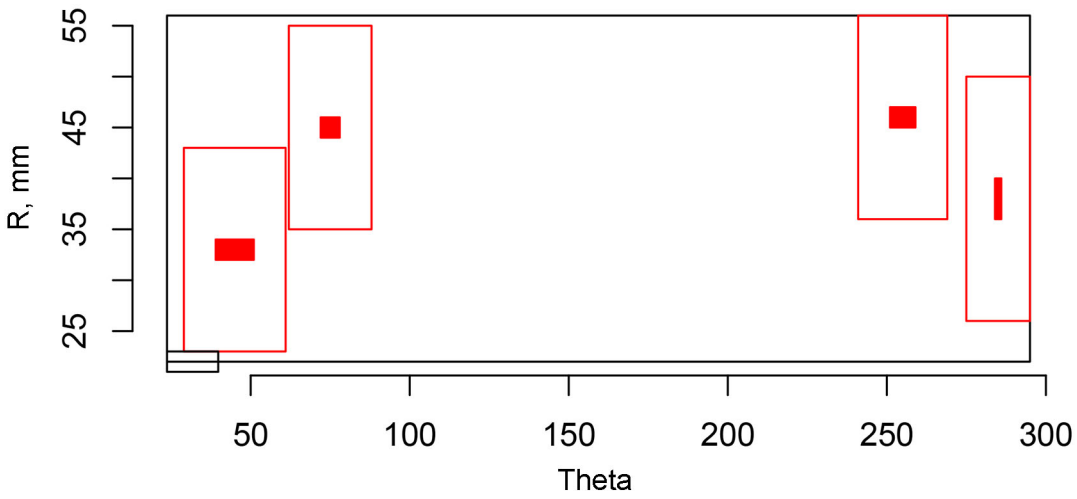

Figure 6.27. Indication Plot for PINC Team 99 (200 kHz, Array Probe) Applied to Test Block 5.10 in PINC (theta – R view)

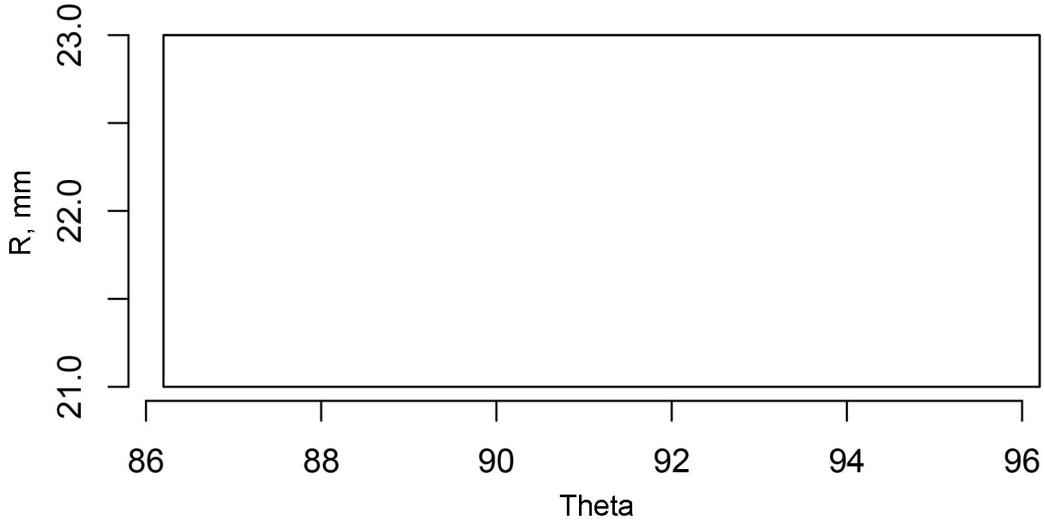

Figure 6.28. Indication Plot for PINC Team 99 (200 kHz, Array Probe) Applied to Test Block 5.11 in PINC (theta – R view)

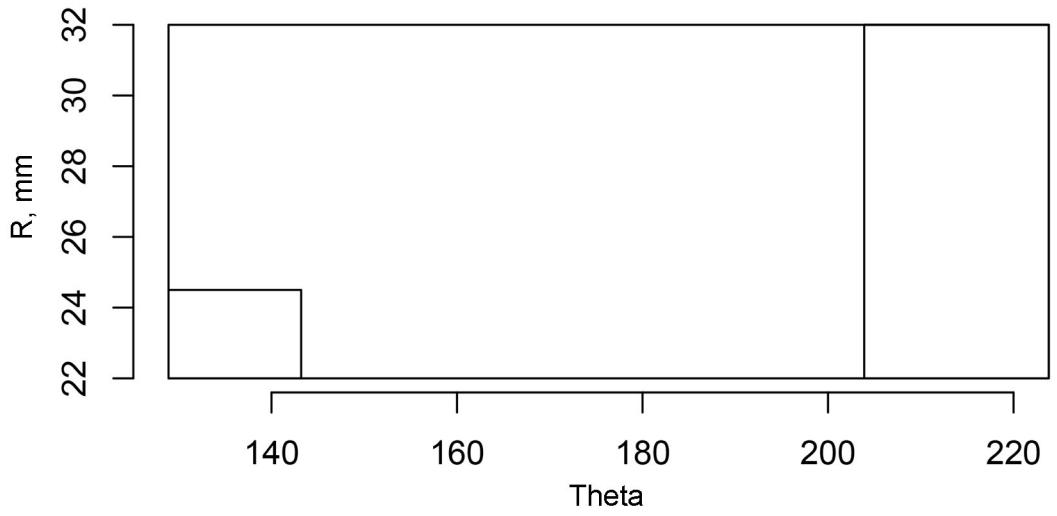

Figure 6.29. Indication Plot for PINC Team 99 (200 kHz, Array Probe) Applied to Test Block 5.12 in PINC (theta – R view)

6.4.3 Indication Plots for PINC Team 373 Examinations (300 kHz, Non-Array Probe)

Indication plots for examinations performed by PINC team 373 on the surface of J-groove weld regions in BMI test blocks in PINC are provided in Figure 6.30 through Figure 6.43. Only a few false calls are observed with one false call in each of test blocks 5.2, 5.3, and 5.10. The false call in test block 5.10 falls just outside of the tolerance boundary of a flaw. Several misses are observed for test blocks 5.1, 5.2, and 5.3. However, three of the missed flaws are non-surface–breaking and result in no penalty. Otherwise, perfect scoring is observed except for 5.9, 5.10, and 5.13. Two misses are observed in test blocks 5.9 and 5.13 and three misses are observed in test block 5.10.

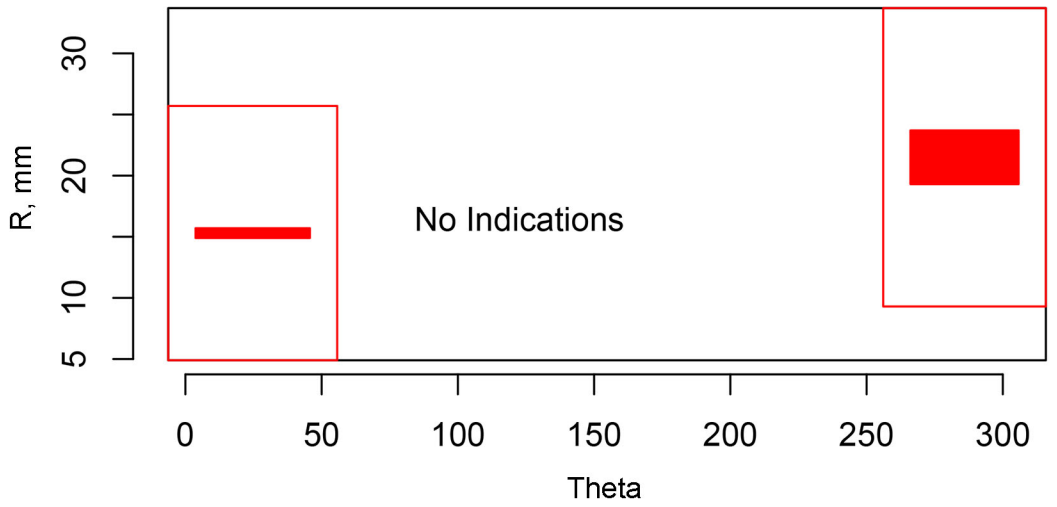

Figure 6.30. Indication Plot for PINC Team 373 (300 kHz, Non-Array Probe) Applied to Test Block 5.1 in PINC (theta – R view)

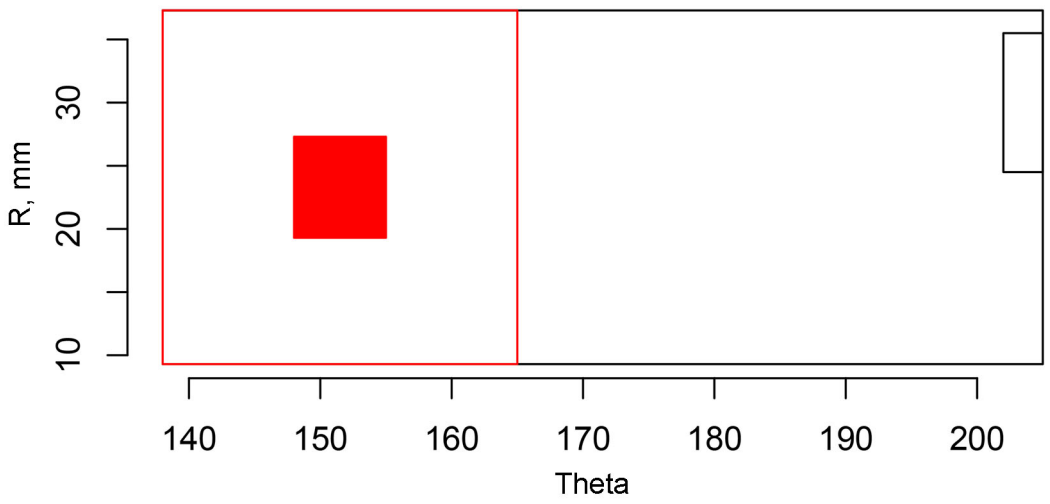

Figure 6.31. Indication Plot for PINC Team 373 (300 kHz, Non-Array Probe) Applied to Test Block 5.2 in PINC (theta – R view)

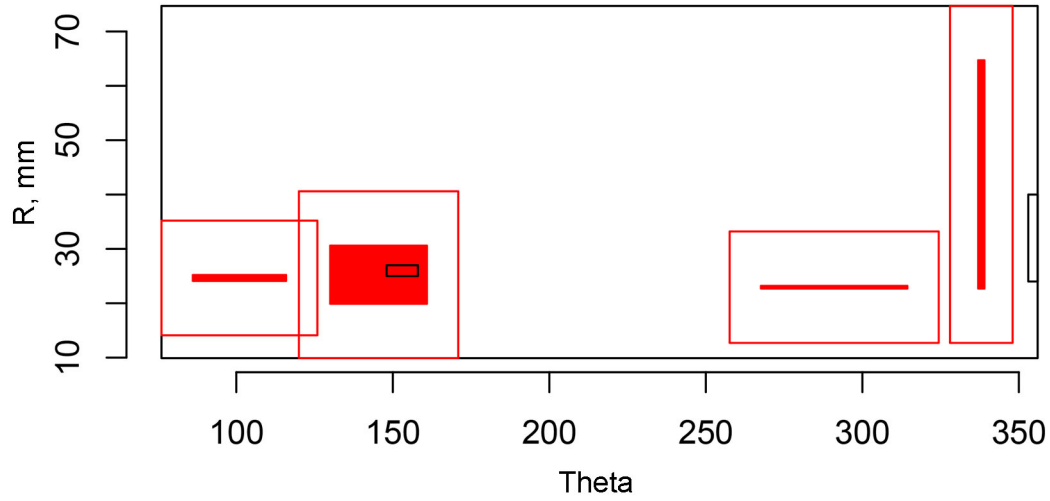

Figure 6.32. Indication Plot for PINC Team 373 (300 kHz, Non-Array Probe) Applied to Test Block 5.3 in PINC (theta – R view)

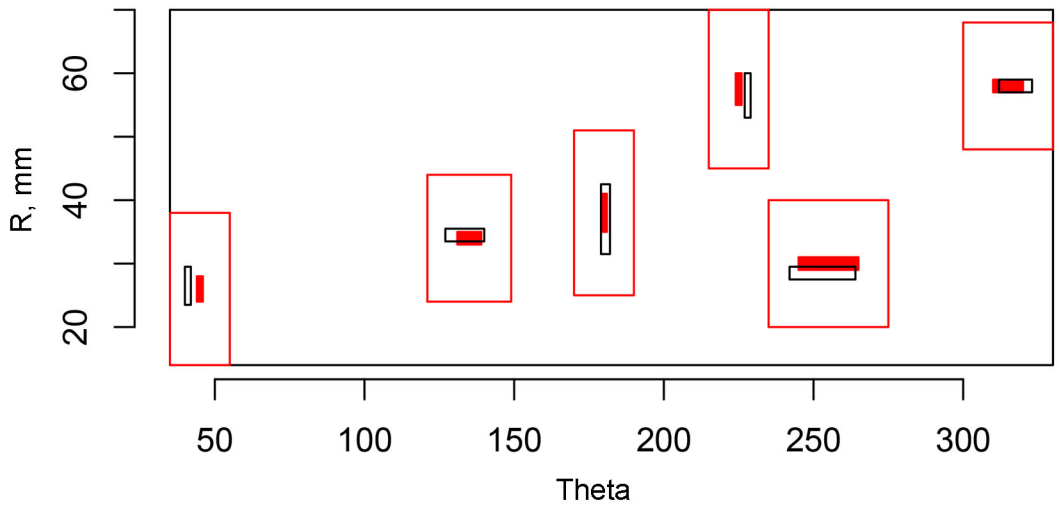

Figure 6.33. Indication Plot for PINC Team 373 (300 kHz, Non-Array Probe) Applied to Test Block 5.6 in PINC (theta – R view)

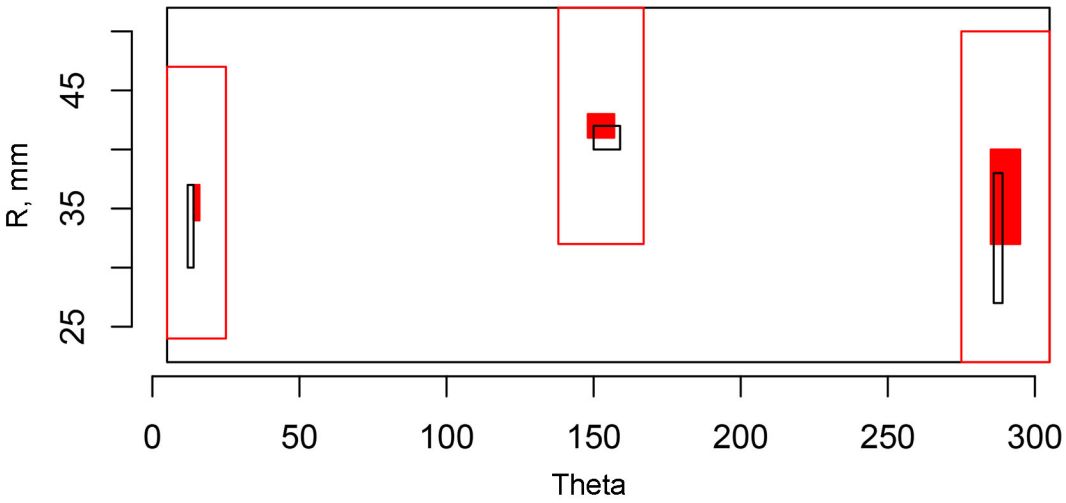

Figure 6.34. Indication Plot for PINC Team 373 (300 kHz, Non-Array Probe) Applied to Test Block 5.7 in PINC (theta – R view)

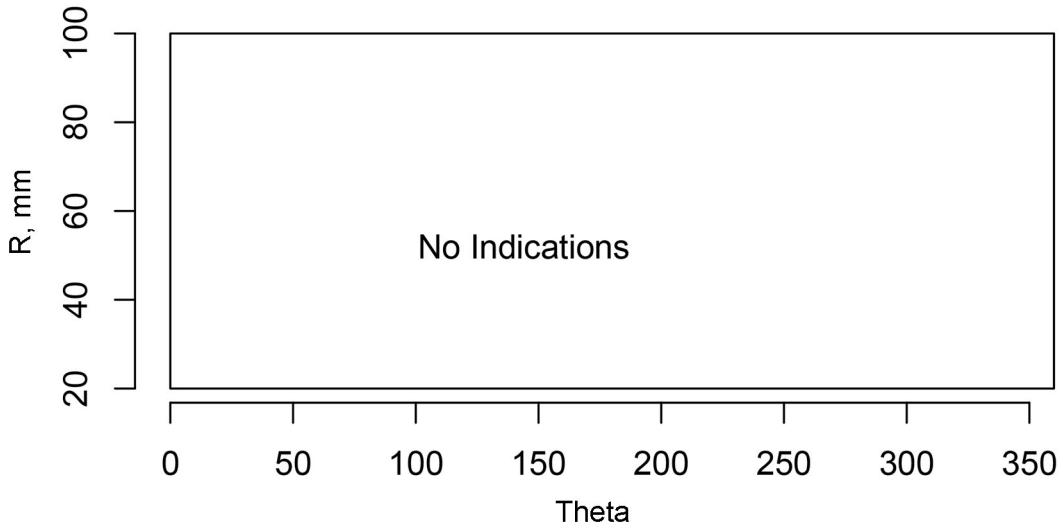

Figure 6.35. Indication Plot for PINC Team 373 (300 kHz, Non-Array Probe) Applied to Test Block 5.8 in PINC (theta – R view)

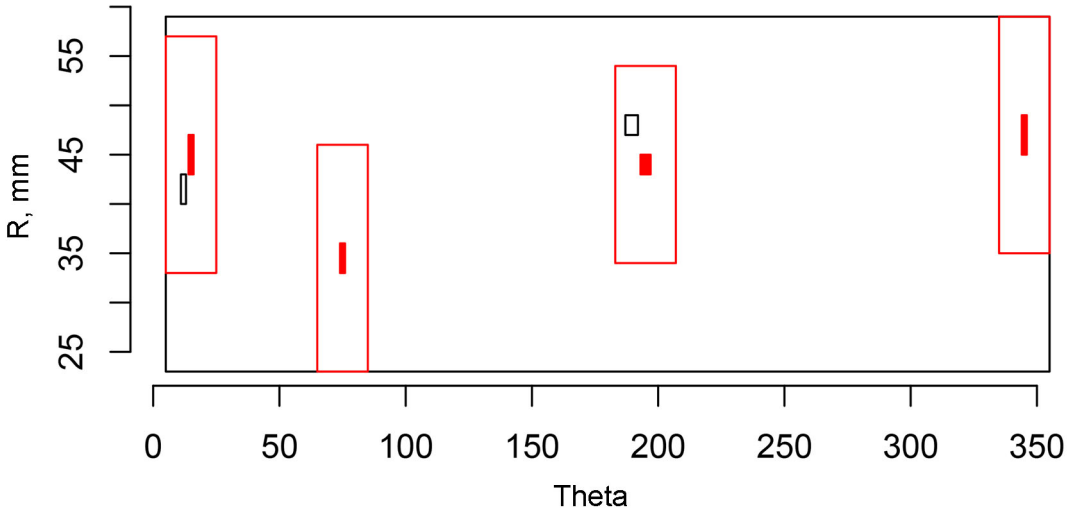

Figure 6.36. Indication Plot for PINC Team 373 (300 kHz, Non-Array Probe) Applied to Test Block 5.9 in PINC (theta – R view)

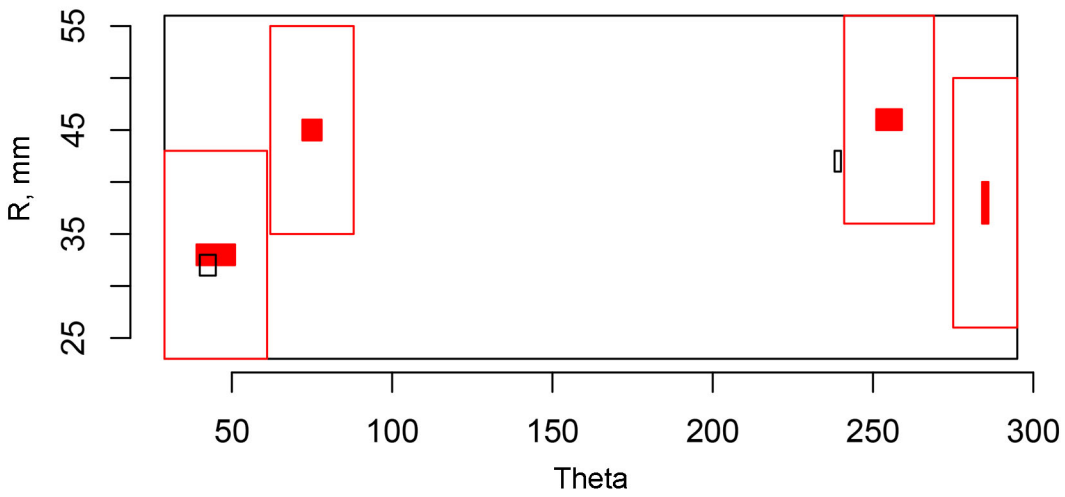

Figure 6.37. Indication Plot for PINC Team 373 (300 kHz, Non-Array Probe) Applied to Test Block 5.10 in PINC (theta – R view)

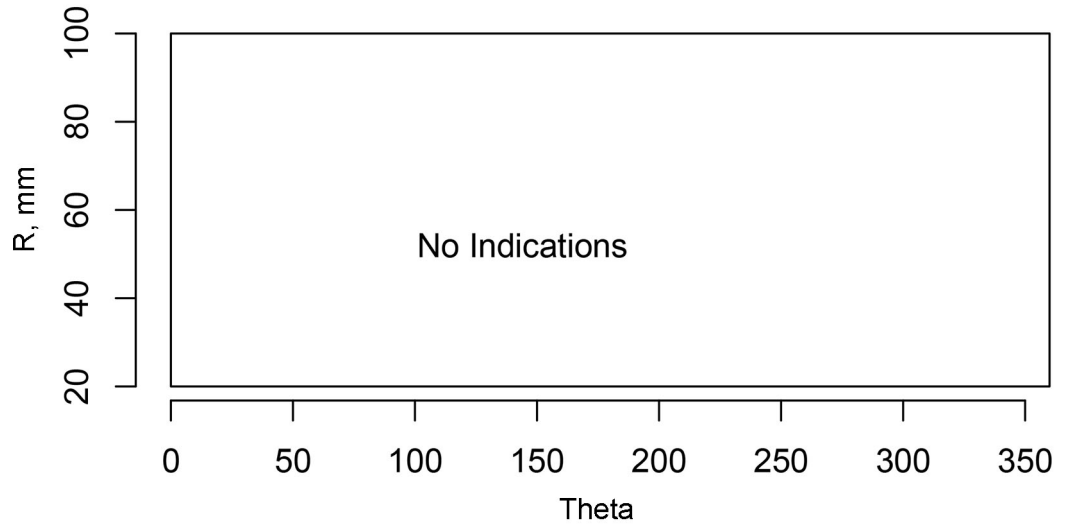

Figure 6.38. Indication Plot for PINC Team 373 (300 kHz, Non-Array Probe) Applied to Test Block 5.11 in PINC (theta – R view)

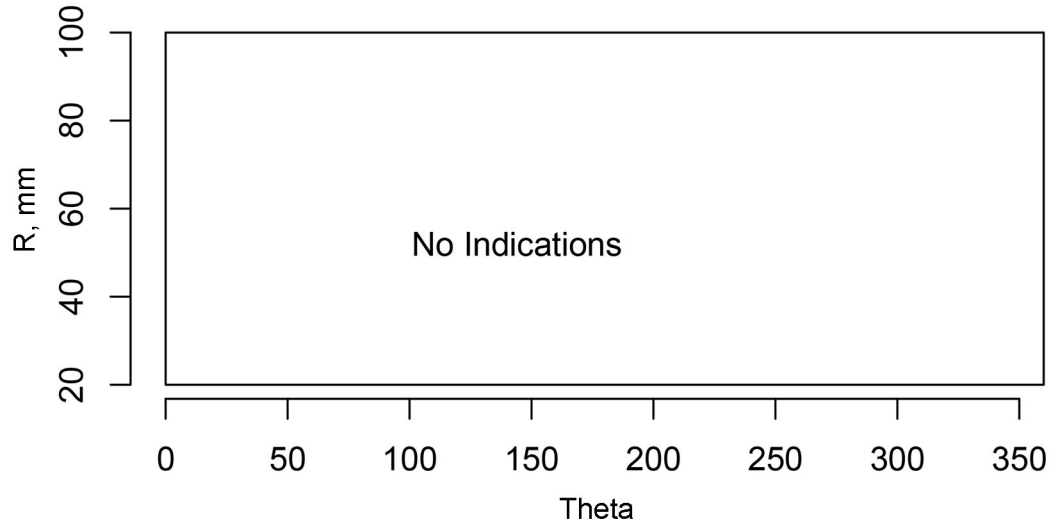

Figure 6.39. Indication Plot for PINC Team 373 (300 kHz, Non-Array Probe) Applied to Test Block 5.12 in PINC (theta – R view)

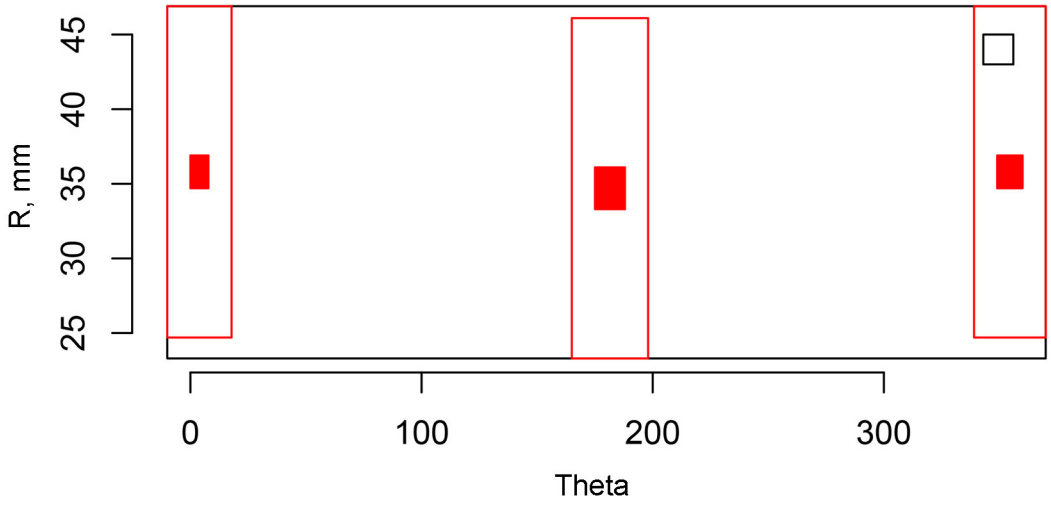

Figure 6.40. Indication Plot for PINC Team 373 (300 kHz, Non-Array Probe) Applied to Test Block 5.13 in PINC (theta – R view)

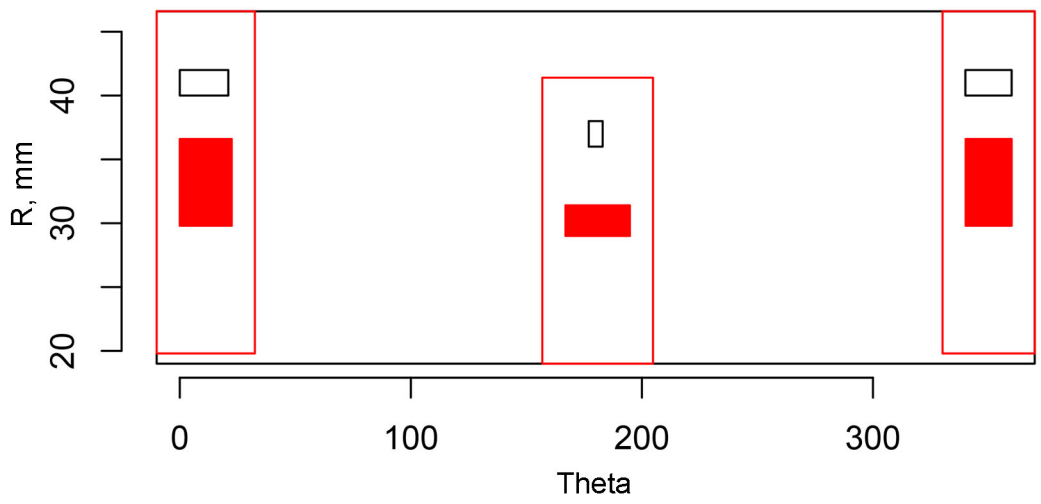

Figure 6.41. Indication Plot for PINC Team 373 (300 kHz, Non-Array Probe) Applied to Test Block 5.14 in PINC (theta – R view)

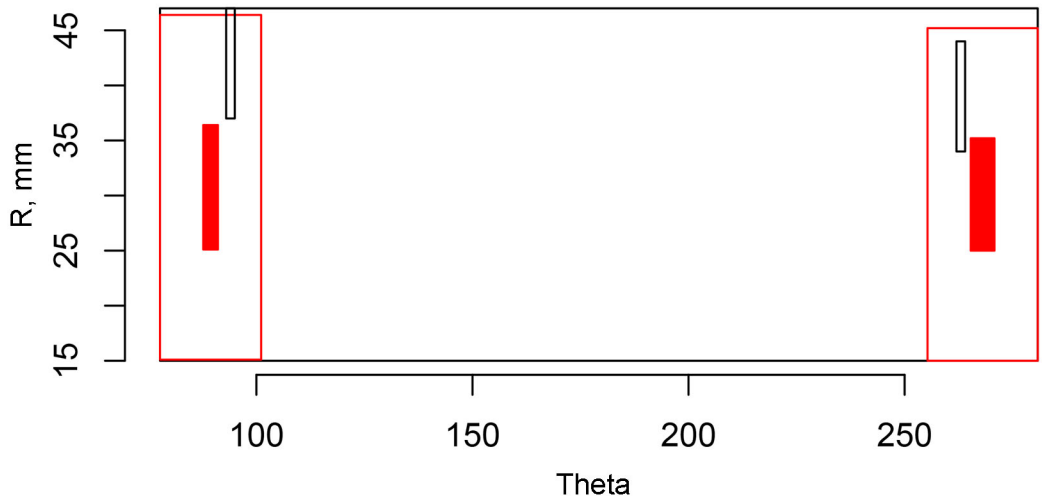

Figure 6.42. Indication Plot for PINC Team 373 (300 kHz, Non-Array Probe) Applied to Test Block 5.15 in PINC (theta – R view)

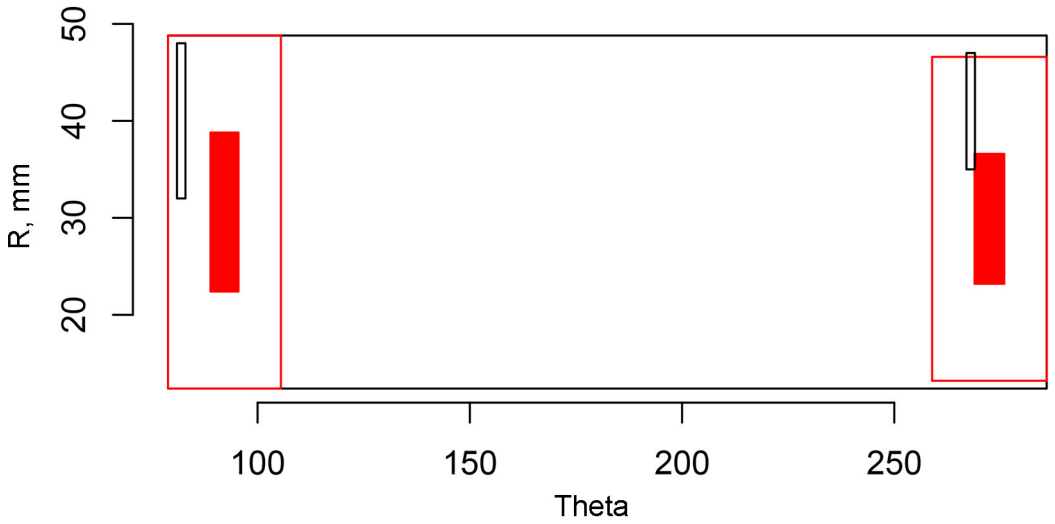

Figure 6.43. Indication Plot for PINC Team 373 (300 kHz, Non-Array Probe) Applied to Test Block 5.16 in PINC (theta – R view)

6.4.4 Indication Plots for PINC Team 70 Examinations (400 kHz, Non-Array Probe)

Indication plots for examinations performed by PINC team 70 on the surface of J-groove weld regions in BMI test blocks in PINC are provided in Figure 6.44 through Figure 6.54. No false calls are observed for examinations of any of the test blocks. Misses are only observed for test blocks 5.9 and 5.10. One miss is observed in test block 5.9 and three misses are observed for test block 5.10.

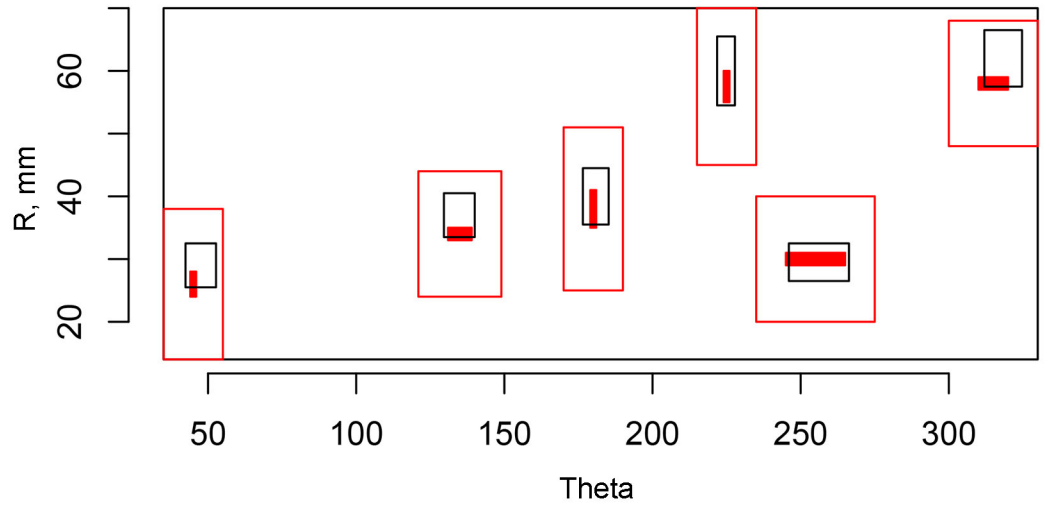

Figure 6.44. Indication Plot for PINC Team 70 (400 kHz, Non-Array Probe) Applied to Test Block 5.6 in PINC (theta – R view)

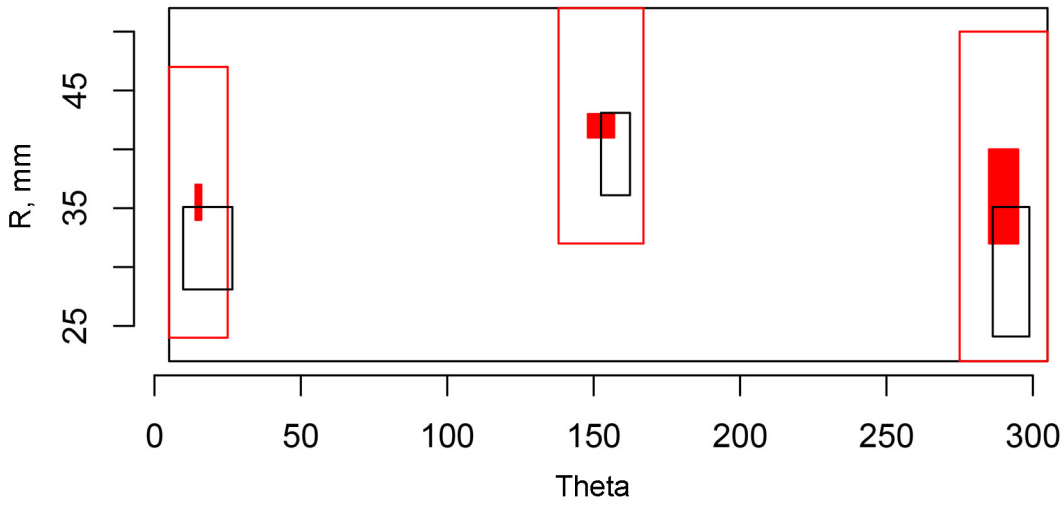

Figure 6.45. Indication Plot for PINC Team 70 (400 kHz, Non-Array Probe) Applied to Test Block 5.7 in PINC (theta – R view)

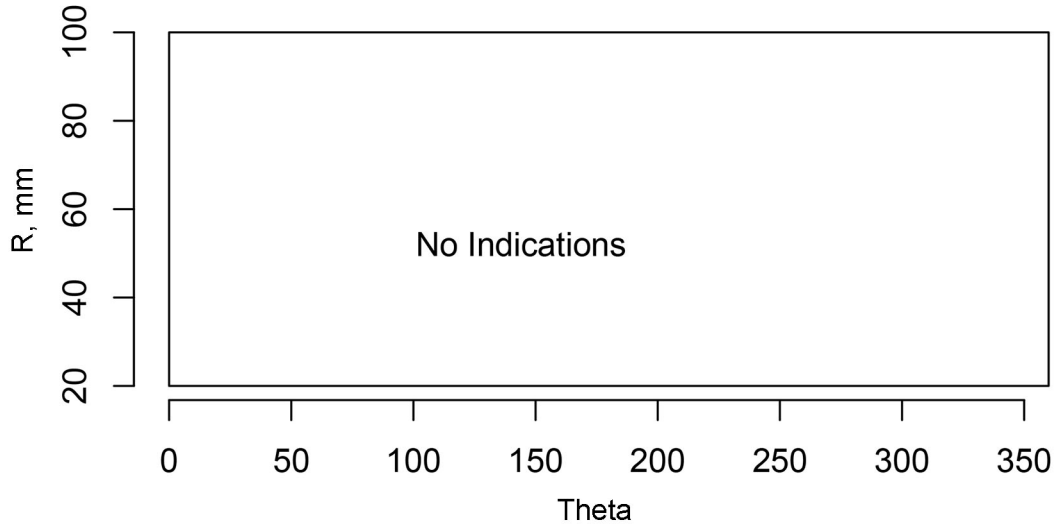

Figure 6.46. Indication Plot for PINC Team 70 (400 kHz, Non-Array Probe) Applied to Test Block 5.8 in PINC (theta – R view)

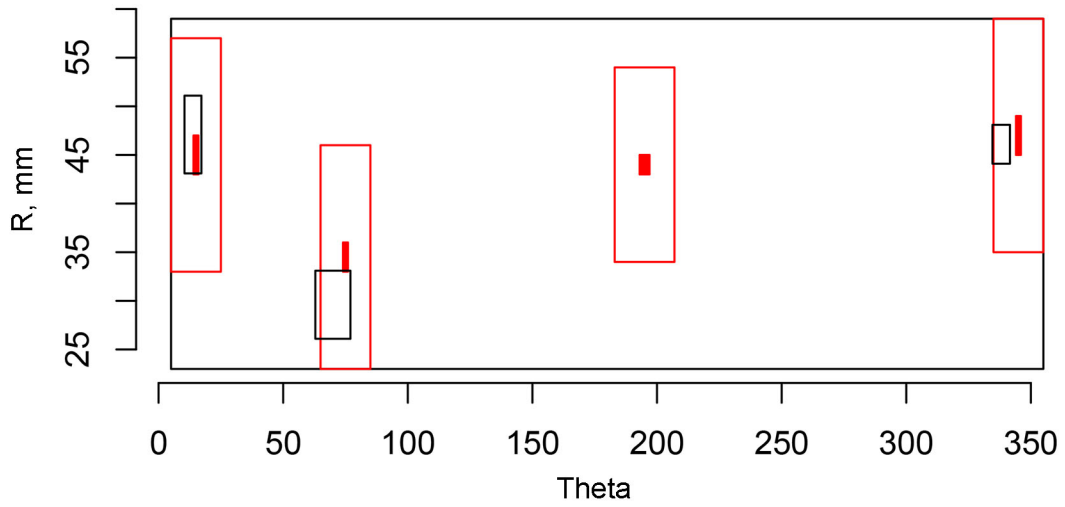

Figure 6.47. Indication Plot for PINC Team 70 (400 kHz, Non-Array Probe) Applied to Test Block 5.9 in PINC (theta – R view)

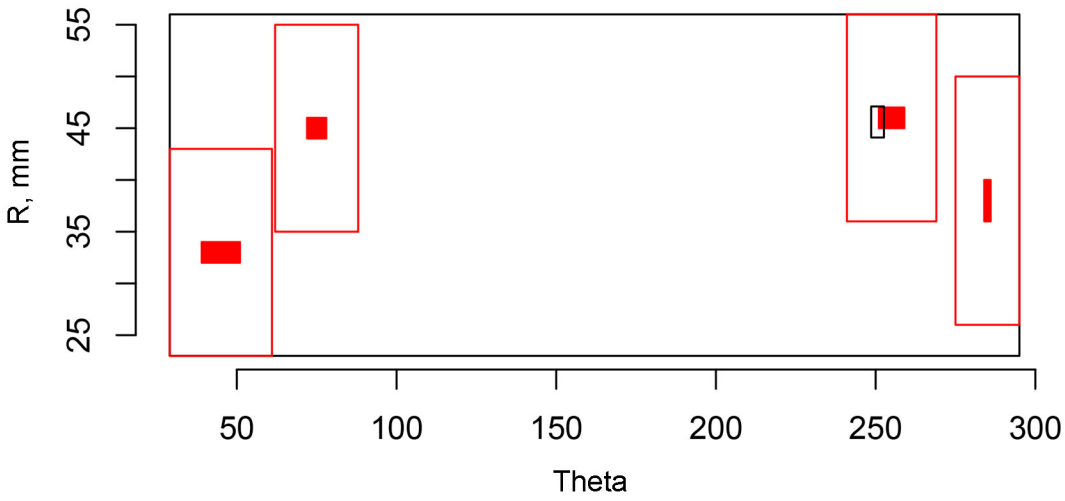

Figure 6.48. Indication Plot for PINC Team 70 (400 kHz, Non-Array Probe) Applied to Test Block 5.10 in PINC (theta – R view)

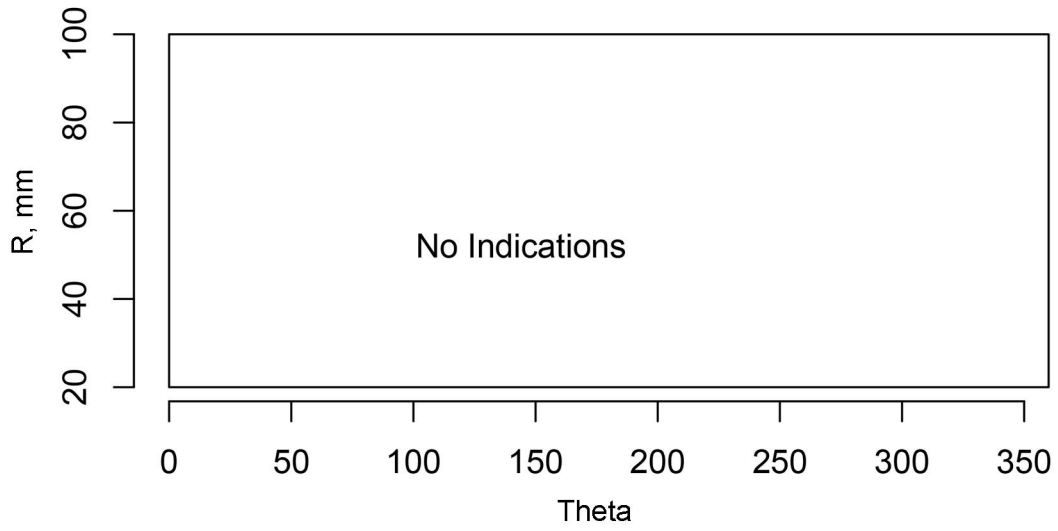

Figure 6.49. Indication Plot for PINC Team 70 (400 kHz, Non-Array Probe) Applied to Test Block 5.11 in PINC (theta – R view)

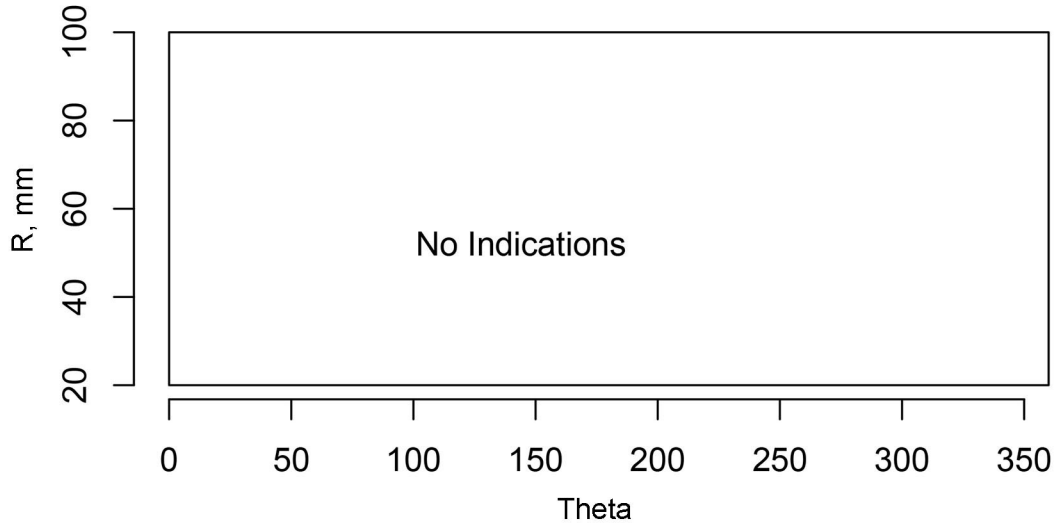

Figure 6.50. Indication Plot for PINC Team 70 (400 kHz, Non-Array Probe) Applied to Test Block 5.12 in PINC (theta – R view)

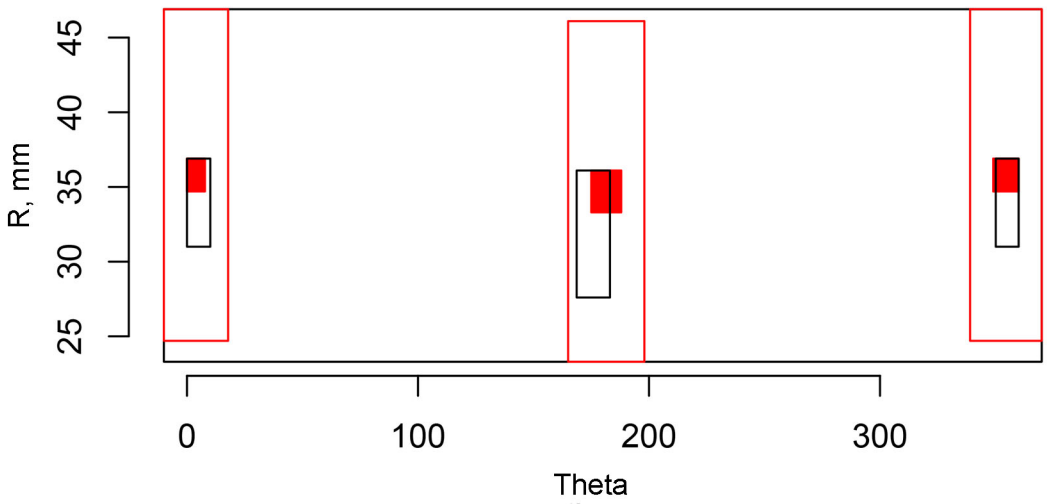

Figure 6.51. Indication Plot for PINC Team 70 (400 kHz, Non-Array Probe) Applied to Test Block 5.13 in PINC (theta – R view)

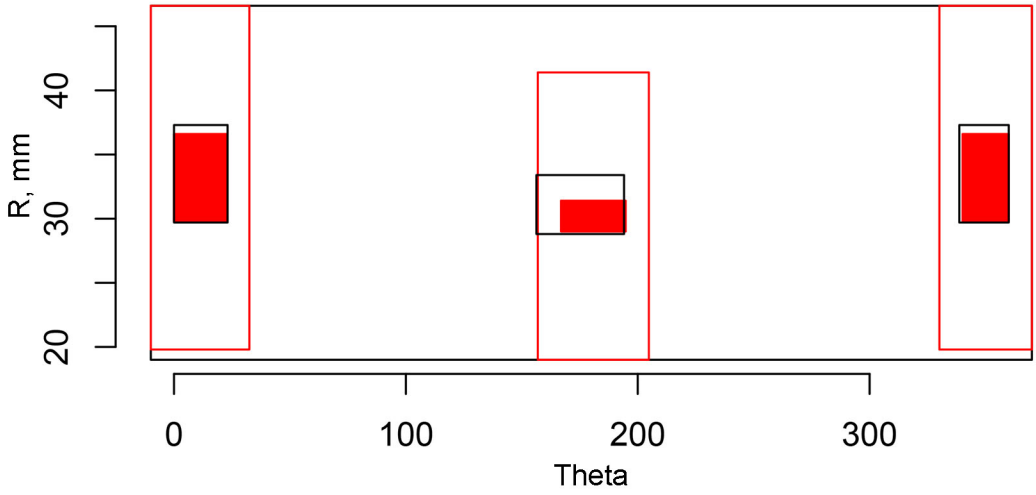

Figure 6.52. Indication Plot for PINC Team 70 (400 kHz, Non-Array Probe) Applied to Test Block 5.14 in PINC (theta – R view)

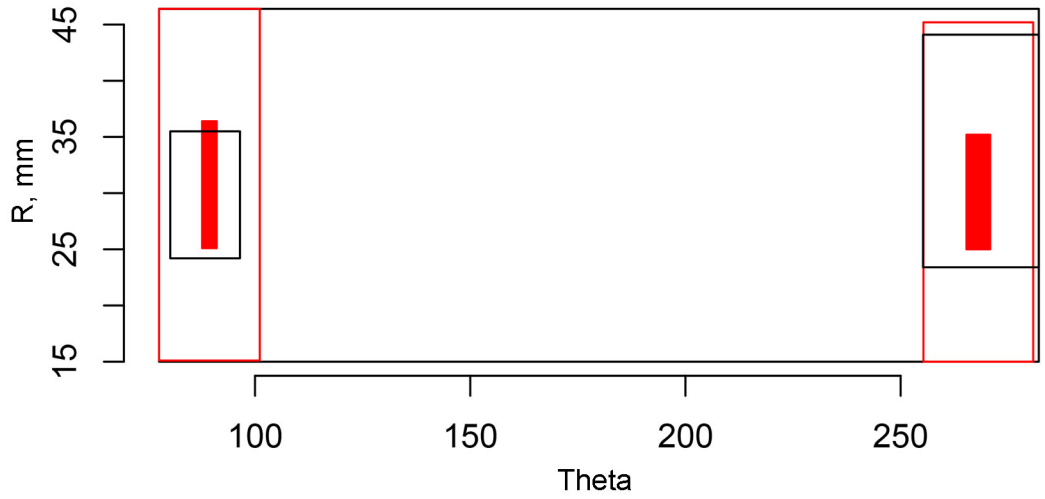

Figure 6.53. Indication Plot for PINC Team 70 (400 kHz, Non-Array Probe) Applied to Test Block 5.15 in PINC (theta – R view)

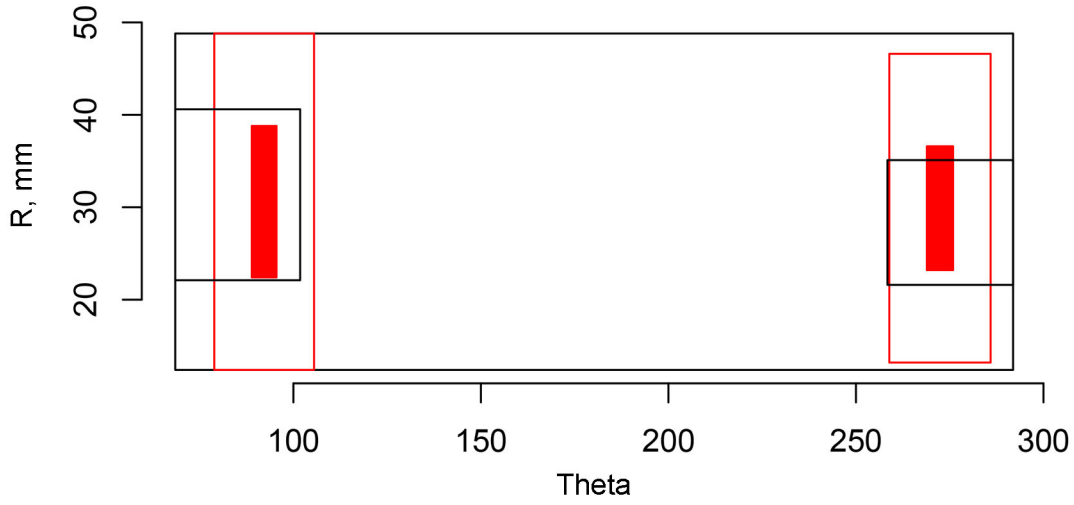

Figure 6.54. Indication Plot for PINC Team 70 (400 kHz, Non-Array Probe) Applied to Test Block 5.16 in PINC (theta – R view)

6.4.5 Indication Plots for PARENT Team 108 Examinations (500 kHz, Array Probe)

Indication plots for examinations performed by PARENT team 108 on the surface of J-groove weld regions in BMI test blocks in PARENT are provided in Figure 6.55 through Figure 6.59. False calls are only observed in examinations of test blocks P26 and P6. Misses are observed for test blocks P25, P26, and P6. However, three of the missed flaws in P25 and P26 are non-surface–breaking and result in no penalty. Branching of thermal fatigue cracks resulted in clustering and overlapping of tolerance boundaries of flaws in the indication plots for P6, P8, and P9. Although shown as distinct flaws in the indication plot, for the purpose of analysis, the clusters are each treated as one flaw and it was only necessary for an indication to overlap with the tolerance boundary of one of the flaws in the cluster to count as a hit for the entire cluster.

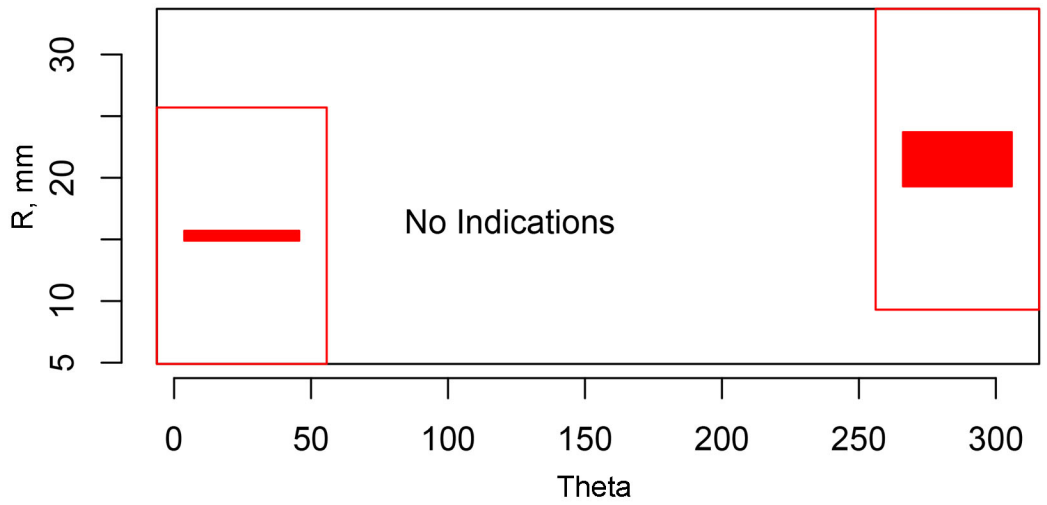

Figure 6.55. Indication Plot for PARENT Team 108 (500 kHz, Array Probe) Applied to Test Block P25 in PARENT (theta – R view)

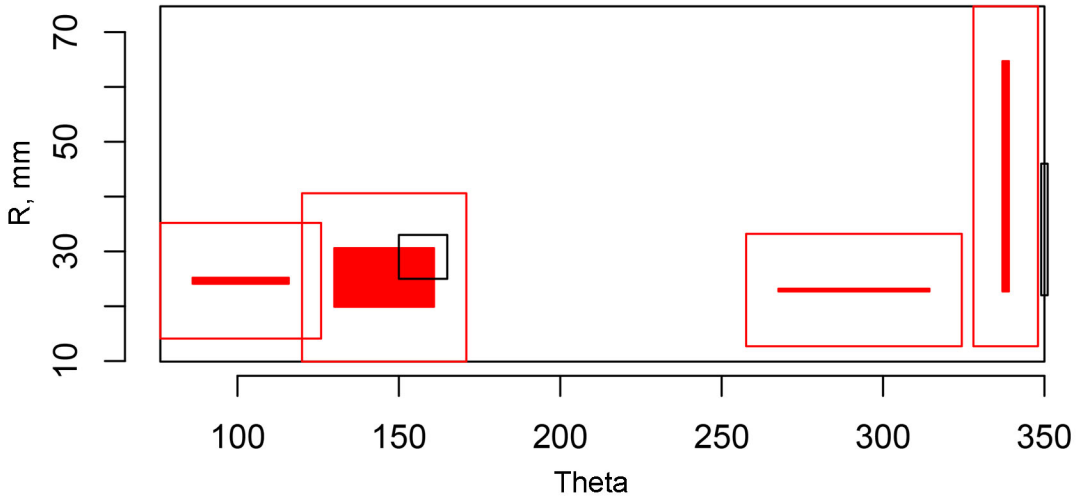

Figure 6.56. Indication Plot for PARENT Team 108 (500 kHz, Array Probe) Applied to Test Block P26 in PARENT (theta – R view)

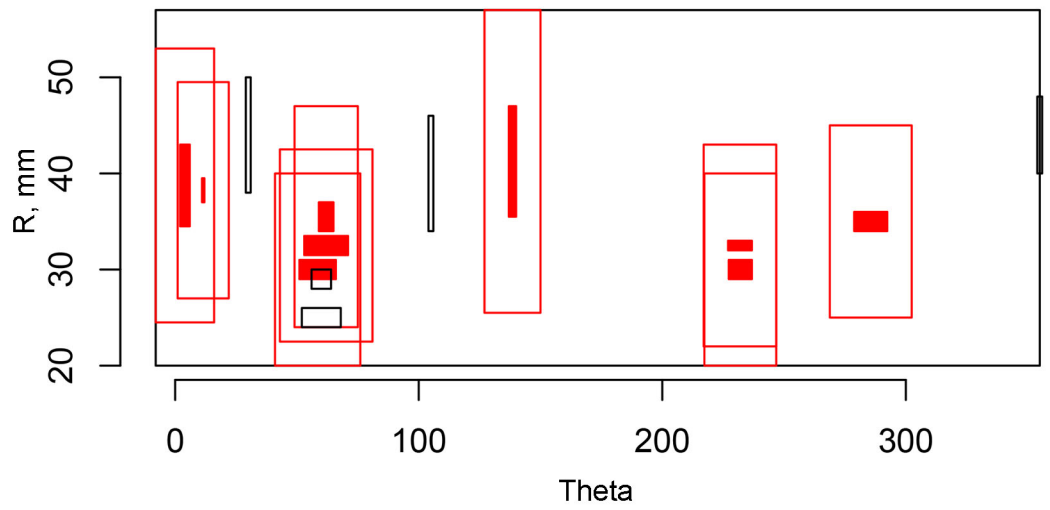

Figure 6.57. Indication Plot for PARENT Team 108 (500 kHz, Array Probe) Applied to Test Block P6 in PARENT (theta – R view)

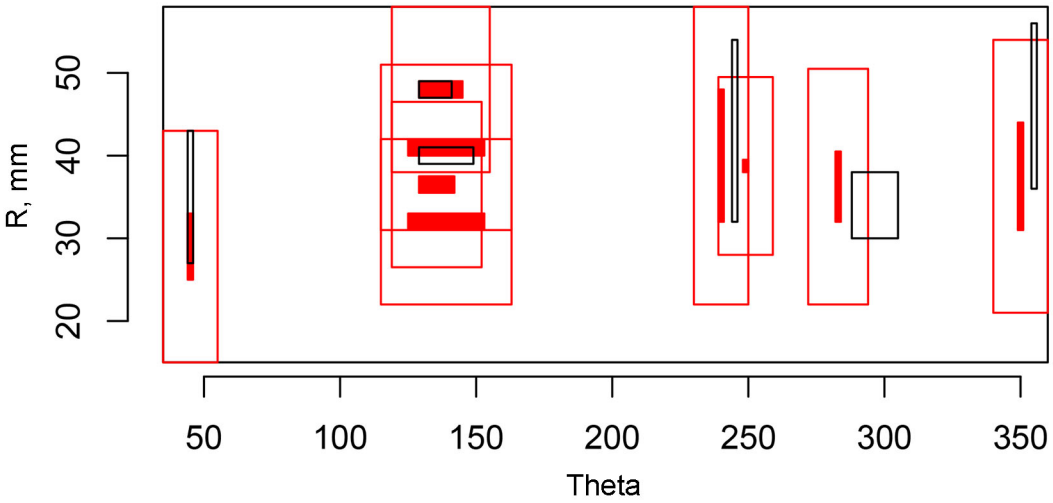

Figure 6.58. Indication Plot for PARENT Team 108 (500 kHz, Array Probe) Applied to Test Block P8 in PARENT (theta – R view)

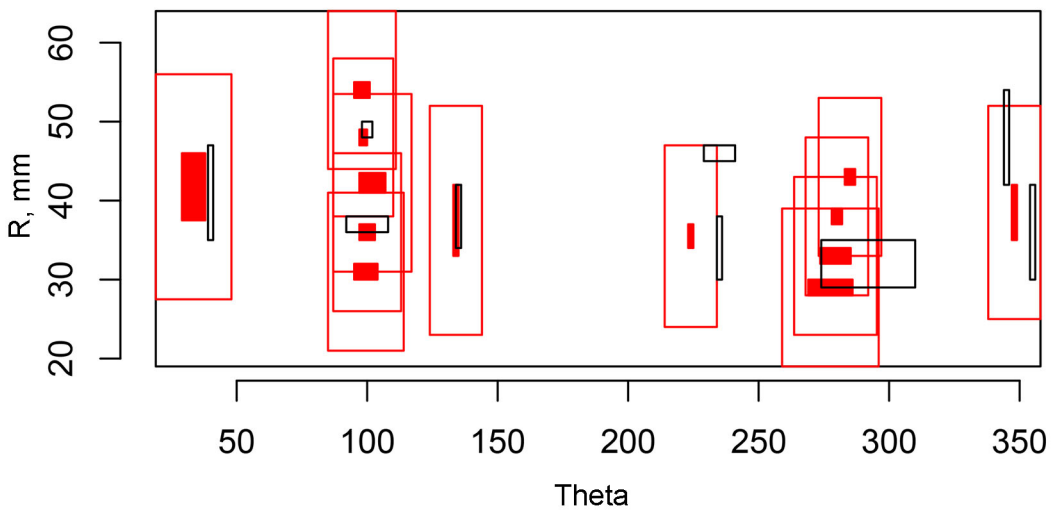

Figure 6.59. Indication Plot for PARENT Team 108 (500 kHz, Array Probe) Applied to Test Block P9 in PARENT (theta – R view)

6.4.6 Indication Plots for PARENT Team 124 Examinations (100 kHz, Non-Array Probe)

Indication plots for examinations performed by PARENT team 124 on the surface of J-groove weld regions in BMI test blocks in PARENT are provided in Figure 6.60 through Figure 6.64. One false call is observed in each of test blocks P6 and P9. Misses are only observed for test blocks P25 and P26. Similar to team 108, three of the missed flaws in P25 and P26 are non-surface–breaking and result in no penalty. The clustered flaws are treated the same way as described for team 108.

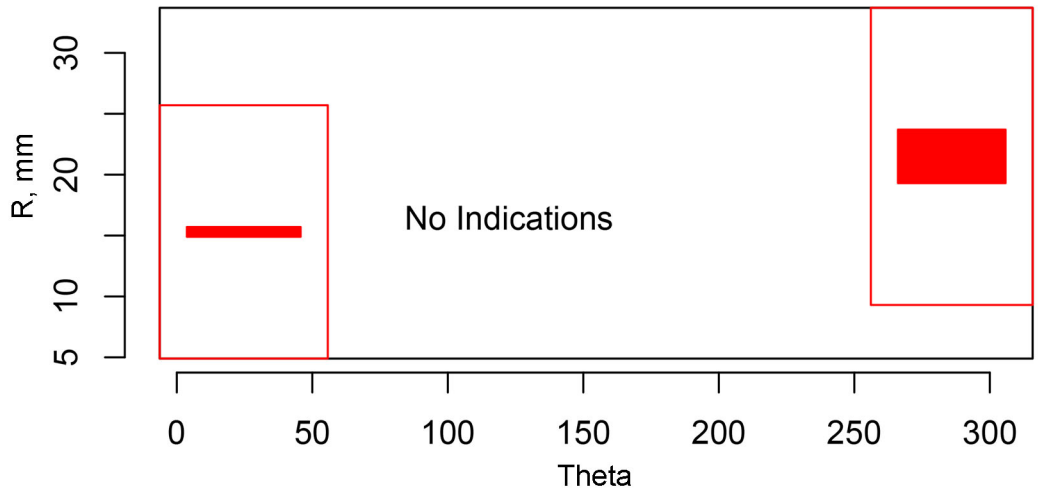

Figure 6.60. Indication Plot for PARENT Team 124 (100 kHz, Non-Array Probe) Applied to Test Block P25 in PARENT (theta – R view)

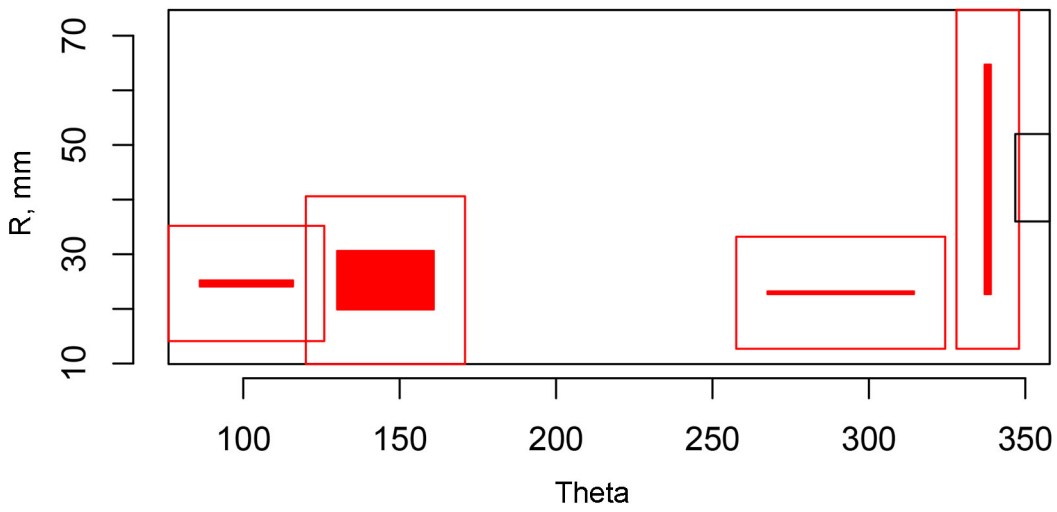

Figure 6.61. Indication Plot for PARENT Team 124 (100 kHz, Non-Array Probe) Applied to Test Block P26 in PARENT (theta – R view)

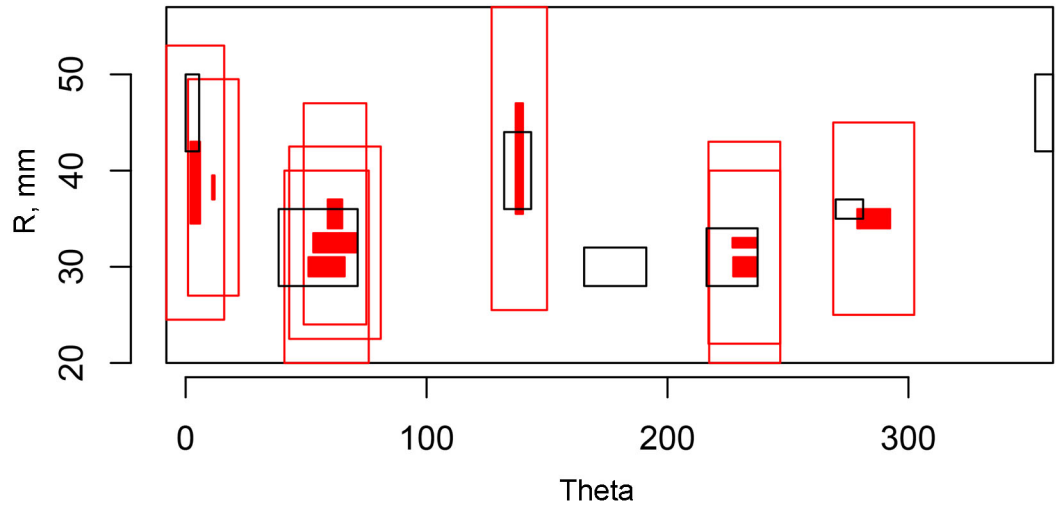

Figure 6.62. Indication Plot for PARENT Team 124 (100 kHz, Non-Array Probe) Applied to Test Block P6 in PARENT (theta – R view)

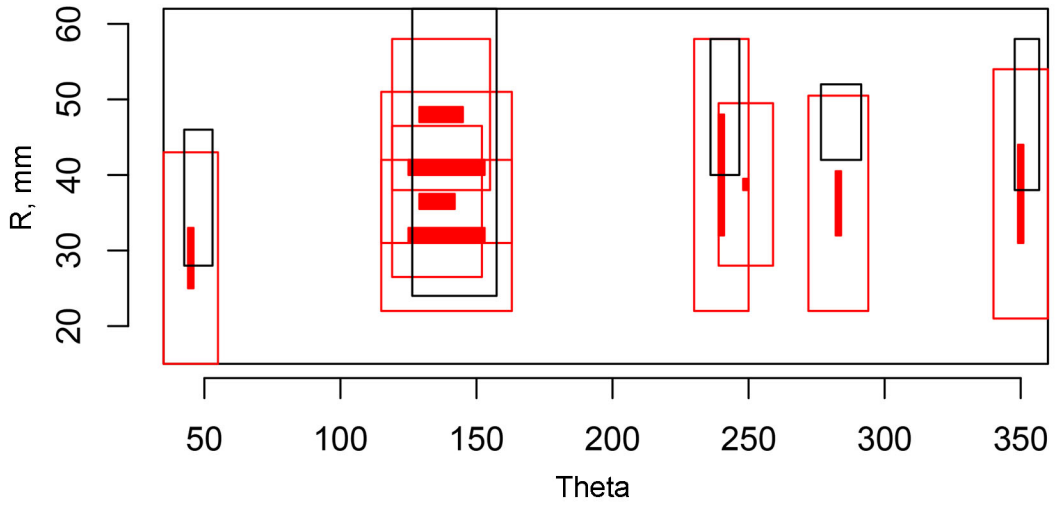

Figure 6.63. Indication Plot for PARENT Team 124 (100 kHz, Non-Array Probe) Applied to Test Block P8 in PARENT (theta – R view)

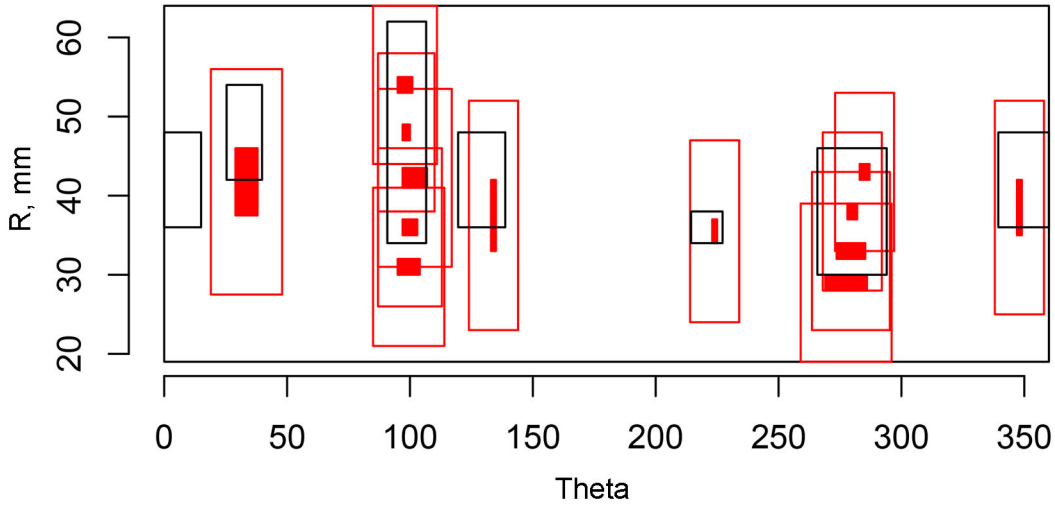

Figure 6.64. Indication Plot for PARENT Team 124 (100 kHz, Non-Array Probe) Applied to Test Block P9 in PARENT (theta – R view)

6.5 Detection Performance Analysis

The results of the detection performance analysis of ECT techniques applied to examination of BMI J-groove weld surfaces are summarized in this section. Results are presented as tables of POD at several discrete flaw sizes (depth and length) and as plots of POD curves as a function of flaw size. The tables also include tabulation of the FCR. An analysis of the effect of several variables such as probe frequency, flaw type, and probe configuration (array vs. non-array) on detection performance is also provided. The following section includes a tabulated summary of overall detection performance for ECT techniques. All of the flaws represented are surface-breaking with the exception of the two flaws in PINC test block 5.1 (PARENT test block P25) and one of the flaws in PINC test block 5.3 (PARENT test block P26). Non-surface–breaking flaws are excluded from the analysis because all of the techniques analyzed are ECT techniques. Thus, teams are not penalized for missing non-surface–breaking flaws and are not credited if they do detect them.

6.5.1 Overall Detection Analysis Results

This section provides a tabulated summary of the overall detection performance of ECT techniques applied to examination of BMI J-groove weld surfaces. In Table 6.9, NOBS which, for overall detection performance, refers to the total number of flaws in the inspected test blocks. POD is these tables is not expressed as a function of any parameter, but is simply the overall POD obtained by dividing the detected flaws by NOBS. The FCR is the number of observed false calls per unit length. The FCP is calculated from Eq. (3.6) (Section 3.3).

Table 6.9. Overall Detection Performance by ECT Techniques Applied to BMI J-groove Weld Surface Examinations in PINC and PARENT.

Team	Frequency (kHz)	Array?	NOBS	POD, %	FCP, %	FCR, #/m
38	100	Y	25	40	46	24.58
99	200	Y	21	43	27	12.42
373	300	N	29	69	3	1.33
70	400	N	25	84	0	0.00
108	500	Y	34	79	17	7.69
124	100	N	34	94	5	1.92

6.5.2 Summary of Detection Performance as a Function of Flaw Depth

Table 6.10 provides a summary of detection performance versus flaw depth for each ECT technique. An aggregate plot of POD versus depth for all ECT techniques is provided in Figure 6.65.

Table 6.10. Summary of POD (%) versus Flaw Depth for ECT Techniques Applied to BMI J-groove Weld Surface Examinations in PINC and PARENT

Team	Frequency (kHz)	Array?	NOBS	FCR	0 mm	5 mm	10 mm	15 mm
38	100	Y	25	24.58	57	49	41	35
99	200	Y	21	12.42	34	34	33	33
373	300	N	29	1.33	13	37	70	87
70	400	N	25	0.00	10	76	99	100
108	500	Y	34	7.69	34	73	93	98
124	100	N	34	1.92	31	84	98	100
All			168	8.52	28	59	84	94

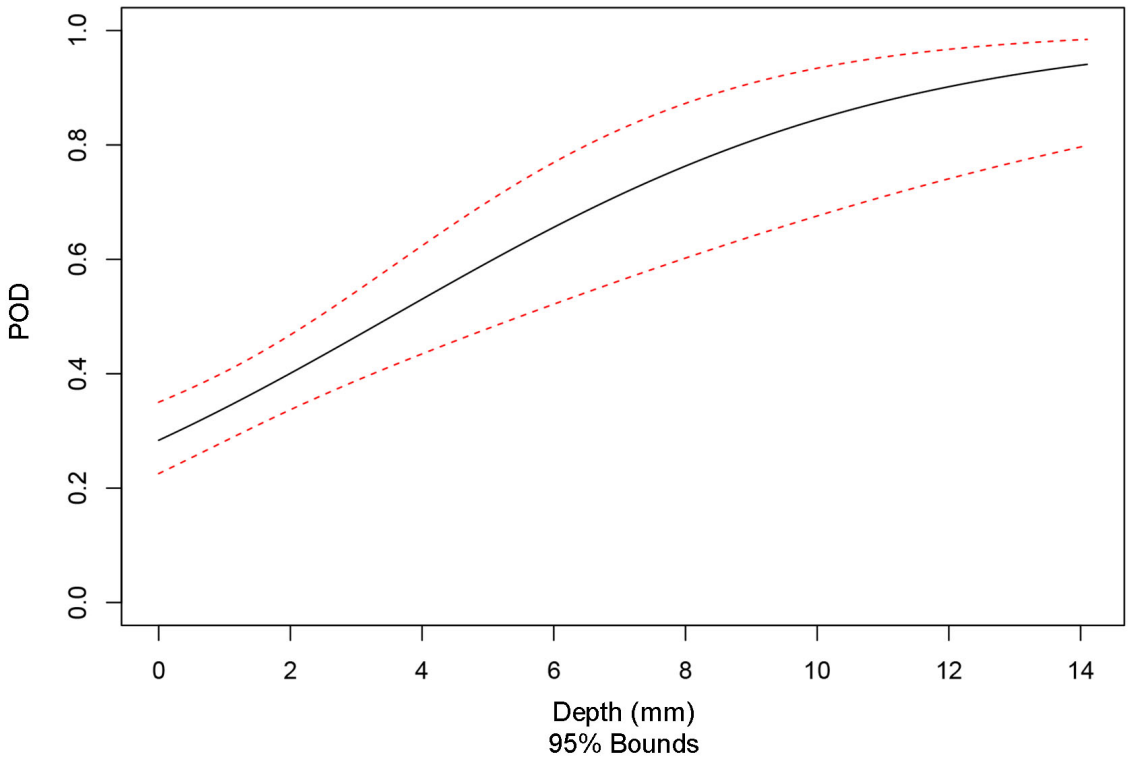

Figure 6.65. Aggregate Probability of Detection Curve versus Depth for ECT Techniques Applied to Examination of J-groove Weld Surfaces in PINC and PARENT

6.5.3 Summary of Detection Performance as a Function of Flaw Length

Table 6.11 provides a summary of detection performance versus flaw depth for each ECT technique. An aggregate plot of POD versus depth for all ECT techniques is provided in Figure 6.66.

Table 6.11. Summary of POD (%) versus Flaw Length for ECT Techniques Applied to BMI J-groove Weld Surface Examinations in PINC and PARENT

Team	Frequency (kHz)	Array?	NOBS	FCR	0 mm	5 mm	10 mm	15 mm
38	100	Y	25	24.58	55	55	55	56
99	200	Y	21	12.42	34	34	35	35
373	300	N	29	1.33	12	25	44	66
70	400	N	25	0.00	6	47	93	99
108	500	Y	34	7.69	51	56	61	66
124	100	N	34	1.92	38	62	82	92
All			168	8.52	28	45	64	79

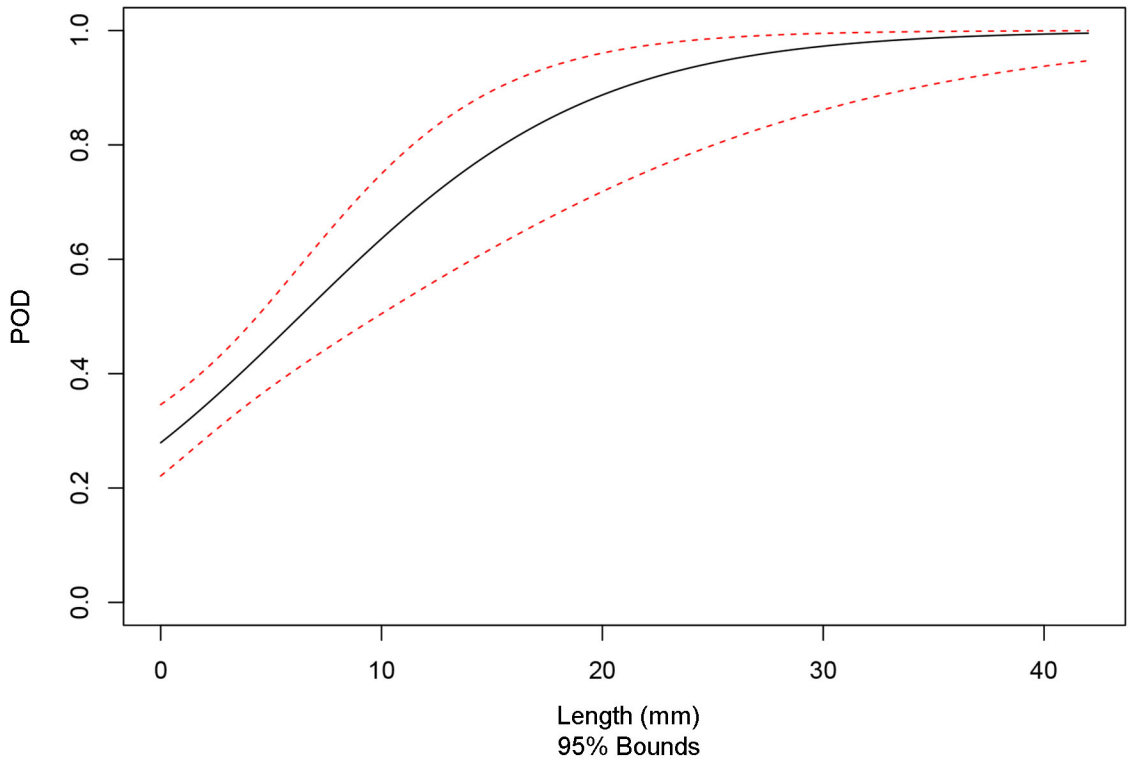

Figure 6.66. Aggregate Probability of Detection Curve versus Length for ECT Techniques Applied to Examination of J-groove Weld Surfaces in PINC and PARENT

6.5.4 Influence of Inspection Variables on Detection Performance

The influence that specific variables associated with the testing have on the results are summarized in this section. Table 6.12 provides a summary of average POD and standard deviation for ECT techniques applied to the J-groove weld surfaces on BMI test blocks in PINC and PARENT round-robin studies for flaw depths binned in ranges from 0 mm, 0–6 mm, 6–10 mm, and greater than 10 mm. These results indicate that PARENT test results were higher than PINC. Aggregated over all flaw sizes, the analysis indicates statistically different performance for PINC and PARENT with a level of significance (i.e., p-value) of 0.000431. This is to be interpreted as the probability that the results in Table 6.12 could be obtained given that PINC results are actually better than PARENT is less than 0.000431. This could be expected given that the flaws in BMI test blocks used in PARENT were thermal fatigue cracks that displayed significant branching at the surface. Thus, these flaws could be expected to have a more significant physical presence at the surface than other flaw types of similar depth. However, Table 6.12 also shows that performance in PINC and PARENT is basically equivalent for flaws deeper than 10 mm.

Table 6.13 provides a summary of average POD and standard deviation for ECT techniques with frequencies below and above 250 kHz for flaw depths binned in ranges from 0 mm, 0–6 mm, 6–10 mm, and greater than 10 mm. The table indicates better performance for frequencies greater than 250 kHz in comparison to frequencies less than 250 kHz over all flaw sizes. Aggregated over all flaw sizes, the analysis indicates statistically different performance for ECT techniques with frequencies greater than 250 kHz in comparison to ECT techniques with frequencies less than 250 kHz with a level of significance (i.e., p-value) of 8.12×10^{-6}. However, this is likely skewed by the results at 0 mm (false call probability), which show a very large gap in performance. Further, the results at 0 mm are counterintuitive as the expectation is that a higher probe frequency would lead to a higher false call rate because of increased

sensitivity to superficial surface features. It is possible that this counterintuitive result is caused by a confounding of the frequency variable with the probe configuration variable. Otherwise, the results indicate a generally expected trend of better detection performance above 250 kHz for flaw sizes of 0–6 mm, 6–10 mm, and greater than 10 mm.

Table 6.14 provides a summary of average POD and standard deviation for ECT probe configurations for flaw depths binned in ranges from 0 mm, 0–6 mm, 6–10 mm, and greater than 10 mm. The probe configurations are denoted as "Array" and "No Array." The table indicates better performance for "No Array" configurations than for "Array" configurations. Aggregated over all flaw sizes, the analysis indicates statistically different performance for ECT probe configurations "Array" and "No Array" with a level of significance (i.e., p-value) of 6.35×10^{-11}. However, similar to Table 6.13, the results in Table 6.14 are likely skewed by the data at 0 mm for which a large gap in performance is indicated. The much larger false call probability for "Array" configurations in comparison to "No Array" configurations may be caused by greater variation of the lift-off and other orientation parameters of individual coils in "Array" probes in comparison to "No Array" probes. In reviewing Table 6.1 and Table 6.2, it is apparent that two "Array" probes have frequencies less than 250 kHz and one "Array" probe has a frequency greater than 250 kHz. Thus, poor false call performance for "Array" probes would contribute to poor false call performance for lower frequency techniques.

Finally, the influence of flaw orientation on detection performance is summarize in Table 6.15 for flaw depths binned in ranges from 0–6 mm, 6–10 mm, and greater than 10 mm. Aggregated over all flaw sizes, the level of significance (i.e., p-value) is 0.599. This means that there is a rather high probability that flaw orientation has no influence on detection performance given the results in Table 6.15.

Table 6.12. Summary of Average POD (in %) and Standard Deviation (in %) by Round Robin Study and Flaw Depth

	0 mm	0–6 mm	6–10 mm	> 10 mm
PARENT	40±16	88±7	96±4	72±11
PINC	52±7	48±7	68±9	75±9

Table 6.13. Summary of Average POD (in %) and Standard Deviation (in %) by ECT Frequency and Flaw Depth

	0 mm	0–6 mm	6–10 mm	> 10 mm
< 250 kHz	85±7	53±8	77±8	67±11
> 250 kHz	20±7	69±8	86±7	79±8

Table 6.14. Summary of Average POD (in %) and Standard Deviation (in %) by ECT Probe Configuration and Flaw Depth

	0 mm	0–6 mm	6–10 mm	> 10 mm
Array	92±6	44±8	73±9	61±12
No Array	13±6	78±7	89±6	83±8

Table 6.15. Summary of Average POD (in %) and Standard Deviation (in %) by Flaw Orientation and Flaw Depth

	0–6 mm	6–10 mm	> 10 mm
Axial	58±8	82±10	74±10
Circumferential	62±9	77±8	79±10
Diagonal	75±23	100±11	50±25

6.6 Length Sizing Performance Analysis Results

The results of length sizing analysis are provided in Table 6.16. From this table it appears that techniques operated at a frequency of 100 kHz performed much worse than all other techniques based on the RMSE and bias data. Regression plots for each of the ECT techniques are included in Figure 6.67 through Figure 6.72. These plots indicate that PINC teams 373 and 70 actually provided the best length sizing response as the regression fits are closest to ideal for these two teams.

Table 6.16. Tabulated Summary of Length Sizing RMSE and Bias for ECT Techniques Applied to J-groove Weld Surface Examinations in PARENT and PINC

Team	Frequency (kHz)	Array?	NOBS	Bias	RMSE
38	100	Y	10	15.6	30.9
99	200	Y	9	−0.4	2.5
373	300	N	20	−0.2	4.0
70	400	N	21	2.8	4.0
108	500	Y	27	3.9	8.1
124	100	N	32	11.2	15.6
All			119	5.6	12.9

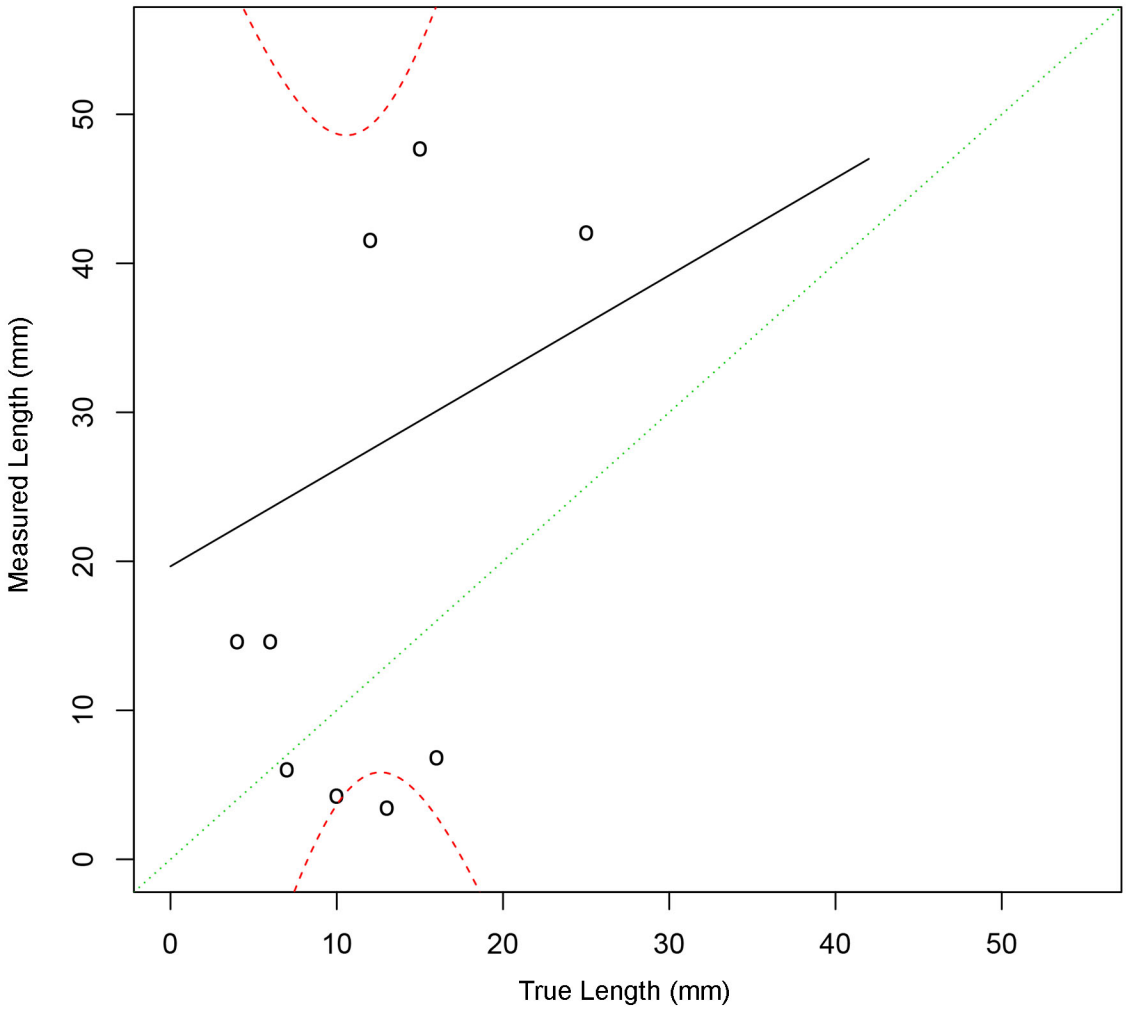

Figure 6.67. Length Sizing Regression Plot for PINC Team 38 Employing a 100 kHz Array ECT Probe to the Surface of J-groove Welds in BMI Test Block Examinations

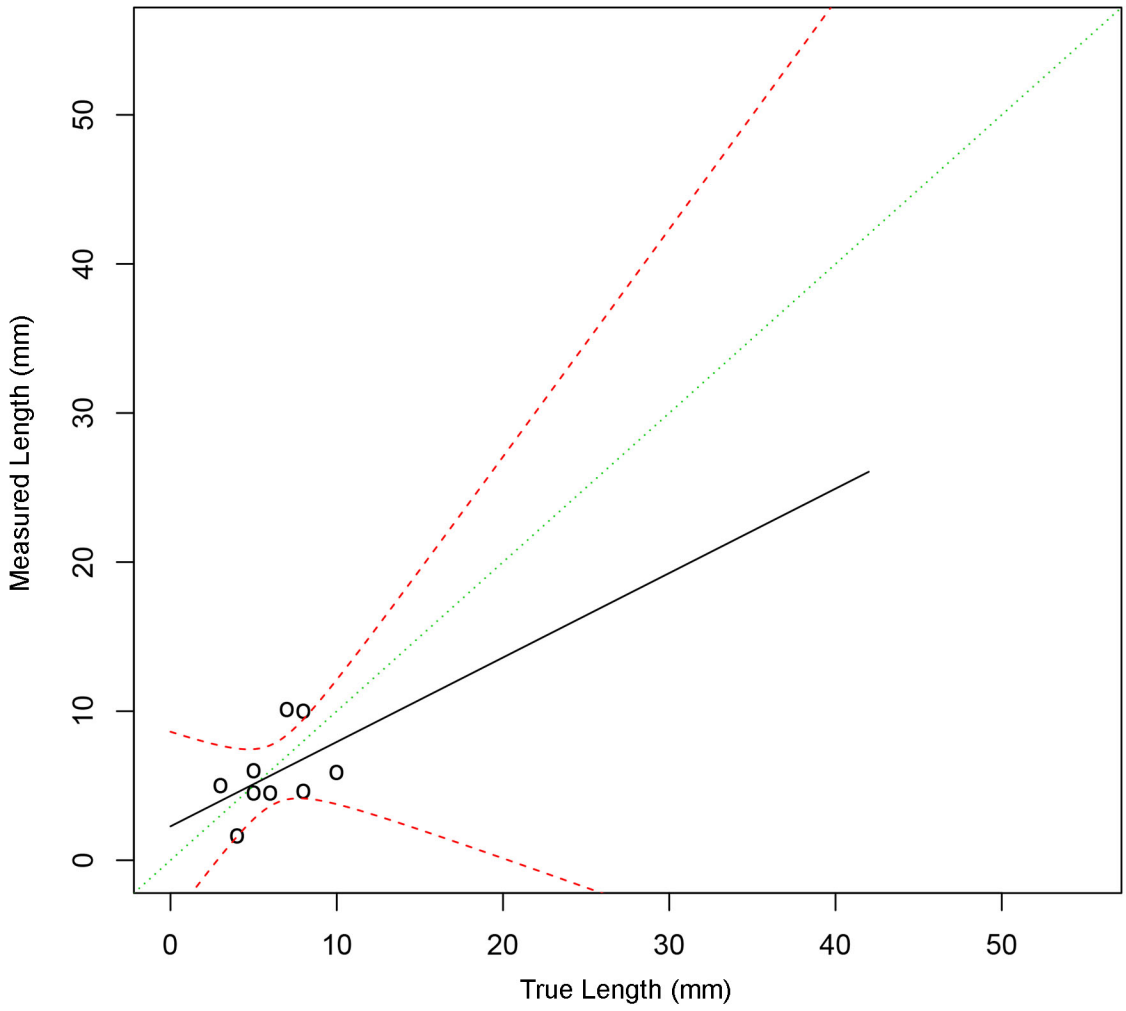

Figure 6.68. Length Sizing Regression Plot for PINC Team 99 Employing a 200 kHz Array ECT Probe to the Surface of J-groove Welds in BMI Test Block Examinations

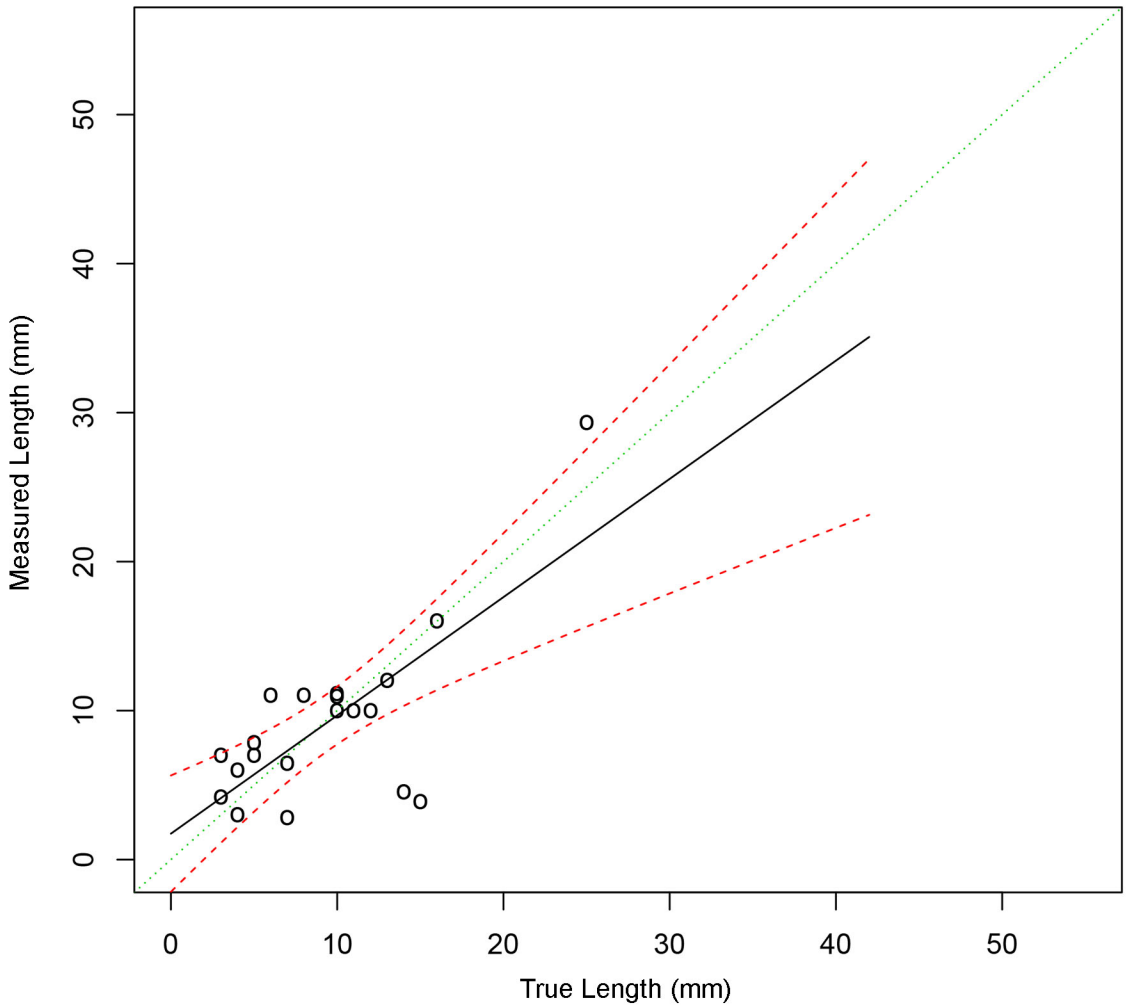

Figure 6.69. Length Sizing Regression Plot for PINC Team 373 Employing a 300 kHz Non-array ECT Probe to the Surface of J-groove Welds in BMI Test Block Examinations

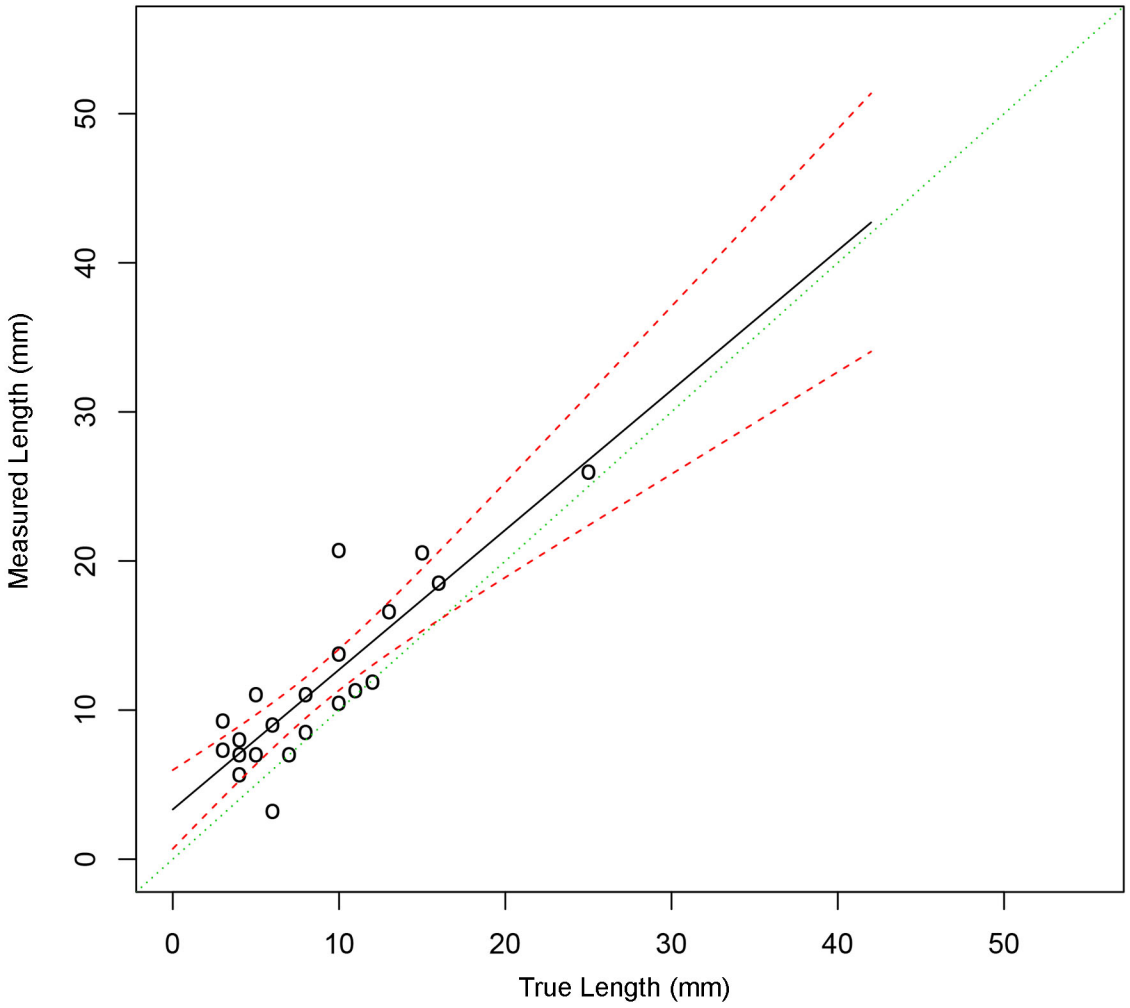

Figure 6.70. Length Sizing Regression Plot for PINC Team 70 Employing a 400 kHz Non-array ECT Probe to the Surface of J-groove Welds in BMI Test Block Examinations

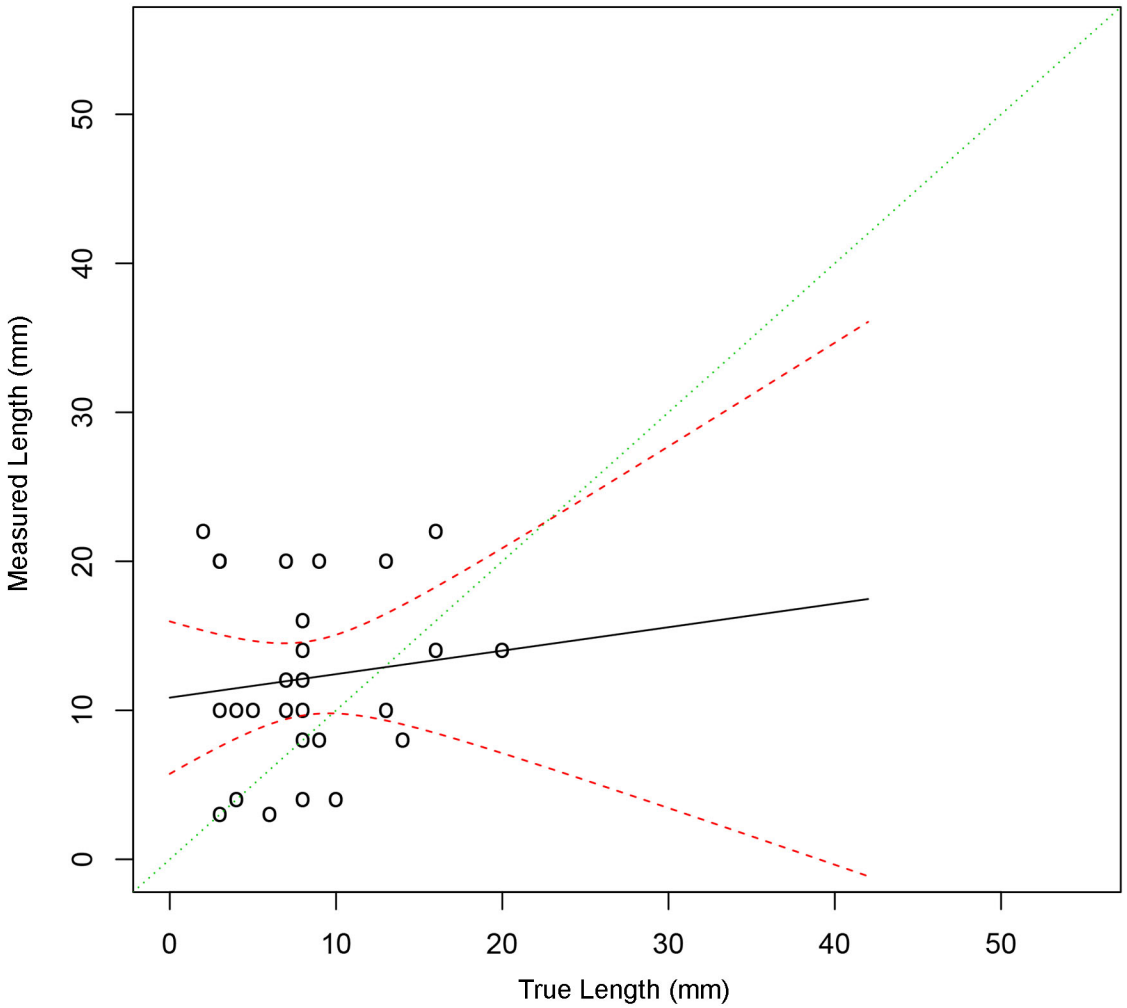

Figure 6.71. Length Sizing Regression Plot for PARENT Team 108 Employing a 500 kHz Array ECT Probe to the Surface of J-groove Welds in BMI Test Block Examinations

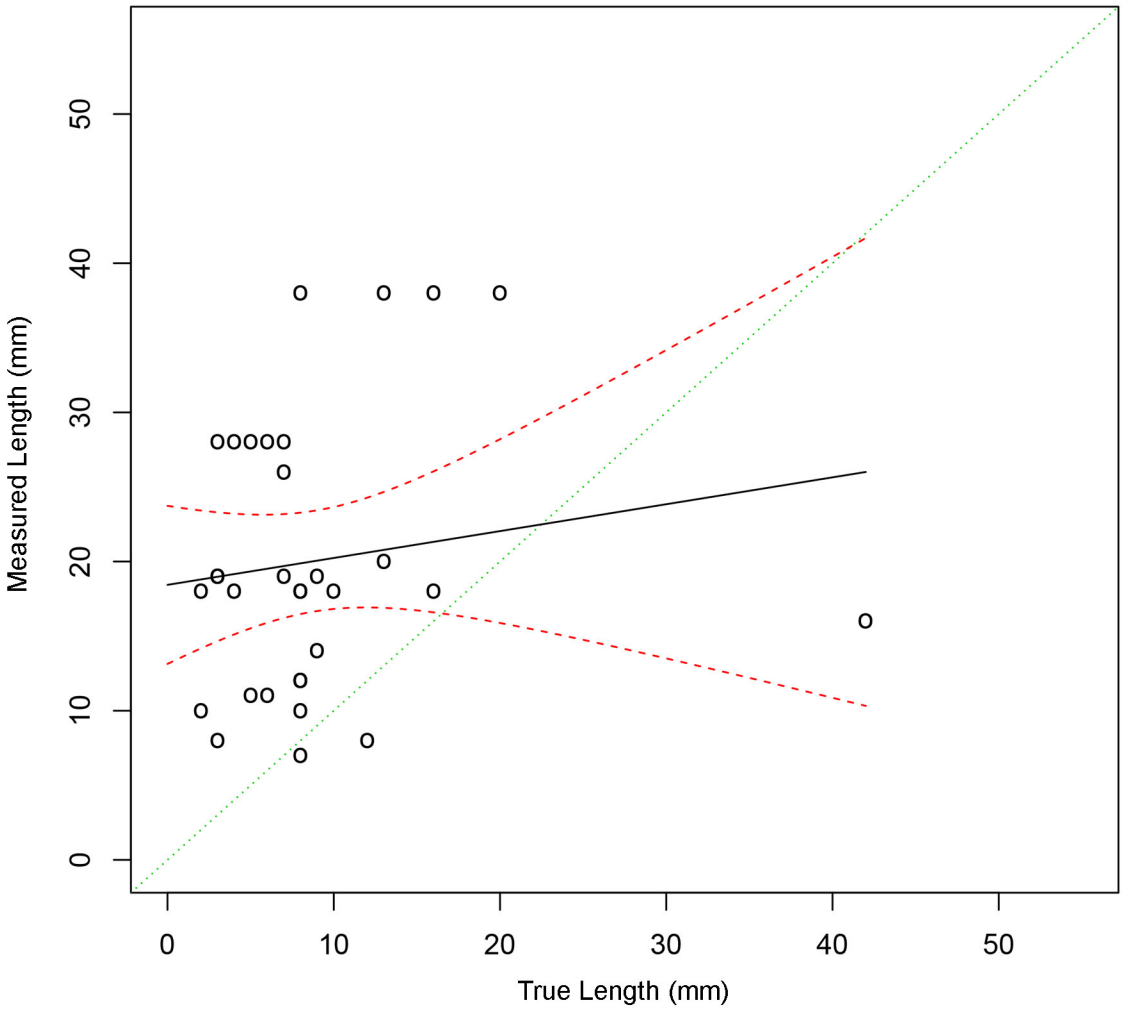

Figure 6.72. Length Sizing Regression Plot for PARENT Team 124 Employing a 100 kHz Non-array ECT Probe to the Surface of J-groove Welds in BMI Test Block Examinations

7.0 Summary and Conclusions

Analysis of PARENT blind test data at the technique level of inspection data is documented along with a combined analysis of PINC and PARENT data collected from inspection of BMI test blocks in this report. In PARENT, an inspection was defined as the application of a procedure by a team to examine a test block. The procedure could include the implementation of one or more techniques for flaw detection and sizing purposes. The outcome of an inspection by a procedure is then determined from combined information obtained from each technique employed by the procedure. In this effort, the analysis of data at the technique level is motivated by the desire to increase the sample size of ECT data collected from DMW test blocks in PARENT and to provide opportunity for more extensive comparison of data collected during "Blind" and "Quickblind" testing. The motivation for performing a combined analysis on data collected on BMIs in PINC and PARENT is also to increase sample size in an effort to derive more insight on the performance of techniques applied to inspect BMI test blocks.

The ECT performance reported in PARENT was worse than the performance reported in PINC. In PINC, ECT techniques were applied to SBDMWs; in PARENT, they were applied to LBDMWs. However, it is not clear why the test block size would have an influence on ECT performance. Another possible factor contributing to the difference in observed ECT performance in PINC and PARENT was the limited sample size in PARENT. In PARENT, only one ECT procedure was applied.

The result of increasing the PARENT ECT data sample size by including technique-level ECT data was an improvement in the estimated detection performance. The sample size was increased by more than a factor of two and the POD at 5 mm and 10 mm flaw depths increased substantially (from 23% to 34% at 5 mm and from 76% to 93% at 10 mm, respectively), making the results more consistent with PINC (80% at 5 mm and 99% at 10 mm).

In PARENT, comparison between Blind and Quickblind testing was made by comparing the performance of procedures that were common to both tests. This limited the comparison to procedure UT.PAUT.113, which was applied in both Blind and Quickblind testing, and to procedures UT.ECT.144 and UT.ECT.106. These procedures are mostly identical with UT.ECT.144 applied to the Blind test and UT.ECT.106 applied to the Quickblind test. A comparison of Quickblind and Blind test results from procedures UT.PAUT.113, UT.ECT.144, and UT.ECT.106 is summarized in Section 6.3 of NUREG/CR-7235 (Meyer and Heasler 2017). A meaningful comparison of detection performance could not be performed because detection performance in Quickblind testing was perfect at the procedure level. With respect to sizing performance, the only distinct trend observed between Blind and Quickblind testing was an apparent strong negative bias in Quickblind length sizing performance relative to Blind length sizing performance.

A more extensive comparison between Blind and Quickblind testing was facilitated by analyzing PAUT and conventional UT data at the technique level. The result of this analysis indicates that detection performance in Quickblind testing was better than detection performance in Blind testing for both PAUT and conventional UT techniques. The comparison of depth sizing analysis results shows that depth sizing performance is similar between Blind and Quickblind testing for both PAUT and conventional UT techniques. Length sizing performance comparisons show that length sizing exhibits a negative bias in Quickblind testing relative to Blind testing when length sizing is performed by comparing the longest dimensions of flaws and associated indications. However, when length sizing is limited to axial flaws in the Blind testing and performed by only comparing the axial dimensions of flaws and associated indications in Blind testing and Quickblind testing, this negative bias is eliminated. The latter analysis was performed because the flaws in Quickblind testing were intended to be axially oriented even though destructive analysis indicated the flaws had a significant circumferential extent. These results indicate that

the flaws in Quickblind test blocks produce NDE responses consistent with axial flaws even though destructive analysis indicated significant branching of the flaws extending in the circumferential directions.

Finally, the sample size for BMI data was increased by combining PARENT data with PINC data. In this case, the number of teams from which results were available increased from two teams to six teams and the number of flaw observations more than doubled. This enabled a more extensive analysis of BMI data and allowed more insights to be gained regarding the performance of techniques applied. The results indicated that higher frequency (> 250 kHz) ECT techniques performed better than lower frequency (< 250 kHz) ECT techniques and that techniques implemented with an array probe configuration performed worse than techniques not implemented in an array probe configuration. Array probe configurations also appeared to be associated with high false call rates. Low frequency (< 250 kHz) techniques were also associated with high false call rates; however, due to some confounding between frequency and array variables, it is likely that the array variable contributed strongly to these false call rates. Finally, significant difference in performance is observed, overall, between PINC and PARENT with PARENT performing better. This is likely caused by the nature of simulated flaws in the test blocks. PARENT test blocks utilized thermal fatigue cracks, which exhibited significant branching at the surface that could make them easier to detect with ECT.

8.0 References

Cumblidge SE, SR Doctor, PG Heasler and TT Taylor. 2010. *Results of the Program for the Inspection of Nickel Alloy Components*. NUREG/CR-7019; PNNL-18713, Rev. 1, U.S. Nuclear Regulatory Commission, Washington, D.C.

Meyer RM and PG Heasler. 2017. *Results of Blind Testing for the Program to Assess the Reliability of Emerging Nondestructive Techniques*. NUREG/CR-7235, PNNL-24196, U.S. Nuclear Regulatory Commission, Washington, D.C.

Pacific Northwest
NATIONAL LABORATORY

Proudly Operated by **Battelle** *Since 1965*

902 Battelle Boulevard
P.O. Box 999
Richland, WA 99352
1-888-375-PNNL (7665)

www.pnnl.gov

Prepared for the U.S. Nuclear Regulatory Commission
under a Related Services Agreement with the U.S. Department of Energy
CONTRACT DE-AC05-76RL01830

U.S. DEPARTMENT OF
ENERGY